p-ISSN 2312-2498
e-ISSN 2414-9381

http://jes.sumdu.edu.ua
jes@sumdu.edu.ua

JOURNAL OF ENGINEERING SCIENCES

BY-NC

ЖУРНАЛ ІНЖЕНЕРНИХ НАУК

ЖУРНАЛ ИНЖЕНЕРНЫХ НАУК

Volume 6
Issue 2 (2019)

The Ministry of Education and Science of Ukraine
Sumy State University

BY-NC

JOURNAL OF ENGINEERING SCIENCES

Scientific Journal

Volume 6, Issue 2 (2019)

p-ISSN 2312-2498
e-ISSN 2414-9381

Founded in 2014

The “Journal of Engineering Sciences” is an open access scientific journal that covers urgent issues of the up-to-date high-tech production, development of new engineering trends and future technologies. General topics of the journal concern manufacturing, mechanical and chemical engineering. The publication language is English. The editorial board represented by scientists from different International research institutions allows covering the journal’s topics and qualitatively evaluate all the submitted papers. The system of the double-blinded reviewing process provides a high-quality presentation of papers. The editorial policy including the submitting, reviewing, acceptance, and publication of the materials are completely transparent.

p-ISSN 2312-2498
e-ISSN 2414-9381

Recommended for publication
by the Academic Council of Sumy State University,
(minutes No. 5 of 12.12.2019)

The Journal is the scientific professional edition of Ukraine (Category “B”) in the field of Engineering Sciences ordered by the Ministry of Education and Science of Ukraine, November 7, 2018, No. 1218.

The information support of the “Journal of Engineering Sciences” is provided by the partners:

– International Association for Technological Development and Innovations (Ukraine): http://dsmie.sumdu.edu.ua;

– Faculty of Mechanical Engineering and Management, Poznan University of Technology (Poland): https://www.put.poznan.pl;

– Faculty of Manufacturing Technologies, Technical University of Kosice (Slovakia): http://www.fvt.tuke.sk;

– Faculty of Mechanical Engineering, University of West Bohemia (Czech Republic): http://www.fst.zcu.cz.

Editorial Board: Apt. LA 207, 2 Rymskogo-Korsakova St., 40007 Sumy, Ukraine
Contact Phones: +38 (0542) 331024; +38 (099) 3845740
E-mail: jes@sumdu.edu.ua
Website: http://jes.sumdu.edu.ua

State registration certificate of the print mass-media No. 20499-10299 PR.

© **Sumy State University, 2019**

JOURNAL OF ENGINEERING SCIENCES
ЖУРНАЛ ІНЖЕНЕРНИХ НАУК
ЖУРНАЛ ИНЖЕНЕРНЫХ НАУК
Web site: http://jes.sumdu.edu.ua
Volume 6, Issue 2 (2019)

TOPICS
OF THE "JOURNAL OF ENGINEERING SCIENCE"

1. Manufacturing Engineering:

- (A) Machines and Tools;
- (B) Technical Regulations and Metrological Support;
- (C) Materials Science.

2. Mechanical Engineering:

- (D) Dynamics and Strength of Machines;
- (E) Computational Mechanics.

3. Chemical Engineering:

- (F) Processes in Machines and Devices;
- (G) Energy Efficient Technologies;
- (H) Environmental Protection.

JOURNAL'S STATISTICS

- **Publication frequency:** biannually (2 issues per year)
- **Papers per issue:** 20
- **Acceptance rate:** 26 %
- **Timeline:**
  - days from submission of the manuscript to first decision: 30
  - days from acceptance at the publisher to published online: 14
- **Editorial Board:**
  - editors: 59
  - institutions: 41
  - countries: 24

EDITORIAL BOARD

EDITOR-IN-CHIEF

Dmytro KRYVORUCHKO, D.Sc., Professor, Sumy State University, Sumy, Ukraine

MANAGING EDITOR

Ivan PAVLENKO, Ph.D., Associate Professor, Sumy State University, Sumy, Ukraine

BOARD OF CO-EDITORS

Manufacturing Engineering

Eddy BAJIC, Ph.D., Professor, University of Lorraine, Nancy, France

Jose MACHADO, Ph.D., Professor, University of Minho, Braga, Portugal

Mechanical Engineering

Thomas MATHIA, Ph.D., Professor, Ecole Centrale de Lyon, Lyon, France

Jan PITEL, Ph.D., Professor, Technical University of Kosice, Presov, Slovakia

Chemical Engineering

Mathieu GAUTIER, Ph.D., Associate Professor, University of Lyon, Lyon, France

Vsevolod SKLABINSKYI, D.Sc., Professor, Sumy State University, Sumy, Ukraine

ADVISORY EDITORIAL BOARD

Praveen AGARWAL, Ph.D., Professor, Anand International College of Engineering, Jaipur, India

Peter ARRAS, D.Sc., Professor, KU Leuven, Leuven, Belgium

Volodymyr ATAMANYUK., D.Sc., Professor, Lviv Polytechnic National University, Lviv, Ukraine

Jean BOUYER, Ph.D., Associate Professor, University of Poitiers, Poitiers, France

Noel BRUNETIERE, Ph.D., Senior Researcher, University of Poitiers, Poitiers, France

Robert CEP, Ph.D., Professor, Technical University of Ostrava, Ostrava, Czech Republic

Olaf CISAK, Ph.D., Associate Professor, Poznan University of Technology, Poznan, Poland

Predrag DASIC, D.Sc., Professor, VTMS Trstenik, Trstenik, Serbia

Kostiantyn DYADYURA, D.Sc., Professor, Sumy State University, Sumy, Ukraine

Milan EDL, Ph.D., Associate Professor, University of West Bohemia, Pilsen, Czech Republic

Alex ENRICH-PRAST, Ph.D., Professor, Linkoping University, Linkoping, Sweden

Domenico GUIDA, Ph.D., Professor, University of Salerno, Salerno, Italy

Oleksandr GUSAK, Ph.D., Professor, Sumy State University, Sumy, Ukraine

Michal HATALA, Ph.D., Associate Professor, Technical University of Kosice, Presov, Slovakia

Koichi HASEGAWA, Ph.D., Associate Professor, Chubu University, Kasugai, Japan

Siamak HOSEINZADEH, Ph.D., Post Doc., University of Pretoria, Pretoria, South Africa

Yury IVANOV, Ph.D., Associate Professor, Chubu University, Kasugai, Japan

Fuat KARA, Ph.D., Assistant Professor, Duzce University, Istanbul, Turkey

Isak KARABEGOVIC, D.Sc., Professor, University of Bihac, Bihac, Bosnia and Herzegovina

Serhii KLIMENKO, D.Sc., Professor, Bakul Institute for Superhard Materials, National Academy of Sciences of Ukraine, Kyiv, Ukraine

Czeslaw KUNDERA, D.Sc., Professor, Kielce University of Technology, Kielce, Poland

Ivan KURIC, Ph.D., Professor, University of Zilina, Zilina, Slovakia

Milovan LAZAREVIC, Ph.D., Associate Professor, University of Novi Sad, Novi Sad, Serbia

Stanislaw LEGUTKO, D.Sc., Professor, Poznan University of Technology, Poznan, Poland

Oleksandr LIAPOSHCHENKO, D.Sc., Professor, Sumy State University, Sumy, Ukraine

Athanasios MAMALIS, D.Sc., Professor, Demokritos National Centre for Scientific Research, Athens, Greece

Arun MATHEW, Ph.D., Associate Professor, Vellore Institute of Technology, Vellore, India

Yurii MATSEVITYI, D.Sc., Professor, Podgornyi Institute for Mechanical Engineering Problems, National Academy of Sciences of Ukraine, Kharkiv, Ukraine

Ronald MERSKY, Ph.D., Associate Professor, Widener University, Chester, USA

Arun NAGARAJAH, D.Sc., Professor, University of Duisburg-Essen, Duisburg, Germany

Eduard Laurentiu NITU, Ph.D., Professor, University of Pitesti, Pitesti, Romania

Dragan PERAKOVIC, Ph.D., Professor, University of Zagreb, Zagreb, Croatia

Alejandro PEREIRA, Ph.D., Professor, University of Vigo, Vigo, Spain

Yurii PETRAKOV, D.Sc., Professor, National Technical University of Ukraine "Kyiv Polytechnic Institute", Kyiv, Ukraine

Roman PETRUS, D.Sc., Professor, Rzeszow University of Technology, Rzeszow, Poland

Leonid PLYATSUK, D.Sc., Professor, Sumy State University, Sumy, Ukraine

Frantisek POCHYLY, Ph.D., Professor, Brno Technical University, Brno, Czech Republic

Erwin RAUCH, Ph.D., Assistant Professor, Free University of Bozen-Bolzano, Bolzano, Italy

Yimin RONG, D.Sc., Professor, South University of Science and Technology, Shenzhen, China

Vitalii SIMONOVSKIY, D.Sc., Professor, Sumy State University, Sumy, Ukraine

Michael STORCHAK, D.Sc., Professor, Institute for Machine Tools of Stuttgart University, Stuttgart, Germany

Fabio TEIXEIRA, D.Sc., Professor, Federal University of Rio Grande do Sul, Porto Alegre, Brazil

Justyna TROJANOWSKA, Ph.D., Assistant Professor, Poznan University of Technology, Poznan, Poland

Kaname TSUTSUMIUCHI, D.Sc., Professor, Chubu University, Kasugai, Japan

Raul TURMANIDZE, D.Sc., Professor, Georgian Technical University, Tbilisi, Georgia

Michal VARCHOLA, Ph.D., Professor, Slovak University of Technology in Bratislava, Bratislava, Slovakia

George-Christopher VOSNIAKOS, Ph.D., Professor, National Technical University of Athens, Athens, Greece

Jozef ZAJAC, D.Sc., Professor, Technical University of Kosice, Presov, Slovakia

Viliam ZALOGA, D.Sc., Professor, Sumy State University, Sumy, Ukraine

Lianyu ZHENG, Ph.D., Professor, Beihang University, Beijing, China

PUBLISHING MANAGER

Kristina BERLADIR, Ph.D., Senior Lecturer, Sumy State University, Sumy, Ukraine

JOURNAL OF ENGINEERING SCIENCES
ЖУРНАЛ ІНЖЕНЕРНИХ НАУК
ЖУРНАЛ ИНЖЕНЕРНЫХ НАУК
Web site: http://jes.sumdu.edu.ua
Volume 6, Issue 2 (2019)

CONTENTS

MANUFACTURING ENGINEERING

MECHANICAL ENGINEERING

CHEMICAL ENGINEERING

JOURNAL OF ENGINEERING SCIENCES
ЖУРНАЛ ІНЖЕНЕРНИХ НАУК
ЖУРНАЛ ИНЖЕНЕРНЫХ НАУК

Web site: http://jes.sumdu.edu.ua

Volume 6, Issue 2 (2019)

To the Memory of Professor Volodymyr MARTSYNKOVSKYY is Dedicating

The world-famous scientist in the field of hydrodynamics, vibroreliability and hermetic sealing of rotary machines, the founder of scientific direction "Hermomechanics", honored worker of science and technology of Ukraine, distinguished professor of Sumy State University, doctor honoris causa, doctor of science, Professor Volodymyr Martsynkovskyy was born in November 25, 1926, in Shepetivka town, Khmelnytskyi region. In June 1941 he graduated from 7 classes of the school № 41 of Shepetivka town. During the German occupation (from September 1941 to October 1942) worked in the forge blacksmith, from October 1942 to December 1943 worked as a logger in the forest. On January 19, 1944, he was sent by the Nazis to Germany, to a camp for Ostarbeiters, where he worked in a locomotive depot on coal unloading, and from August 1944 he was a stoker on a steam locomotive. In December 1944 he was imprisoned in a solitary cell in Zwickau, from where he was released half-alive on April 16, 1945, by US troops. After his release, he moved to the Eastern Zone, and on May 15, 1945, he was called up by a field enlistment office to Pirna town (Germany) to the Soviet Army. He served as a driver (after short-term courses) in Germany, Czechoslovakia, Hungary, Bulgaria, and from May 1948 in Leningrad, where he was allowed to attend evening school for his excellent service. He graduated the 10 grades with a gold medal in 1951, after being demobilized from the army in October 1950.

After demobilization, he worked as a stoker in a boiler room in Leningrad until July 1951. After leaving school, he entered the Engineering and Physical Faculty of Kharkiv Polytechnic Institute in the specialty "Dynamics and Strength of Machines". He graduated with honors from the Institute in March 1957. During his studies at the Institute from September 1954 to April 1957, he worked as a part-time teacher of physics at the school of working youth No. 32 in Kharkiv. In 1956, he married Galina Yunchenko, a teacher of Russian and literature at the school where he worked.

From March 1, 1957, he worked as a junior researcher of the Hydromachine Laboratory of the Academy of Sciences of the USSR (now the A. Pidgorny Institute of Mechanical Engineering Problems, NAS of Ukraine), where he was engaged in experimental and theoretical studies of high-pressure feed pumps vibrations. On April 1, 1960, he was transferred to the Special Design Bureau of Feed Pumps, now the Research and Design Institute for Atomic and Power Pumpbuilding is JSC VNIIAEN, in Sumy. He worked as head of the calculation and experimental department, deputy chief engineer for scientific work. In December 1964, he defended his candidate of science (Ph.D.) thesis without interruption from production.

On September 1, 1966, he was admitted to the associate professor position and since November 11 this year - to the post of head of the General Scientific Disciplines Department of Sumy branch of Kharkiv Polytechnic Institute. Since September 8, 1972, he was the head of the Theoretical Mechanics Department.

On June 28, 1974, he defended his D.Sc. thesis in the specialty "Hydraulic Machines and Hydropneumatic Units". On April 7, 1978, he was awarded the academic rank of professor by the USSR VAK.

Since 1976 he has been invariably chairman of the Organizing Committees of International Scientific and Technical Conferences "Hermetic Sealing, Vibration Reliability and Ecological Safety of Pump and Compressor Machinery" – "HERVICON". And in 1981 initiated the industrial research laboratory of the Chemical and Petroleum Engineering Ministry, the Problem Laboratory of Vibroreliability, which became later be called Laboratory Hermomehanics and Vibrodiagnostics.

For a significant personal contribution to the development of national science and education, success in educating young people, prof. Volodymyr Martsynkovskyy was awarded the Order of Honor in 1986.

In 1992, prof. Volodymyr Martsynkovskyy started training specialists in the specialty "Dynamics and Strength". And from April 1995 to September 2014, he was the head of the General Mechanics and Machine Dynamics Department, which was renamed from the Theoretical Mechanics Department.

Volodymyr Martsynkovskyy was the chairman of the Specialized Scientific Council for the defending of candidate of science theses at Sumy State University, the Editor-in-Chief of the Scientific-Technical Journal "Visnyk of Sumy State University" (series "Technical Sciences"), and later the Honorary Editor of the "Journal of Engineering Sciences".

In 1997 he was awarded the honorary title of Honored Worker of Science and Technology of Ukraine for his significant personal contribution to the development of national education, success in education and training of young people, and on December 9, 2004, he was awarded the title of Honorary Professor of Sumy State University.

In 2008, Volodymyr Martsynkovskyy was awarded the Honorary Distinction of Sumy City Council for Merit to the City. In 2009, he received an International Award from Pompy Pompownie Journal (Poland) for his great contribution to pumpbuilding. In 2010 he was awarded the title of Doctor Honoris Causa of Kielce University of Technology (Kielce, Poland). In 2011, he received the Honorary Sign "For Scientific Achievements" from the head of the Sumy Regional State Administration. And on March 26, 2017, the Order of Merit of the Republic of Poland was presented to him from the President of the Poland Republic, Andrzej Duda.

He is the author of more than 300 printed scientific and methodological works, including 11 monographs on problems of reliability and hermetic sealing of centrifugal pumps and compressors and more than 50 patents. Under the scientific supervision of Professor Martsynkovskyy, 24 Ph.D. and 5 D.Sc. theses were defended.

Volodymyr Martsynkovskyy worked not only in the field of solving complex scientific problems, but also actively engaged in sports, in particular, mountaineering and mountain tourism. He conquered with his students more than one mountain peak, not one pass, or one scientific problem.

The heart of the famous scientist stopped on June 29, 2019, in the circle of people closest to him.

Each of us comes to life in order to leave his mark in the history of mankind, Volodymyr Martsynkovskyy has forever etched his name due to his scientific achievements, created by him scientific school, which will continue to develop Ukrainian science and technology.

JOURNAL OF ENGINEERING SCIENCES
ЖУРНАЛ ІНЖЕНЕРНИХ НАУК
ЖУРНАЛ ИНЖЕНЕРНЫХ НАУК

Web site: http://jes.sumdu.edu.ua

DOI: 10.21272/jes.2019.6(2).a1/ Volume 6, Issue 2 (2019)

Simplified Grinding Temperature Model Study

Lishchenko N. V.[1*], Larshin V. P.[2], Krachunov H.[3]

[1] Odessa National Academy of Food Technologies, 112 Kanatna St., 65039 Odessa, Ukraine;
[2] Odessa National Polytechnic University, 1 Shevchenko Ave., 65044 Odessa, Ukraine;
[3] University of Varna, Studentska Str., Varna, 9010, Bulgaria

Article info:
Paper received: June 12, 2019
The final version of the paper received: September 3, 2019
Paper accepted online: September 8, 2019

***Corresponding Author's Address:**
odeslnv@gmail.com

Abstract. A study of a simplified mathematical model for determining the grinding temperature is performed. According to the obtained results, the equations of this model differ slightly from the corresponding more exact solution of the one-dimensional differential equation of heat conduction under the boundary conditions of the second kind. The model under study is represented by a system of two equations that describe the grinding temperature at the heating and cooling stages without the use of forced cooling. The scope of the studied model corresponds to the modern technological operations of grinding on CNC machines for conditions where the numerical value of the Peclet number is more than 4. This, in turn, corresponds to the Jaeger criterion for the so-called fast-moving heat source, for which the operation parameter of the workpiece velocity may be equivalently (in temperature) replaced by the action time of the heat source. This makes it possible to use a simpler solution of the one-dimensional differential equation of heat conduction at the boundary conditions of the second kind (one-dimensional analytical model) instead of a similar solution of the two-dimensional one with a slight deviation of the grinding temperature calculation result. It is established that the proposed simplified mathematical expression for determining the grinding temperature differs from the more accurate one-dimensional analytical solution by no more than 11 % and 15 % at the stages of heating and cooling, respectively. Comparison of the data on the grinding temperature change according to the conventional and developed equations has shown that these equations are close and have two points of coincidence: on the surface and at the depth of approximately threefold decrease in temperature. It is also established that the nature of the ratio between the scales of change of the Peclet number 0.09 and 9 and the grinding temperature depth 1 and 10 is of 100 to 10. Additionally, another unusual mechanism is revealed for both compared equations: a higher temperature at the surface is accompanied by a lower temperature at the depth.

Keywords: grinding temperature, heating stage, cooling stage, dimensionless temperature, temperature model.

1 Introduction

Abrasive machining works by forcing the abrasive particles, or grains, into the surface of the workpiece so that each particle cuts away a small bit of material. Abrasive machining is similar to conventional machining (metal cutting), such as milling or turning, because each of the abrasive particles acts like a miniature cutting tool. However, unlike conventional machining, the grains are much smaller than a cutting tool, and the geometry and orientation of individual grains are not well defined. As a result, abrasive machining is less power efficient and generates more heat. The grain size may be different based on the machining. For rough grinding, coarse abrasives are used. For fine grinding, fine grains (abrasives) are used.

Abrasive machining processes can be divided into two categories based on how the grains are applied to the workpiece.

In bonded abrasive processes, the particles are held together within a matrix, and their combined shape determines the geometry of the finished workpiece. For example, in grinding the particles are bonded together in a wheel. As the grinding wheel is fed into the part, its shape is transferred onto the workpiece.

In loose abrasive processes, there is no structure connecting the grains. They may be applied without lubrication as a dry powder, or they may be mixed with a lubricant to form a slurry. Since the grains can move independently, they must be forced into the workpiece with another object like a polishing cloth or a lapping plate.

Common abrasive processes are listed below. Fixed (bonded) abrasive processes: grinding, honing, superfinishing, tape finishing, abrasive belt machining, abrasive sawing, diamond wire cutting, wire saw sanding.

Loose abrasive processes: polishing, lapping, abrasive flow machining (AFM), hydro-erosive grinding, water-jet cutting, abrasive blasting mass finishing, tumbling, open barrel tumbling, vibratory bowl tumbling, centrifugal disc tumbling, centrifugal barrel tumbling.

Grinding is an abrasive machining process that uses a grinding wheel as the cutting tool. Grinding practice is a large and diverse area of manufacturing and tool making. It can produce very fine finishes and very accurate dimensions. At the same time, in mass production, it can also rough out large volumes of metal quite rapidly. It is usually better suited to the machining of very hard materials than is "regular" machining (that is, cutting larger chips with cutting tools such as tool bits or milling cutters), and until recent decades it was the only practical way to machine such materials as hardened steels. Compared to “regular” machining, it is usually better suited to taking very shallow cuts, such as reducing a shaft’s diameter by half a thousandth of an inch or 12.7 μm.

Grinding is a subset of cutting, as grinding is a true metal-cutting process. Each grain of abrasive functions as a microscopic single-point cutting edge (although of high negative rake angle) and shears a tiny chip that is analogous to what would conventionally be called a “cut” chip (turning, milling, drilling, tapping, etc.). However, among people who work in the machining fields, the term cutting is often understood to refer to the macroscopic cutting operations, and grinding is often mentally categorized as a "separate" process (abrasive machining). This is why the terms (“grinding” and “metal cutting”) are usually used separately in shop-floor practice.

The designing, monitoring and diagnosing computer subsystems are widely used on CNC grinding machines to adapt the grinding system to higher throughput. Abrasive machining compared with metal cutting is more labor-intensive and costly. That is why the grinding system study is caused by the search for ways to improve the productivity of man and machine [1]. In this connection, there is some modern knowledge to boost the grinding system throughput. This knowledge is more important with automated computer-controlled systems than it has ever been before because quantitative knowledge is needed to design and operate these systems [2].

By means of electrical signals from sensors, you can judge the state of the machine under control and the environment. Therefore, the more sensors used, the more information you can be obtained about the grinding system and environment. However, it should be borne in mind that in real conditions there is such information which is impossible directly to take off with the help of sensors.

This situation may occur, for example, when the measured signal is distorted by noise or the controlled value cannot be converted to an electrical signal as well as when due to cost or spatial constraints you cannot use the required sensor. If in such cases the noise properties or dynamic characteristics of the object, which are held observations, are known then with the help of appropriate calculations you can evaluate the signal you are interested in [3].

This situation fully applies to the grinding temperature signal in the grinding zone which is located between a grinding wheel and a workpiece to be ground. For this reason, the development of an acceptable mathematical model for determining the grinding temperature is an urgent task in the grinding technology on CNC machines. In terms of metrology, such solution to the problem is an example of indirect measurement. This opens the way to building “hierarchically intelligent control systems” developed by Sarid is on the basis of his principle of “increasing precision with decreasing intelligence” [4]. All this mentioned above ultimately predetermines the development of the main industries in developed countries [5] and corresponds to the so-called tendency of “sustainable development”.

2 Literature Review

The state of the problem in the field of the grinding thermo-physical theory can be considered taking into account the following philosophical technical concepts that predetermine the corresponding particular approaches to the problem solution. Firstly, it is the concept of dry and wet grinding, which predetermines the absence or accounting of convective heat transfer under the action of grinding fluid. Secondly, it is the concept of macro- and micro-grinding, which allows considering integral (due to averaging) or local heat fluxes with and without taking into account the effect on temperature of instantaneous cutting elements – sections of abrasive grains separated by pores of the grinding wheel (highly porous grinding wheels) as well as their accidental impact on the surface being ground. This concept involves the separation of the grinding process into categories of continuous and discontinuous (with pulsed heat flux), including the grinding with and without convective heat transfer. Thirdly, the concept of super-micro-grinding, which involves taking into account the effect of individual cutting grains of the grinding wheel, with and without taking into account convective heat transfer. The first concept most closely corresponds to the theory of the Jaeger moving heat source [6, 7], on the basis of which simplified formulas for determining the maximum grinding temperature are given in a number of sources without corresponding justifications [8–10].

3 Research Methodology

3.1 Mathematical model

In the grinding theory, the contact spot is usually considered as a certain zone on the surface to be ground, which belongs to both the grinding wheel and the workpiece (Figure 1).

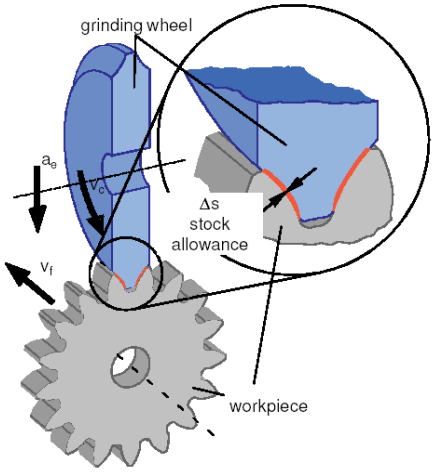

a

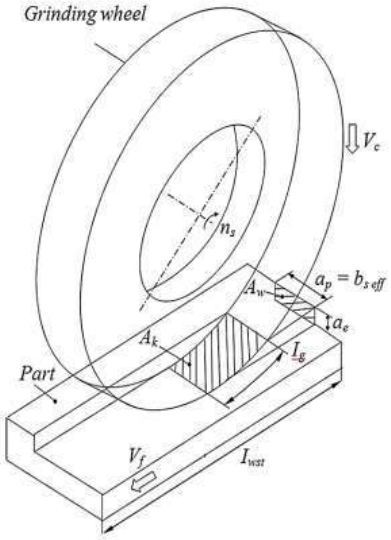

b

Figure 1 – Schemes of profile gear grinding (a) and flat grinding (b) with the discrete radial feed a_e of the grinding wheel to the workpiece

From the grinding thermal physics point of view, these schemes can be converted into the so-called moving heat source, indicated by the numbers 1234 in Figure 2.

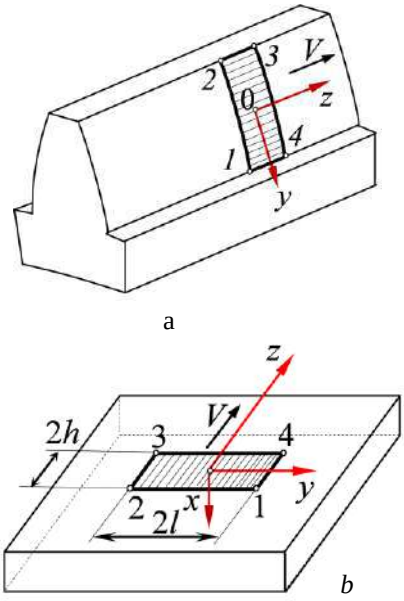

a

b

Figure 2 – Real (a) and equivalent (b) schemes of thermal sources

It was previously established the general view of the grinding temperature equations for research: three-, two-, and one-dimension ones [11, 12]. These equations are used when the Peclet number $H = \dfrac{Vh}{2a}$ is more than 4, i. e. $H \geq 4$. It is assumed here that a band heat source with the width of $2h$ moves over the flat surface of a semi-infinite body along and in the positive direction of the z-axis and is infinitely long in the direction of the y-axis (Figure 2). The heat flux density q (in W/m^2) over the entire surface of the moving contact is uniform, i. e. $q = \text{const}$. The coordinate system is referenced to the moving heat source. The transition from the two-dimensional thermophysical scheme with a moving heat source to the corresponding one-dimensional schemes with unlimited and limited unmoving flat sources is performed by replacing the velocity parameter V of the heat source (in m/s) by the time τ_H of its action. For these conditions, we have the following general view of the equations for research. Firstly, we have the basic grinding temperature equation at the stages of heating (with the index "H") and cooling (with the index "C"):

$$\Theta_H(X,H) = 2\pi\sqrt{H}\,\text{ierfc}\frac{X}{2\sqrt{H}},\ 0 \leq H \leq H_H, \qquad (1)$$

$$\Theta_C(X,H,H_H) = 2\pi \times$$

$$\times\left[\sqrt{H}\,\text{ierfc}\frac{X}{2\sqrt{H}} - \sqrt{H-H_H}\,\text{ierfc}\left(\frac{X}{2\sqrt{H-H_H}}\right)\right], \qquad (2)$$

$$H_H < H.$$

Secondly, we have the simplified equation (obtained in the previous paper) at the stages of heating (3) and cooling (4):

$$\Theta^*_H\left(X,H\right)=2\pi\sqrt{H}\,\frac{1}{\sqrt{\pi}}10^{-\left(\frac{X}{2\sqrt{H}}\right)},\ 0\le H\le H_H\,, \qquad (3)$$

$$\Theta^*_C\left(X,H\right)=2\sqrt{\pi}\times$$
$$\times\left[\sqrt{H}\,10^{-\left(\frac{X}{2\sqrt{H}}\right)}-\sqrt{H-H_H}\,10^{-\left(\frac{X}{2\sqrt{H-H_H}}\right)}\right], \qquad (4)$$
$$H_H<H.$$

From equations (1) and (3), we can find that the maximum dimensionless surface temperatures (i. e. at $X=0$) according to these equations are the same (they are equal to each other). They correspond to the action time of the moving heat source which is equal to $\tau_H=2h_H/V$ (Figure 2). That is

$$\Theta_{H\max}=\Theta^*_{H\max}=2\pi\sqrt{H}\left(\frac{1}{\sqrt{\pi}}\right)=2\sqrt{\pi H}\,. \qquad (5)$$

3.2 Error in calculating the grinding temperature

The dependences of the change in the dimensionless temperature over the depth of the subsurface layer, including the surface at $X=0$ for $H=0.09$ (Fig. 3, *a*), $H=9$ (Figure 3 b), $H=90$ (Figure 3 c) and $H=900$ (Figure 3 d) are studied.

Data in Figure 3 allows estimating practical change intervals of dimensionless variables H, X and $X/(2H^{1/2})$, which, first, correspond to a change range of regime parameters for conventional operations of flat, round and profile grinding, and secondly, at which there is a dimensionless temperature field at the heating stage (Table 1).

It can be seen (Figure 3) that the error of the simplified equation (3) compared to the original equation (1) in the zone of a ten-fold temperature drop is alternating (first lowering the temperature, then its overestimation) and the lowest errors occur at high and medium temperatures. This is just in the region of significant temperature values that affect the nature and depth of the defective layer during grinding.

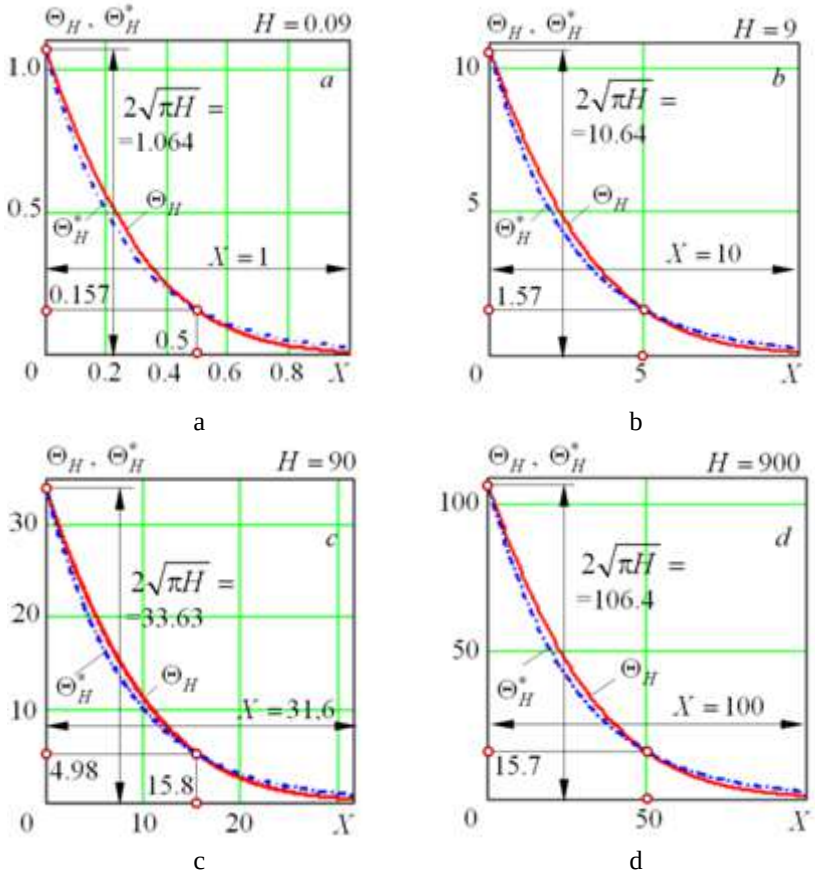

Figure 3 – The dimensionless temperatures $\Theta_H\left(X,H\right)$ and $\Theta^*_H\left(X,H\right)$ changes at the heating stage vs depth of the subsurface layer X in a range of 0–1 (a), 0–5 (b), 0–30 (c), and 0–100 (d)

Table 1 – Formal and real intervals of changing the dimensionless parameters at the heating stage at the heating stage

Formal interval	Real interval
$0 \le X \le 41.7$	$0 \le X \le 14$
$0.047 \le H \le 104.063$	$4 \le H \le 20$
$0 \le \frac{X}{2\sqrt{H}} \le 96$	$0 \le \frac{X}{2\sqrt{H}} \le 1$

3.3 Comparing the models

To estimate the errors of the simplified dependencies (3) and (4) obtained, it is necessary to compare them with the similar more exact dependencies (1) and (2) at the heating and cooling time intervals, which were choose the same. Expressed through a dimensionless parameter H (Peclet number), the interval of dimensionless heating time for a wide range of grinding modes is $0 \le H \le 100$.

The study will be carried out, for example, in the most unfavorable case with $H = 0.09$, since for $H = 4$ the coincidence of the two-dimensional solution with the one-dimensional solution by equations (1) and (2) is most pronounced [11–14]. As an example in Figure 4 shows graphs of the change in the dimensionless grinding temperature at $H = 0.09$, constructed from equation (2), that is, in the cooling stage.

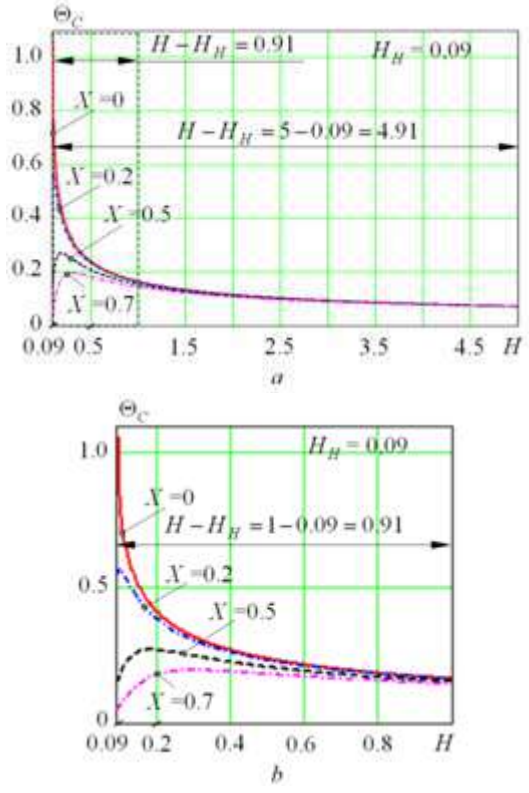

Figure 4 – The change in the dimensionless grinding temperature $\Theta_C = \Theta_C(X, H, H_H)$ according to equation (21) at the cooling stage depending on the Peclet number H at fixed distances from the surface X at $H_H = 0.09$ in the intervals $0 \le H \le 5$ (a) and $0 \le H \le 1$ (b)

It can be seen in Figure 4 that a change of H_H from $H_H = 9$ to $H_H = 0.09$ (a hundred times) leads to an increase in the scale of the dimensionless cooling time by ten times, i. e. just as it was noted in Figure 5.

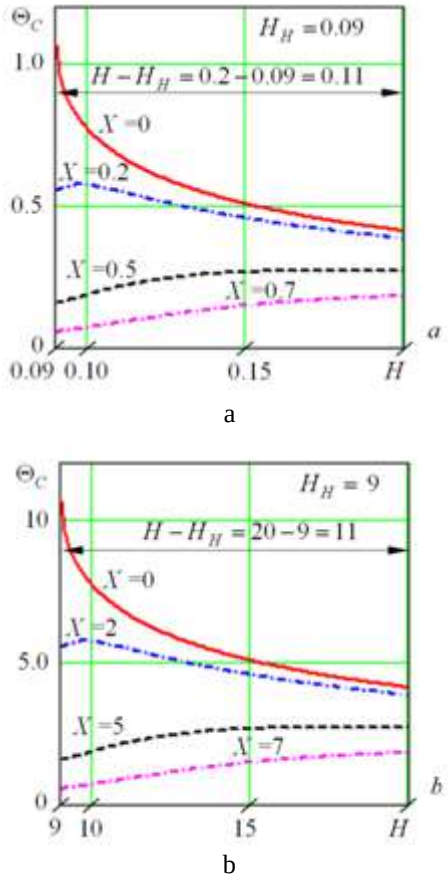

Figure 5 – The change in the dimensionless temperature depending on the Peclet number H at the cooling stage (without cooling liquid) at fixed distances from the surface X at $H_H = 0.09$ (a) and $H_H = 9$ (b)

Comparison of the data on the grinding temperature change by equations (2) and (4) is shown graphically in Figure 5. It can be seen that, as at the heating stage, equations (2) and (4) are close and have two points of coincidence: at 0 (i.e. on the surface) and at the depth of approximately threefold decrease in temperature. You can also see that the nature of the ratio between the scales of change of the H_H (0.09 and 9) and the X (1 and 10) is of 100 (9/0.09) to 10 (10/1).

In addition, another unusual mechanism is revealed for both compared equations: a higher temperature at the surface is accompanied by a lower temperature at the depth (Figure 6).

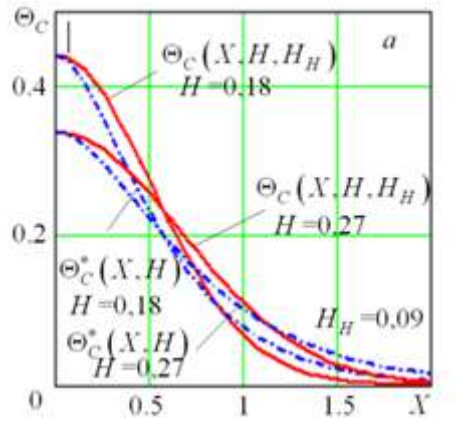

a

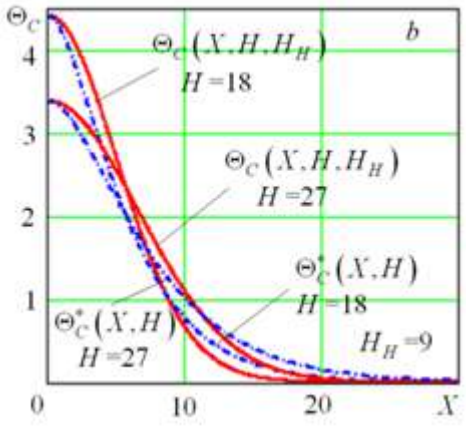

b

Figure 6 – The change in dimensionless temperature depending on the dimensionless depth X in the cooling stage (without a cooling liquid) for $H_H = 0.09$ at $H = 0.18$ and $H = 0.27$ (a), and for $H_H = 9$ at $H = 18$ and $H = 27$ (b)

The areas of use of the approximate expressions (3) and (4) are determined by comparing them with the corresponding more exact expressions (1) and (2). To do this, we limit the allowable amount of error between the compared expressions, for example, by the levels $\delta_H = 11\ \%$ at the heating stage and $\delta_C = 15\ \%$ at the cooling stage (Table 2).

Table 2 – Allowable intervals for changing the dimensionless parameters X and H

H	Heating stage	Cooling stage
0.09	$0 \le X \le 0,6$	$0 \le X \le 1$
20	$0 \le X \le 8,5$	$0 \le X \le 15$
100	$0 \le X \le 19,5$	$0 \le X \le 33$

The data given in Table 2 do not contradict the previously found area of their change (see Table 1). It can be seen in Table 1 that the obtained expressions (3) and (4) can be used in fairly wide intervals of X and H variation to estimate the grinding temperature and its distribution over the depth of the surface layer.

4 Conclusions

Temperatures Θ_H and Θ_H^* as well as the depth X of the fixed temperature penetration, under otherwise equal conditions, are proportional to the square root of the Peclet number. The coordinates of the same point of the previous (i-1)-th solutions $\Theta(X_{i-1}, H_{i-1})$ and $\Theta^*(X_{i-1}, H_{i-1})$ with the subsequent i-th solutions $\Theta(X_{i-1}, H_{i-1})$ and $\Theta^*(X_{i-1}, H_{i-1})$ are the same and differ in the $\sqrt{H_i / H_{i-1}}$ times. For example, when going from $H_{i-1} = 0.09$ to $H_i = 9$, the coordinate of the coincidence points on the ordinate axis changes from 1.064 to 10.64, and on the abscissa axis - from 0.5 to 5.0, i. e. $\sqrt{H_i / H_{i-1}} = \sqrt{9 / 0,09} = 10$ times.

A study of the developed grinding temperature mathematical model made it possible to establish its continuity with the existing solution of the one-dimensional differential equation of heat conduction under boundary conditions of the second kind on the surface. At the same time, the developed new mathematical model, in contrast to the mentioned one-dimensional solution, makes it possible to explicitly determine the penetration depth of any previously set grinding temperature.

References

1. King, R. I., Hahn, R. S. (1986). *Handbook of Modern Grinding Technology*. Chapman and Hall, New York, London.
2. DeVries, W. R. (1991). *Analysis of Material Removal.* Springer-Verlag, New York.
3. Isii, T., Simoyama, I., Inoue, H., et al. (1988). *Mechatronics.* The Piece, Moscow.
4. Lima, P. U., Saridis, G. N. (1996). *Design of Intelligent Control Systems Based on Hierarchical Stochastic Automata*. World Scientific Publishing Co Pre Ltd., Singapore.
5. Ross, A. (2016). *The Industries of the Future*. New York, Simon & Schuster Inc.
6. Carslaw, H. S., Jaeger, J. C. (1959). Conduction of Heat in Solids. 2nd edition. Oxford University Press, Oxford.
7. Jaeger, J. C. (1942). Moving sources of heat and temperature at sliding contacts. *Proceedings of the Royal Society*, Vol. 76, pp. 203–224.
8. Malkin, S., Guo, C. (2008). *Grinding Technology: Theory and Application of Machining with Abrasives*. Industrial Press Inc., New York.

9. Akbari, M., Sinton, D., Bahrami, M. (2011). Geometrical effects on the temperature distribution in a half-space due to a moving heat source. *Journal of Heat Transfer*, Vol. 133(6), pp. 064502-1–064502-10.
10. Sipaylov, V. A. (1978). *Thermal Processes during Grinding and Surface Quality Control*. Mashinostroenie, Moscow.
11. Lishchenko, N., Larshin, V. (2020). Temperature field analysis in grinding. *Advances in Design, Simulation and Manufacturing II, DSMIE 2019, Lecture Notes in Mechanical Engineering, Springer*, pp. 199–208. Springer, Cham.
12. Larshin, V., Lishchenko, N. (2019). Adaptive profile gear grinding boosts productivity of this operation on the CNC machine tools. *Advances in Design, Simulation and Manufacturing, DSMIE 2018, Lecture Notes in Mechanical Engineering, Springer*, pp. 79–88.
13. Larshin, V. P., Kovalchuk, E. N., Yakimov, A. V. (1986). Application of solutions of thermophysical problems to the calculation of the temperature and depth of the defective layer during grinding. *Interuniversity Collection of Scientific Works*, pp. 9–16.
14. Lishchenko, N. V. (2018). *Profile Grinding Productivity Increasing on CNC Machines on the Basis of Grinding System Elements Adaptation*. D.Sc. thesis, 05.02.08 – Manufacturing Engineering. National Technical University "Kharkiv Polytechnic Institute", Kharkiv.

УДК 621.923.1

Дослідження спрощеної моделі температури шліфування

Ліщенко Н. В.[1*], Ларшин В. П.[2], Крачунов Х.[3]

[1] Одеська національна академія харчових технологій, вул. Канатна, 112, 65039, м. Одеса, Україна;
[2] Одеський національний політехнічний університет, просп. Шевченка, 1, 65044, м. Одеса, Україна;
[3] Технічний Університет м. Варна, вул. Студентська, 1, 9010, м. Варна, Болгарія

Анотація. У роботі проведене дослідження спрощеної математичної моделі визначення температури шліфування. За отриманими рівняннями цієї моделі є відмінність результатів від відповідного більш точного розв'язання одновимірного диференціального рівняння теплопровідності за граничних умов другого роду. Досліджувана модель представлена системою з двох рівнянь, що описують температуру шліфування на етапах нагрівання і охолодження без використання примусового охолодження. Обсяг досліджуваної моделі відповідає сучасним технологічним операціям шліфування на верстатах із ЧПК для умов, коли числове значення числа Пекле перевищує 4. Це, у свою чергу, відповідає критерію Егера для так званого джерела тепла, яке швидко рухається, для якого параметр швидкості заготовки може бути еквівалентно за температурою замінений часом дії джерела тепла. Це дає можливість використовувати більш простий розв'язок одновимірного диференціального рівняння теплопровідності при граничних умовах другого роду (одновимірна аналітична модель) замість аналогічного двовимірного розв'язку з невеликим відхиленням результатів розрахунку температури шліфування. Встановлено, що запропонований спрощений математичний вираз для визначення температури шліфування відрізняється від більш точного одновимірного аналітичного розв'язку не більше ніж на 11 % і 15 % на етапах нагрівання та охолодження відповідно. Порівняння даних щодо зміни температури шліфування за звичайним і розробленим рівняннями показало, що ці рівняння близькі та мають дві точки збігу: на поверхні та на глибині (приблизно зниження температури втричі). Також встановлено, що характер співвідношення між масштабами зміни числа Пекле (0,09 та 9) та глибиною температури подрібнення (1 та 10) становить 100 (9/0,09) і 10 (10/1) відповідно. Крім того, розкрито ще один нетрадиційний механізм для обох порівняних рівнянь: більш висока температура на поверхні супроводжується нижчою температурою на глибині.

Ключові слова: температура шліфування, етап нагрівання, етап охолодження, безрозмірна температура, температурна модель**.**

JOURNAL OF ENGINEERING SCIENCES
ЖУРНАЛ ІНЖЕНЕРНИХ НАУК
ЖУРНАЛ ИНЖЕНЕРНЫХ НАУК
Web site: http://jes.sumdu.edu.ua
Volume 6, Issue 2 (2019)

ICIE
INTERNATIONAL CONFERENCE
INNOVATION IN ENGINEERING
2020

https://icieng.eu/

Guimarães – Portugal
University of Minho

ICIE'2020:
July 08th-10th

Steering Committee:

- **22 people;**
- **12 countries;**
- **20 institutions**

The proceedings will be published in Springer "Lecture Notes in Mechanical Engineering" indexed by Scopus

JOURNAL OF ENGINEERING SCIENCES
ЖУРНАЛ ІНЖЕНЕРНИХ НАУК
ЖУРНАЛ ИНЖЕНЕРНЫХ НАУК

Web site: http://jes.sumdu.edu.ua

DOI: 10.21272/jes.2019.6(2).b1 Volume 6, Issue 2 (2019)

Dynamic Modulus and Field Performance of Cold-in-Place Recycled Asphalt Pavement

Islam M. R.[1*], Kalevela S. A.[1], Rivera J. A.[1], Rashid T. B.[2]

[1] Department of Engineering Technology, Colorado State University, Pueblo, CO 81001, Colorado, USA;
[2] Department of Electrical and Computer Engineering, University of Colorado at Colorado Springs, CO 81001, Colorado, USA

Article info:
Paper received: September 1, 2019
The final version of the paper received: November 23, 2019
Paper accepted online: November 28, 2019

***Corresponding Author's Address:**
md.islam@csupueblo.edu

Abstract. This study investigates the dynamic modulus of cold-in-place recycling (CIR) asphalt material and its performance using pavement performance data and laboratory dynamic modulus testing. Colorado Department of Transportation (CDOT) has 37 projects with over 8 million square yards using CIR materials. Sites from ten projects were selected to monitor the performances and collect samples for laboratory testing. Dynamic modulus testing on the CIR cores was conducted by the CDOT. Results show measured distresses of CIR rehabilitation techniques are mostly below the threshold values during the service period. International Roughness Index, rutting, and transverse cracking never exceeded the threshold values during the studied period. Only two CIR pavements exceeded the threshold values for fatigue cracking after 8-10 years of service. Measured distresses of CIR rehabilitation techniques are similar to conventional pavements based on engineering judgment. The laboratory dynamic modulus test results show CIR has about 50 % less dynamic modulus compared to the traditional asphalt mixture.

Keywords: asphalt pavement, cold-in-place recycling, dynamic modulus, fatigue cracking, transverse cracking.

1 Introduction

With the advancement of milling equipment and a rise in asphalt binder's price, pavement rehabilitation becomes very popular in different pavement design and construction agencies. Of the several rehabilitation technologies, Cold-in-Place Recycling (CIR) technology may be the cheapest and the environment-friendliest compared to the others. To adopt this technology, its properties and performance data must be available to the pavement design and construction agencies.

Recycling of Hot-Mix Asphalt (HMA) has increased in popularity since the late 1970s, primarily due to increased oil prices. Previously, the cost of recycling old pavements was greater than placing the new HMA (1996). The invention of milling machines allowed asphalt recycling to become more cost-effective compared to new construction (Cross and Jakatimath, 2007). Cold-in-Place Recycling (CIR) is the processing and treatment of existing HMA pavements to restore the pavement without heating the asphaltic materials (ARRA 2014).

The deteriorated top 2 to 4 inches of HMA is removed by a milling machine and the milled material is crushed and screened on-site to produce a specified gradation. Binding additives such as emulsion, cement, lime, or fly ash are mixed into the milled material. The mixture is then placed back on the roadway and graded to the final elevation. After compaction of the mixture, a fog seal or thin overlay may be applied if traffic volume is relatively high.

CIR is economically and environmentally beneficial for it uses less aggregate, does not need transportation of materials to and from the site, and involves less energy consumption. The use of CIR is environment-friendly as it may decrease carbon dioxide emission by up to 9% compared to traditional HMA mixes; the carbon dioxide emission is 54 % less considering the phase of recycling only (Giani et al., 2015). In 2016, Schwartz reported that CIR technologies decrease the carbon dioxide emission by 80 % compared to traditional HMA application. Additionally, CIR technology saves 60 % asphalt binder compared to HMA.

2 Literature Review

In 2007, Cross and Jakatimath compared the properties and performances of CIR to conventional HMA mixtures used in Oklahoma by laboratory and field investigation and found that CIR material is comparable with conventional HMA mixture. In laboratory samples, they found that CIR mixtures were not as stiff as typical HMA mixtures. CIR mixtures showed the same increase in stiffness

with long-term oven aging as did conventional HMA samples. Field evaluation consisted of rehabilitating two sections with CIR and slurry crack injection to retard reflection cracking. A third section was rehabilitated with more conventional treatment of a fabric interlayer and HMA overlay. They conducted field distress surveys for three years at which time the two CIR test sections had less transverse cracking than the conventional test section. Based on this research, CIR appears to be a viable procedure for rehabilitation of transverse cracked pavements. Schwartz [5] showed the dynamic modulus of CIR is approximately 50 % of the conventional HMA. The study also determined that CIR is 18 % lighter than conventional HMA and requires an additional 25 % of thickness to obtain the same strength of HMA.

In 2015, Bhavsar conducted laboratory tests and field observation for long-term CIR performance using two different Reclaimed Asphalt Pavement (RAP) mixtures. The purpose of this study was to compare two types of CIR materials: 1) full CIR and 2) CIR with conventional asphalt mixtures. Using visual inspections, Bhavsar found large amounts of deteriorations where a greater number of trucks, poor drainage, and low speeds were prevalent. This study did not show a difference in laboratory or field performance between the two mixtures. Based on a field survey, Kim et al. [7] found, CIR roads would last between 21 and 25 years based on the best-fit regression model where the roads were predicted to reach a fair pavement condition. The average service life of CIR roads with good subgrade support was predicted to last up to 34 years, whereas that of CIR roads with poor subgrade support was predicted to last up to 22 years. CIR is applicable for lower volume roads that may only require simple surface treatment. A cracked pavement may be restored by CIR if it is structurally sound and has well-drained bases and subgrade. CIR is generally not appropriate for pavement with excessive rutting, unstable base-subgrade, and moisture-related damage that cannot be fully recycled by the depth of the CIR treatment applied to the roadway.

In 2009, Kim et al. recommended the material characterization tests such as penetration and dynamic shear rheometer tests be performed for the residual asphalt in RAP materials. In 2007, Kim et al. conducted dynamic modulus and repeated load tests on CIR foam mixtures with RAP materials collected from different CIR project sites. It was found that both the dynamic modulus and flow number were dependent on the RAP sources and foamed asphalt constituents. In 2009, Kim and Lee prepared foamed CIR samples at different temperatures and conducted indirect tensile strength tests to determine whether the RAP temperature would affect the strength of the CIR materials. After testing the samples, they found that temperature of RAP materials has a significant impact on the wet indirect tensile strength of CIR foam mixtures and the optimum foam content differs with the temperature. In 2019, Islam et al. found an equivalent hot-mix asphalt for a cold mix. However, the field performance is cold mix is yet to be known.

From the above discussion, the mechanical properties and performance of CIR are dependent on RAP sources and properties, and the residual binders. The local study is essential to determine the performance and measurement of CIR's effectiveness. The main objective of this research is to evaluate the effectiveness of the CIR in Colorado's pavement. Specific objectives are mentioned below:

– to evaluate the performance of the CIR rehabilitated pavements with comparison to the conventional pavements;

– to document and recommend the dynamic modulus values of CIR materials for mechanistic pavement design.

3 Research Methodology

3.1 Materials collection

Ten asphalt cores were collected from each site. Samples collected had the following characteristics:

– CIR cores were bound materials;

– layer separation between the CIR and underlying HMA bonding was common;

– the bottom layer (old asphalt layer) had deteriorated. Since the CIR layer was a bound material, it was possible to conduct dynamic modulus tests.

The CIR material used in this study uses emulsion as the softening agent. In 2017, it was obtained that emulsion is also used in producing the warm-mix-asphalt.

3.2 Dynamic modulus testing

In 2010, the dynamic modulus testing on collected field cores following the AASHTO TP 62 test protocol using the Asphalt Mixture Performance Tester (AMPT) testing device. The procedure is described below:

– label each core and identify the cold-in-place layer using construction data and by visually inspecting each core. The diameter of the cores collected from the sites is 150 mm;

– cut a 50 mm diameter core horizontally out of the cold-in-place layer;

– trim the cores to 110 mm in height;

– record the exact measurements of each 110 mm specimen;

– attach the gauge points for an AMPT instrumentation;

– run the dynamic modulus test on each specimen at 4, 20, and 35 °C at 0.1, 1.0, and 10.0 Hz respectively.

3.3 Dynamic modulus test results

Six dynamic modulus tests have been conducted for each test site and the average results are used in the analysis. Mastersolver was used to determine the master curve of dynamic modulus to be used in the PMED software. The dynamic modulus is determined using the following equation:

$$\log\left|E^*\right| = \log\left(Min\right) + \frac{\left(\log\left(Max\right) - \log\left(Min\right)\right)}{1 + e^{\beta+\gamma\log\omega_r}} \quad (1)$$

where $|E^*|$ – dynamic modulus; ω_r – the reduced frequency, Hz; *Max* – limiting maximum modulus, ksi; *Min* – limiting minimum modulus, ksi; β, γ – fitting parameters. The reduced frequency is computed using the Arrhenius given below:

$$\log(\omega_r) = \log \omega + \frac{\Delta E_a}{19.14714}\left(\frac{1}{T} - \frac{1}{T_r}\right) \quad (2)$$

where ω_r – the reduced frequency at the reference temperature; ω – loading frequency at the test temperature; T_r – reference temperature, K; T – test temperature, K; ΔE_a – activation energy (treated as a fitting parameter).

The combination of the above mentioned two equations gives the following equation:

$$\log|E^*| = \log(Min) + \frac{(\log(Max) - \log(Min))}{1 + e^{\beta + \gamma\left\{\log\omega + \frac{\Delta E_a}{19.14714}\left(\frac{1}{T} - \frac{1}{T_r}\right)\right\}}} \quad (3)$$

The shift factors for each temperature are given by the following equation:

$$\log[a(T)] = \frac{\Delta E_a}{19.14714}\left(\frac{1}{T} - \frac{1}{T_r}\right) \quad (4)$$

where $a(T)$ – shift factor at temperature T.

The maximum limiting modulus is estimated from mixture volumetric properties using the Hrisch model shown below and a limiting binder modulus of 1 GPa:

$$|E^*|_{\max} = P_c\left[4,200,000\left(1 - \frac{VMA}{100}\right) + 435,000\left(\frac{VMAxVFA}{10,000}\right)\right] + \frac{1 - P_c}{\left[\frac{\left(1 - \frac{VMA}{100}\right)}{4,200,000} + \frac{VFA}{435,000VFA}\right]} \quad (5)$$

where

$$P_c = \frac{\left(20 + \frac{435,000VFA}{VMA}\right)^{0.58}}{650 + \left(\frac{435,000VFA}{VMA}\right)^{0.58}} \quad (6)$$

$|E^*|_{max}$ – limiting maximum dynamic modulus, psi; VMA – voids in mineral aggregates, %; VFA – voids filled with asphalt, %.

4 Results

4.1 Average raw dynamic modulus

To determine a recommended dynamic modulus for CIR from AMPT (master curve) data, the average raw dynamic modulus, VMA and VFA of all ten sites were combined, the average value calculated, and then fitted using the Mastersolver.

The average raw dynamic modulus data are presented in Table 1.

Table 1 – Average raw dynamic modulus of ten sites

Temperature, °C	Frequency, Hz	Modulus, ksi
4	0.1	753
4	1.0	918
4	10.0	1100
20	0.1	419
20	1.0	512
20	10.0	678
35	0.01	135
35	0.1	181
35	1.0	266
35	10.0	401

The average VMA and VFA are 13.3 % and 26.6 % respectively. After the execution of the Mastersolver, the final parameters and the fitting parameters are given below. The PMED input modulus is listed in Table 2: $|E^*|_{max}$ = 3102.4 ksi; $|E^*|_{min}$ = 0.5 ksi; β = 1.34; γ = 0.19; ΔE_a = 241692 Pa; R_2 = 0.989; S_e/S_y = 0.07.

The dynamic modulus for all 10 sites has been plotted in Figure 1. The figure also has one conventional (NMAS = 12.5 mm, PG 64-22 binder and 100 gyrations) mixtures' dynamic modulus for the comparison. The volume characteristics of the conventional mixtures are the same as the CIR mixtures as both have the same mix design. There are several reasons for comparing the dynamic modulus of CIR and that of a conventional mix. Dynamic modulus is the primary material property used in the mechanistic-empirical pavement design. Lower dynamic modulus at lower frequency of loading (or high temperature) dictates that the mix is very susceptible to rutting as less stiff material at high temperature deform a lot. On the other hand, lower dynamic modulus at higher frequency of loading (or low temperature) dictates that the mix is good against low-temperature cracking. Figure 5 shows that at lower reduced frequency (or higher temperature zone), the dynamic modulus of CIR materials are higher than that of the control mixture. At higher reduced frequency (or lower temperature), the dynamic modulus of CIR materials is smaller (roughly 50 %) than that of the control mixture. This means CIR is more susceptible to rutting but less susceptible to cracking compared to conventional mixtures. The fitted dynamic modulus (named as "Fit" in Figure 1), lies almost in the middle of the all dynamic modulus range. The fitted dynamic modulus data can be used by CDOT for future CIR overlay design. As full details of CIR of individual sites are not available, different dynamic modulus values for different CIR mixes cannot be recommended.

4.2 Field performance data collection

Ten pavement sites where CIR has been used were selected for this research. A control site was selected for each test site for comparison of the CIR pavement versus traditional HMA pavement. The control sites were selected and were chosen for being the best fit for pavement

location, materials, geometry, climate, traffic volume, and time of construction (i.e., the projects were built during the same year or close to the year. The control test sites were located near the CIR sites. It is important to mention that the control sites were not constructed using CIR technology, rather traditional HMA.

Table 2 – Fitted dynamic modulus of CIR material

No.	Temperature		Frequency	Shift factor	Reduced frequency	E^*	
	°C	°F	Hz			ksi	GPa
1	–10.0	14	25	4.91	2018759	1664.7	11.48
2	–10.0	14	10	4.91	807503	1590.4	10.97
3	–10.0	14	5	4.91	403751	1533.3	10.58
4	–10.0	14	1	4.91	80750	1398.5	9.65
5	–10.0	14	0.5	4.91	40375	1339.8	9.24
6	–10.0	14	0.1	4.91	8075	1203.2	8.30
7	4.4	40	25	2.41	6456	1184.3	8.17
8	4.4	40	10	2.41	2582	1107.0	7.64
9	4.4	40	5	2.41	1291	1049.2	7.24
10	4.4	40	1	2.41	258	917.6	6.33
11	4.4	40	0.5	2.41	129	862.6	5.95
12	4.4	40	0.1	2.41	25	739.8	5.10
13	21.1	70	25	–0.16	17.19515	710.1	4.90
14	21.1	70	10	–0.16	6.87806	645.1	4.45
15	21.1	70	5	–0.16	3.43903	598.0	4.12
16	21.1	70	1	–0.16	0.68781	496.3	3.42
17	21.1	70	0.5	–0.16	0.34390	455.8	3.14
18	21.1	70	0.1	–0.16	0.06878	370.2	2.55
19	37.8	100	25	–2.46	0.08645	381.7	2.63
20	37.8	100	10	–2.46	0.03458	337.2	2.33
21	37.8	100	5	–2.46	0.01729	306.1	2.11
22	37.8	100	1	–2.46	0.00346	242.1	1.67
23	37.8	100	0.5	–2.46	0.00173	217.9	1.50
24	37.8	100	0.1	–2.46	0.00035	169.1	1.17
25	54.4	130	25	–4.53	0.00074	191.1	1.32
26	54.4	130	10	–4.53	0.00030	165.1	1.14
27	54.4	130	5	–4.53	0.00015	147.4	1.02
28	54.4	130	1	–4.53	0.00003	112.5	0.78
29	54.4	130	0.5	–4.53	0.00001	99.9	689.0
30	54.4	130	0.1	–4.53	0.00000	75.4	519.9

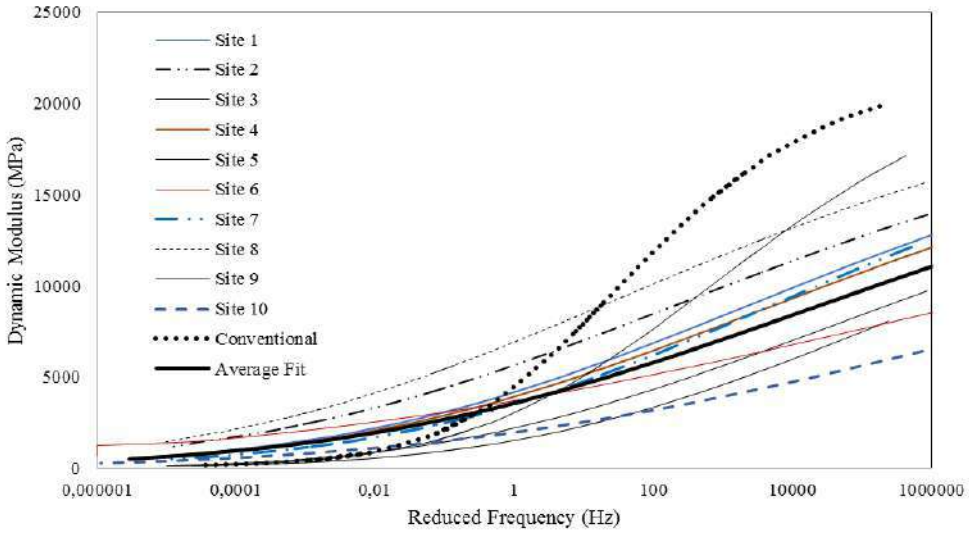

Figure 1 – Dynamic modul of all mixes including conventional mixtures

To collect the pavement management data, an automated data collection van is driven over the entire roadway network. The collected data are reported in tenth-of-mile (tenth-mile) increments and include surface roughness (IRI), permanent deformation (rutting), and fatigue cracking. The definitions of the distress measured are provided below. The International Roughness Index (IRI) is the roughness index most commonly obtained from

measured mean longitudinal road profiles of each wheel path. IRI is a quantification of functional adequacy and is calculated using a quarter-car vehicle math model, whose response is accumulated to yield a roughness index with units of slope, mm/km. IRI is the cumulative effect of rutting, fatigue cracking, and thermal cracking.

Rutting is the longitudinal surface depression in the wheel path resulting from the permanent deformation in each pavement layer along the wheel path. Ruts are particularly evident after a rain when they are filled with water. The rut depth is the vertical difference in elevation between the transverse profile of the surface and a wire-line across the lane width.

Fatigue cracks consist of both the bottom-up and the top-down fatigue cracking. A series of interconnected cracks looking similar to a chicken wire or back of an alligator is defined as the bottom-up cracking. This crack initiates at the bottom of asphalt layer for the repeated tensile strain due to repeated (fatigue) wheel load-related and propagates to the surface. Therefore, this crack is often called the bottom-up fatigue crack. Longitudinal cracks, near the wheel paths, parallel to the centerline of the roadway are called the top-down longitudinal cracks. The top-down longitudinal cracks initiate at the surface of asphalt layer due to repeated tensile and/or shear strain caused by wheel loading. They can also develop along the construction joint between adjacent passes of the paver or at a location that corresponds to the center of the paver.

Transverse top-down surface cracking (also known as transverse cracking or thermal cracking) is caused by single cooling due to extreme cold temperature or high rate of cooling may cause low-temperature cracking. Low-temperature cracking occurs when the induced tensile stress by the decrease in temperature exceeds the tensile strength of the asphalt concrete.

The collection of the rutting data is accomplished using a five-sensor rut bar that measures the pavement's permanent deformation to the hundredth of an inch. The IRI data is collected with an inertia profile consisting of laser sensors, accelerometer, and distance transducer. The van is also equipped with digital cameras; one camera is positioned for a windshield view, and four cameras (one over each wheel) to view the pavement. The cameras take photos/videos of the pavement showing the type, amount, length, and severity of the cracking. The data collected is recorded and sent to the vendor's data reduction office where it is viewed and rated. The raw data is given in tenth-mile intervals. Thus, IRI is reported as the average mm/km over a tenth-mile section. Bottom-up fatigue cracking is reported as percentage of total lane cracked and is defined by a series of small, jagged, interconnecting cracks caused by failure of the asphalt concrete surface under repeated traffic loading. Top-down longitudinal cracking is reported as the total linear feet in a tenth-mile and is defined as cracking that is parallel to the pavement centerline. The top-down longitudinal cracking with bottom-up fatigue cracking was combined and refer as fatigue cracking. Transverse cracks are reported in two different ways, first as a numerical count such as 1, 2, or 3 per tenth-mile, the second is by linear feet per tenth-mile. Transverse cracks are defined as cracking that is perpendicular to the pavement centerline.

4.3 Pavement performance summary

Field performance data for fatigue cracking, rutting, transverse cracking, and IRI were collected from 10 selected sites using CIR and 10 control sites constructed using conventional HMA. Two types of comparisons were made, first, with the CDOT recommended threshold values of performance criteria for the rehabilitation of flexible pavement projects obtained from the CDOT 2017 Pavement Design Manual [15], and second, with the distresses of the control sites. Table 3 summarizes the maximum distress data collected from 10 selected sites using CIR and 10 control sites using conventional HMA.

Table 4 lists the recommended threshold values of performance criteria for rehabilitation of flexible pavement projects. First, IRI, Rutting and Transverse Cracking did not exceed the threshold values during the service period. For fatigue cracking, CIR exceeds the threshold value at Site 5, and Site 8 after 8–10 years of service. All these locations are from Interstates (I-25 and I-70). Most distress data for interstates are within the threshold values. Due to high volume of traffic, CIR may not be an appropriate option for interstates.

The comparison of the measured distresses with the control sites is summarized in Table 5. It shows CIR performed better at three sites, similar at one site and worse at six sites compared to the control projects for fatigue cracking. Results of rutting show CIR performed better at four sites, similar at two sites and worse at four sites compared to the control site. For transverse cracking, CIR performed better at five sites, and worse at five sites compared to the control projects. CIR performed better at four sites, and worse at six sites compared to the control projects for IRI. Considering all these results, it can be said that measured distresses of CIR rehabilitation techniques are similar to conventional pavements.

Combining all the data, it shows that CIR performs better for 40 % distresses, similar for 7.5 % distresses, and worse for 52.5 % distresses compared to the traditional pavement. Thus, it can be said that CIR is very similar to conventional pavements based on engineering judgment. However, CIR technology has about 50 % cost saving as discussed in the literature and it has many more benefits considering environment for energy-saving and less pollution, traffic control, noise, dust, and so on.

Table 3 – Measured maximum distresses

Project	Average annual daily traffic AADT	Years of data	Location	IRI mm/km	Rutting mm	fatigue cracking % of lane	No. of transverse cracking
Site 1	4000	9	CIR	1121	4.6	0.95	11
			Control Site	1405	4.8	2.42	8
Site 2	4800	9	CIR	1957	8.4	0.22	8
			Control Site	1783	6.1	1.23	24
Site 3	11000	9	CIR	1594	4.1	0.70	3
			Control Site	994	4.3	0.65	7
Site 4	2200	5	CIR	1342	4.6	0.20	1
			Control Site	1215	3.6	1.12	5
Site 5	19000	8	CIR	1263	5.8	48.12*	55
			Control Site	852	5.6	4.00	18
Site 6	3000	10	CIR	1499	6.1	7.18	7
			Control Site	1278	5.6	0.42	2
Site 7	7400	10	CIR	1215	6.1	13.52	18
			Control Site	1105	8.9	8.98	6
Site 8	20000	10	CIR	1294	4.3	26.15*	135
			Control Site	1326	6.4	13.23	11
Site 9	12000	11	CIR	963	7.4	13.13	5
			Control Site	1357	4.6	11.35	24
Site 10	12000	8	CIR	1231	6.1	0.30	1
			Control Site	1641	4.1	4.68	27

* recommended by CDOT.

Table 4 – Recommended threshold values of performance criteria for rehabilitation of flexible pavement projects

Project	IRI, mm/km	Rutting, mm	Total fatigue cracking, % of lane	No. of transverse cracking
Interstate	2525	14.0	23.3	125
Principal arterial	3157	16.5	39.2	125

Table 5 – CIR performance compared to conventional pavement, sites no.

Performances	Locations favoring the CIR	Neutral locations	Locations against the CIR
Fatigue cracking	1, 4, 10	3	2, 5–9
Rutting	1, 3, 7, 8	5, 6	2, 4, 9, 10
Transverse cracking	2–4, 9, 10	–	1, 5–8
IRI	1, 8–10	–	2–7
Total no.	16	3	21

5 Conclusions

Based on the study, the following conclusions are made. Firstly, measured distresses of CIR rehabilitation techniques are mostly below the threshold values during the service period. IRI, Rutting and Transverse Cracking never exceeded the threshold values during the studied period. Only two CIR pavements exceeded the threshold values for fatigue cracking after 8–10 years of service. Secondly, measured distresses of CIR rehabilitation techniques are similar to conventional pavement based on engineering judgment. Finally, the CIR has a smaller dynamic modulus compared to the conventional asphalt mixture at low temperature (or high frequency).

The conclusions drawn in the previous section are based on limited data available from the current study. Future research should incorporate cement-treated or foam treated material to determine the best CIR product. The effect of emulsion content may also be studied.

6 Acknowledgments

The Colorado State University-Pueblo (CSU-Pueblo) research team appreciates the research funding (Funding No. CDOT 415.02) by the Colorado Department of Transportation (CDOT).

References

1. AASHTO TP 62 (2010). *Standard Method of Test for Determining Dynamic Modulus of Hot-Mix Asphalt Concrete Mixtures*, AASHTO Designation TP 62. AASHTO Provisional Standards, AASHTO, Washington DC.
2. ARRA (2014). Basic Asphalt Recycling Manual, 2nd Edition, Asphalt Recycling & Reclaiming Association (ARRA), Annapolis, Maryland.
3. Bhavsar, J. (2015). *Comparing Cold In-Place Recycling (CIR) and Cold In-Place Recycling with Expanded Asphalt Mixture (CIREAM)*. M.Sc. thesis, Department of Civil Engineering, University of Waterloo, Ontario, Canada.
4. CDOT (2017). *CDOT M-E Pavement Design Manual*. Colorado Department of Transportation, Denver, CO.
5. Cross, S. A., Jakatimath, Y. (2007). *Evaluation of Cold In-Place Recycling for Rehabilitation of Transverse Cracking on US 412*, Report No. FHWA/OK 07 (04), Oklahoma Department of Transportation, Planning and Research Division, Oklahoma City, OK.
6. Giani, M., Dotelli, G., Brandini, N., Zampori, L. (2015). Comparative life cycle assessment of asphalt pavements using reclaimed asphalt, warm mix technology and cold in-place recycling. *Resources, Conservation and Recycling*, Vol. 104, pp. 224–238.
7. Islam, M. R., Kalevela, S. A., Rivera, J. A. (2019). Finding an Equivalent Hot-Mix Asphalt for Cold-in-Place Recycled Asphalt suing Laboratory Testing and Numerical Analysis. *Journal of Engineering Science*, King Saud University, doi: 10.1016/j.jksues.2019.10.001.
8. Kim, J., Lee, H., Jahren, C., Heitzman, M., Chen, D. (2009). Long-Term Field Performance of Cold In-Place Recycled Roads in Iowa. *Journal of Performance of Constructed Facilities*, Vol. 24(3) pp. 265–274.
9. Kim, Y., Lee, H., Heitzman, M. (2007). Validation of New Mix Design Procedure for Cold In-Place Recycling with Foamed Asphalt. *Journal of Materials in Civil Engineering*, Vol. 19(11), pp. 1000–1010.
10. Kim, Y., Lee, H., Heitzman, M. (2009). Dynamic Modulus and Repeated Load Tests of Cold In-Place Recycling Mixtures Using Foamed Asphalt. *Journal of Materials in Civil Engineering*, Vol. 21(6), pp. 279–285.
11. Roberts, F. L., Kandhal, P. S., Brown, E. R., Lee, D.-Y., Kennedy, T. W. (1996). *Hot Mix Asphalt Materials, Mixture Design, and Construction*. NAPA Research and Education Foundation.
12. Schwartz, C. W. (2016). Structural Characteristics and Environmental Benefits of Cold-Recycled Asphalt Paving Materials. *National Pavement Preservation Conference*, October 12–14, 2016, Nashville, TN.

УДК 625.7/.8

Динамічний модуль та експлуатаційні характеристики перероблено асфальтового покриття

Islam M. R.[1*], Kalevela S. A.[1], Rivera J. A.[1], Rashid T. B.[2]

[1] Кафедра інженерних технологій, Державний університет Колорадо, 81001, м. Пуебло, штат Колорадо, США;
[2] Кафедра електротехніки та комп'ютерної інженерії, Університет Колорадо в Колорадо-Спрінгс, 81001, м. Пуебло, штат Колорадо, США

Анотація. У цьому дослідженні вивчається динамічний модуль асфальтового матеріалу та продуктивність його перероблення за допомогою даних про експлуатацію та лабораторних випробувань. Кафедра транспорту Колорадо має 37 проектів з використання даного матеріалу площею більше 8 км^2. Для відстеження результатів і збирання дослідних матеріалів для лабораторних досліджень було відібрано зразки з десяти проектів. Тестування динамічного модуля для даного матеріалу відбувалось у лабораторії кафедри транспорту Державного університету Колорадо. Результати свідчать про те, що досліджувані показники якості є переважно нижчими за порогові значення впродовж періоду експлуатації. Зокрема, міжнародний показник шорсткості та поперечне розтріскування ніколи не перевищували порогові значення впродовж усього періоду дослідження. Лише два асфальтні покриття перевищили порогові показники для втомних тріщин після 8–10 років експлуатації. Ґрунтуючись на технічних міркуваннях, виміряні показники аналогічні до показників для звичайних тротуарів. Результати лабораторних досліджень показали, що матеріал має приблизно на 50 % менший динамічний модуль порівняно з традиційною асфальтовою сумішшю.

Ключові слова: асфальтне покриття, холодне перероблення на місці, динамічний модуль, втомна тріщина, поперечне розтріскування.

JOURNAL OF ENGINEERING SCIENCES
ЖУРНАЛ ІНЖЕНЕРНИХ НАУК
ЖУРНАЛ ИНЖЕНЕРНЫХ НАУК

Web site: http://jes.sumdu.edu.ua

DOI: 10.21272/jes.2019.6(2).b2 Volume 6, Issue 2 (2019)

The Role of Smart Sensors in Production Processes and the Implementation of Industry 4.0

Karabegovic I.[1*], Karabegovic E.[2], Mahmic M.[2], Husak E.[2]

[1] Academy of Sciences and Arts of Bosnia and Herzegovina, 7 Bistrik St., 71000 Sarajevo, Bosnia and Herzegovina;
[2] University of Bihac, Irfana Ljubijankica St., 77000 Bihac, Bosnia and Herzegovina

Article info:
Paper received: August 11, 2019
The final version of the paper received: December 5, 2019
Paper accepted online: December 10, 2019

[*]Corresponding Author's Address:
isak1910@hotmail.com

Abstract. In the world of global competition, customers have increasing demands that companies must meet in order to remain active in the global market. For this reason, it is necessary to use new technologies in the production processes, i.e. to implement Industry 4.0. In other words, we need to create a connected company through the digital transformation that enables production processes to discover new ways to increase productivity and improve overall business performance. Companies need to get involved and start a digital system, and from supplier to customer. It is a key to the hidden value that can contribute to the company's productivity, compliance, profitability, as well as the quality of the finished product, and eventually the introduction of flexible industrial automation of production processes. The aforementioned technologies and Internet of Things connect the physical and virtual world with a purpose to better collect and analyze data, transforming them into information that reaches decision-makers. To do this, it is necessary to implement smart sensors that provide information at all times. The implementation of Industry 4.0 in production processes is unthinkable without smart sensors and provides the following: faster product development time, lower overall costs, improved use of production processes and their optimization, as well as company risk management. The paper will outline the motives for the implementation of smart sensors and applications of smart sensors in production processes.

Keywords: production process, smart sensor, Industry 4.0, production automation, digital transformation, flexible automation.

1 Introduction

There is a steady increase in global demand in the world, which puts constant pressure on the world production industry, so companies have to constantly increase productivity and product quality. In order to survive in the global market and meet the above requirements, most companies in the world are using new technologies that monitor production data, monitor production processes, change and adjust the parameters of optimal production, thus creating new business values. Implementing the new technologies that form the core of the Industry 4.0 (smart technologies) in the production processes, real-time control is obtained, as well as information available on the platforms and devices that monitor the company's production processes. Industry 4.0 increases productivity and improves the overall business performance of the company. Smart sensors are the foundation of Industry 4.0. They present the sensors with integrated electronics, a combination of sensors with a microcontroller, which can perform one or more logical functions, two-way communication, and store data for future analysis. They have new applications and new features that can perform communication with other devices. Smart sensors are an integral part of integrated systems, mainly because of MEMS (micro-mechanical systems) manufacturing technology, which performs functions that could not be performed before or that were not economically viable. Smart sensors have built-in communication modules with which they can exchange information and communicate with other objects, as well as built-in signal processing components, which is the goal of the Internet of Things (IoT). The Internet of Things / Digitization / Industrial IoT is a network of devices that are connected and mutually communicating [1–8, 10, 11]. By implementing the basic Industry 4.0 technologies in the production processes, including smart sensors, the company can improve productivity gains with continuous advancement, improve performance of the production system, improve business adaptability by quickly responding to market changes, improve product development time through efficiency system design and the integration of the production process itself, extend the product life cycle, secure environment and reduce energy consumption, miti-

gate security risk to assist with important tools such as people, equipment and information, etc. A new way of managing production processes aims to improve performance, better use of the existing data, and use a combination of tools that can act to improve the system or production process. By implementing the new technologies of Industry 4.0 each company will have an advantage and be competitive since technology continues to drive innovation. The digitalization throughout the company, and the integration of processes, serials, and discrete drives shift the company towards one connected infrastructure, thus increasing efficiency and productivity across all segments of the company. When we have access to production data in the production process at any time in real-time, it allows us to monitor and improve the performance of the production process itself, or we can have insight into energy consumption so that we can make the decision to supply energy at optimal prices or manage peak energy consumption. Companies implementing Industry 4.0 have new visibility that will enable them to provide value-added services, and a competitive advantage for product design, thus increasing the company's revenue [9–11]. In order to monitor parameters and any other data from the production processes, we need to implement smart sensors that deliver the data and connect them to the technology to be visible and controllable.

2 Research Methodology

2.1 Integration of smart sensors with other devices

Sensors are devices that convert an input signal into an electrical analog or digital output that is readable. The sensor converts a physical parameter (e.g. temperature, speed, humidity, etc.) into a signal that can be measured electrically. Sensors work by receiving a signal from a device such as a transducer, then respond to that signal by converting it to an easy-to-read and understandable output. In other words, the transducer converts one form of energy to another, while the sensor consisting of the transducer converts the output of the transducer to a readable format. Sensors are used in all aspects of life to detect or measure different conditions. Many companies in the world have developed different sensor designs to measure different physical sizes. Many changes are happening every day in all industries, including the transformation of production processes, the increased flexible automation of production processes, new form of delivery of finished products, and new way of consumption, as a result of the implementation of Industry 4.0, which is based on new technologies such as the IoT, 3D printers, robotic technology, radio frequency identification, etc.

The application of the aforementioned Industry 4.0 technologies would not be possible without the use of a smart sensor. Based on Figure 1, which presents a schematic illustration of a smart sensor, we see those smart sensors with built-in IO-Link (the first standardized IO technology in the world (IEC 61131-9) for communication with sensors and actuators) act as standard I/O sensors used until they connect to the IO-Link Master [16, 17]. When the sensors are connected to the IO-Link Master, we are able to access all the advanced data and configuration capabilities that IO-Link has to offer.

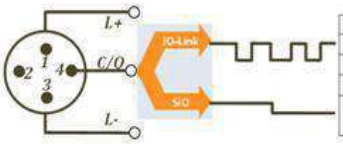

Pin	Signal	Remark
1	L+	24V
2	out	Depends on Sensor
3	L-	Ground
4	C/Q	Communication/ Switching Signal

Figure 1 – Schematic illustration of the function of the smart sensor

Many companies in the world have developed a range of smart sensors for temperature, pressure, speed, proximity sensors, photoelectric sensors, laser sensors, etc. The leader in the implementation is company Rockwell Automation from the USA. Due to limitations, we can show only a small fraction of the design solutions of smart sensors in Figure 2 [16, 17].

Figure 2 – Smart sensors of different construction designs

The application of smart sensors in production processes has been greatly simplified through the standardization of process data and the latest developments of IO-Link devices with regard to self-interface and integration with many different engineering tools. If they are smart sensors with variable parameters, they allow us to change their parameters in a moment, which is one of their good features. Their adjustment to the subsequent parameters can also be executed in a moment, because changes in the production process are automatically delivered to the smart sensors, and they can be adjusted for that production process. The advantage of smart sensors is that the staff does not have to remember the multiple processes of instructing the sensors. In addition, we constantly have information not only about the monitored parameters but also about sensor damage, sensor replacement when necessary, whether the lens is dirty or clean, etc. Multiple profiles can be stored with smart sensors to support flexible image production 3.

The storage function, which ensures that device parameters are automatically downloaded, without tools, after the device is replaced, has also been successfully tested on various major devices and devices currently available in the market. These are two key user benefits when it comes to the practical application of IO-Link technology.

Figure 3 – Smart sensors connected to other data-monitoring devices

The first smart sensor profile devices are already available in the market. We need to mention that IO-Link wireless devices are already in the implementation and that a wide range of device classes are already expanded, so IO-Link is increasingly used outside the traditional manufacturing process automation. Decision-making data is obtained and monitored with the help of smart sensors. They are an integral part of the Industry 4.0 and tend to improve production in the following: detection of defects, efficient downtime, and maintenance planning, more efficient supply chain management, increased efficiency and productivity, rapid transition to the production of another product, increase of safety and health of workers, ensured high quality of production, reduced and planned electricity consumption in the production process, etc. [9, 12, 13]. Unless we have information on what is happening on machines that are installed in production processes minute by minute, it is impossible to maintain optimal productivity and efficiency at any time, and we are unable to avoid unplanned downtime and losses that occur in the production process. The integration of smart sensors provides the data we need to create a comprehensive image at any point in the production process, making it easy to apply and operate smart machines that increase the productivity and efficiency of the production process. Companies implementing Industry 4.0 have new visibility that will enable them to provide value-added services, and a competitive advantage for product design, thus increasing the company's revenue [9–13].In order to monitor parameters and any other data from the production processes, we need to implement smart sensors that deliver the data and connect them to the technology to be visible and controllable.

2.2 The fundamentals of smart sensor implementation

The implementation of smart sensors in production processes provides a comprehensive view of the production process operation. Smart sensors are available for every possible parameter from temperature to pressure, flow rate, movement to distance, control of the accuracy of the performed operation, and many others that we have not listed. By knowing the current situation in the production system and the condition of the sensor, we can ensure and timely identify any type of potential malfunction, including the sensor itself [16–18]. The application of smart sensors with other necessary equipment in the production process is schematically presented in Figure 4.

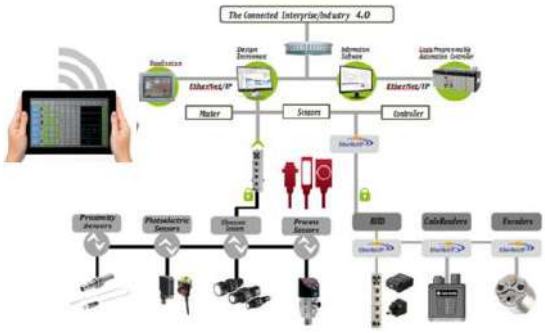

Figure 4 – Schematic representation of smart sensors implemented in the production process

Smart sensors provide a continuous flow of the valuation process and diagnostic data. They provide a visualization system, information software and a programmable controller such as the configuration shown in Figure 4, which enables the company's connectivity, benefits, and efficiency. Creating a connected company with smart sensors and smart machines reduces the complexity of production processes and errors. They simplify access to available data that can help achieve overall equipment efficiency and the average time between failures. The real-time diagnostics allows optimizing preventive maintenance and troubleshooting of problems that occur in the production process, thus reducing the resolution time by about 90 % [20]. Fully adjustable sensors improve the production process, as well as reduce the change time for each sensor. There is an option for automatic device configuration to reduce the error when replacing the sensor itself. Within each production process, there are many operations such as material handling, material transport, performing certain operations, assembly, packaging, varnishing, sorting, etc., where it is necessary to install smart sensor so that we can have information about the smooth performance of the operation or task at any time. Work assignment execution can be broken down into smaller events such as control, counting, indexing, ejecting, spraying, and transmitting, in which smart sensor helps us detect changes in conditions associated with the action and event. When implementing smart sensors in the production process, we need to identify key operations within the production system and define the focus area in which we need to verify the conditions. We need to know what the system is doing or what we want it to do, such as counting products, performing quality checks, orienting parts, etc. We need to know the feedback for each function, and what conditions must be met after each function in order to confirm that the function was correctly executed [16, 17]. Once we have identified the areas where the action is taking place in the production process, it is necessary to analyze whether each area is as important from the point of view of automating the production process and monitoring the data important in the production process. After obtaining the answer to the question about the damage caused by the errors occurring at that location, we decide on the application of the smart

sensor, and determine the best position or location to install the smart sensor.

2.3 Software

The statistical data on the implementation of smart sensors wits service robots for logistics were downloaded from the International Federation of Robotics (IFR), the UN Economic Commission for Europe (UNECE) and the Organization for Economic Co-operation and Development (OECD). For the calculation of statistical descriptions parameter and graphical presentation of data, we used standard statistical analysis methods and software system MS-Excel.

3 Results

It is a well-known fact that "Industry 4.0" is present in all industrial branches in production processes for more than a decade. Its application is continuously increasing, including transportation, and supplying customers with finished products. All new technologies, including smart robots, are responsible for the development of robotic technology, so there has been an enormous increase in the application of service robots for logistics, as shown in Figure 5 [11].

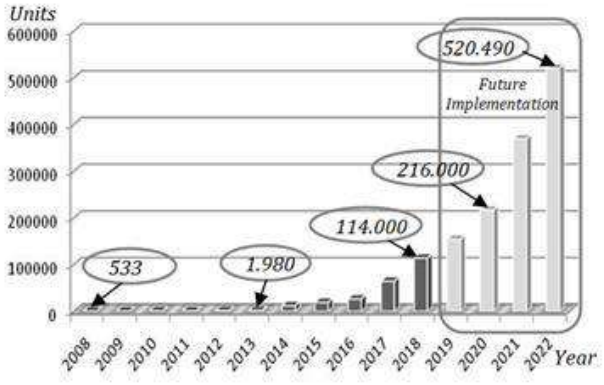

Figure 5 – The implementation of service robots for logistics in the world for the period 2008-2018 and estimated implementation by 2022

Based on Figure 5, it can be seen that the trend of application of service robots for professional use is continuously increasing. In the last five years, the application trend has gained exponential function, so that 271.000 service robots have been applied in 2018. The growth trend in the implementation of logistics service robots is also expected in the coming years, and it is estimated that in 2022 around 520.490 units of service robots for logistics in production processes will be applied. Company Mobile Industrial Robots – MiR has developed various designs of service robots for logistics (Figure 6), which apply smart sensors. Many companies, including Mobile Industrial Robots – MiR, have developed software solutions and service robots for logistics to optimize internal transport for heavy cargo pallets up to 1000 kg, as shown in Figure 6.

Figure 6 - The role of smart sensors in freight transport by service robots [14]

Mobile Industrial Robots – MiR service robots are collaborative and autonomous and can maneuver safely around all kinds of obstacles. If a person comes out in front of a robot, it will stop. Advanced technology and sophisticated software allow the robot to navigate independently and choose the most efficient route to its destination. When it encounters an obstacle, it automatically moves around it and can divert the route to avoid stopping or delaying material delivery thanks to smart sensors. Another example of the implementation of smart sensors in a single production process and setup site is shown in Figure 7 [17].

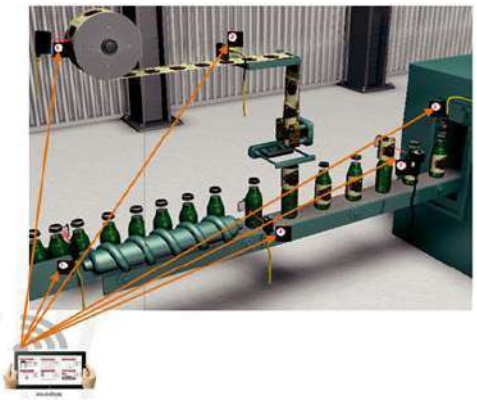

Figure 7 – The application of smart sensors in the production process of the process industry – Bottled product control

In the production operation of the process industry – bottled product control, smart sensors were used for the following: 1-Laser Measurement Sensor for bottle label diameter control, 2-Color Registration Mark Sensor for label registration, 3-Photoelectric Sensor A for detecting products exiting the battery, 4-Photoelectric Sensor B for label placement control, 5-Photoelectric Sensor for incorrect label control, and 6-Inductive Proximity Sensor for control of bottle cap presence. We can implement smart sensors in any production process depending on the role to be performed.

4 Conclusions

The development of new technologies has led to the development of sensor technology, resulting in smart sensors, which are continuously being developed and implemented in all segments of society. Many developed companies in the world are implementing Industry 4.0. They are digitizing all processes from raw material to end customers, which would be unthinkable without the smart sensors that support Industry 4.0. The implementation of smart sensors in production processes connects the company and reduces the complexity of production processes and errors.

They simplify access to available data that can help achieve overall equipment efficiency and the average time between failures. There are many advantages of implementing smart sensors in the production process, some of which are: detection of defects, efficient downtime and maintenance planning, more efficient supply chain management, increased efficiency and productivity, rapid transition to other product production, increased worker safety and health, high production quality, reduction and planning of electricity consumption in the manufacturing process, etc. The paper presents an example of the implementation of smart sensors in the production process with the aim of encouraging decision-makers to implement Industry 4.0 as soon as possible.

References

1. Sihn, W., Jager A., Humme, V., Ranz F. (2016). *Implications for Learning Factories from Industry 4.0*. ESB Business School, Reutlingen University, Reutlingen, Germany.
2. Bunse, B., Kagermann, H., Wahlster, W. (2017). *Industrie 4.0: Smart Manufacturing for the Future*. Brochure, 20750, Germany Trade and Invest, Gesellschaft für Außenwirtschaft und Standortmarketing GmbH, Berlin, Germany.
3. Dolecek, V., Karabegovic, I. (2008). *Robots in the Industry*. Technical Faculty of Bihac, Bihac, Bosnia and Herzegovina.
4. Rockwel Automation (2016). *Condition Sensors and Switches*, Publication 836E-BR001C-EN-P, USA.
5. Rockwel Aotomation. (2017). *Get Smart, Key Considerations for Developing Smart Machines and Equipment.* Publication: OEM-SP019B-EN-P, USA.
6. Byeong, W. A., Jung, H. S., So-Yun, K., Joohee, K., Sangyoon, J., Jihun, P., Youngjin, L., Jiuk, J., Young-Geun, P., Eunjin, C., Subin, J., Jang-Ung, P. (2017). Smart Sensor systems for wearable electronic devices. *Polymers*, Vol. 9(303), pp. 1–32.
7. Karabegovic, I., Karabegovic, E., Mahmic, M., Husak, E. (2015). The application of service robots for logistics in manufacturing processes. *Advances in Production Engineering and Management*, Vol. 10(4), pp. 185–194.
8. Jeremy, M. (2015). Robotics for manufacturing applications: Current state of collaborative robotics and flexible automation. *Collaborative Robotics Workshop 2015, Advantages and Challenges for Small Manufacturers*. Charles I. Ecker Business Training Center Columbia, USA, pp. 14–29.
9. Karabegovic, I., Karabegovic, E., Mahmic, M., Husak, E. (2019). Implementation of Industry 4.0 and industrial robots in production processes. *In: Isak Karabegović (eds) New Technologies, Development and Application II 2019. Lecture Notes in Networks and Systems, Springer Nature Switzerland AG*, Vol. 76, pp. 96–102.
10. Karabegovic I., Husak, E. (2018). Industry 4.0 Based on Industrial and Service Robots with Application in China. *Mobility and Vehicle*, Vol. 44(4), pp. 59–71.
11. Johan, H. H., Frank, R. R., Gertvan H. (1994). Developments in integrated smart sensors. *Sensors and Actuators A: Physical*, Vol. 43(1–3), pp. 276–288.
12. Karabegovic, I. (2017). The role of industrial and service robots in fourth industrial revolution with focus on China. *Journal of Engineering and Architecture*, Vol. 5(2), pp. 110–117.
13. Andreas, S., Nikolai, H., Tizian, S. (2018). Sensors 4.0 – smart sensors and measurement technology enable Industry 4.0. *Published by Copernicus Publications on behalf of the AMA Association for Sensor Technology*, Vol. 359–371.
14. Gary, W. H., Joseph, R. S., Peter, J. H., Chung-Chiun L. (2010). *Smart Sensor Systems*. The Electrochemical Society Interface, pp. 29–34.
15. Rockwel Automation (2016). *Smart Sensors, Enabling Smart Machines for The Connected Enterprise*. Publication IOLINK-BR001B-EN-P, USA.
16. Rockwel Automation (2011). *Sensor Application Guide*. PublicationSENS-AT001B-EN-P–May2011, USA.
17. Rockwel Automation (2016). Integrated Smart Sensors, Publication SENSOR-BR002A-EN-P, USA.
18. Manali, C., Srinu, D. (2014). Study of smart sensors and their applications. *International Journal of Advanced Research in Computer and Communication Engineering*, Vol. 3(1), pp. 5031–5034.

УДК 339.9:551.568.85

Роль розумних датчиків у виробничому процесі та впровадженні Індустрії 4.0

Карабегович І.[1*], Карабегович Е.[2], Махміч М.[2], Гусак Е.[2]

[1] Академія науки та мистецтва Боснії і Герцеговини, вул. Бистрик, 7, 71000, м. Сараєво, Боснія і Герцеговина;
[2] Університет м. Біхач, вул. І. Любіянкіча, 77000, м. Біхач, Боснія і Герцеговина

Анотація. У світі глобальної конкуренції клієнти висувають все більші вимоги, яким повинні відповідати промислові підприємства, щоб залишатися активними на світовому ринку. З цієї причини необхідно використовувати нові технології у виробничих процесах, впроваджуючи Індустрію 4.0. Іншими словами, потрібно створювати мережі компаній за допомогою цифрової трансформації, що дозволить виробничим процесам відкривати нові способи підвищення продуктивності та покращувати загальну ефективність виробничого процесу. Компаніям потрібно долучатися до запуску цифрових систем від постачальника до замовника. Це шлях, який сприятиме підвищенню продуктивності виробництва і рентабельності підприємства та якості готової продукції, а також впровадженню гнучкої промислової автоматизації виробничих процесів. Вищезазначені технології та Інтернету речей пов'язують фізичний і віртуальний світи з метою кращого збору та аналізу даних, перетворюючи їх на інформацію, яка доходить до осіб, які приймають рішення. Для цього необхідно впроваджувати розумні датчики, які надають інформацію у режимі реального часу. Впровадження Індустрії 4.0 у виробничі процеси, що реалізуються із застосуванням розумних датчиків, забезпечує зменшення часу на розроблення продукту, зменшення загальних витрат, удосконалення використання виробничих процесів і їх оптимізації, а також реалізує якісне управління ризиками виробничої компанії. У статті викладені шляхи впровадження інтелектуальних датчиків і їх практичного застосування у виробничих процесах.

Ключові слова: виробничий процес, розумний датчик, Індустрія 4.0, автоматизація виробництва, цифрове перетворення, гнучка автоматизація.

JOURNAL OF ENGINEERING SCIENCES
ЖУРНАЛ ІНЖЕНЕРНИХ НАУК
ЖУРНАЛ ИНЖЕНЕРНЫХ НАУК
Web site: http://jes.sumdu.edu.ua
Volume 6, Issue 2 (2019)

JOURNAL OF ENGINEERING SCIENCES
ЖУРНАЛ ІНЖЕНЕРНИХ НАУК
ЖУРНАЛ ИНЖЕНЕРНЫХ НАУК

Web site: http://jes.sumdu.edu.ua

DOI: 10.21272/jes.2019.6(2).c1 Volume 6, Issue 2 (2019)

Biosynthesis of Silver Nanoparticles Extracted Using Proteus

Shameran J. S.[1*], Sewgil S. A.[2], Awara Kh. S.[3]

[1] Department of Chemistry, Koya University, D. Mitterrand Blvd., Koya, Iraq;
[2] Hawler Medical University, 100 M St.; PO Box 178, Erbil, Iraq;
[3] Department of Biology, Koya University, D. Mitterrand Blvd., Koya, Iraq

Article info:
Paper received: January 29, 2019
The final version of the paper received: April 7, 2019
Paper accepted online: April 12, 2019

[*]**Corresponding Author's Address:**
shameran.jamal@koyauniversity.org

Abstract. This study is focused on the evaluation of dependable and eco-friendly methods for the synthesis of metal nanoparticles is a significant step in the area of application of nanotechnology. One of the alternatives to obtain this purpose is to use natural techniques such as biological approach. Here, we examine biosynthesis of metallic nanoparticles using extract Proteus sp. the metal nanoparticles were successfully synthesized via reduction of silver sulfate employed extracted cell of bacterium Proteus sp. Nevertheless, the extracellular acts as a reducing agent to convert silver ion from its aqueous solution and the synthetic were formed within 2 hrs. On the other hand, scanning electron microscopy (SEM) which describes the surface morphology of bio-reduction of Ag-nanoparticles demonstrated that the spherical nature occurred through the bio-synthesis process and the particles are mostly circular and irregular in shape, UV-visible exhibit a peak at 423 nm corresponding to the plasmon of silver nanoparticle and XRD pattern was taken and presented that all peaks were indexed by hexagonal wurtzite phase (PIXcel 1D). In spite of that, the band gap energy measured (2.93 eV) and suggested strong scattering of the X-ray in the crystalline phase. Finally, we concluded that this study offers the remarkable report that biological synthetic of metal nanoparticle is helpful to avoid the negative influence of physical and chemical process that is inappropriate for medical applications.

Keywords: bandgap, Proteus, bio-reduction, metallic nanoparticle.

1 Introduction

Noble metallic nanoparticles have now become the target of focused study. It is known that the chemical methods use corrosive chemicals to the synthesis of nanoparticles. In addition, the need in this time is the development of methods for the synthesis of nanoparticles by eco-friendly benign methods. Researchers in this field are eagerly looking into bio-synthesis for non-toxic systems. The biological process of the microorganism and bacterium origin have suggested eco-friendly methods for the synthesis of nanoparticles [1, 3]. However, the fabrication, characterization, and application of biologically synthesized nanomaterials have become a significant section of nanotechnology Bio-motivate techniques extremely lead to the synthesis of nanostructures that are uniform in the shape and size. The demands of biosynthesis of nanoparticles were started as the chemical and physical processes were been costly [2]. Many researches confirmed that the biosynthetic of silver nanoparticles using via chemical process produce some unwanted materials which absorbed on the surface of the nanoparticles may have hostile effects in medical applications. Thus, many of the latest antibacterial agents developed in the last decades; none of them has been achieved its activity against multi-drug resistant bacteria [5, 7]. Newly, nanotechnology has very remarkable in the pharmaceutical and biomedical field as alternative antimicrobial agent design in the view of the fact that renovation the occurrence and infective diseases of antibiotic-resistant strains, especially within gram-negative bacteria. Also, there is an increasing concern for silver nanoparticles on account of the antimicrobial properties [14]. Silver is a powerful inorganic antimicrobial agent, safe and non-toxic that is capable of killing about 600 types of diseases [11].

2 Literature Review

Recently, nanoparticles are being viewed as a fundamental building-blocks of nanotechnology. The most significant and distinct property of these nanoparticles is their enormous surface area to volume ratio, thus increasing their antimicrobial power as they would interact better with the cell of microorganism surfaces at a tiny

amount of dosage [3]. Definitely, in the case of silver nanoparticles, the broad spectrum antimicrobial activity enhances their use in biomedical applications, food production, cosmetics, clothing, numerous household products, and water and air purification [2, 3, 9]. Synthesis of nanoparticles via biosynthetic process provided non-toxic, eco-friendly and economic through an alternative to the various chemical and physical methods. Microbial such as yeasts, mold fungi, and bacteria are mostly preferred for nanoparticles biosynthetic due to their rapid rate of growth, ease of cultivation and their ability to grow at obtainable conditions of pressure, pH and temperature [5]. In a previous study, pointed out that bacterial sp. have various ranges of capability to adsorb heavy metals and produce nanoparticles during detoxification methods [6]. Designation of nanoparticles with suitable shape and size disparity is one of the great challenges of current nanotechnology [10].

3 Research Methodology

3.1 Proteus sp.

Proteus is included under the Enterobacteriaceae and is gram-negative, a rod shape, non-capsulated, motile, non-lactose fermenting, swarm across the surface of blood agar [16, 17]. It is one of the most common bacteria in soil and water containing decaying organic matter of animal origin and usually occurs in large numbers in sewage.

3.2 Experiments

Proteus sp. was obtained at the Department of Medical Microbiology of Koya University. The bacterial stock cultures were maintained on nutrient agar slants at 4 °C. Gram staining technique for the bacterial sample has been conducted to confirm Proteus sp. Fresh bacterial sample inoculated into 200 ml of nutrient broth and incubated in a shaker incubator at 37 °C for 24 hrs. To obtain the biomass the culture medium centrifuged at 5 000 rpm for 15 min, then washed many times with double distilled water to obtain a wet amount of the biomass (cells) [22]. The collected cells digested in 100 mL double distilled water for 24 hrs, the biomass was separated via 0.15–0.21 mm using Durapore membrane and the resulted filtrate was extracted from the cell. The final solution was light yellow and used for the reduction of silver sulfate (0.0006M). The converted time (Ag^+ ions to Ag^0) was 2 hrs to get brownish colloids. Further, the batch experiment carried out in bright condition (Figure 1).

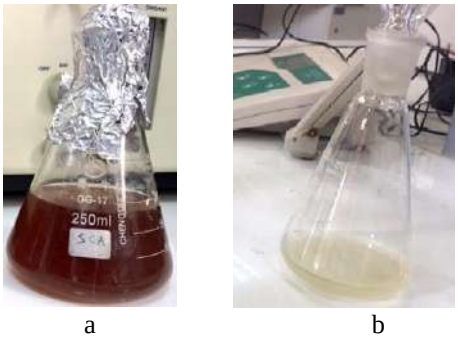

a b

Figure 1 – Colloids of silver nanoparticles and the extracted cells filtrate of Proteus sp.

4 Results

Proteus, both in mixed and pure cultures, has been found to be associated with a variety of pathological conditions. Pathogens found mainly in urinary tract infection or commensals found in the normal intestine and sewage [17]. Proteus species are opportunistic pathogens found with varying frequencies in the normal intestinal flora and differ from another group of Enterobacteriaceae in the production of very potent Urease which aids their rapid identification [R2004]. As shown in Figure 2 the bacteria are gram-negative, bacilli shaped [18].

Figure 2 – Gram stain of Proteus sp.

UV–visible spectroscopy measurement was accomplished by utilizing a double-beam spectrophotometer NORAN operated and scans in the range of 300–700 nm at a resolution of 2.0 nm [15]. The photo-absorption ability of the Ag- nanoparticle was detected by the spectrum as validated in Figure 3. The Ag-nanoparticles exhibited strong absorption at a wavelength of 423 nm.

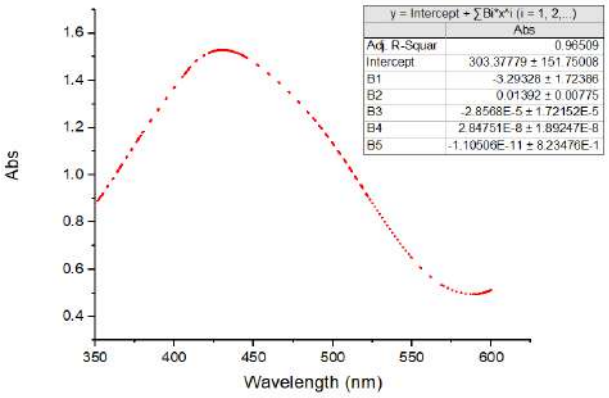

Figure 3 – Spectrum of Ag colloids measurement

Nevertheless, the band gap energy of the Ag-nanoparticles measured by the following formula:

$$E_g = \frac{1240}{\lambda_g}, \quad (1)$$

Where, λ_g is the wavelength (Figure 4), validated that the high ability of Ag-nanoparticles to absorb light by recorded form the measurement of the band gap energy which is $E_g = 2.93$ eV of the biosynthesis Ag-colloids after the addition of extracted cells of Proteus [16].

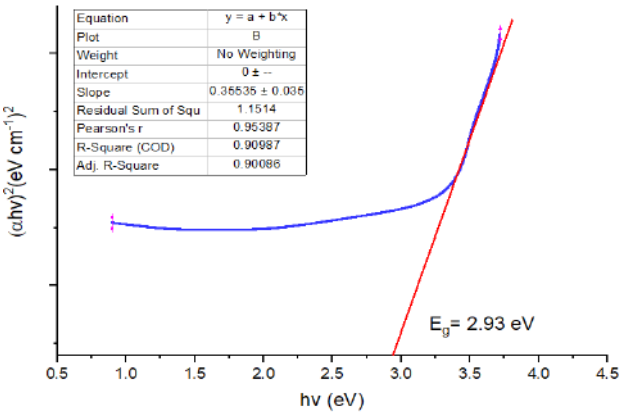

Figure 4- Band gap plot measurement of Ag-nanoparticles

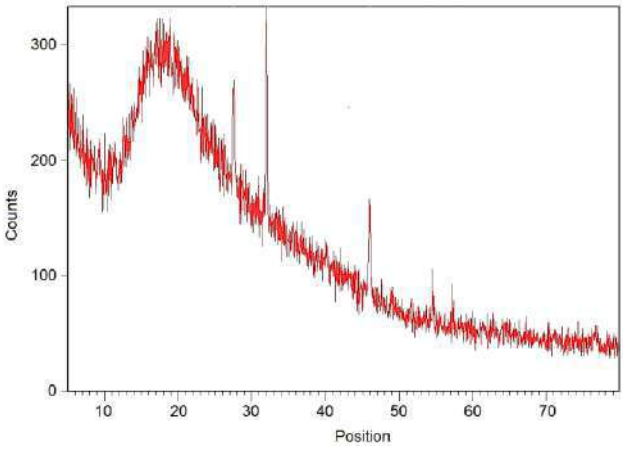

Figure 5 – X-ray spectra of extracellular-biosynthetic of Ag-nanoparticles from Proteus

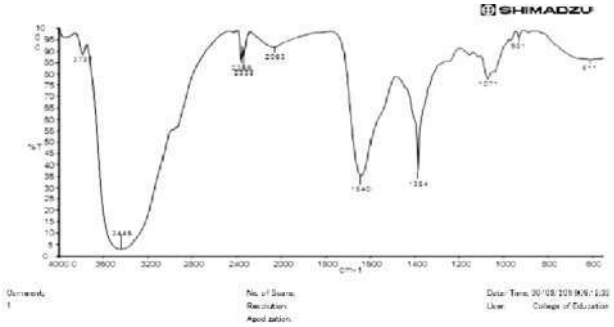

Figure 6 – FT-IR spectra of bio-reduction and formation of Ag-nanoparticles

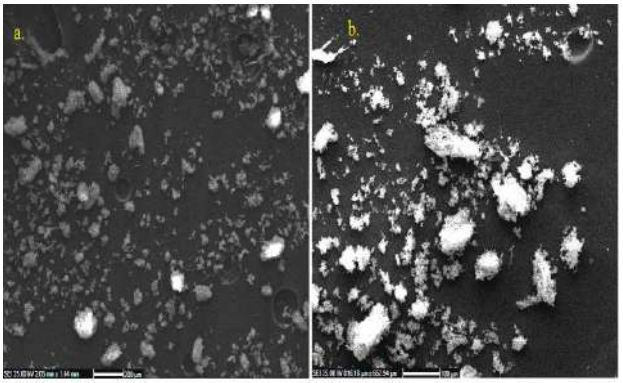

Figure 7 – Images of surface morphology of biosynthetic Ag-nanoparticles in both form

Figure 5 proves the crystalline nature of Ag-nanoparticles using X-ray spectra. However, the diffraction patterns at the values 38.011, 44.113, 45.293 and 54.483 elucidated the reflections of metal silver [19]. Besides with the four peaks above some other unassigned peaks were also observed at 26.540, 30.010, 32.670, 41.713 54.394 and 59.270. Finally, the high intensity of these peaks confirmed strong scattering of the X-ray in the crystalline phase [20].

The FT-IR spectra of Ag-nanoparticles synthesized from extracellular of Proteus are given in Figure 6. The measurements were achieved to characterize the possible bio-molecules responsible for capping and effective stabilization of the Ag-nanoparticles biosynthesized by extracted Proteus which indicate peaks at 3 445, тв. 3 787 cm^{-1} assigned to stretching aldehyde C-H stretching and O-H respectively. The peaks 2 338, 2 063, and 2 359 cm^{-1} corresponds to C-N stretching of amine [15]. This proposed that the biological molecules might be possibly performed functions of stabilization and formation of Ag-nanoparticles in the aqueous media [12, 21].

Surface morphology of biosynthetic of Ag-nanoparticles (Figure 7) clearly demonstrated the presence of nanoparticles in both dispersed and aggregated form. The size diameter of the Ag-nanoparticles has been noticed to lie between 20 to 40 nm and the shapes were indicated as spherical. Similarly, in a size range of 30–50 nm was reported elsewhere [12, 18]. Also, [22] reported that morphology analysis (SEM) of Ag-nanoparticles synthesized from a mushroom revealed the spherical nature of Ag-nanoparticles and size distribution in a range of 40 nm [13].

5 Conclusions

The bio-reduction of silver ions has been successfully occurred through biosynthetic extracellular microorganisms. Here, we demonstrate that materials released from intera-cell and cell wall of Proteus. The expected mechanism for the formation of Ag-nanoparticles includes reduces polysuccerides and enzymes into wall and cell that occurred by Proteus. In fact, this work showed relevant materials to produce more metallic-nanoparticles with good shape, size, and morphology. Also, we suggest taking more studies in this area. Finally, we also suggest the biosynthetic of Ag-nanoparticles to be a suitable candidate for optoelectronic devices and sensors.

References

1. Pliatsuk, L. D., Chernysh, Y. Y., Ablieieva, I. Y., Kozii, I. S., Balintova, M., Matiash, Y. O. (2018). Sulfur utilization in the systems of biological wastewater denitrification. *Journal of Engineering Sciences*, Vol. 5(1), pp. H7–H15, https://doi.org/10.21272/jes.2018.5(1).h2
2. Ghosh, S., Jagtap, S., More, P., Shete, U. J., Maheshwari, N. O., Rao, S. J., Pal, J. K. (2015). Dioscorea bulbifera mediated synthesis of novel Au core Ag shell nanoparticles with potent antibiofilm and antileishmanial activity. *Journal of Nanomaterials*, Vol. 16(1), pp. 161.
3. Salih, S. J., Smail, A. K. (2016). Synthesis, characterization and evaluation of antibacterial efficacy of zinc oxide nanoparticles. *Pharmaceutical and Biological Evaluations*, Vol. 3(3), pp. 327–333.
4. Saravanan, M., Barik, S. K., MubarakAli, D., Prakash, P., Pugazhendhi, A. (2018). Synthesis of silver nanoparticles from Bacillus brevis (NCIM 2533) and their antibacterial activity against pathogenic bacteria. *Microbial Pathogenesis*, Vol. 116, pp. 221–226.
5. Sarsar, V., Selwal, M. K., Selwal, K. K. (2015). Biofabrication, characterization and antibacterial efficacy of extracellular silver nanoparticles using novel fungal strain of Penicillium atramentosum KM. *Journal of Saudi Chemical Society*, Vol. 19(6), pp. 682–688.
6. Fariq, A., Khan, T., Yasmin, A. (2017). Microbial synthesis of nanoparticles and their potential applications in biomedicine. *Journal of Applied Biomedicine*, Vol. 15(4), pp. 241–248.
7. Balashanmugam, P., Santhosh, S., Giyaullah, H., Balakumaran, M. D., Kalaichelvan, P. T. (2013). Mycosynthesis, characterization and antibacterial activity of silver nanoparticles from Microporusxanthopus: a macro mushroom. *International Journal of Innovative Research in Science, Engineering and Technology*, Vol. 2(11), pp. 1–9.
8. Kalpana, D., Lee, Y. S. (2013). Synthesis and characterization of bactericidal silver nanoparticles using cultural filtrate of simulated microgravity grown Klebsiella pneumoniae. *Enzyme and Microbial Technology*, Vol. 52(3), pp. 151–156.
9. Ali, D. M., Sasikala, M., Gunasekaran, M., Thajuddin, N. (2011). Biosynthesis and characterization of silver nanoparticles using marine cyanobacterium, Oscillatoria willei NTDM01. *Digest Journal of Nanomaterials and Biostructures*, Vol. 6(2), pp. 385–390.
10. Vahabi, K., Mansoori, G. A., Karimi, S. (2011). Biosynthesis of silver nanoparticles by fungus Trichoderma reesei (a route for large-scale production of AgNPs). *Insciences Jornal*, Vol. 1(1), pp. 65–79.
11. Hosseini, M. R., Sarvi, M. N. (2015). Recent achievements in the microbial synthesis of semiconductor metal sulfide nanoparticles. *Materials Science in Semiconductor Processing*, Vol. 40, pp. 293–301.
12. Salih, S. J., Rashid, B. Z. (2015). Cranberry stem as an efficient adsorbent and eco-friendly for removal of toxic dyes from industrial wastewater. *Physico Studies. International Journal of Pharmaceutical Chemistry*, Vol. 5(6), pp. 207–217.
13. Usman, A. R., Kuzyakov, Y., Lorenz, K., Stahr, K. (2006). Remediation of a soil contaminated with heavy metals by immobilizing compounds. *Journal of Plant Nutrition and Soil Science*, Vol. 169(2), pp. 205–212.
14. Yanovska, H. O., Bolshanina, S. B., Kuznetsov, V. M. (2017). Formation of hydroxyapatite coatings with addition of chitosan from aqueous solutions by thermal substrate method. *Journal of Engineering Sciences*, Vol. 4(2), 2017. https://doi.org/10.21272/jes.2017.4(2).f1
15. Salih, S. J., Anwer, S. S., Faraj, R. H. (2017). A biosorption of Mercury from wastewater using isolated Aspergillus sp. Modified 1, 10-Phenanthroline: Hill isotherm model. *Science Journal of University of Zakho*, Vol. 5(4), pp. 288–295.
16. *Ray, C. G., Ryan, K. J. (2004). Sherris Medical Microbiology: An Introduction to Infectious Diseases*. McGraw-Hill.
17. Mobley, H. L., Belas, R., Lockatell, V., Chippendale, G., Trifillis, A. L., Johnson, D. E., Warren, J. W. (1996). Construction of a flagellum-negative mutant of Proteus mirabilis: effect on internalization by human renal epithelial cells and virulence in a mouse model of ascending urinary tract infection. *Infection and Immunity*, Vol. 64(12), pp. 5332–5340.
18. Jayaseelan, C., Rahuman, A. A., Kirthi, A. V., Marimuthu, S., Santhoshkumar, T., Bagavan, A., Rao, K. B. (2012). Novel microbial route to synthesize ZnO nanoparticles using Aeromonas hydrophila and their activity against pathogenic bacteria and fungi. *Spectrochimica Acta Part A: Molecular and Biomolecular Spectroscopy*, Vol. 90, pp. 78–84.
19. Singh, P., Kim, Y. J., Zhang, D., Yang, D. C. (2016). Biological synthesis of nanoparticles from plants and microorganisms. *Trends in Biotechnology*, Vol. 34(7), pp. 588–599.
20. Hussain, I., Singh, N. B., Singh, A., Singh, H., Singh, S. C. (2016). Green synthesis of nanoparticles and its potential application. *Biotechnology Letters*, Vol. 38(4), pp. 545–560.
21. Agarwal, H., Kumar, S. V., Rajeshkumar, S. (2017). A review on green synthesis of zinc oxide nanoparticles – An eco-friendly approach. *Resource-Efficient Technologies*, Vol. 3(4), pp. 406–413.
22. Moghaddam, A., Namvar, F., Moniri, M., Azizi, S., Mohamad, R. (2015). Nanoparticles biosynthesized by fungi and yeast: a review of their preparation, properties, and medical applications. *Molecules*, Vol. 20(9), pp. 16540–16565.

УДК 546.57:54.05

Біосинтез наночастинок срібла, екстрагованих із застосуванням Proteus

Шамеран Й. С.[1], Севґіл С. А.[2], Авара Х. С.[2]

[1] Університет м. Койа, б-р Д. Міттерана, м. Койа, Ірак;
[2] Медичний університет ім. Хоулера, вул. 100 М, 178, м. Ербіл, Ірак

Анотація. Запропоноване дослідження спрямоване на оцінювання надійних і екологічних методів синтезу металевих наночастинок, що дозволили зробити значний крок у сфері застосування нанотехнологій. Однією з альтернатив для досягнення поставленої цієї мети є використання природних методів, закрема біологічного підходу. У роботі розглядається біосинтез металевих наночастинок з використанням екстракту Proteus. При цьому металеві наночастинки успішно синтезувались за допомогою відновлення сульфату срібла, що екстрагується клітками бактерії Proteus. Тим не менш, позаклітинне середовище діє як відновник для перетворення іонів срібла з його водного розчину, і синтез відбувається впродовж 2 год. З іншого боку, скануюча електронна мікроскопія, що описує морфологію поверхні біоредукції наночастинок срібла, продемонструвала, що у процесі біосинтезу утворюється сферична форма, а частинки в основному круглої та неправильної форми, видимі в ультрафіолетовому спектрі частинки проявляють пік при довжині хвиль 423 нм, що відповідає плазмону наночастинок срібла, а рентгенографічна картина показала, що всі піки були визначены гексагональною фазою сульфыда цинку. Незважаючи на це, визначено енергію 2,93 еВ, а також запропоновано сильне рентгенівське випромінювання для кристалічної фази. У результаті зроблено висновок, що проведене дослідження підтверджує той факт, що біосинтез металевих наночастинок дозволяє запобігти негативного впливу фізичних і хімічних процесів , що відбуваються у засобах медичного застосування.

Ключові слова: бандгап, Proteus, біоредукція, металева наночастинка.

JOURNAL OF ENGINEERING SCIENCES
ЖУРНАЛ ІНЖЕНЕРНИХ НАУК
ЖУРНАЛ ИНЖЕНЕРНЫХ НАУК
Web site: http://jes.sumdu.edu.ua
DOI: 10.21272/jes.2019.6(2).c2 Volume 6, Issue 2 (2019)

Application of Reinforcing Thermocycling Treatment for Materials of Stamps Hot Deformation

Berladir K.[1*], Hovorun T.[1], Bondarenko M.[1], Shvetsov D.[1], Vorobiov S.[2]

[1] Sumy State University, 2 Rymskogo-Korsakova St., 40007 Sumy, Ukraine;
[2] Institute of Physics, P. J. Safarik University in Kosice, 2 Srobárova St., 041 54, Kosice, Slovakia

Article info:
Paper received: July 26, 2019
The final version of the paper received: December 6, 2019
Paper accepted online: December 11, 2019

***Corresponding Author's Address:**
kr.berladir@pmtkm.sumdu.edu.ua

Abstract. The paper is devoted to the search for technological methods of increasing the resistance of the stamp tool for hot deformation. New non-standard combinations of cyclization schemes and parameters of thermocycling processing within the regime were developed. This is allowed the creation of managed structural states in the metal due to the grinding of grain, the creation of high density of defects, and the acceleration of diffusion processes to effectively manage the structure, increase the mechanical, operational properties and prevent the destruction of the working surfaces of the tool. New modes of thermocycling treatment, which have a positive effect on the mechanical characteristics of HNM5 steel, have been developed and tested. The conducted heat treatment in experimental modes, consisting of thermocycling treatment as a preliminary, quenching and tempering as the final, allows obtaining a more homogeneous structure with the preservation of fine grain and a given hardness. The grain size of the steel HNM5 structure after the use of thermocycling treatment decreases from 5–6 to 7–8 points, and after the final heat treatment – to 9–10 points.

Keywords: stamp of hot deformation, thermocycling treatment, strength, relative narrowing, thermal resistance.

1 Introduction

Hot volume stamping is used to produce blanks for the responsible parts of cars, tractors, agricultural machines, airplanes, railway cars, machines, etc. [1]. It is quite common to use steel HNM5 for hot deformation stamps, which is now the widespread material in the production of hot stamping tools in batch production [2].

The problem of improving the quality, reliability, and durability of the tool for hot deformation of metal is relevant in connection with the improvement of the design of rolling mills and forging and pressing equipment, if necessary, to achieve greater compression forces and deformation rates. Therefore, the priority of materials science at the present stage is the development of new high-efficiency modes of strengthening, which allow increasing the level of physical, mechanical and operational properties of the tool.

Currently, thermocycling treatment (TCT) is the heat treatment under conditions of cyclic thermal influences that are intensively distributed [3]. However, it is used in production for a very limited list of products. The solution to this problem can be achieved by finding new non-standard combinations of cycling circuits and TCT parameters within the regime, which would allow the creation of managed structural states in the metal by grinding grain, creating a higher density of defects, accelerating diffusion processes and other physical effects.

2 Literature Review

The authors investigated the influence of the TCT process on the microstructure, mechanical and operational properties of stamp steels [4–9].

In [4], steels for stamps hot deformation – HNM5, H2NMF5, H3V3MFS5 were selected for the study. It was established that TCT with constant T_{max}, cooling between cycles in air up to 350 °C, cooling in oil from the last heating crushes the structure and makes it more homogeneous, which increases the mechanical properties of steel HNM5 after thermal cycling and tempering at a given hardness: KCU 1.4–1.6 times, durability characteristics by 5–8 %, ductility characteristics twice and more.

The authors of [5] describe an invention related to the field of metallurgy and can be used for heat treatment of steels in the manufacture of tools and machine parts in mechanical engineering: carbon tool steel is subjected to heat treatment, including repeated heating above Ac_1 at 40–80 °C at a speed of 4–8 °C/s, cooling in a cycle below

Ac_1 to 250–300 °C at a rate of 1–7 °C/s, tempering at 160–240 °C.

In [6], the authors tested TCT modes on stamps made of steel HNM5, the parameters of which were obtained experimentally and focused on obtaining an improved complex of mechanical properties (with high impact strength).

The application of the proposed method of thermocycling processing allows increasing the toughness of carbon tool steel by 4–6 times compared with traditional hardening while maintaining high hardness and strength [7].

3 Research Methodology

3.1 Objects of research

Chromium-nickel steel for stamps hot deformation HNM5 and its properties were selected as the object of study.

Steel HNM5 is tool-grade, high-quality, medium-alloy, semi-heat-resistant, high-viscosity and high-throughput. Its chemical composition and mechanical properties are shown in Tables 1, 2 (data according to GOST 5950-73).

Table1 – The chemical composition of steel HNM5, %

C	Mn	Si	Cr	Ni
0.5–0.6	0.5–0.8	0.1–0.4	0.5–0.8	1.4–1.8
Mo	W	P	S	Cu
0.15–0.30	–	0.03	0.03	0.3

Table2 – Mechanical properties of steel HNM5 after treatment

$\sigma_{0.2}$, MPa	σ_B, MPa	δ, %	ψ, %	*KCU*, kJ/m^2	Hardness	
					surface HRC	core HB
1270	1470	11	38	440	40–44	352–397

Steel has the following purpose: the production of hammer stamps, steam and pneumatic hammers with a mass of parts falling more than 3 tons, press stamp machine speed stamping during hot deformation of light-colored alloys, blocks of stamps for inserts of horizontal forging machines.

3.2 Methods of research

Metallographic methods and standard mechanical properties tests were used to study the mechanisms of hardening steel: impact and tensile tests.

It was used a pendulum coper MK-30A with a variable energy reserve in the range from 10 to 300 J and tensile machine P-20 for static testing of specimens of metals by static tensile loads in accordance with GOST 7855-68.

Koper pendulum MK-30A meets the requirements of GOST 10708-82 and is intended for testing of materials for shock bending in accordance with GOST 9454-78. Koper is intended for work in the premises of laboratory type. The tests were performed on specimens with sharp cuts of defined shape and size, in accordance with GOST 9454-78.

Hardness measurements were performed using Rockwell hardness tester.

Metallographic analysis of the structure of steel was carried out on a microscope MIM 7.

4 Results

The influence of technological methods on increasing the mechanical properties of steel HNM5 was investigated by the following methods:

1. Carrying out of heat treatment of steel HNM5 according to the standard (Figure 1) and experimental modes of thermocycling as preliminary heat treatment (Figure 2).

2. Determination of mechanical properties of the material for hot deformation stamps in the initial state and after the completed modes of heat treatment (Tables 3, 4).

3. Metallographic analysis of the structure of steel after previous and final modes of heat treatment (Figures 3–7).

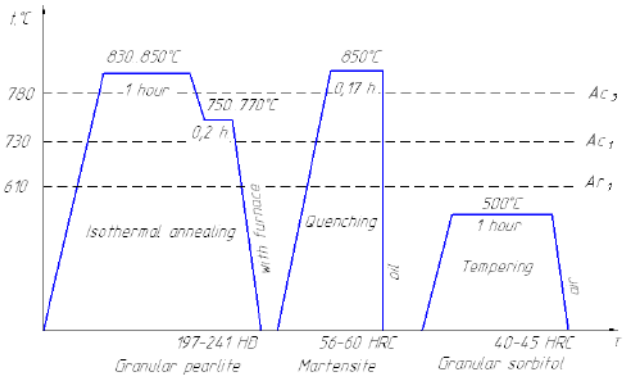

Figure 1 – Standard heat treatment of steel HNM5

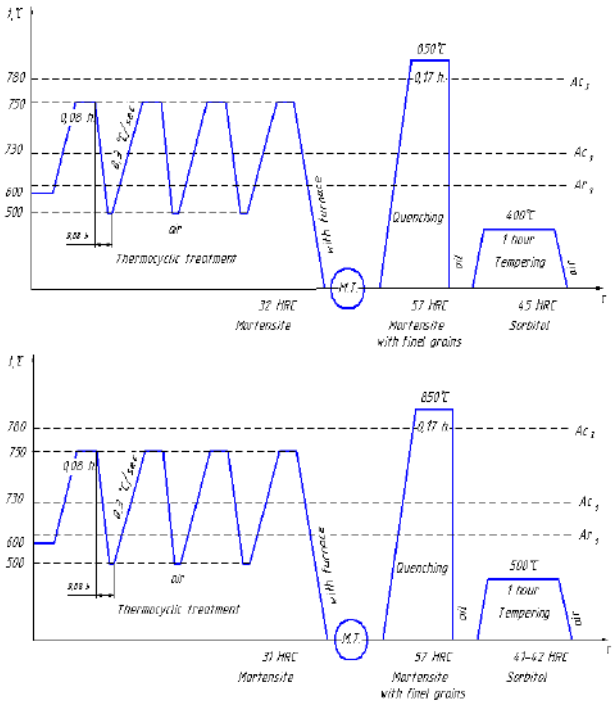

Figure 2 – Experimental modes of heat treatment

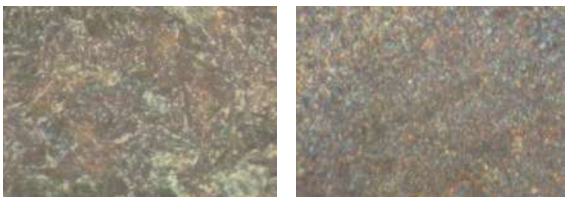

a b

Figure 3 – Microstructure of steel HNM5 after isothermal annealing (b) and thermocycling treatment (b), x480

Figure 4 – Microstructure of steel HNM5 after standard heat treatment, x500

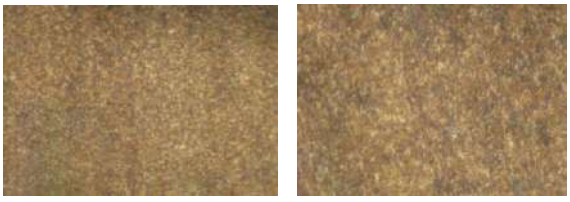

a b

Figure 5 – Microstructure of steel HNM5, x480: a – after thermocycling 750 °C + quenching 850 °C + tempering 400 °C; b – after thermocycling 750 °C + quenching 850 °C + + tempering 500 °C

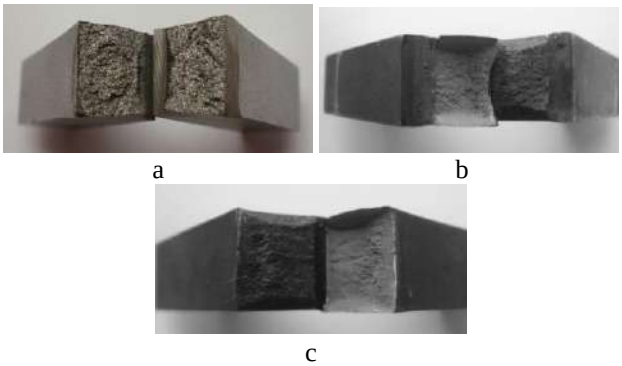

a b c

Figure 6 – Macrostructure of samples of steel HNM5 after impact test: a – before thermal cycling; b – after thermal cycling 750 °C + quenching 850 °C + tempering 400 °C; c – after thermocycling 750 °C + quenching 850 °C + tempering 500 °C

a b c

Figure 7 – Macrostructure of samples of steel HNM5 after tensile test: a – before thermal cycling; b – after thermal cycling 750 °C + quenching 850 °C + tempering 400 °C; c – after thermal cycling 750 °C + quenching 850 °C + tempering 500 °C

Table 3 − Results of the impact test

Mode of heat treatment	The work, which was spent on the destruction of the sample $A_н$, N	Impact viscosity $a_н$, kN/m²
Without heat treatment	24.0	300
Isothermal annealing 850 °C, quenching 850 °C + + tempering 500 °C	35.2	450
Thermal cycling + + quenching 850 °C + + tempering 400 °C	166.0	2075
Thermal cycling + + quenching 850 °C + + tempering 500 °C	190.0	2375

Table 4 − Results of the tensile test

Mode of heat treatment	σ_B, MPa	δ, %	ψ, %
Isothermal annealing 850 °C, quenching 850 °C + + tempering 500 °C	1470	11.0	38.0
Without heat treatment	794	16.0	42.6
Thermal cycling + quenching 850 °C + tempering 400 °C	1654	6.7	42.9
Thermal cycling + quenching 850 °C + tempering 500 °C	1498	14.3	43.0

5 Discussion

Standard heat treatment of steel HNM5 includes isothermal annealing as pre-heat treatment, quenching, and tempering as final heat treatment (Figure 1).

The mode of pre-heat treatment is annealing temperature 830–850 °C; the exposure is about 1 hour; slow cooling to 750–770 °C, holding for 0.2 hours, cooling with the oven. The result is a structure of granular perlite with a hardness of 197–221 HB, grain perlite grain score is 5–6 points (Figure 3 a).

The structure of the steel after quenching is martensite. Steel HNM5 is characterized by low resistance to the growth of austenite grain because its carbide phase is mainly composed of soluble particles of the M_3C type. The hardness after quenching is 56–60 HRC.

The reduction of the hardness of steel HNM5 with an initial hardened structure can be achieved by tempering at a high temperature of 500 °C. After heat treatment, the steel has a structure of granular tempered sorbite with hardness 40–45 HRC (Figure 4).

After conducting a literary patent search and analyzing the literature data on the influence of thermocycling processing on the microstructure, mechanical and operational properties of tool steels, and stamped ones, two experimental modes of heat treatment were developed (Figure 2). Samples of steel HNM5 underwent thermal cycling according to the regime, which included four-cycle heating to a constant temperature of 750 °C and intermediate cooling in air to a temperature of 500 °C (above M_n). The hardness of the steel after TCT is 31 HRC, the grain score – 7–8 points, the structure after the experimental mode of thermocycling is shown in Figure 3 b.

After thermocycling, the specimens were machined. The final heat treatment was then carried out − quenching by standard heat treatment for steel HNM5 − heating to a temperature of 850 °C, the exposure for 0,1 hour and cooling in oil, and tempering − in one mode to a temperature of 400 °C, and in another − to 500 °C.

The hardness of steel HNM5 after quenching is 57 HRC, after tempering at 400 ° C − 45 HRC, after tempering at 500 °C – 41–42 HRC. The grain score of the structure after tempering at 400 °C is 9-10 points, at 500 °C – 8–9 points. Figure 5 shows the microstructures of steel HNM5 after two experimental heat treatment modes.

So, the conducted heat treatment in experimental modes, consisting of TCT as a preliminary, quenching and tempering as the final, allows obtaining a more homogeneous structure with the preservation of fine grain and a given hardness.

The impact tests showed (Table 3, Figure 6):

1. The use of TCT experimental mode, which included four cycles with heating to 750 °C, cooling between cycles in air, from the last cycle − with the oven, quenching with heating to 850 °C and tempering at 400 °C, allows increasing the value of KCU 4 times compared to typical heat treatment.

2. The use of TCT experimental mode, which included four cycles with heating to 750 °C, cooling between cycles in air, from the last cycle − with the oven, quenching with heating to 850 °C and tempering at 500 °C, allows increasing the value of KCU 5 times compared to typical heat treatment.

The tensile tests showed in Table 4 and Figure 7 are:

1. In the samples after heat treatment, which included TCT, quenching and tempering at 400 °C, the strength indices increased by 150 MPa with a simultaneous increase in the relative narrowing compared to typical heat treatment.

2. In the samples after heat treatment, which included TCT, quenching and tempering at 500 °C, the strength indices increased by 50 MPa with a simultaneous increase of 5 % relative elongation and relative narrowing compared to typical heat treatment.

6 Conclusions

The experimental modes of thermocycling that included 4 cycles of heating to 750 °C, cooling in the last cycle with the furnace, quenching of heating to 850 °C with cooling in oil and tempering to 400 ° and 500 °C, allow obtaining a more homogeneous structure with preservation of fine grains.

The grain size of steel structure after using thermocycling decreases from 5–6 to 8–7 points, after the final heat treatment the grain score was 9–10 points.

The tests of mechanical properties showed that for the obtained fine grain structures of steel HNM5 is tended a significant increase in ultimate strength (σ_B is about 100 MPa) while increasing the relative narrowing of about 1.5 times and KCU in 4–5 times after thermocycling, quenching and tempering, which significantly superior properties of steel after standard heat treatment.

References

1. Karbasian, H., Tekkaya, A. E. (2010). A review on hot stamping. *Journal of Materials Processing Technology*, Vol. 210, pp. 2103–2118, doi: 10.1016/j.jmatprotec.2010.07.019.
2. Berladir, K. V., Dunaeva, M. N. (2012). Heat treatment of the stamp hot deformation. *The* 6*th Scientific and Practical University Conference of LSNC*. Sumy, Sumy State University, pp. 81−82.
3. Fedyukin, V. K., Smagorinskiy, M. Ye. (1989). *Thermocycling Processing of Metals and Machine Parts*. Engineering, Saint Petersburg [in Russian].
4. Ivashenko, V. Yu., Cheylyah, A. P. (2011). The use of thermocycling for treatment of stamps. *Bulletin of the Priazovsk State Technical University. Series "Technical Sciences"*, Vol. 22, pp. 108–112 [in Russian].
5. Guryev, A. M., Voloshin, L. G., et al. (1997). The method for thermocycling processing of tool steels. *Patent, Russia, No. 2078440, MPK S21D1/78*, Bulletin No. 16 [in Russian].
6. Ivashenko, V. Yu., Cheylyah, A. P. (2009). On increasing the resistance of stamps for hot deformation. *Construction, Materials, Engineering: A Collection of Scientific Papers*, Vol. 48(1), pp. 114–118 [in Russian].
7. Guryev, A. M., Voroshnin, L. G., Kharayev, Yu. P., et al. (2005). Thermocycling and chemical-thermocycling strengthening of steels. *Polzunovsky Bulletin*, Vol. 2(2), pp. 36–43 [in Russian].
8. Pchelintsev, V. O., Hovorun, T. P., Rab, V. M., Berladir, K. V. (2012). Thermocycling treatment of shaft of 40Cr steel centrifugal pump of the NKV type. *Bulletin of Sumy State University. Series "Technical Sciences Series"*, Vol. 4, pp. 123–132 [in Ukrainian].
9. Guryeva, O. A., Zemlyakov, S. A., Guryev, A. M. (2005). Optimization of thermocycling processing of tool steel. *Bulletin Alt-STU*, Vol. 3-4, pp. 167–173 [in Russian].

УДК 669.018.291

Застосування зміцнювального термоциклічного оброблення для матеріалів штампів гарячого деформування

Берладір Х. В.[1], Говорун Т. П.[1], Бондаренко М. Є.[1], Швецов Д. В.[1], Воробйов С. І.[2]

[1] Сумський державний університет, вул. Римського-Корсакова, 2, 40007, м. Суми, Україна;
[2] Інститут фізики, Університет ім. П. Й. Шафарика у м. Кошице, вул. Шробарова, 2, 041 54, м. Кошице, Словаччина

Анотація. Стаття присвячена пошуку технологічних методів підвищення стійкості штампового інструмента для гарячого деформування. У результаті дослідження були розроблені нові, нестандартні сполучення схем циклування і параметрів термоциклічного оброблення (ТЦО) у межах режиму. Це дозволило створити в металі керовані структурні стани за рахунок подрібнення зерна, створення підвищеної щільності дефектів і прискорення дифузійних процесів з метою ефективного управління структурою, підвищення механічних, експлуатаційних властивостей та запобігання руйнуванню робочих поверхонь інструмента. Розроблено і випробувано нові режими ТЦО, які позитивно впливають на механічні характеристики сталі 5ХНМ. Проведене термічне оброблення відповідно до експериментальних режимів, що складалось із попереднього термоциклічного оброблення з послідуючими гартуванням і відпуском, дозволяє отримати більш однорідну структуру металу із збереженням дрібного зерна і заданої твердості. Розмір зерна структури сталі 5ХНМ після використання термоциклічного оброблення зменшується з 5–6 до 7–8 балів, а після остаточного термічного оброблення – до 9–10 балів.

Ключові слова: штамп гарячого деформування, термоциклічне оброблення, міцність, відносне звуження, термостійкість.

JOURNAL OF ENGINEERING SCIENCES
ЖУРНАЛ ІНЖЕНЕРНИХ НАУК
ЖУРНАЛ ИНЖЕНЕРНЫХ НАУК

Web site: http://jes.sumdu.edu.ua

DOI: 10.21272/jes.2019.6(2).d1 Volume 6, Issue 2 (2019)

Advancement of Fault Diagnosis and Detection Process in the Industrial Machine Environment

Altaf S.[1], Mehmood M. S.[2], Soomro M. W.[3]

[1] Auckland University of Technology, 55 Wellesley St., 1010 Auckland, New Zealand;
[2] Sajid Brothers Engineering Industries (Pvt.) Ltd, 52250 Punjab, Gujranwala, Pakistan;
[3] Manukau Institute of Technology, Newbury St., 2023 Aukland, New Zealand

Article info:
Paper received: July 5, 2019
The final version of the paper received: September 15, 2019
Paper accepted online: September 20, 2019

***Corresponding Author's Address:**
saud.altaf@aut.ac.nz

Abstract. Machine fault diagnosis is a very important topic in industrial systems and deserves further consideration in view of the growing complexity and performance requirements of modern machinery. Currently, manufacturing companies and researchers are making a great attempt to implement efficient fault diagnosis tools. The signal processing is a key step for the machine condition monitoring in complex industrial rotating electrical machines. A number of signal processing techniques have been reported from last two decades conventionally and effectively applied on different rotating machines. Induction motor is the one of widely used in various industrial applications due to small size, low cost and operation with existing power supply. Faults and failure of the induction machine in industry can be the cause of loss of throughput and significant financial losses. As compared with the other faults with the broken rotor bar, it has significant importance because of severity which leads to a serious breakdown of motor. Detection of rotor failure has become significant fault but difficult task in machine fault diagnosis. The aim of this paper is indented to summarizes the fault diagnosis techniques with the purpose of the broken rotor bar fault detection.

Keywords: machine fault diagnosis, signal processing technique, induction motor, condition monitoring.

1 Introduction

Machine fault diagnosis and condition monitoring are very important in industrial engineering system, and it needs more attention considering increasing the performance needs of modern machinery. Machine fault and failure will have quality implications and sometimes may cause of shutdown of machinery and many financial losses. Therefore, it is necessary to develop intelligent diagnosis systems that will be helpful to provide a reliable and accurate diagnosis which can be able to provide accurate information regarding the present machine condition [1].

Induction machine (IM), which is also called the asynchronous motor, is a critical component of mostly industrial machinery system which is widely using in the petrochemical, transportation, manufacturing and power systems just because of its simplicity, reliability, high excess power load [2]. IM consist of a magnetic circuit connected with the two electrical circuits which rotate to each other. Compared with the Direct Current (DC) motors, IM is low cost, less rugged configuration, in small size, less maintenance and can operate on the accessible power line [3]. The range size of induction motors is from tiny to over 104 hp. But, in the practical applications, IM is subjected to inescapable electrical, mechanical and thermal stresses and become the cause of different faults [4]. Sometimes these faults may cause of shutdown of machinery and many financial losses [5]. An efficient diagnosis technique can reduce the unscheduled maintenance cost and trace the fault at early development stages. Basically, IM was invented by N. Tesla [6]. The rotating parts of IM do not need the linking electricity due to the energy which is provided by the electromagnetic induction [7]. The stator can generate a rotating magnetic field which induces a substituting electromagnetic energy and power current in rotor. This inferred power current in rotor and the rotating field in stator are communicated to each other and induce a motor torque [8].

2 Literature Review

Numerous methods of induction motor fault diagnosis were developed in the last decades and many techniques have been proposed [9, 10]. The most common approach is the motor current signature analysis (MCSA) [11]. Several of induction motor faults detection and identification techniques are based on Fast Fourier Transform

spectral signature analysis [12–14]. Other techniques include vibration analysis, temperature measurements, harmonic analysis of speed fluctuations [15, 16], vibration monitoring [17], state and parameters estimation [18], either axial flux or air-gap torque analysis [19], acoustic noise measurement, and magnetic field analysis [20–23]. Currently, more and more new techniques based on artificial intelligence (AI) have been utilized for diagnostic induction motor faults, such as fuzzy logic [24, 25], genetic algorithms [26], neural network [27], Bayesian classifiers [28], and envelope of the three-phase stator current with AI-based on Gaussian mixture models and reconstructed phase spaces (RPSs) [29].

The methods used to diagnose broken bars can be broadly categorized into two types, invasive and non-invasive fault diagnosis techniques [30]. The invasive methods diagnose broken bars by monitoring the deviation of the magnetic potential vector and asymmetrical magnetic flux distribution, gyration radius, asymmetrical magnetic flux distribution, torque and speed fluctuation and so on [31]. In these methods, sensors and costly measurement equipment's are needed, which will increase the complexity and expense of the diagnostic method [32]. Induction motor faults often generate particular frequency components in the current spectrum. The abnormal harmonics contain potential information of motor faults. Therefore, the frequency analysis approach is the most commonly used method to diagnose induction motor faults. The aim of this paper is indented to investigate a broad list of references to the recent advancement and summarizes the fault diagnosis techniques with the purpose of BRB fault detection.

3 Research Methodology

3.1 Rotor structure in induction motor

In Induction motor, there are two types of rotor, i. e. Squirrel cage and wound rotor. Squirrel Cage Rotor (SCR) is a very simple and widely used rotor for IM manufacturing. SCR is consists of the plastic-coated iron core and it is slotted around its circuit lengthwise. Solid aluminium or copper bars are firmly embedded or pressed into rotor slots [33]. Short-Circuiting rings are embedded or welded to the bars at both edges of rotor. Short-Circuiting bars don't have to be particularly insulated from the core just because of resistance which is below the core [34]. For the placement of rotor core, in some kind of rotors, the end rings and bars are cast as a single cage component. The short-circuiting components are induced in the shorted turns by the stator flux. As compared with the wound rotor with the SCR, the SCR is comparatively simple and easy to fabricate [35].

Under average operating situations, great thermal and mechanical stresses are presents when the machine is being constantly restarted and with heavily loaded [36]. It is well known that the rotor current during starting can be increased ten times the normal full load current and can be the cause of large stresses in the rotor circuit. The bar cracks have increased the resistance and produced the heat at the crack. The crack bar will almost break, and arcing will happen across the break. This arcing will then damage the laminations around the faulted bar. The nearest bar will carry an increased current and lead to increase the current and could do damage the stator winding and rest of rotor bars as well [37, 38].

By applying the threshold rules to diagnose the BRB fault in healthy induction motors, the following authors in Table (1) proposed the different estimation practical models in [15–17]. These models are used by the other researchers in [16] which put aside usage of proposed models for the BRB fault detection in various practical applications such as compressors, fan, pumps, etc.

Generally, Benbouzid and Thomson present in their papers an insignificantly higher estimation the number of rotor broken bars based on the almost similar results as shown in Figure 1. The intensity of both sideband (left and right) based on the different load conditions of IM. Some of the similarity between Benbouzid and Thomson models results shows similarity between the lower values of LSB magnitude values i.e. 5-8 dB. Shaft load should always be in good condition during experiment but it's difficult to maintain in practice to precisely nominal load on an investigated IM. The main disadvantage of the discussed models is the relationship with IM slide necessary to calculate sidebands frequencies, and IM frequency slip which is consist of intensity, experimental load conditions and fluctuation of the load between diffident motors were not presented in proper way.

Table 1 – Broken bar detection experimental results* [10–12]

Author	BRB models	The amplitude at left side band (LSB)			
		50.91 dB	27.51 dB	30.06 dB	40.16 dB
Benbouzid [10]	$\frac{I_{BRB}}{I} = \frac{\sin\alpha}{2p(2\pi-\alpha)}$	0.39	4.00	3.45	3.39
Bellini [11]	$\frac{I_{BRB}}{I} = \frac{n}{N}$	0.09	2.04	1.58	1.57
Thomson [12]	$\frac{I_{BRB}}{I} = \frac{n}{2N-np}$	0.18	2.10	2.88	2.86

* where $\alpha = 2\pi pn/N$; I_{BRB} – amplitude of the LSB; I – basic supply current; N – number of rotor bars; n – number of broken bars; p – number of pole pairs.

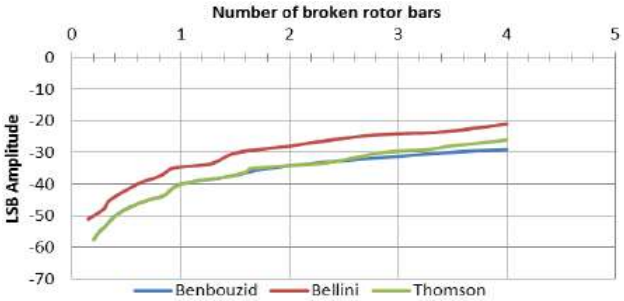

Figure 1 – Comparison of broken bar models

3.2 Common rotor related faults

Rotor related faults are generally related to magnetic stresses from electromagnetic forces, thermal stresses, residual stresses in unsatisfactory mechanized and some environmental stresses that are caused by moisture [39]. Various stresses are comprehensively has been described in [40]. Rotor related faults are normally starting at server resistance and produce the high temperature, and then lead to the damage the rotor bar [41]. This fault normally takes place at end rings of cage. For the detection of BRB fault, most of important parameters are needed to observe in which vibration, variation in speed, motor current signature, and air-gap flux are significant parameters. Rotor related failure into IM can be categorized into breakage of rotor bars, rotor eccentricity, and breakage of end-rings. The following section concisely describes the abovementioned faults in rotor [42].

The rotor bar breakage is the key fault in the rotor of IM. Breakage of rotor bars does not normally result in an instant failure of the IM and can cause increased heating, loss of torque and stressing the neighboring bars [43]. During the operational mode of IM, the rotor bars can be fractionally and completely cracked due to the stresses. Breakage of rotor bars does not normally result in an instant failure of the IM. Broken bars can cause a loss of torque and increased heating and stressing of nearby bars [44]. Being able to identify the broken or cracked bars early decreases shutdown time and lowers repair expenses since the repairs are generally only for the rotor. If the bars are not repaired and the motor continues to operate, additional bar breakage is likely as well as damage to other components in the motor [45]. The more rotor bars that break, the larger the loss of torque and the higher the current in adjacent bars. The higher current causes higher temperatures in the area near the broken bars and will also cause stator damage due to excessive heat. Oscillations in speed and torque are indications breakage of rotor bars, which can cause increased wear of other motor components. Hafezi et al [46] presented the distinctive reasons for the BRB failure used by the prediction based model using the instantaneous angular speed (IAS) analysis to simulate the IM performance in healthy and in breakage rotor bar condition. To observe the behavior of IM, Runge Kutta Integration (RKI) algorithm was applied to resolve the rotor bar failure problem.

Eccentricity related faults in rotor cause a consistent air gap that corresponding the unbalanced magnetic force and non-consistent air gap magnetic field which producing the vibration and noise on stator [47–49]. Most of the research [50–54] has been published in last years about the vibration and noise on Permanent magnet synchronous (PMS) and DC motors but little research has been done on the eccentricity related fault in rotor to observe the vibroacoustic behavior of IM motors. In ideal operating motor [55], basically the rotor is centrally lined up with the stator and rotation of the rotor's center is similar to the stator geometric center. A rotor eccentricity can take place in both static and dynamic eccentricity conditions. In static eccentricity condition, the position is fixed for the minimal radial rotor air-gar length in space [56].

4 Results

4.1 Fault diagnosis techniques for BRB

When any fault happens, some of the machine parameters have to be changed. These parameter changes depend upon the severity of the fault and interaction with other parameters. A broad range of survey [34–44] has been done from different researchers and many techniques (e. g. thermal monitoring [50, 51], current analysis [47, 48], torque monitoring [54, 55], noise monitoring [52, 53] and vibration analysis [49]) for fault detections has been investigated, but all other techniques except MCSA are required some expensive sensors for monitoring machine condition [20, 45]. This is the reason the current monitoring techniques is non-intrusive and also may use for the remote monitoring in the central motor control center. Several IM Faults diagnoses techniques are based on the Fast Fourier Transform (FFT) spectrum signature analysis using the stator current [47]. The methods used to detect the BRB fault in IM can be classified into two categories, invasive and non-invasive method [56]. The conventional static relay and electromechanically diagnosis techniques in the industries are based on the invasive method because of insertion of temperature sensor in IM which is used to the measure temperature impact significant on degree of protection. On the other hand, non-invasive method is more using and preferable technique in the industries these days because of inexpensive and easily accessible measurement to observe the machine healthy and abnormal conditions without separation of IM from system [57].

4.2 Motor current signature analysis

Motor current signature analysis (MCSA) is novel methods for diagnosing the BRB fault in IM due to its low cost and simplicity. Basically, this method is based on the produced sidebands around the fundamental supply frequency in stator current [57]. Several works [58–60] has been reported in previously published papers for the development of machine condition monitoring application using MCSA among different industrial case studies [47]. The MCSA use the current spec-

trum of machine for finding the required attributes of fault frequencies at what time a fault present. Literature shows in [58–60] that the critical point about MCSA is sensing electrical signal which has current sensing mechanism that can detect the broken rotor bar, shorted turn, and airgap eccentricity faults, etc. at early stages of fault development and avoid the severe damage or completely shutdown of machine. The classification of different available diagnosis techniques for BRB as follows in Figure (2).

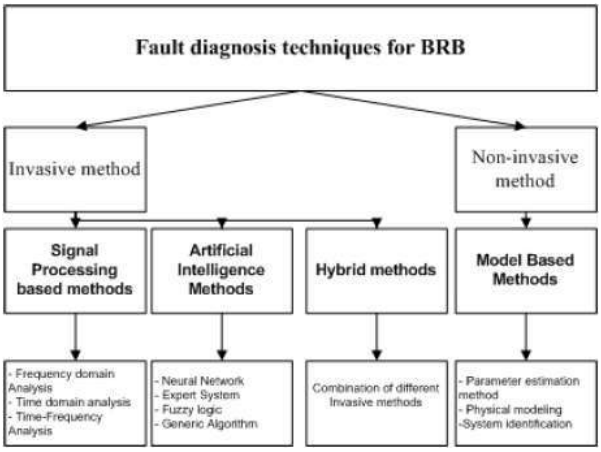

Figure 2 – Fault diagnosis techniques for BRB fault

Ahmed et al in [61] presents an online machine fault system which senses the current without any user interpretation at unspecified load. A frequency filter applied which contain frequency characteristic of induction machine of normal load condition using a set of some expert system. All these generated frequencies managed through a table and neural networks clustering algorithm inputs compare with the initial machine performance characterizes. While training the system, it only requires the good condition of the machine. Since a fault is going to present and demean the current signature while it progresses in excess of time, the system compares these changes with the originally learned spectra which are stored in table, and if some change in the spectra, it indicates the fault condition and generates an alarm. The Author's claimed that the combination of rule-based expert system frequency filter and neural network clustering algorithm increase the system's capability to detect the machine faults with small spectral changes.

In [62], Ayhan et al. stated that MCSA utilized the outcomes of spectral analysis of stator current. Noise and distortion always become a cause of disturbing the signal and effecting on the procedure of detection faults at early stages. The research work shows that using Fast Fourier Transform (FFT), the frequency signature spectrum of some asymmetrical machine faults including broken bar, rotor asymmetry, bearing failure, etc. can be easily identified which leads to better understanding of motor current spectra. Supangat concludes in another paper [63] is that FFT technique is useful for many application those are using in machine fault detection where signal is stationary. But this is not good for the analysis of those signal in which frequency get some variation and non-stationary signals. This issue can be resolved through time-frequency techniques. i.e. Short Time Fourier Transform (STFT).

4.3 Spectral feature selection and fault characteristics

One of the important tasks in BRB fault diagnosis process is to analyze the spectrum and selection of sensitive frequency features. Hence, there is a need to identify and select the most valuable features which are very important in machine fault identification and localization process. To use the complete set of feature sets will cause much cost of time and low performance because in the original features set there are numerous irrelevant and laid off features existed [47].

The frequency characterizations of different fault condition models have been illustrated from previous literature on current signature analysis. We aim to use these frequencies models in a further phase of our research to identify the fault frequencies from current spectrum. Faults in electrical machine produce characteristic fault frequencies that could be examined by using spectrum analysis of one or more sensor quantities such as current. The current can be used to compute the instantaneous power. The following Table 2 shows some typical faults conditions and the frequency components indicators of abnormality.

Table 2 – Typical faults and associated frequencies* [40–42]

Fault	Frequency characteristics, Hz
Broken rotor bar (BRB)	$f_{brb} = f_1(1 \pm 2s)$
Air gap eccentricity	$f_{ecc} = f_1[(1 - s)R/p \pm k]$
Shorted turn fault frequency	$f_{st} = f_1[(1 - s)n/p \pm k]$

* where f_1 – supply frequency; s – per unit slip; R – number of rotors; p – number of poles-pairs; k, n – harmonic number; $n = 1, 2, 3, \ldots$

4.4 Signal processing techniques for brb fault detection

Most of the successful machine fault diagnosis and condition monitoring tools depend on different signal processing techniques. Through signal analysis, it is possible to decide the healthy and faulty frequencies of various machine components in time and frequency domain. The severity of the fault can be measure through amplitude of signal both in time and frequency domain. Fast Fourier transform (FFT) is very simple, fast and easy to apply on current spectrum signal in frequency domain but the main problem with FFT is that not appropriate for the transient signal [50]. But this problem is not significant in that condition when the signal is stationary.

To overcome this deficiency, the Short-Time Fourier Transform (STFT) can be used for analyzing the non-stationary and transient signal in the time-frequency domain. But the main problem with this technique is that it can be analyzed the signal for all frequencies with a set sized of window [51].

STFT is also presented the poor frequency resolution. These two problems of STFT can be overcome by applying the wavelet transform which provides the flexible extended time interval and better frequency resolution. A detailed comparison of the different signal processing methods is illustrated in Table 3.

Table 3 – Comparison between different signal processing techniques

Technique	Faults diagnozed	Advantages	Disadvantages
FFT [66]	• broken rotor bar fault • short winding fault • air gap eccentricity • bearing faults	• suitable for high load conditions • easy to implement • good for visualization fault symptoms	• lost time information • not effective in light load condition
STFT [67]	• broken rotor bar fault • bearing faults	• fast speed • suitable for varying load conditions	• analyze signal with a fixed-sized window • poor frequency resolution
Wavelet transform [68, 69]	• broken rotor bar fault • short winding fault • bearing faults • load fault	• fast speed • suitable for varying load and light load conditions • excellent low time and frequency resolution for low-frequency sideband components	• absence of phase information for a complex-valued signal • poor directionality • shift sensitive for input-signal causes an unpredictable change in transform coefficients in time

5 Conclusions

This paper presents a comprehensive comparison review on a broad list of references to the recent advancement and summarizes the fault diagnosis techniques with the purpose of BRB fault detection.

A comprehensive attempted based on the recent references is summarized and development in the field of machine condition monitoring and fault diagnosis. It is anticipated that this research will be very helpful for those who are concerned with understanding the dominant capability of machine condition monitoring and fault diagnosis. The chosen reference list is intended to cover all possible significant area in machine condition monitoring and published in recent years.

References

1. Bonnett, A. H., Soukup, G. C. (2013). Analysis of rotor failures in squirrel cage induction motors. *IEEE Transactions on Industry Applications*, Vol. 24(6), pp. 1124–1130.
2. O'Donnell, P. (2005). Report of large motor reliability survey of industrial and commercial installations. Part 1. *IEEE Transactions on Industry Applications*, Vol. IA-21(4).
3. O'Donnell, P. (2005). Report of large motor reliability survey of industrial and commercial installations. Part 2. *IEEE Transactions on Industry Applications*, Vol. IA-21(4).
4. O'Donnell, P. (2017). Report of large motor reliability survey of industrial and commercial installations. Part 3. *IEEE Transactions on Industry Applications*, Vol. IA-23(4), pp. 153–158.
5. Vas, P. (1999). *Parameter Estimation, Condition Monitoring, and Diagnosis for Electrical Machines*. Clarendon, Oxford, UK.
6. Seinsch, H. O. (2001). Monitoring und diagnose elektrischer maschinen und antriebe. *ETG-Workshop Monitoring und Diagnose Elektrischer Maschinen und Antriebe*, VDE-Haus, Frankfurt am Main.
7. Albrecht, P. F., Appiarius, J. C., McCoy, R. M., Owen, E. L., Sharma, D. K. (2012). Assessment of the reliability of motors in utility applications. *IEEE Trans. Energy Convers.*, Vol. EC-1(1), pp. 39–46.
8. Albrecht, P. F., Appiarius, J. C., Sharma, D. K. (2009). Assessment of the reliability of motors in utility applications. *IEEE Transactions on Energy Conversion*, Vol. 1, pp. 39–46.
9. Bonnett, A. H. (2010). Root cause failure analysis for ac induction motors in the petroleum and chemical industry. *Proceedings of the 57th Annual Petroleum and Chemical Industry Conference*.
10. Benbouzid, M. E. H. (2016). A review of induction motors signature analysis as a medium for faults detection. *IEEE Trans. on Industrial Electronics*, Vol. 47(5), pp. 984–993.
11. Bellini, A., Filippetti., F., Franceschini, G., Tassoni, C., Kliman, G. B. (2011). Quantitative evaluation of induction motor broken bars by means of electrical signature analysis. *IEEE Trans. on Ind. Appl.*, Vol. 37(5), pp. 1248–1255.
12. Thomson, W. T. (2011). On-line fault diagnosis in induction motor drives via MCSA. EM diagnostics Ltd. *Proceedings of the 37th Turbo-Machinery Symposium*, Scotland.

13. Matic, D., Kulic, F., Climente-Alarcon, V., Puche-Panadero, R. (2012). Artificial neural networks broken rotor bars induction motor fault detection. *10th Symposium on Neural Network Applications in Electrical Engineering (NEUREL)*, pp. 49–53.
14. Induction Motors. Retrieved from: http://electriciantraining.tpub.com/14177/css/14177_94.htm.
15. Nandi, S., Toliyat, H. A., Li, X. (2015). Condition monitoring and fault diagnosis of electrical motors – a review. *IEEE Transactions on Energy Conversion*, Vol. 20, pp. 719–29.
16. Bonnett, A. K., Soukup, G. C. (1999). Cause and analysis of stator and rotor failures in 3-phase squirrel cage induction motors. *Pulp and Paper Industry Technical Conference*, pp. 22–42.
17. Nandi S., Bharadwaj, R., Toliyat, H. A., Parlos, A. G. (2009). Study of three phase induction motors with incipient rotor cage faults under different supply conditions. *Proc. IEEE-IAS Annual Meeting*, Vol. 3, pp. 1922–1937.
18. Ben Sasi, A. Y., Gu, F., Li, Y., Ball, A. D. (2016). A validated model for the prediction of rotor bar failure in squirrel-cage motors using instantaneous angular speed. *Mechanical Systems and Signal Processing*, Vol. 20(7), pp. 1572–1589.
19. Dorrell, D. G., Chindurza, I., Cossar, C. (2015). Effects of rotor eccentricity on torque in switched reluctance Machines. *IEEE Transactions on Magnetics*, Vol. 41(10), pp. 3961–3963.
20. Rezig, A., Mekideche, M. R., Djerdir, A. (2017). Effect of rotor eccentricity faults on noise generation in permanent magnet synchronous motors. *Progress in Electromagnetics Research C*, Vol. 15, pp. 117–132.
21. Gereis, G. F., Wang, C., Lai, J. C. (2006). *Noise in Polyphase Electric Motors*, Taylor & Francis, USA.
22. Gereis, G. F., Wang, C., Lai, J. C., Ertugrul, N. (2017). Analytical prediction of noise of magnetic origin produced by permanent magnet brushless motors. *Electrical Machines and Drives Conference IEMDC*, Antalya, Turkey.
23. Wang, S., Aydin, M., Lipo, T. A. (2015). Electromagnetic vibration and noise assessment for surface mounted PM machines. *IEEE Power Engineering Society Summer Meeting*, Vancouver, Canada.
24. Didier, G., Ternisien, E., Caspary, O., Razik, H. (2017). A new approach to detect broken rotor bars in induction machines by current spectrum analysis. *Mechanical Systems and Signal Processing*, Vol. 21, pp. 1127–1142.
25. Ahmed, I., Ahmed, M. (2018). Comparison of stator current, axial flux and instantaneous power used to detect the broken rotor bar fault in machines. *Australian University Power Engineering Conference*, Sydney, Australia.
26. Vas, P. (1993). *Parameter Estimation, Condition Monitoring, and Diagnosis of Electrical Machines*. Clarendon, Oxford, UK.
27. Heller, B, Hamata, V. (1977). *Harmonic Field Effects in Induction Machine*. Elsevier, New York.
28. Cameron, J. R., Thomson, W. T., Dow, A. B. (2016). Vibration and current monitoring for detecting airgap eccentricity in large induction motors. *Proc. Inst. Elect. Eng. B*, Vol. 133(3), pp. 155–163.
29. Basak, D., Tiwari, A., Das, S. P. (2016). Fault diagnosis and condition monitoring of electrical machines – A review. *IEEE International Conference on Industrial Technology (ICIT 2006)*, pp. 3061–3066.
30. Gandhi, A., Corrigan, T., Parsa, L. (2017). Recent advances in modeling and online detection of stator interturn faults in electrical motors. *IEEE Transactions on Industrial Electronics*, Vol.58(5), pp. 1564–1575.
31. Da, Y., Shi, X., Krishnamurthy, M. (2014). Health monitoring, fault diagnosis and failure prognosis techniques for Brushless Permanent Magnet Machines. *IEEE Vehicle Power and Propulsion Conference (VPPC)*, pp. 1–7.
32. Bellini, A., Immovilli, F., Rubini, R., Tassoni, C. (2008). Diagnosis of bearing faults of induction machines by vibration or current signals: a critical comparison. *Industry Applications Society Annual Meeting*, pp. 1–8.
33. Verucchi, C. J., Acosta, G. G. (2007). Fault detection and diagnosis techniques in induction electrical machines. *Latin America Transactions*, Vol. 5(1), pp. 41–49.
34. Pandian, A., Ali, A. (2009). A review of recent trends in machine diagnosis and prognosis algorithms. *World Congress on Nature & Biologically Inspired Computing*, pp. 1731–1736.
35. Behbahanifard, H., Karshenas, H., Sadoughi, A. (2008). Non-invasive on-line detection of winding faults in induction motors – A review. *International Conference on Condition Monitoring and Diagnosis*, pp. 188–191.
36. Ciandrini, C., Gallieri, M., Giantomassi, A., Ippoliti, G., Longhi, S. (2010). Fault detection and prognosis methods for a monitoring system of rotating electrical machines. *IEEE International Symposium on Industrial Electronics (ISIE)*, pp. 2085–2090.
37. Hajiaghajani, M., Madani, S. M. (2005). A new method for analysis of rotor broken bar fault in induction machines. *IEEE International Conference on Electric Machines and Drives*, pp. 1669–1674.
38. Tavner, P. J. (2008). Review of condition monitoring of rotating electrical machines. *Electric Power Applications*, Vol. 2(4), pp. 215–247.
39. Zhang, P., Du, Y., Habetler, T. G., Lu, B. (2009). A survey of condition monitoring and protection methods for medium voltage induction motors. *Energy Conversion Congress and Exposition*, pp. 3165–3174.
40. Jayaswal, P., Wadhwani, A. K., Mulchandani, K. B. (2008). Machine fault signature analysis. International *Journal of Rotating Machinery*, Vol. 2008, art. no. 583982.
41. Jung, J.-H., Lee, J.-J., Kwon, B.-H. (2006). Online diagnosis of induction motors using MCSA. *IEEE Transactions on Industrial Electronics*, Vol. 53(6), pp. 1842–1852.
42. Bellini, A., Filippetti, F., Franceschini, G., Tassoni, C., Kliman, G. (2001). Quantitative evaluation of induction motor broken bars by means of electrical signature analysis. *IEEE Transactions on Industry Applications*, Vol. 37, pp. 1248–1255.

43. Benbouzid, M. (1998). A review of induction motors signature analysis as a medium for faults detection. *Proceedings of the 24th Annual Conference of the IEEE Industrial Electronics Society*, Vol. 4, pp. 1950–1955.
44. Sadoughi, A., Ebrahimi, M., Razaei, E. (2006). A new approach for induction motor broken bar diagnosis by using vibration spectrum. *International Joint Conference SICE-ICASE*, pp. 4715–4720.
45. Cheng, S., Du, Y., Restrepo, J. A., Zhang, P., Habetler, T. G. (2012). A nonintrusive thermal monitoring method for induction motors fed by closed-loop inverter drives. *IEEE Transactions on Power Electronics*, Vol. 27(9), pp. 4122–4131.
46. Hafezi, H., Jalilian, A. (2006). Design and construction of induction motor thermal monitoring system. *Proceedings of the 41st Universities Power Engineering Conference*, Vol. 2, pp. 674–678.
47. Vico, J., Voloh, I., Stankovic, D., Zhang, Z. (2010). Enhanced algorithm for motor rotor broken bar detection. *Conference Record of 2010 Pulp and Paper Industry Technical Conference (PPIC)*, pp. 1–8.
48. Antonino-Daviu, J., Aviyente, S., Strangas, E., Riera-Guasp, M. (2011). A scale invariant algorithm for the automatic diagnosis of rotor bar failures in induction motors. *IEEE International Symposium on Industrial Electronics (ISIE)*, pp. 496–501.
49. Lima-Filho, A. C., Gomes, R. D., Adissi, M. O., da Silva, T. A. B, Belo, F. A., Spohn, M. A. (2012). Embedded system integrated into a wireless sensor network for online dynamic torque and efficiency monitoring in induction motors. *IEEE/ASME Transactions on Mechatronics*, Vol. 17(3), pp. 404–414.
50. Toscani, S., Faifer, M., Rossi, M., Cristaldi, L., Lazzaroni, M. (2012). Effects of the speed loop on the diagnosis of rotor faults in induction machines. *IEEE Transactions on Instrumentation and Measurement*, Vol. 61(10), pp. 2713–2722.
51. Chudasama, K. J., Shah, V. (2012). Induction motor non-invasive fault diagnostic techniques: A review. *International Journal of Engineering Research and Technology*, Vol. 1(5).
52. Aroui, T., Koubaa, Y., Toumi, A. (2018). Magnetic coupled circuit modelling of induction machines oriented to diagnostics. *Leonardo Journal of Sciences*, Vol. 13, pp. 103–121.
53. Mehala, N., Dahiya, R. (2018). Motor Current Signature Analysis and its Applications in Induction Motor Fault Diagnosis. *International Journal of Systems Applications, Engineering and Development*, Vol. 2(1), pp. 29–35.
54. Mehala, N., Dahiya, R. (2008). Motor current signature analysis and its applications in induction motor fault diagnosis. *International Conference on Signal Processing, Robotics and Automation (ISPRA-08)*, pp. 442–448.
55. Thomson, W. T., Gilmore, R. J. (2013). Motor current signature analysis to detect faults in induction motor drives – Fundamentals. *Proceedings of the 32nd Turbomachinery Symposium on Data Interpretation and Industrial Case Histories*, Texas, A&M University, USA.
56. Schoen, R. R., Lin, B. K., Habetler, T. G., Schlag, J. H., Farag, S. (2015). An unsupervised, on-line system for induction motor fault detection using stator current monitoring. *IEEE Transactions on Industry Applications*, Vol. 31(6), pp. 1280–1286.
57. Benbouzid, M. E. H., Nejjari, H., Beguenane, R., Vieira, M. (2019). Induction motor asymmetrical faults detection using advanced signal processing techniques. *IEEE Transactions on Energy Conversion*, Vol. 14(2), pp. 147–152.
58. Benbouzid, M. E. H. (2000). A review of induction motors signature analysis as a medium for faults detection. *IEEE Transactions on Industrial Electronics*, Vol. 47(5), pp. 984–993.
59. Moin, S. K., Giri, V. K. (2012). Broken rotor bar fault detection in induction motors using wavelet transform. *International Conference on Computing, Electronics and Electrical Technologies (ICCEET)*, pp. 1–6.
60. Ayhan, B., Chow, M.-Y., Song, M.-H. (2006). Multiple discriminant analysis and neural-network-based monolith and partition fault-detection schemes for broken rotor bar in induction motors. *IEEE Transactions on Industrial Electronics*, Vol. 53(4), pp. 1298–1308.
61. Ahmed, I., Ahmed, M. (2018). Comparison of stator current, axial leakage flux and instantaneous power to detect broken rotor bar faults in induction machines. *Power Engineering Conference*, Australasian Universities, pp. 1–6.
62. Ayhan, B., Chow, M.-Y., Song, M.-H. (2015). Multiple signature processing-based fault detection schemes for broken rotor bar in induction motors. *IEEE Transactions on Energy Conversion*, Vol. 20(2), pp. 336–343.
63. Supangat, R., Ertugrul, N., Soong, W. L., Gray, D. A., Hansen, C., Grieger, J. (2010). Broken rotor bar fault detection in induction motors using starting current analysis. *European Conference on Power Electronics and Applications*, pp. 1–10.

УДК 629.3

Удосконалення процесу діагностування несправностей у промислових умовах

Алтаф С.[1], Мехмуд М. С.[2], Сумро М. В.[3]

[1] Технологічний університет м. Окленд, вул. Велслі, 55, 1010, м. Окленд, Нова Зеландія;
[2] ТОВ "Sajid Brothers Engineering Industries", 52250, м. Пенджаб, Пакістан;
[3] Технологічний інститут Манукау, вул. Ньюбері, 2023, м. Окленд, Нова Зеландія

Анотація. Діагностика несправностей машин є дуже важливою прблемою у промислових системах і заслуговує на подальший розгляд з огляду на зростаючі вимоги до складності та підвищення експлуатаційних характеристик сучасних машин. У даний час виробничі компанії та дослідники роблять значні спроби впровадити ефективні засоби діагностики несправностей. Оброблення сигналів є ключовим кроком у моніторингу стану машини в складних промислових електричних роторних машинах. За останні роки було розроблено ряд методів оброблення сигналів, які традиційно застосовуються у різних роторних машинах. Зокрема, індукційні двигуни є широко уживаними в різних галузях промисловості завдяки їх невеликим розмірам, низькі собівартості та роботі з існуючим джерелом живлення. Несправності індукційної машини можуть стати причиною значних промислових і фінансових втрат на підприємстві. Порівнянюючи різні несправності, можна зробити висновок, що діагностування дефектів валу має важливе значення через складність наслідків цього дефекту, що призводить до серйозної несправності двигуна. При цьому виявлення цієї несправності є надскладною проблемою технічної діагностики несправностей машини. Тому метою цієї роботи є узагальнення методів технічного діагностування несправностей машин для виявлення дефектів валу.

Keywords: діагностування несправностей машини, методика оброблення сигналу, індукційний двигун, моніторинг стану.

JOURNAL OF ENGINEERING SCIENCES
ЖУРНАЛ ІНЖЕНЕРНИХ НАУК
ЖУРНАЛ ИНЖЕНЕРНЫХ НАУК

Web site: http://jes.sumdu.edu.ua

DOI: 10.21272/jes.2019.6(2).d2 Volume 6, Issue 2 (2019)

Design Optimization and Simulation Analysis of Formula SAE Frame Using Chromoly Steel

Kumar M. D.*, Teja P. S., Krishna R., Sreenivasan M.

PACE Institute of Technology and Sciences, 523 272 Ongole, Andhra Pradesh, India

Article info:
Paper received: September 7, 2019
The final version of the paper received: December 4, 2019
Paper accepted online: December 9, 2019

***Corresponding Author's Address:**
mdineshautomobile@gmail.com

Abstract. Compliance with the rules and regulations of competition "Student Formula Car Racing" that conducted annually by the 'Society of Automotive Engineers' (SAE) India, the car frame must be designed and built with supreme priority. The major task posed is to design and fabricate a light weighed vehicle chassis frame without compensating the safety. This paper boards various methods of material selection, technical design optimization and Finite Element Analysis using ANSYS. The basic design is based on the anthropological study data of the specified human (95th percentile male) al-lowing fast 'way-in' and 'way-out' access from the car. According to the rules book specification on material selection, AISI 4130 chromoly steel was the first time identified for the frame design. Resulting in the final design of the vehicle frame, various analyses were done using ANSYS and the successive results are plotted and discussed. The entire design optimization and simulation analysis are based on the 2019 Formula SAE rules book.

Keywords: finite element analysis, AISI 4130 chromoly steel, frame construction, Society of Automotive Engineers.

1 Introduction

The Formula SAE (FSAE) competition is a sponsorship contest held annually by the Society of Automotive Engineers (SAE), India from the period of 1998 to till date. Student teams from various engineering colleges all over India participate in this event, battle each other in car racing.

The teams are awarded points, based on different criteria of designing, fabricating and trail running the car. Basically, the criteria are based on the rulebook framed by SAE INDIA [1]. As per the rulebook, this paper examines numerous traits of design of the vehicle frame, with an application emphasis to an open-wheeled, space-frame race car chassis, as used in Formula racing. The design is based upon considerations like load transfer through the structure, different deformation modes, stiffness of the frame in each deformation modes and its respective effect on the dynamic response of the car [2]. The model is designed and analyzed using Solid Works and ANSYS respectively and an optimum result was obtained. A tubular frame structure was designed and analyzed, taking the specifications mentioned in the rule book into the concern for the design.

2 Research Methodology

2.1. Basic design

For designing a Formula SAE chassis frame, it is the following primary design parameter that always comes in the picture namely the suspension points, powertrain layout, driver position and controls and the safety aspects [3]. For the car to perform as intended, these parameters must be incorporated together to form an effective package.

2.2 Suspension points

The suspension points are used to describe the coordinates for all other vehicle parts. Such points need to be defined and set in order to define the vehicle's remaining points. The suspension system preserves the vehicle's balance when the car is exposed to any of its axes at times.

2.3 Powertrain layout

As FSAE cars are powered using motorcycle engines, mounting the engine to the car is easier as alike in the motorcycle. The engine position in addition to the wheelbase of the vehicle has the most important role in the distribution of the weight of the car. A simple way to combat this is to shift more weight of the car towards the driven wheels to maximize the vertical load on the tires [4].

2.4 Driver position and controls

The driver alignment and controls are other important aspects of the chassis layout. Driver comfort considerations include seating orientation, room for the elbow, and head height in relation to the front of the car and activity controls.

2.5 Driver seating

The seating orientation was determined primarily by the driver, testing under different seatback angles in a plywood seat mockup. The angle between 45 and 50 degrees from horizontal was calculated to be optimal for a driver's safety and comfort. The shallower seat position has a favorable impact by decreasing the driver's head and chest lower and the average center of gravity of the vehicle is therefore reduced [1]. With the driver's head lower, it will be more difficult for short drivers to see over the front roll hoop and bulkhead. Nonetheless, as the contest driver of the team is between 5'6" and 5'8", the decision made to retain the shallow chair. Another benefit on 2019 rules on the cockpit space helps the driver to have more elbow room. This led to operating the steering wheel more effectively as the driver able to have more leverage in the cockpit.

2.6 Safety

The Rules committee developed a set of rules specifying tube sizes in areas of the frame, essential to driver safety. For the front bulkhead, front roll hoop, central roll hoop, side-impact piping, roll hoop bracing and front impact areas, these guidelines describe external diameters and wall thicknesses. Without exception, the specified rules are adhered, so that the driver can be protected and the vehicle can pass the practical examination in action.

Table 1 – Chemical composition of chromoly steel

Element	Composition, %
Iron (Fe)	97.0–98.2
Chromium (Cr)	0.80–1.10
Molybdenum (Mo)	0.40–0.60
Carbon (C)	0.27–0.33

3 Materials

According to the constraint of the rulebook, the carbon content for the frame material should be at least 0.1 %. Following a comprehensive market survey, Chromoly Steel is the material commercially available and currently being used for an open-wheeled race car [5]. Based on that, this paper concludes on choosing AISI 4130 Chromoly Steel as the material for the frame design.

3.1 Chromoly steel

Chromoly steel is a low-alloy steel type named after the addition of "chromium" and "molybdenum" – the two primary elements of the alloy composition. This class of steel identifies under the AISI 41xx designations. Chromoly steel is typically an alloy steel grade 4130. The number 30 designates that material has 0.33 % carbon by weight. The inclusion of chromium and molybdenum leads to better material properties in comparison to the mild steel containing the equivalent carbon content. The chromium contents lead to an increased material strength that renders it immune to rust, whereas the molybdenum increases toughness. Another advantage of AISI 4130 is the ability to be easily hardened by heat treatment or work hardening process. At an annealed condition AISI 4130 has greater formability, machinability and is quite easily weldable, which reduces the complexity of joining the frame parts. The physical properties and the chemical composition of the selected material are illustrated in Table 1 and Table 2 respectively.

Table 2 – Properties of AISI 4130 chromoly steel

Density, kg/m^3	7860.0
Ultimate tensile strength, MPa	520.0
Bending stress, MPa	1572.3
Young's modulus, GPa	200.0
Shear modulus, GPa	80.0
Poisson's ratio	0.29

The FSAE deck regulations involve a front and rear roll bar, side-impact frame, a front bulkhead and respective supports for the above elements. Figure 1 displaying the simplest possible frame member configuration which contains the above described necessary components.

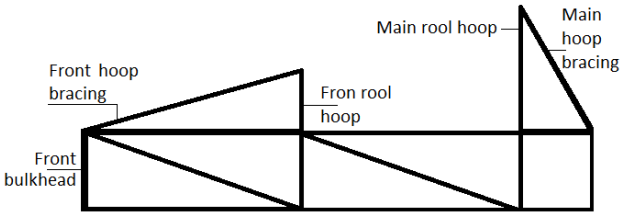

Figure 1 – Representation of frame members as per the rulebook

3.2 Side impact requirements

The lateral impact design includes two frame members and one diagonal member to avoid impact [1]. There is a 2-inch gap on both sides of the driver seat inside the cockpit. The upper side member is attached to the central hoop and 1000 mm from the surface is the maximum height of the roll hoop.

3.3 Consideration of frame design

Tools used: Solid Works and ANSYS. Tubular section, tube size: 25.0×1.2 mm (outer diameter × wall). Weight: 28 kg. Material: AISI 4130 (0.2–0.3 % of carbon). Configuration: triangular (no bend pipe other than the main hoop and front hoop).

3.4 Frame construction

The frame comprises front and main hoops, shoulder harness line, side-impact protection, bracing and support for roll hoops, support for front bulkheads [6]. The chassis must be made of 95th percentile a male cockpit.

Figure 2 shows the vertical passage through the opening of the cockpit until it reaches the top bar of the lateral impact framework.

Table 3 – Technical specification of the frame

Dimension	Metric
Length, mm	2813
Width, mm	1455
Height, mm	1230
Track (front / rear), mm	1270 / 1321
Wheelbase, mm	1214
Car weight (with a passenger), kg	320
Chassis type	Tubular spaceframe

3.5 Frame modeling

The framework was designed to ensure maximum load path, space of different components and comply with regulations, considering the suspension points location [7]. The driver cell has ample space, offering storage for the gear lever, batteries, fuel tank, guaranteeing the safety of the operator and fast egress. 4130 Steel is used as it is an ideal material for the frame due to its machine durability, ease of manufacturing, tolerance to scaling and corrosion, lean and smooth finish.

While the designing phase is carried out, the center of gravity of the car is concerned as a major objective keeping an eye on comfort and safety for the driver [8]. The seating level has been lowered to reduce the center of gravity of the car, keeping as low as possible, generating maximum downforce for greater traction and increased stability that the car should meet or even exceed safety standards. The analysis part is done using ANSYS (Figures 2–6).

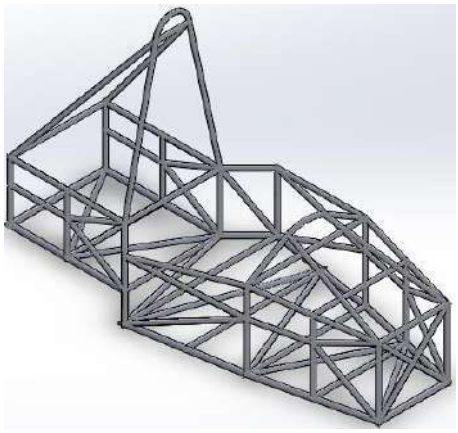

Figure 2 – Isometric view of chassis frame designed

4 Results and Discussion

4.1 Front impact test

Like any mechanical design, this chassis frame must be analyzed to determine whether it meets its goals of strength and rigidity. ANSYS tool is used for Finite Element Modelling and Analysis. BEAM-188 for the tubing and SOLID-187 for the engine are the component forms used in this study. BEAM-188 is based on the theory of Timoshenko beams and is used in slender beam design structure 1. SOLID-187 elements are tetrahedral 3D, 10-node elements used for nearly any solid part 2.

The important part of the text file is the description of the material and section properties for meshing. This also requires modeling of a-arms, pushrods, bell cranks, shocks and pivoting joints defined using key-points and lines.

The impact test is carried out, assuming the vehicle of mass 320 kg hits a static rigid wall at speed of 120 KMPH. The impact attenuator is made of foam absorbs all the impact load on collision happens for 0.3 S. As per calculation based on the impulse-momentum equation, deceleration of 10 g is assumed for the loading which is equivalent to a static force of 35.6 kN.

Boundary conditions: rear suspension mounts are clamped.

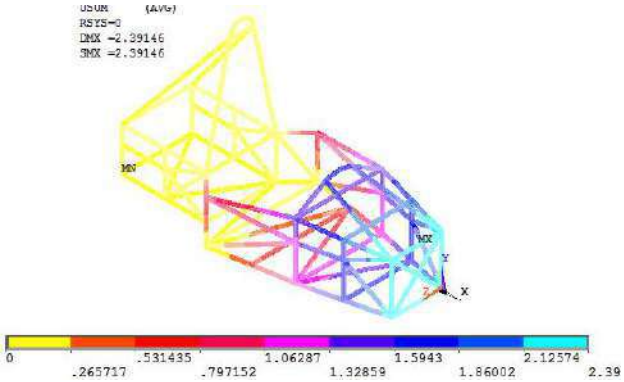

Figure 3 – Deformation during the front impact test

4.2 Side impact test

The fixed side-impact assessment is done, which is applied to the impact zone by adding a diagonal member as per rule book. Based on the calculation, deceleration of 6 g is assumed for loading that is equal to the static force of 18 kN. The vehicle's mass is to be 320 kg at the total impact speed is 120 KMPH is assumed to hit on the designed vehicle of the same mass.

Boundary conditions: the right-side front and back ends of the suspension were clamped.

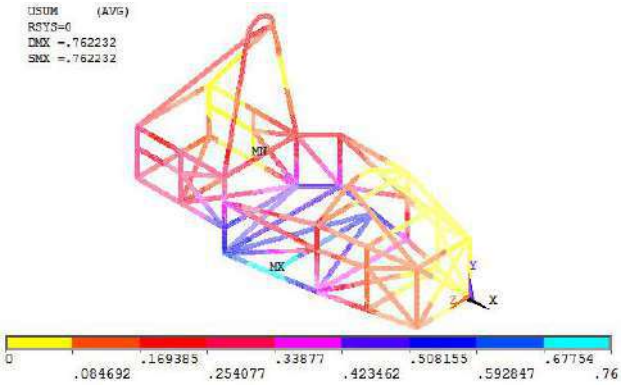

Figure 4 – Deformation during the side impact

4.3 Rear impact test

The rear impact test is carried out by assuming a Vehicle at speed of 120 KMPH having the mass of 320 kg hit the rear portion of the designed vehicle at stationary state. Boundary conditions: front suspension mounts are clamped.

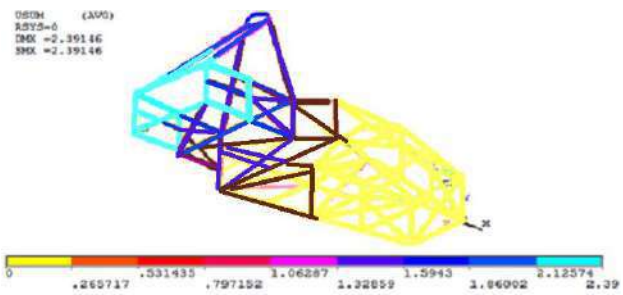

Figure 5 – Deformation during a rear impact

4.4 Torsional impact test

One of the most important tests validating the frame construction is torsional rigidity analysis. In this case, it is assumed that the chassis acts as a cantilever with the end of the rear suspension ends and the front suspension ends are fixed subject to equal and opposite torsional loads (couple) around its longitudinal axis. Boundary conditions: the force of 2.25 kN was loaded at each node.

The torsional stiffness K is calculated by the ratio of the torque T to the angle of rotation θ. The angle of rotation and torque are given by the following formulas:

$$\theta = \text{arctg}(2a/L);\ T = mgL = 2Fw, \qquad (1)$$

where a – displacement; L – length; m – mass; g – gravity acceleration; F – force; w – force's arm.

The stress, deformation, and factor of safety (FOS) for the respective tests were tabulated in Table 4.

From the above tabulation, it can be observed that the use of Chromoly material is more successful than the typical conventional frame material used in FSAE racing.

The tabulation further shows that the use of Chromoly reduces the vehicle self-weight, thus increasing the optimum performance by installing aero packages in the automobile.

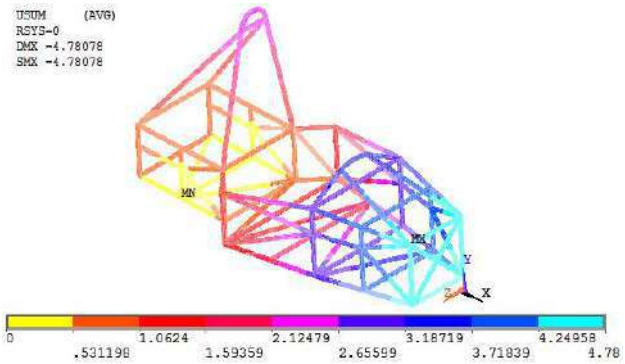

Figure 6 – Deformation during torsional stiffness

Table 4 – Test results

Test	Stress, MPa	Deformation	FOS
Frontal impact test	114.6	2.39	4.5
Side impact test	87.3	0.73	5.2
Rear impact test	303.9	3.45	1.8
Torsional stiffness test	108.0	4.78	4.8

5 Conclusions

The conclusions of the work are as follows. Using Solid Works software, an ideal frame was designed for FSAE car racing. Specific parameters are analyzed for Chromoly Steel as the frame material using ANSYS for different tests according to the FSAE rule book. Based on the results, the chosen material was considered to be suitable for the frame compared to conventional materials used.

References

1. Mohamad, M. L., Rahman, M. T. A., Khan, S. F., Basha, M. H., Adom, A. H., Hashim, M. S. M. (2017). Design and static structural analysis of a race car chassis for Formula Society of Automotive Engineers (FSAE) event. *Journal of Physics: Conference Series*, Vol. 908(1), article number 012042.
2. Yamanouchi, N., Ishii, K., Moriyama, H., Kato, H. (2019). Structural characteristics of the racing car in the student formula SAE competition. *Proceedings of the School of engineering of Tokai University, Series E*, Vol. 44, pp. 7–13.
3. Vasanthakumar, R., Manojkumar, P. R., Kesavaraj, M., Manikandan, G., Student, F. Y. U. (2019). Design and analysis of Formula-3 frame. *International Journal of Engineering Science*, article number 20840.
4. More, A., Chavan, C., Patil, N., Ravi, K. (2017). Design, analysis and optimization of space frame chassis. *International Journal of Engineering and Technology*, Vol. 9(2), pp. 1411–1422.
5. Kamble, M., Shakfeh, T., Moheimani, R., Dalir, H. (2019). Optimization of a composite monocoque chassis for structural performance: a comprehensive approach. *Journal of Failure Analysis and Prevention*, Vol. 19(5), pp. 1252–1263.
6. Sethupathi, P. B., Chandradass, J., Sharma, A., Baliga, A. B., Sharma, S. (2018). Design and optimization of FSAE chassis using FEA. *IOP Conference Series: Materials Science and Engineering*, Vol. 402(1), article number 012184.
7. Slimarik, D., Bauer, F. (2013). *Design of Tubular Space Frame for Formula Student Race Car*. Department of Technology and Automobile Transport, Mendel University, Czech Republic.

8. Forrest, J. (2016). *SAE Series Frame Design*. Doctoral dissertation, University of Cincinnati, College of Engineering and Applied Science.
9. Thakar, P., Ail, S., Ranade, J. Mehta, P. (2019). Design, manufacture and testing of an impact attenuator for a FSAE car. *Proceedings of the International Conference on Intelligent Manufacturing and Automation, Springer, Singapore*, pp. 151–159.
10. Krzikalla, D., Mesicek, J., Petru, J., Sliva, A., Smiraus, J. (2019). Analysis of torsional stiffness of the frame of a Formula Student vehicle. *Applied Mechanical Engineering*, Vol. 7, pp. 315.
11. Sodisetty, V. N. B. P., Pandey, A., Iyer, D. B., Kumar, N. (2019). Torsional stiffness analysis of a tubular space-frame chassis. *SAE Technical Paper*, No. 2019-28-0033.
12. Rahman, A., Rahman, M. T. A., Manaf, E. H. A., Rahman, A. S. A. (2018). Design and analysis of impact attenuator for a formula student car: A study between singular and bi-tubular tubes of varying geometries. *IOP Conference Series: Materials Science and Engineering*, Vol. 429(1), article number 012049.
13. Yang, L., Li, Q., Wang, C., Zhang, Y. (2017). Loads analysis and optimization of FSAE race car frame. *SAE Technical Paper*, No. 2017-01-0423.
14. Shukla, S., Agnihotri, S., Sahoo, R. R. (2016). Design and analysis of formula SAE chassis. *Journal of Aeronautical and Automotive Engineering*, Vol. 3(1), pp. 26–32.
15. Bell, M. (2018). Development of a weight-saving carbon-fibre-reinforced polymer component for a FSAE race car. *The UNSW Canberra at ADFA Journal of Undergraduate Engineering Research*, Vol. 9(2).
16. Chandan, S. N., Sandeep, G. M., Vinayaka, N. (2016). Design, analysis and optimization of race car chassis for its structural performance. *International Journal of Engineering Research and Technology*, Vol. 5(7), pp. 361–367.

УДК 624.014

Оптимізаційний розрахунок конструкції автомобільної рами зі сталі 30ХМА

Кумар М. Д., Тея П. С., Крішна Р., Срінівасан М.

Інститут технологій та наук ім. Пейс, 523 272, м. Онголе, Індія

Анотація. Відповідно до правил та правил змагань “Racing Formula Car Racing”, що проводиться щорічно товариством інженерів-автомобілістів (Індія), рама автомобіля повинна бути розроблена та побудована з найвищим пріоритетом. Основним завданням є розробка та виготовлення легкої зваженої рами шасі автомобіля без втрати її надійності. У цій статті розглядаються різні методи вибору матеріалів та проведено процедуру оптимізаційного розрахунку конструкції рами на основі скінченноелементного аналізу за допомогою програмного комплексу ANSYS. Базова конструкція обґрунтована даними антропологічного дослідження зазначеної людини (водія) автомобіля. Відповідно до існуючих рекомендацій щодо вибору матеріалу, хромомолібденова стать 30ХМА була застосована для побудови рамної конструкції. У результаті, для остаточної конструкції рами транспортного засобу було виконано аналіз напружено-деформованого стану за допомогою програмного комплексу ANSYS, а отримані результати проаналізовані. Процедура оптимізаційного розрахунку конструкції рами ґрунтується на загальних правилах SAE 2019.

Ключові слова: скінченноелементний аналіз, хромо-молібденова сталь, рамна конструкція, товариство інженерів-автомобілістів.

JOURNAL OF ENGINEERING SCIENCES
ЖУРНАЛ ІНЖЕНЕРНИХ НАУК
ЖУРНАЛ ИНЖЕНЕРНЫХ НАУК

Web site: http://jes.sumdu.edu.ua

DOI: 10.21272/jes.2019.6(2).d3 Volume 6, Issue 2 (2019)

Ensuring the Vibration Reliability of Rotors Connected by Spline Joints

Verbovyi A.[1*], Neamtu C.[2], Sieryk, M.[1], Vashyst B.[1], Pavlenko V.[3], Simonovskiy V.[1], Pavlenko, I.[1]

[1] Sumy State University, 2 Rymskogo-Korsakova St., 40007 Sumy, Ukraine;
[2] Technical University of Cluj-Napoca, 28 Memorandumului St., 400114 Cluj-Napoca, Romania;
[3] Machine Building College of Sumy State University, 17 T. Shevchenka Ave., 40000 Sumy, Ukraine

Article info:
Paper received: August 17, 2019
The final version of the paper received: December 5, 2019
Paper accepted online: December 10, 2019

[*]Corresponding Author's Address:
anton.verbovoi@gmail.com

Abstract. This article is devoted to the development of refined numerical mathematical models of rotor dynamics of high-performance turbomachines having a spline connection. These models consider the dependence of the critical frequencies of the shaft on the angular stiffness of the spline connection, as well as the procedure of virtual balancing. As a result of the complex application of this approach, the methods of calculation of vibration characteristics taking into ac-count variable values of angular rigidity of splined connection are offered. In addition, the method of evaluating the system of initial imbalances with the corresponding displacements of the rotor axis in the correction and calculation sections has also been improved. The proposed approaches, based on the integrated application of CAE software and computational intelligent systems, allow for modal and harmonic analysis and implement virtual balancing with a significant reduction in preparation and machine time without loss of relative accuracy. In addition, the developed mathematical model of free and forced vibrations of rotor systems have been implemented in the program code operational files "Critical Frequencies of the Rotor" and "Forced Oscillations of the Rotor" of the computer algebra system MathCAD that allows improving the dynamic balancing procedure for evaluating primary imbalances. The high accuracy of the proposed approach is confirmed by checking the dynamic deviations of the rotor axis by the system of residual imbalances in accordance with the standards of vibration stability.

Keywords: turbomachine, spline connection, angular stiffness, virtual balancing, modal analysis, harmonic analysis.

1 Introduction

Nowadays, due to the increasing demand for the use of such power equipment as rotary machines, in particular, turbo-pump turbochargers and units, the question of their vibration reliability become more and more urgent. The main source of vibration of any pump unit is an unbalanced rotor. But in addition to an unbalanced rotor, there are also many other factors that create in their totality a complex effect on the vibrational state of the unit. This can be the body stiffness, stiffness of the bearing seals and various types, the compression ratio of the axial rotor, the type and technical condition of the connection of the rotors of the unit and the engine, and others. One type of shaft connection with the engine is a connection that wears out with the operation process and, as a consequence, loses angular stiffness.

The article is devoted to the study of the influence on the vibration state of turbopump units with angular stiffness of splined joints based on the finite element method with the use authors' files "Critical frequencies of the rotor" and "Forced oscillations of the rotor" of the computer algebra system Mathcad.

2 Literature Review

The problem posed above can be solved after the study of special scientific literature on the topic of extreme research in computer modeling of rotor dynamics. For example, in work [1] dynamics of rotor systems of turbopump units with the present splined connection, and also the calculation of vibrational characteristics of a rotor taking into account its preliminary axial preload is considered. The research work [2] is devoted to methods of research of dynamics of a rotor on ball bearings with the combined application of spatial and beam settlement models. In the research work [3], the influence of different classes of bearings on vibrations is considered.

In research papers [4–7], examples of the introduction of neural network technology in computer calculation in solving problems of increasing vibration reliability are described for various rotary machines. Methods of nonlinear identification of stiffness characteristics of bearing supports were also developed in the works [8, 9, 10]. Up-to-date trends in the field of rotor dynamics analysis are discovered in the research papers [11, 12, 13].

3 Research Methodology

3.1 Evaluation of eigenfrequencies

The object of the study was the shaft line of a liquid-propellant engine, which consists of an oxidizer rotor and a fuel pump rotor connected to each other by means of a splined connection. During the operation of the unit, the phenomenon of wear of the slots is inevitable, as a result of which the angular stiffness of this connection changes, which in turn leads to corresponding changes in the natural frequency spectrum.

The computer program "Critical Frequencies of the Rotor", which is based on the finite element method, allows determining the natural frequencies of the shaft, the scheme of which is presented in Figure 1.

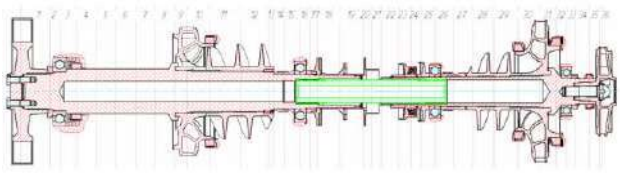

Figure 1 – The design scheme of the rotor

To further study the dynamics of the rotor, it is necessary to create a computational model. In the program "Critical frequencies of the rotor" was created beam finite element model (Figure 2).

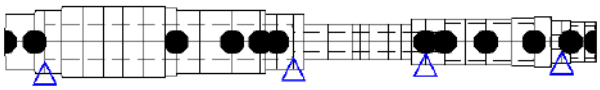

Figure 2 – The finite element model of the rotor dynamics with spline joint using the file "Critical Frequencies of the Rotor"

In this paper, the critical frequencies of the shaft line are for two variants: "Hinge" and "Rigid connection". For the first option, the values of the stiffness of the bearings were taken the minimum, wherein the spline connection for the shafts was taken hinged. For the second option, the maximum stiffness for the bearings was adopted, and the splined connection was taken according to the scheme of rigid fastening. The connection of both parts of the rotors in the shaft through the slot forms a weak dynamic connection between them.

3.2 Simulation of forced oscillations

The program "Forced oscillations of the rotor", allows one to calculate the forced oscillations of the rotor at a given speed of rotation under the influence of certain imbalances. The result of the calculation is the amplitude and shape of the rotor deflection when operating at a certain operating frequency.

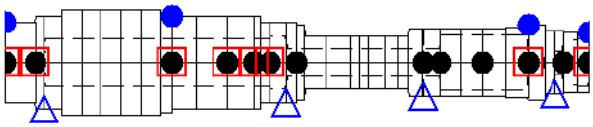

Figure 3 – The finite element model of the rotor dynamics with a splined joint for calculation of forced oscillations using the file "Forced Oscillations of the Rotor"

The calculation of forced oscillations in the program is performed using the already known beam finite element model and the same mathematical algorithms that are laid down to solve the problems of finding eigenfrequencies and critical frequencies, but the right side of the matrix equation when-van rotating rotor, divided into finite elements of the beam type-other than zero:

$$\bar{M}\ddot{\bar{U}} + \bar{K}\bar{U} = \bar{E}\bar{M}_d\omega^2, \quad (1)$$

where $\bar{E}$ – column-vector of the eccentricity of the unbalanced local masses; M_d – column-vector of the unbalanced local masses; ω – operating frequency.

To solve the problem of forced oscillations requires data such as density and modulus of elasticity of the material, the length of each section, external and internal diameter sections, mass details, support stiffness, the working speed of the rotor, the modulus and phase of point imbalances.

Theoretically, the unbalance of a flexible rotor is characterized by a certain spatial continuous curve, which is a hodograph of a continuous set of imbalance vectors normal to the rotor axis. Therefore, since this method of setting is quite time-consuming, then in further calculations it is sufficient to limit the task to a finite number of point imbalances located in the planes of the impellers and in the plane of the wheel since these elements are the most influential on the overall imbalance.

All the calculations and mode shapes of forced oscillations were performed using the MathCAD software.

3.3 The performance of the virtual rotor balancing

Due to the above-mentioned results, the first critical frequency of the oxidizer's rotor is close to the first critical frequency of the turbopump unit and not significantly increased the maximum rotor speed. According to the practice of designing and exploitation of pumping units, this relatively small deviation from the resonance (about 10 %) determines the dynamic characteristics of a rotor as a flexible one. In this case, the rotary system needs balancing both at operating and critical frequencies. Moreover, the total number of correction planes should be not less than three.

A system of imbalances $\overline{D}_{i\delta}$ $(i = \overline{1,l})$ has been introduced to balancing the rotor at all operating frequencies. Then the deflection $\overline{Y}_k^{(v)}$ at each measurement point at

any operating frequency ω_v, $(v = \overline{1,n})$ must be equal to zero. Therefore, for each measurement frequency $\omega_1, \omega_2, \dots, \omega_n$ can be written:

$$\begin{cases} \overline{Y}_1^{(v)} = \overline{Y}_{10}^{(v)} + \overline{W}_{11}^{(v)}\overline{D}_{1\delta} + \overline{W}_{12}^{(v)}\overline{D}_{2\delta} + \dots + \overline{W}_{1l}\overline{D}_{l\delta} = 0 \\ \overline{Y}_2^{(v)} = \overline{Y}_{20}^{(v)} + \overline{W}_{21}^{(v)}\overline{D}_{1\delta} + \overline{W}_{22}^{(v)}\overline{D}_{2\delta} + \dots + \overline{W}_{2l}\overline{D}_{l\delta} = 0 \\ \dots \\ \overline{Y}_n^{(v)} = \overline{Y}_{k0}^{(v)} + \overline{W}_{k1}^{(v)}\overline{D}_{1\delta} + \overline{W}_{k2}^{(v)}\overline{D}_{2\delta} + \dots + \overline{W}_{kl}\overline{D}_{l\delta} = 0 \end{cases} \quad (2)$$

As a result, the system $n \times k \times v$ a linear equation with complex coefficients is achieved to determine l complex balancing weights $\overline{D}_{1\delta}, \dots, \overline{D}_{l\delta}$. Dynamic complex weights are defined by the following equation:

$$\overline{W}_{ai}^{(v)} = \frac{\overline{Y}_{ai}^{(v)} - \overline{Y}_{a0}^{(v)}}{D_t}, \quad (3)$$

where a – number of points (a = 1, 2, …, k); i – initial number of measured points (i = 1, 2, ..., l); l – number of correction planes; $\overline{Y}_{a,i}^{(\mu)}$ – deflection at the measurement point a when setting the test imbalance in the correction plane i at the rotor speed μ; D_t – trial imbalance. The system of equations (3) can be rewritten in a matrix form:

$$\overline{\overline{Y}} = \overline{\overline{W}}\,\overline{\overline{D}}, \quad (4)$$

where $\overline{\overline{Y}} = (-\overline{Y_{10}^{(v)}}, \dots, -\overline{Y_{k0}^{(v)}})^T$, $(v = 1..n)$ – the column vector of complex amplitudes, measured at the "zero" start; $\overline{\overline{D}} = (\overline{\overline{D_{1b}}}, \dots, \overline{\overline{D_{lb}}})^T$ – a column vector of the estimated complex balancing of masses; $\overline{\overline{W}}$ - a rectangular matrix $k \times l$ of complex mass coefficients $\overline{W}_{ai}(a = \overline{1,k}, i = \overline{1,l})$.

The linear regression formula cannot be used directly to solve the matrix equation (4). It is necessary to form relations between the two vectors with the corresponding real and imaginary components. Vector $\overline{\overline{Y}}$ and k of complex amplitudes correspond to the vector 2k real and imaginary components $\overline{Y}$:

$$\overline{Y} = (Y_1^{(r)}, Y_1^{(i)}, Y_2^{(r)}, Y_2^{(i)}, \dots, Y_k^{(r)}, Y_k^{(i)})^T. \quad (5)$$

Accordingly, an elongated vector with 2l real and imaginary imbalances can be introduced:

$$\overline{D} = (D_{1\delta}^{(r)}, D_{1\delta}^{(i)}, D_{2\delta}^{(r)}, D_{2\delta}^{(i)}, \dots, D_{l\delta}^{(r)}, D_{l\delta}^{(i)})^T \quad (6)$$

So, the matrix of mass coefficients $\overline{W}$ $2k \times 2l$ can be presented in the following form:

$$\overline{W} = \begin{bmatrix} W_{11}^{(r)}, -W_{11}^{(i)}, W_{12}^{(r)}, -W_{12}^{(i)}, \dots, W_{1l}^{(r)}, -W_{1l}^{(i)} \\ W_{11}^{(i)}, W_{11}^{(r)}, W_{12}^{(i)}, W_{12}^{(r)}, \dots, W_{1l}^{(i)}, W_{1l}^{(r)} \\ \dots\dots\dots\dots\dots\dots\dots\dots\dots\dots\dots\dots\dots\dots\dots\dots \\ W_{k1}^{(r)}, -W_{k1}^{(i)}, W_{k2}^{(r)}, -W_{k2}^{(i)}, \dots, W_{kl}^{(r)}, -W_{kl}^{(i)} \\ W_{k1}^{(i)}, W_{k1}^{(r)}, W_{k2}^{(i)}, W_{k2}^{(r)}, \dots, W_{kl}^{(i)}, W_{kl}^{(r)} \end{bmatrix}, \quad (7)$$

where the arbitrary coefficient of the matrix W is defined by the formula:

$$\overline{W}_{ai} = W_{ai}^{(r)} + iW_{ai}^{(i)}(a = \overline{1,k}; i = \overline{1,l}). \quad (8)$$

The complex matrix equation (4) corresponds to the real matrix equation:

$$\overline{\overline{Y}} = \overline{\overline{W}}\,\overline{\overline{D}} \quad (9)$$

where the columns of vectors Y and D are determined by equations (5), (6). The linear regression formula can be implemented in the resulting equation (8). In this case, the system of imbalances D is estimated by the vector of measured displacements $\overline{Y}^*$ by the following formula:

$$\hat{\overline{D}} = \left[\overline{W}^T\overline{W}\right]^{-1}\overline{W}^T\overline{Y}^* \quad (10)$$

If the balancing procedure is provided by the measure at multiple frequencies $\omega_v(v = \overline{1,n})$, the vector $\overline{\overline{Y}}$ has size $k \times n$:

$$\overline{\overline{Y}} = (\overline{Y_1}^{(1)}, \dots, \overline{Y_k}^{(1)}; \dots; \overline{Y_1}^{(n)}, \dots, \overline{Y_k}^{(n)})^T, \quad (11)$$

and the elongated vector Y has size $2 \times k \times n$

$$\overline{Y} = (Y_{11}^{(r)}, Y_{11}^{(i)}, \dots, Y_{k1}^{(r)}, Y_{k1}^{(i)}; \dots; Y_{1n}^{(r)}, Y_{1n}^{(i)}, \dots, Y_{kn}^{(r)}, Y_{kn}^{(i)})^T \quad (12)$$

The matrix W will be expanded n times vertically and have size $2k \times n \times l$.

Each matrix $\overline{W}_1(v = \overline{1,n};)$ is similar to the matrix $\overline{W}$. To assess the system of imbalances

$$\hat{\overline{D}}_i = D_i^{(r)} + iD_i^{(i)} \quad (13)$$

the balancing process is implemented by establishing a mass balancing system $D_{\delta i} = \left|\overline{D}_i\right|$ in the planes of correction under the phase angles:

$$\varphi_{\delta i} = \arg(\overline{D}_i), (i = \overline{1,l}) \quad (14)$$

On the basis of a series of virtual experiments, it is shown that the turbopump rotor (which initially has a system of imbalances) gives an unsatisfactory level of vibration at the rotor operating speed and cannot be balanced at low rotor speed in two correction planes. Therefore, it is necessary to balance the rotor as flexible at operating frequencies.

3.4 Assessment of the quality of rotor balancing

Residual imbalances are estimated by the algorithms described above, namely by the formulas:

The equation of the dependence of the deflection amplitudes on the imbalance is as follows:

$$\overline{Y_0} = \overline{WD}\,, \tag{15}$$

where $\overline{Y_0}$ – a column vector of the deflection amplitudes; $\overline{W}$ – matrix of influence coefficients; $\overline{D}$ – vector-column of estimated imbalances.

If we introduce the concept of the *i*-th vector of trial imbalances, as a certain set of imbalances consisting of a trial imbalance *D* set in the *i*-th plane of correction, then or the *i*-th start of the rotor (*i* = 1, 2, …, 8) you can write the equation:

$$\overline{Y_i} = \overline{W}\left(\overline{D} + \overline{D_{i_{np}}}\right) \tag{16}$$

or

$$\overline{Y_i} = \overline{W}\left(\overline{D} + D_{np} \cdot \overline{E}\right), \tag{17}$$

where D = 0.01 kg·m – the scalar value of trial imbalance; $\overline{E}$ - identity matrix.

Subtracting (16) from (17), one can define a matrix of influence coefficients, each element of which is equal to

$$\overline{W_{a,i}} = \frac{\overline{Y_{a,i}} - \overline{Y_{0a}}}{D_{np}}, \tag{18}$$

where k = 8 – number of nodes with estimated imbalances; l = 8 – number of runs excluding zero.

The value of the trial imbalance is assumed D = 0.01 kg·m.

Amplitudes of deflections in correction planes 1, 3, 10, 11, 29–31, 36 as components of the column-vector $\overline{Y_0}$.

4 Results

4.1 Critical frequencies of the rotor

In Table 1, data of calculations of critical frequencies of rotors and a shaft of the turbopump unit which have turned out by means of beam models result.

The lower and upper border corresponds to both “joint” and “solid shaft” connections. From the results of calculations, it can be seen that the first two critical frequencies of the rotor of the oxidizing turbopump are almost the same as the first two critical frequencies of the continuous shaft line. Therefore, we see that the forms of free oscillations also coincide for the first and second.

Therefore, to assess the displacement of the rotor system of the turbopump unit from the resonant modes, it is possible to consider only the dynamics of the rotor to the oxidizer turbopump unit.

Table 1 – Critical frequencies of rotor systems found in the computer program “Critical Frequencies of the Rotor”, rad/s

System	Number of critical frequency		
	1	2	3
Oxidizer	2623–3101	3251–6513	5429–10100
Fuel pump	3974-5270	5675-13420	7369-14310
Turbopump	2600–3363	3252–6211	3832–6615

4.2 Results of calculation of forced oscillations of the shaft line

Calculations and forms of forced oscillations that are performed using the Mathcad program are presented below.

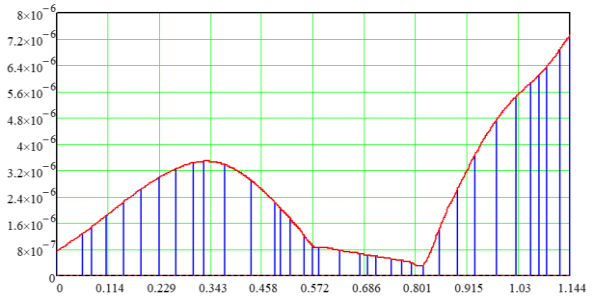

a

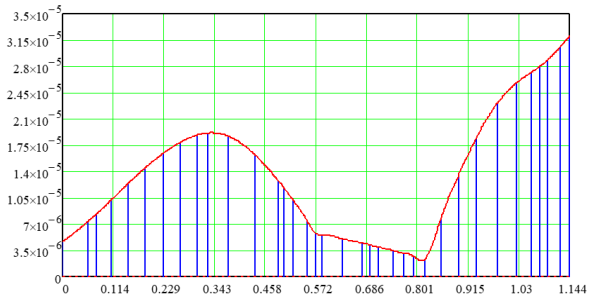

b

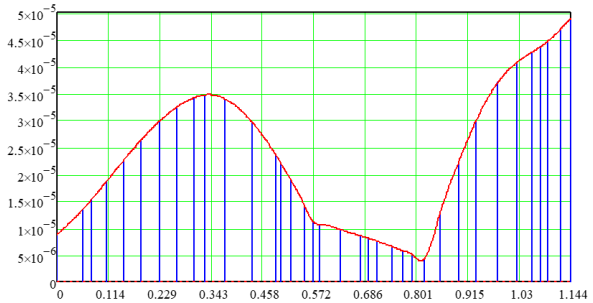

c

Figure 4 – Mode shapes of forced oscillations before balancing at 1100 rad/s (a), 1963 rad/s (b), and 2215 rad/s (c), m

4.3 Balancing quality assessment

After the procedure of virtual balancing in the program "Forced oscillations of the rotor", forced oscillations of the shaft under the influence of residual imbalances were simulated. The characteristics of such forced oscillations are shown in the figures below.

Table 2 – Deflections in the correction planes found in the computer program "Critical frequencies of the rotor", μm

Node number	Rotor speed, rad/s		
	1100	1963	2215
1	0.77	4.65	8.79
3	1.49	8.38	15.35
10	3.49	19.16	34.65
11	3.39	18.75	33.99
29	1.45	7.81	12.97
30	2.64	13.56	22.11
31	3.71	18.58	29.99
36	6.38	28.88	44.67

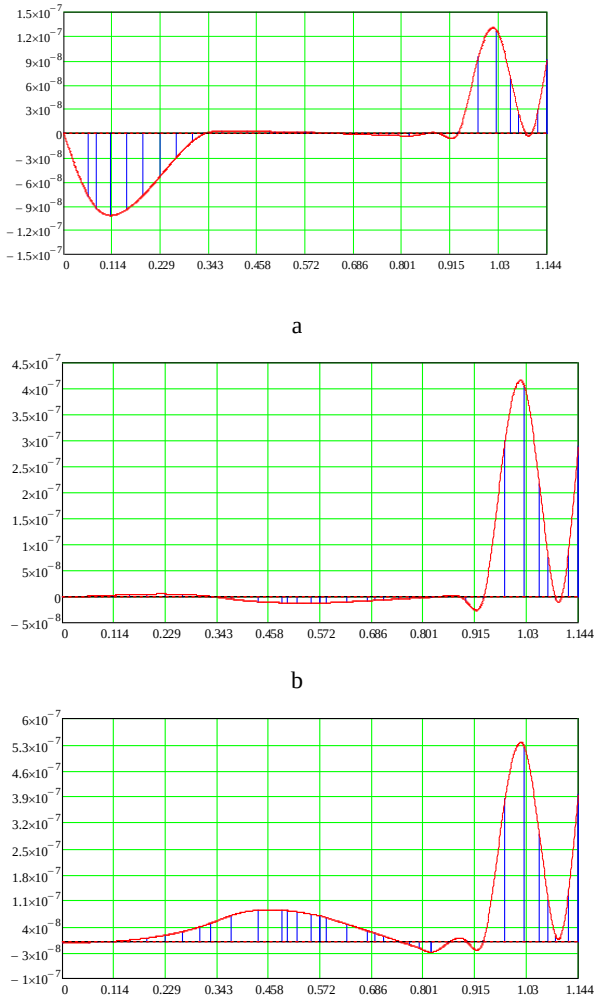

Figure 5 – Mode shapes of forced oscillations after balancing at 1100 rad/s (a), 1963 rad/s (b), and 2215 rad/s (c), m

Hence, the maximum amplitude after balancing has been decreased by two orders.

5 Conclusions

As a result of the work, free and forced oscillations of the shaft pipeline for two variations "joint" and "solid shaft" were obtained. We considered the existing methods of taking into account the stiffness of the splined joint at the critical frequencies of the rotor of the turbopump unit.

The Mathcad and ANSYS programs performed calculations and obtained the results of the maximum permissible critical frequencies of the oxidizer rotor for the turbopump, the fuel pump rotor and for the solid shaft line.

The rotor of the oxidizer turbopump and the fuel pump is a rigid rotor design in fact, that the value of the maximum operating frequency lies below the first critical frequency of both the entire shaft design and both rotors separately.

The values of the first critical frequency obtained from the calculation are 2600 rad/s (option "joint") and 3363 rad/s (option "solid shaft").

The next step was to obtain deflections in the nodes belonging to the correction planes in the initial state of the rotor. Determined that the maximum deflection is 45 μm, this result is unacceptable. Therefore, it is necessary to balance the rotor.

In order to reduce the vibration of the shaft, it was decided to conduct a virtual balancing of the rotor. The corresponding algorithm for calculating the vibration state of the rotor is implemented using the working file "Forced Oscillations of the Rotor" of the computer program MathCAD, followed by its improvement by a virtual balance to obtain results that meet the standards of GOST ISO 1940-1-2007 "Vibrations. Requirements to Quality of Balancing of Rigid rotors" and GOST ISO 11342-95 "Methods and Criteria of Balancing of Flexible Rotors".

6 Acknowledgments

The results of the research were partially obtained as a part of the research work funded by the State Design Bureau "Yuzhnoye" (Ukraine). Additionally, the part of scientific results related to the computer modeling was obtained jointly by Sumy State University (Ukraine) and Technical University of Cluj-Napoca (Romania) within the international grant "Ensuring the Vibration Reliability of Numerical Methods and Studies of the Dynamics of Rotors of Centrifugal Machines" funded by EU Program Erasmus+, as well as a part of Ph.D. thesis of A. Verbovyi and B. Vashyst.

References

1. Pavlenko, I. V., Simonovskiy, V. I., Pitel', J., Demianenko, M. (2018). *Dynamic Analysis of Centrifugal Machines Rotors with Combined Using 3D and 2D Finite Element Models*. Sumy State University, Sumy, Ukraine.
2. Pavlenko, I. V., Simonovskiy, V. I., Demianenko, M. M. (2017). Dynamic analysis of centrifugal machines rotors supported on ball bearings by combined application of 3D and beam finite element models. *IOP Conference Series: Materials Science and Engineering*, Vol. 233(1), article number 012053, doi: 10.1088/1757-899X/233/1/012053.

3. Yashchenko, A. S., Rudenko, A. A., Simonovskiy, V. I., Kozlov, O. M. (2017). Effect of bearing housings on centrifugal pump rotor dynamics. *IOP Conference Series: Materials Science and Engineering*, Vol. 233(1), article number 012054, doi: 10.1088/1757-899X/233/1/012054.
4. Pavlenko, I., Ivanov, V., Kuric, I., Gusak, O., Liaposhchenko, O. (2019). Ensuring vibration reliability of turbopump units using artificial neural networks. *Advances in Manufacturing II - Volume 1. Lecture Notes in Mechanical Engineering. Springer, Cham*, pp. 165–175, 2019, doi: 10.1007/978-3-030-18715-6_14.
5. Pavlenko, I., Simonovskiy, V., Ivanov, V., Zajac, J., Pitel, J. (2019). Application of artificial neural network for identification of bearing stiffness characteristics in rotor dynamics analysis. *Advances in Design, Simulation and Manufacturing, DSMIE 2018, Lecture Notes in Mechanical Engineering, Springer*, pp. 325–335, doi: 10.1007/978-3-319-93587-4_34.
6. Ding, F., Wang, Z., Qin, F. (2015). Two kinds of neural network fusion of aero-engine rotor vibration signal fault diagnosis. *4th International Conference on Mechatronics, Materials, Chemistry and Computer Engineering*, pp. 1546–1552.
7. Tanoh, A., Konan, D. K., Koffi, M., Yeo, Z., Kouacou, M. A., Koffi, B. K., N'guessan, K. R. (2008). A neural network application for diagnosis of the asynchronous machine. *Journal of Applied Sciences*, Vol. 8, pp. 3528–3531, doi: 10.3923/jas.2008.3528.3531.
8. Pavlenko, I., Neamtu, C., Verbovyi, A., Pitel, J., Ivanov, V., Pop, G. (2019). Using computer modeling and artificial neural networks for ensuring the vibration reliability of rotors. *CEUR Workshop Proceedings*, Vol. 2353, pp. 702–716.
9. Pavlenko, I., Trojanowska, J., Gusak, O., Ivanov, V., Pitel, J., Pavlenko, V. (2019). Estimation of the reliability of automatic axial-balancing devices for multistage centrifugal pumps. *Periodica Polytechnica Mechanical Engineering*, Vol. 63(1), pp. 277–281, doi: 10.3311/PPme.12801.
10. Kim, Y. W., Jeong, W. B. (2018). Reliability evaluation technique of compressor using pressure pulsation and vibration signals. *Journal of Physics: Conference Series*, Vol. 1075, article number 012076, doi: 10.1088/1742-6596/1075/1/012076.
11. Ben Rahmoune, M., Hafaifa, A., Guemana, M. (2015). Neural network monitoring system used for the frequency vibration prediction in gas turbine. *3rd International Conference on Control, Engineering and Information Technology*, article number 15418537, doi: 10.1109/CEIT.2015.7233185.
12. Pavlenko, I., Trojanowska, J., Ivanov, V., Liaposhchenko, O.: Scientific and methodological approach for the identification of mathematical models of mechanical systems by using artificial neural networks. *3rd Conference on Innovation, Engineering and Entrepreneurship, Regional HELIX 2018, Lecture Notes in Electrical Engineering, Springer*, Vol. 505, pp. 299–306, doi: 10.1007/978-3-319-91334-6_41.
13. Manjurul, M. M., Kim, I.-M. (2018). Motor bearing fault diagnosis using deep convolutional neural networks with 2D analysis of vibration signal. *Lecture Notes in Computer Science*, Vol. 10832, pp. 144–155, doi: 10.1007/978-3-319-89656-4_12.

УДК 621.671:534.1

Підвищення вібраційної надійності роторів, з'єднаних шліцьовим з'єднанням

Вербовий А. Є.[1], Неамцу К.[2], Сєрик М. Л.[1], Вашист Б. В.[1], Павленко В. В.[3], Симоновський В. І.[1], Павленко І. В.[1]

[1] Сумський державний університет, вул. Римського-Корсакова, 2, 40007, м. Суми, Україна;
[2] Технічний університет міста м. Клуж-Напока, вул. Меморандума 28, 400114, м. Клуж-Напока, Румунія;
[2] Машинобудівний коледж СумДУ, просп. Т. Шевченка, 17, 40000, м. Суми, Україна

Анотація. Стаття присвячена розробленню уточнених математичних моделей динаміки роторних систем енергоємних турбомашин, що мають шліцьове з'єднання, та числових методів дослідження їх вільних і вимушених коливань. Запропоновані моделі враховують залежності критичних частот валопровода від кутової жорсткості шліцьового з'єднання, а також реалізують процедуру його віртуального балансування. У результаті комплексного застосування такого підходу запропоновано методи розрахунку вібраційних характеристик турбомашин з урахуванням можливої зміни кутової жорсткості шліцьового з'єднання. Крім цього, було вдосконалено методику оцінювання системи початкових дисбалансів за даними зміщень осі ротора у площинах колекції та розрахункових площинах. Запропоновані підходи, засновані на комплексному застосуванні програмного забезпечення на основі методу скінченних елементів та обчислювальних інтелектуальних систем, дозволяють проводити модальний і гармонічний аналіз та реалізовувати віртуальне балансування зі значним зменшенням підготовчого і машинного часу без втрати відносної точності. Крім того, розроблені математичні моделі вільних і вимушених коливань роторних систем були реалізовані у вигляді програмних кодів робочих файлів "Critical Frequencies of the Rotor" та "Forced Oscillations of the Rotor" системи комп'ютерної алгебри MathCAD, що дозволяє удосконалити процедуру динамічного балансування для оцінкювання системи початкових дисбалансів. Висока точність запропонованого підходу підтверджується перевіркою динамічних відхилень осі ротора у результаті дії системи залишкових дисбалансів відповідно до міжнародних стандартів вібраційної надійності.

Ключові слова: турбомашина, шліцьове з'єднання, кутова жорсткість, віртуальне балансування, модальний аналіз, гармонічний аналіз.

JOURNAL OF ENGINEERING SCIENCES
ЖУРНАЛ ІНЖЕНЕРНИХ НАУК
ЖУРНАЛ ИНЖЕНЕРНЫХ НАУК
Web site: http://jes.sumdu.edu.ua
Volume 6, Issue 2 (2019)

INTERNATIONAL CONFERENCE ON FUTURE GENERATION FUNCTIONAL MATERIALS AND RESEARCH 2020 (ICFMR 2020)

March 12–14, 2020, PACE Institute of Technology and Science, India

Functional Materials are any materials which possess particular native properties and functions of their own. They are found in all class of materials, such as ceramics, polymers, metals, alloys and organic molecules. The primary goal of ICFMR 2020 is to promote research and development activities needed for the next generation and focused on all facets of the Functional Materials.

Recent Advances in functional materials is a multifaceted topic dealing with the discovery and designing of Nobel materials. Numerous of the most pressing scientific problems, humans currently face are due to limitations of materials and hence a step forward in material science has a significant impact on the future technology.

The conference will provide an ideal platform for the constructive ideas and innovative approach for efficient use of materials in the field of energy such as electro- and magnetocaloric materials, energy storage, and solar harvesting functions, manufacturing and nanotechnology devices.

The conference will provide a promising novel look in various expertise areas of functional materials through a comprehensive visualization and a multiple dimensional approach. It will be an open discussion platform for researchers, engineers, and scientists from around the world to share views and experiences in Functional Materials and related areas.

Extended versions of the original papers will be considered to publish in the Journal of Engineering Sciences.

Website of the conference: http://www.pace.ac.in/ICFMR2020.

JOURNAL OF ENGINEERING SCIENCES
ЖУРНАЛ ІНЖЕНЕРНИХ НАУК
ЖУРНАЛ ИНЖЕНЕРНЫХ НАУК

Web site: http://jes.sumdu.edu.ua

DOI: 10.21272/jes.2019.6(2).e1 Volume 6, Issue 2 (2019)

Numerical Study of the Effect of Changing Tube Pitches on Heat and Flow Characteristics from Tube Bundles in Cross Flow

Petinrin M. O.[1*], Towoju O. A.[2], Ajiboye S. A.[1], Zebulun O. E.[1]

[1] University of Ibadan, Oduduwa Rd., Ibadan, Nigeria;
[2] Adeleke University, P.M.B. 250, Ede-Osogbo Rd., Ede, Osun State, Nigeria

Article info:
Paper received: September 26, 2018
The final version of the paper received: April 4, 2019
Paper accepted online: April 9, 2019

[*]**Corresponding Author's Address:**
layopet01@yahoo.com

Abstract. Tube bundles are found in various heat transfer equipment for thermal energy transfer between fluids. However, the inter-spatial arrangement of the tubes of any tube bundle is a determining factor for its thermal and hydraulic performance. In this paper, the effect of varying the transverse and longitudinal pitches downstream staggered circular tube bundle on the heat transfer and flow characteristic was numerically analyzed. Seven variations of tube arrangements were studied by changing the tube pitches within a Reynolds number range of 7 381 to 22 214. The analyses were carried out using the k-ε equation model imposed with the realizability constraint and were solved with finite volume CFD code, COMSOL Multiphysics. The results obtained were found to be in good agreement with existing correlations. The tube bundles with decreasing pitches demonstrated better heat transfer performance while those with increasing pitches exhibited a lower friction factor. Thus, the best thermal-hydraulic performance was obtained from increasing pitch arrangements.

Keywords: cross flow, varying pitch, tube bundle, heat transfer, thermal-hydraulic performance.

1 Introduction

Tube bundle consists of multiple arrangements of tubes in series or parallel and is commonly found in heat exchangers [1, 2]. In any typical arrangement, transfer of heat takes place between a fluid moving across/over the tubes and another at a different temperature passing through the tubes [2–4]. Applications of fluid flow and heat transfer across tube bundles in heat exchangers find application in many industrial processes, as is seen in air conditioner cooling, tubular heat exchangers, waste heat recovery and economizers, steam generators, high-temperature gas-cooled reactors and so on [3, 5, 6].

There are many possible arrangements of tubes that can be obtained for effective heat transfer between fluids. The most common arrangements are the in-line and the staggered arrangements, and their spatial distributions are defined by transverse, longitudinal and diagonal pitches [2, 3, 7]. The difference in the recirculation and behaviour of flow becomes larger as the tube bundle compactness increases from a single tube [7]. This becomes more pronounced on the heat energy transfer and flow characteristics as spatial distributions and/or shapes of the tubes continue to change [8]. The flow resistance, which is in the form of pressure drop, over the tube bundles proportionately affects the fluid pumping power [2, 9].

Numerous studies have been conducted on the arrangements and geometries of tubes in efforts of improving the thermal performance of tube bundles without compromising the associated pressure drop, for effective designs of heat exchangers [8, 10]. The results of the analytical study of heat energy transfer in cross flow for a tube bundle using the integral method by Khan et al. [3] showed that the more compact the tube banks the higher the heat transfer rates recorded and that the staggered arrangement had better heat transfer output then the in-line arrangement. Tahseen et al. [11] studied experimentally, the laminar forced convection of air over in-line flat tube bundles. It was discovered that the average Nusselt number increased with the incremental changes in the heat flux when the Reynolds number increased from 527 to 880. Mohanty et al. carried a study on the inline and staggered arrangement of mixed tubes of circular and elliptical forms and observed that the heat transfer decreased while pressure drop increased tube while form changed from pure circular to mixed form arrangement [12].

Buyruk [8] investigated the flow and heat transfer around cylinders in cross-flow with blockages. It was discovered that the local Nusselt number and pressure coefficient distributions were significantly affected by blockage ratios. They reported that the lower aspect-ratio

tubes had more effect on flow and thermal characteristics of tube bundles as the angle of attack changes than the higher aspect-ratio tubes. Jeong et al. [4] carried out both experimental and numerical studies of heat transfer performance over a mini-channel tube bundle. With the use of two, the log means temperature difference (LMTD) and surface temperature methods to evaluate the transfer coefficients of the convective heat of the tube bundles. It was discovered that the experimental and numerical studies were in close agreement and the average Nusselt number based on the LMTD method was 22.6 % less than that of the surface temperature method.

Barcellos [13] investigated the effect of angle of inclination of a tube bundle of circular tubes on heat transfer and pressure drop in an experiment. The heat transfer rate and pressure drop recorded increased with inclination angle and were at the maximum at angle 45° to the normal. The higher pressure drop was attributed to vortex shedding and secondary flow due to recirculation. A similar study on the effect of angles of attack was performed experimentally by Toolthaisong and Kasayapanand [14] on flat tubes with different aspect ratios in staggered arrangement.

Numerical studies performed by Lee et al. [15] on the impact of uneven longitudinal pitch on the heat transfer performance of in-line tube bundle in cross flow showed that the overall heat transfer was improved by increasing the longitudinal pitch for uniformly distributed tubes. Their correlations were in close agreement with experimental data from the literature. Also, in the computational study of wall-bounded tube bundles in cross flow by Li et al. [1], the heat transfer coefficient in the near wall tubes and turbulence intensity of the near wall flow passages were lower than those in the middle of the bundle.

Several studies have also been carried out on tube bundles with extended surfaces. Hofmann et al. [16] experimentally investigated forced convection over tube bundles with different serrated and solid fin geometries. The Nusselt number and the pressure drop coefficient correlations compared well with literature. Similar research works on extended surfaces, the serrated finned-tube bundles were carried out by Hofmann et al. [17,18]. Insights into the heat transfer and fluid dynamic performance of tube bundles with non-circular geometries other than flat tubes are on the rise because of the satisfactory performance of the tubes [19]. Some of the research works on non-circular tubes includes: the numerical study of Horvat et al. [20] on cylindrical, ellipsoidal and wing-shaped tubes in staggered arrangement; the experimental studies of Mangrulkar et al. [10], Nouri-Borujerdi and Lavasani [21], and Lavasani et al. [22] on cam-shaped tube bundles in cross flow; and the work of Du et al. [23] on finned oval-tube cross-flow heat exchanger.

Thus, the findings from the previous studies have shown that arrangements, geometrical configurations, and surface treatments have a pronounced effect on the flow and thermal characteristics of tube bundles in cross flow. However, from these studies, there has been little or no emphasis on changes in transverse and longitudinal pitches downstream of tube bundles. In the present study, the effect of the downstream variation in the transverse and longitudinal pitches on the heat transfer and flow characteristic across the staggered circular tube bundle will be numerically investigated.

2 Research Methodology

2.1 Geometry of the tube bundles

Computational studies were conducted on tube bundles with varying pitches in a staggered arrangement to determine the temperature change and pressure drop of the air flowing across it. The arrangements of the tubes were made in seven forms:

– tube bundle with fixed pitch (TBFP), standard;

– tube bundle with decreasing longitudinal pitch (TBDLP);

– tube bundle with decreasing transverse pitch (TBDTP);

– tube bundle with decreasing pitches, both transverse and longitudinal (TBDP);

– tube bundle with increasing longitudinal pitch (TBILP);

– tube bundle with increasing transverse pitch (TBITP);

– tube bundle with increasing pitches, both transverse and longitudinal (TBIP).

Three extreme cases of the tube arrangements are as depicted in Figure 1. The TBFP is a standard tube arrangement having transverse pitch ratio $p = 1.50$. Therefore, its transverse pitch, p_T was determined as

$$p_T = 1.5 d_0. \tag{1}$$

To form an equilateral triangular tube layout, the longitudinal pitch was calculated as

$$p_L = \frac{\sqrt{3}}{2} p_T. \tag{2}$$

The transverse pitches for other tube arrangements were determined from the products of the outer diameter, d_0 and pitch ratios of 1.60, 1.55, 1.50, 1.45 and 1.40, which gives an average of 1.50. Their longitudinal pitches (p_{L1}, p_{L2}, p_{L3}, and p_{L4}) were chosen with an arbitrary decrement or increment of 0.69 mm. However, for all the three arrangements, the distances between their first and last columns were the same. The geometrical parameters of the tube bundles are as depicted in Table 1.

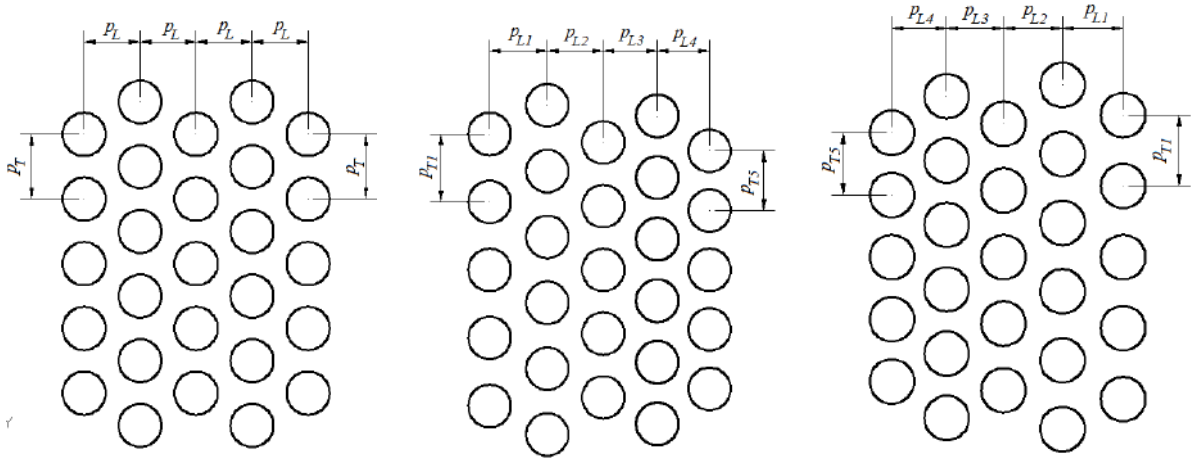

a b c

Figure 1 – The tube layout arrangements of TBFP, TBDP, and TBIP

Table 1 – The geometrical parameters of the tube bundles

Parameter		Value
Tube outside diameter d_0, mm		15.88
Tube thickness t, mm		1.62
Tube length L, mm		150
Tubes number n		27
Tubes number of rows		11
Tubes number of columns		5
Transverse pitch, mm	TBFP, TBDLP, TBILP	23.81
	TBDP, TBDTP	25.40, 24.61, 23.81, 23.02, 22.23
	TBITP, TBIP	22.23, 23.02, 23.81, 24.61, 25.40
Longitudinal pitch, mm	TBFP, TBDTP, TBITP	20.62
	TBDLP, TBDP	21.65, 20.97, 20.28, 19.59
	TBILP, TBIP	19.59, 20.28, 20.97, 21.65

2.2 Numerical simulation

In the computational model, the thermo-physical properties of the fluid and tube materials were assumed to be constant. Also, the cross flow over the tube bundles was considered to be steady and incompressible, because the highest Mach number of flow obtained from preliminary calculation was less than the threshold of 0.3 [10]. Thus, the flow over the tube bundles follows as:

The continuity equation:

$$\frac{\partial U_j}{\partial x_j} = 0 \tag{3}$$

Reynolds averaged Navier-Stokes (RANS) equations:

$$\rho \frac{\partial \left(U_j U_i\right)}{\partial x_j} = -\frac{\partial P}{\partial x_i} + \frac{\partial}{\partial x_j}\left[\mu\left(\frac{\partial U_i}{\partial x_j} + \frac{\partial U_j}{\partial x_i}\right) - \rho\overline{u_i' u_j'}\right] \tag{4}$$

Energy equation:

$$\rho c_p \frac{\partial \left(U_j T\right)}{\partial x_j} = \frac{\partial}{\partial x_j}\left(\left(\eta + \eta_T\right)\frac{\partial T}{\partial x_j}\right) \tag{5}$$

where x_i (i = 1, 2) is the coordinates, U_i represents the velocity vector, p is the pressure, T stands for temperature, ρ is the density, μ is the dynamic viscosity, μ_T is the turbulent eddy viscosity, c_p represents the specific heat capacity, η is the thermal conductivity, η_T stands for turbulent thermal conductivity and $\rho\overline{u_i' u_j'}$ is the Reynolds stress tensor.

The turbulent eddy viscosity as obtained from [24–28] to impose the realizability constraint is

$$\mu_T = \rho \times \max\left(\mu_{\min}, l_m\sqrt{k}\right) \tag{6}$$

and

$$l_m = \min\left(C_\mu \frac{k^{3/2}}{\varepsilon}, l_{\max}, \frac{\sqrt{k}}{3}\frac{1}{\max \lambda_e}\right) \tag{7}$$

Here μ_{min} is a fraction or a value of the laminar viscosity, μ and l_m is the limited mixing length. l_{max} is the maximum permissible mixing length and λ_e (e = 1, 2, 3) are strain rate tensor eigenvalues.

Also, the turbulent thermal conductivity is defined as

$$\eta_T = \frac{\mu_T c_p}{\mathrm{Pr}_T} \tag{8}$$

The Boussinesq closure approximation to the Reynolds stress tensor in equation (4) is given as [29–31]

$$-\rho\overline{u_i' u_j'} = \mu_T\left(\frac{\partial U_i}{\partial x_j}+\frac{\partial U_j}{\partial x_i}\right)- \frac{2}{3}\rho k\delta_{ij} \tag{9}$$

Thus, in resolving the RANS equations, the k-ε turbulent model was employed with the following additional transport equations:

Turbulent kinetic energy:

$$\rho\frac{\partial\left(U_j k\right)}{\partial x_j} = \frac{\partial}{\partial x_j}\left[\left(\mu+\frac{\mu_T}{\sigma_k}\right)\frac{\partial k}{\partial x_j}\right]+ \left[\mu_T\left(\frac{\partial U_i}{\partial x_j}+\frac{\partial U_j}{\partial x_i}\right)-\frac{2}{3}\rho k\delta_{ij}\right]\frac{\partial U_i}{\partial x_j}- \rho\varepsilon \tag{10}$$

Turbulent dissipation energy:

$$\rho\frac{\partial\left(U_j\varepsilon\right)}{\partial x_j} = \frac{\partial}{\partial x_j}\left[\left(\mu+\frac{\mu_T}{\sigma_\varepsilon}\right)\frac{\partial\varepsilon}{\partial x_j}\right]+ C_{\varepsilon 1}\frac{\varepsilon}{k}\left[\mu_T\left(\frac{\partial U_i}{\partial x_j}+\frac{\partial U_j}{\partial x_i}\right)-\frac{2}{3}\rho k\delta_{ij}\right]\frac{\partial U_i}{\partial x_j}- C_{\varepsilon 2}\rho\frac{\varepsilon^2}{k} \tag{11}$$

The closure constants for the transport equations are given as $C_{\varepsilon 1}$ = 1.44, $C_{\varepsilon 2}$ = 1.92, C_φ = 0.09, σ_k = 1.0, and σ_ε = 1.3

2.3 Initial and boundary conditions with the mesh structure

The initial velocity, pressure, and temperature of the fluid were set at zero, atmospheric pressure and 298 K, respectively. Velocity-inlet and temperature-inlet conditions were imposed at the inlet of the computational domain. The velocity was varied from 5 to 15 m/s at the constant inlet temperature of 301.15 K. The temperature of the tube walls was fixed at 332.15 K. Outlet boundary condition was set at the exit with zero gauge pressure and zero gradients for other primitive variables. Wall functions were applied to the walls of the tubes and the channels. The detail description of the boundary conditions as being applied to the computational domain is shown in Figure 2.

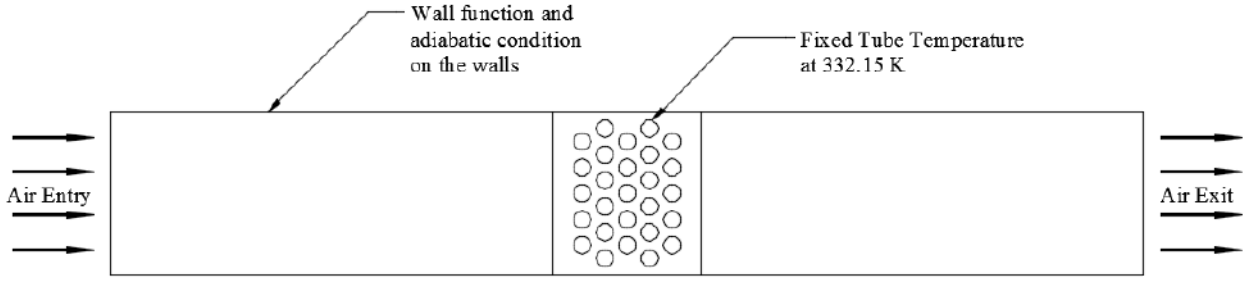

Figure 2 – The detail description of the boundary conditions

The finite element based COMSOL Multiphysics CFD code was used to solve the governing equations on the computational domain. The mesh structure of the domain contains both triangular and rectangular elements as shown in Figure 3. In order to resolve the sharp temperature and velocity gradients in the region of the near-wall, the mesh in this region was refined well with rectangular elements. Five different mesh grids were generated to carry out the numerical independence of the grids. They are 18 150, 26 732, 44 464, 62 714, 98 100 and 125 522 finite elements. The last three mesh elements had small relative differences of 0.8 and 4 % for the coefficient of heat transfer and overall pressure drop, respectively. Therefore, 98 100 mesh grid was selected for this study to save computational time. The dimensionless sublayer-scaled wall distance at which the logarithmic layer intersects the viscous sublayer was found to be at approximately 11.06.

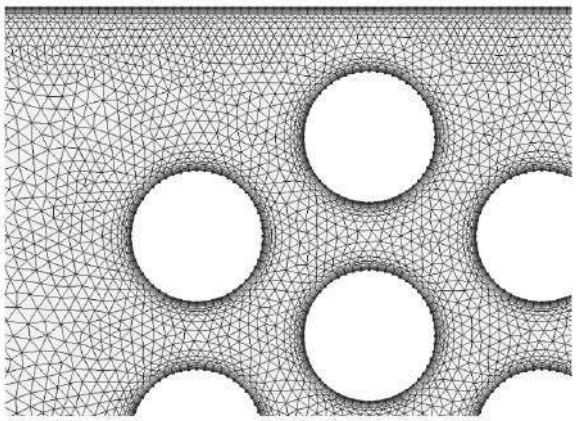

Figure 3 – The finite element grid

2.4 Data reduction

It was assumed that the outer wall temperature, T_w of each tube was the same as the bulk temperature of the hot water. This is the average of the water temperatures in the jackets. Also, the heat loss to the surroundings was assumed to be negligible. Thus, the heat transfer rate between the walls of the tube bundles and the air flow is given by [19, 32]

$$Q = hA\Delta T_{LM} \tag{12}$$

The log mean temperature difference is

$$\Delta T_{LM} = \frac{(T_w - T_{in}) - (T_w - T_{out})}{\ln \dfrac{(T_w - T_{in})}{(T_w - T_{out})}} \tag{13}$$

The tubes outer surface area was calculated from

$$A = \pi d_o L n \tag{14}$$

Thus, in order to determine the coefficient of heat transfer, the rate of heat transfer from equation (12) was obtained from the heat that accompanied the temperature difference within the air stream as

$$Q = mc_p (T_{out} - T_{in}) \tag{15}$$

Therefore, the Nusselt number was calculated as

$$Nu = \frac{hd_o}{k} \tag{16}$$

The air flow Reynolds number through the tube bundle as obtained from Bergman et al. [9] was estimated as

$$\mathrm{Re} = \frac{\rho v_{\max} d_o}{\mu} \tag{17}$$

where v_{max} is a mean velocity of the most narrow section of the tubes. Using TBFP arrangement, it is determined as follows

$$v_{\max} = \frac{p_T}{2(p_D - d_o)} v \tag{18}$$

The friction factor from the pressure drop across the tube bundle was calculated from Holman [33] as

$$f = \frac{\Delta p}{2\rho v_{\max}^2 N} \left(\frac{\mu}{\mu_w} \right)^{0.14} \tag{19}$$

where N is the main resistance of the flow.

Thermal-hydraulic performance factor of the tube bundles is defined as [22]

$$\eta = \frac{(Nu/f)_{TBFP}}{(Nu/f)} \tag{20}$$

2.5 Model validation

The present predictions from the study were compared with the results of correlations available in the literature (Cengel, Incropera7). The comparisons as obtained for the tube bundle with fixed pitch are presented in Figure 4 for the Nusselt number and friction factor. It is clearly shown that the predicted values were in good agreement with the existing experimental and analytical correlations. However, the variations of Nusselt number in the present study from Zukauskas [34], Aiba [35] and Khan [3] correlations were found to be 28.5, 12.6 and 8.1 %, respectively. The predicted friction factor has a variation of 18.0 from Jakob's correlation [33]. The observed discrepancy might be as a result of making the few tubes wall-bounded and also differences caused by the uncertainties of the numerical simulations and the correlations.

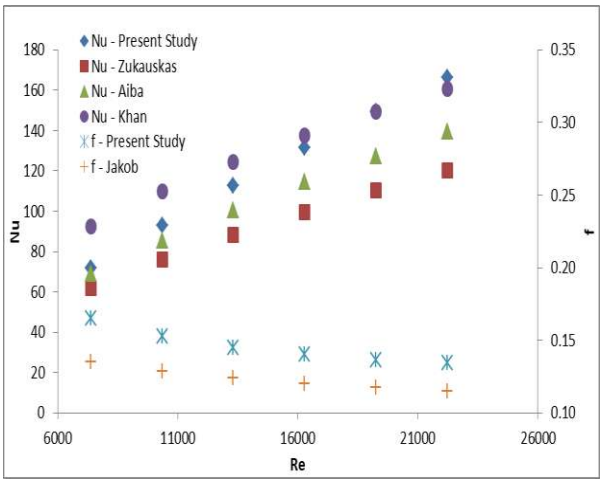

Figure 4 – Comparison of results with existing correlations

3 Results and Discussion

The streamlines and distributions of fluid velocity across the tube bundles for TBFP, TBDP, and TBIP at Reynolds numbers of 7 381 and 22 214 are as indicated in Figure 5. These arrangements were selected as extreme cases to explain the flow distributions. From the figure, the maximum flow velocity can be found within the regions in-between the tubes, and the tubes and walls. The wakes developed behind each tube are similar for all the tube arrangements and these regions are characterized with very low velocity. Wakes behind the first four columns are smaller as compared with the last column, and this could be attributed to the delay in onset of flow separation and change in flow structure caused by the tube columns behind the first four columns. However, in the wake region, the heat transfer rate would be at its lowest.

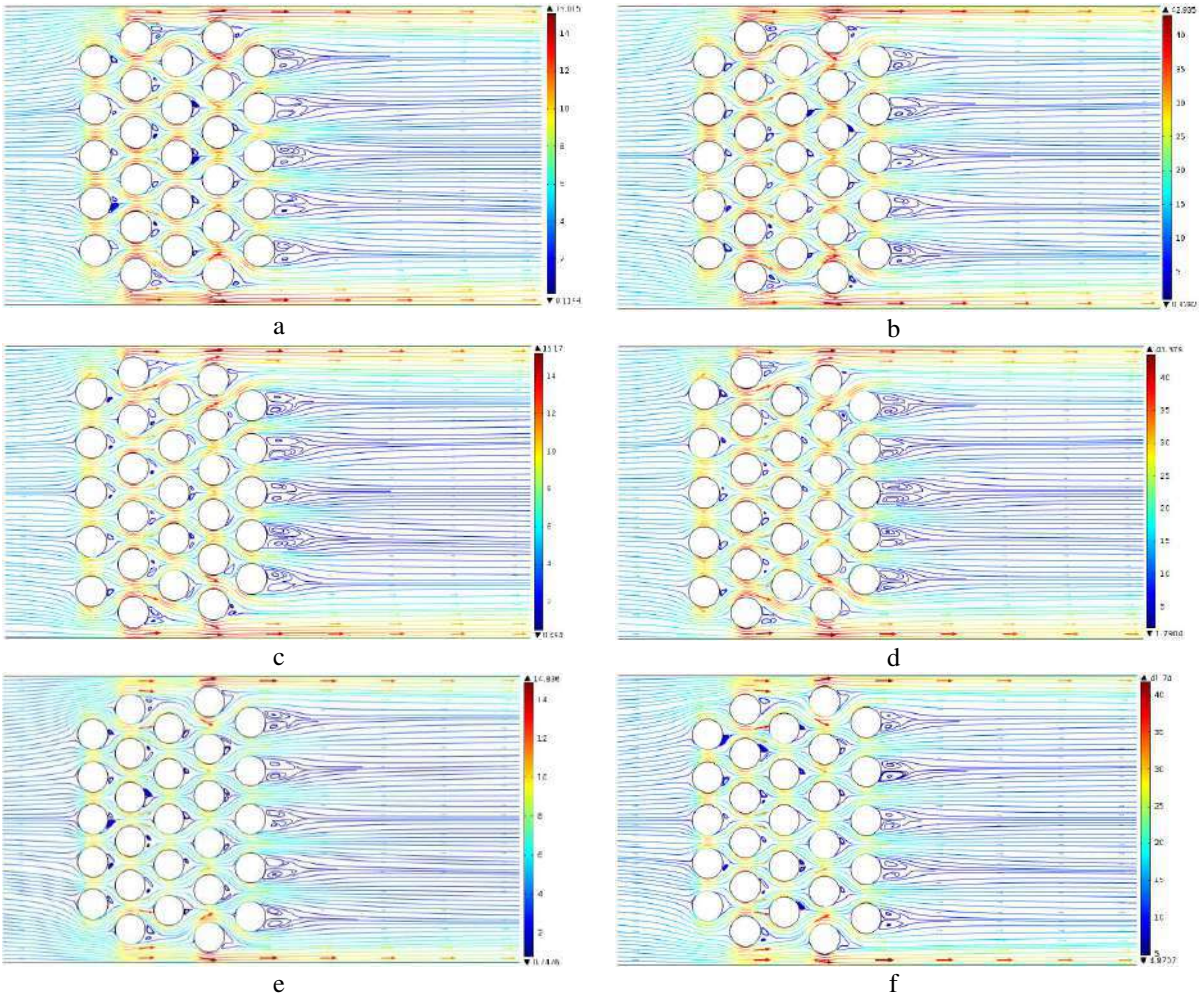

Figure 5 – Streamlines and distributions of fluid velocity across the tube bundles:
a – TBFP at Re =7 381; b – TBFP at Re = 22 214; c – TBDP at Re = 7 381;
d – TBDP at Re = 22 214; e – TBIP at Re = 7 381; f – TBIP at Re = 22 214

The distribution patterns of the turbulent kinetic energy within the tube bundles for TBFP, TBDP, and TBIP at Reynolds numbers of 7 381 and 22 214 are as shown in Figure 6. The maximum energy averagely increases from 16 to 140 m^2/s^2 as the Reynolds number increases between the two bounds. There is a sharp increase in turbulent energy as the tube column increases; this is partly due to the effect of the preceding columns on the tubes downstream. The flow turbulence intensity, which is seen to be more pronounced at the leading edges and the spaces in-between tubes will eventually cause a higher heat transfer rate at these regions. However, the low-intensity turbulence found in the trailing edges of the tubes may be attributed to the characteristically low velocity wakes in the regions, thereby reducing thermal energy transfer [10]. As seen from the figure, the TBDP and TBIP produced higher and lower turbulent kinetic energy, respectively. This is an indication that the downstream decrease in tube pitch creates more interaction between the fluid and the tube surfaces.

Figure 7 shows the comparison of the Nusselt number for all the tube arrangements over a range of Reynolds number. It can be observed for each of the tube arrangement that the Nusselt number increases as the Reynolds number increases. However, there were very small variations in the Nusselt number; the value for TBFP, which is tube bundle with fixed pitch, is averagely greater with 0.7, 0.9, 0.1, and 0.9 % than TBDLP, TBILP, TBITP, and TBIP, respectively. However, its Nusselt number is less with 1.0 and 1.6 % than TBDTP and TBDP, respectively. Except for TBDLP, there was an increase in the Nusselt number as the pitches decrease downstream, this is partly due to an increase in turbulent interaction within the fluid, and fluid with tube surfaces.

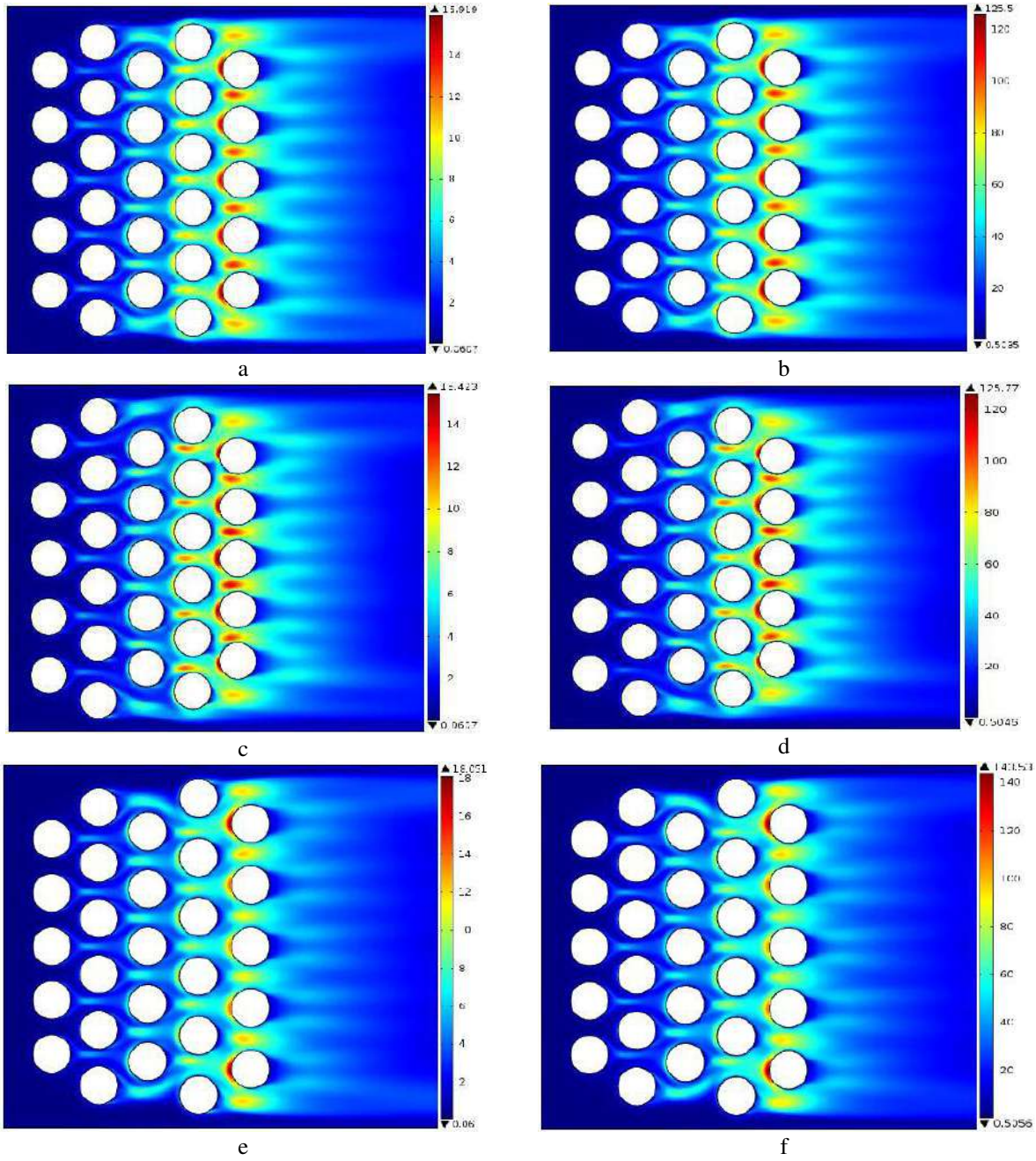

Figure 6 – Turbulent kinetic energy distributions within the tube bundles:
a – TBFP at Re = 7 381; b – TBFP at Re = 22 214; c – TBDP at Re = 7 381;
d – TBDP at Re = 22 214; e – TBIP at Re = 7 381; f – TBIP at Re = 22 214

The friction factor for all the tube arrangements as against the Reynolds number is as presented in Figure 8. It is obvious that the friction factor reduces with increasing Reynolds number for all arrangements. The friction factor is lowered for dominantly increasing the kinetic energy of the fluid with increasing Reynolds number. From the figure, the friction factor of TBFP (standard) is about 1.0, 1.1, and 1.4 % less than TBDLP, TBDTP and TBDP, respectively. While the friction factor of the TBFP is greater than TBILP, TBITP and TBIP with 1.1, 0.9, and 1.2 %, in that order. The trend indicates that the pitches of the tube columns downstream have a more pronounced effect on friction factor as compared with the pitches upstream.

The plot of the thermal-hydraulic performance factor for all tube arrangements as against the Reynolds number is as shown in Figure 9. There is no significant variation in the efficiency with the range of Reynolds numbers, except for TBDLP which decreases over the range. It can be seen that the increasing pitch arrangements display better thermal-hydraulic performance while the performance of the decreasing pitch arrangements is lower than the tube arrangement with a fixed pitch.

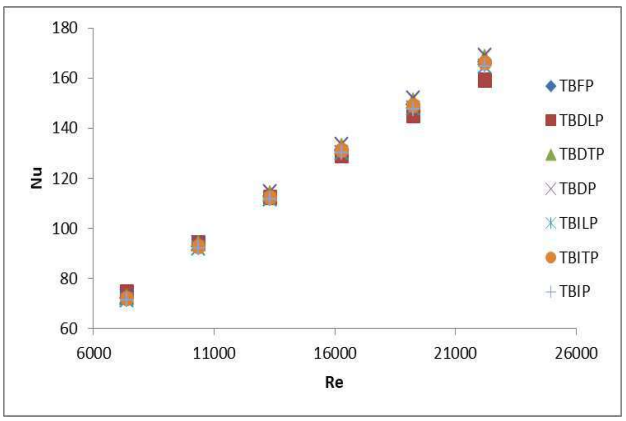

Figure 7 – The tube bundles average Nusselt number against the Reynolds number

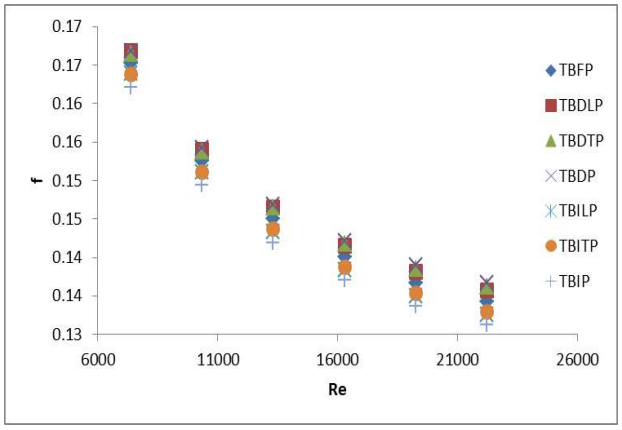

Figure 8 – The friction factor across the tube bundles against the Reynolds number

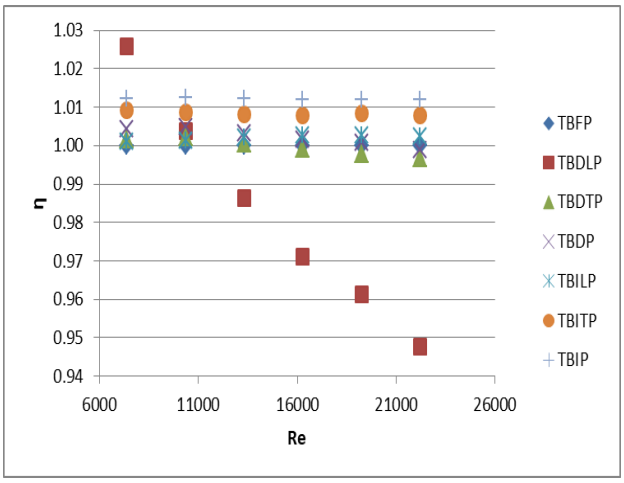

Figure 9 – The thermal-hydraulic performance factor of the tube bundles against the Reynolds number

4 Conclusion

The effects of varying downstream, the transverse and longitudinal pitches on the thermal-hydraulic performance of staggered tube arrangements were studied numerically. Seven tube arrangements were considered within a Reynolds number range. The results obtained indicated that the changes in the tube pitches affected the performance of the cross-flow heat transfer over the tube bundles. The tube bundles with decreasing pitches had the highest heat transfer performance. The lowest friction factor was obtained from the tube bundles with increasing pitches, which also gave the best thermal-hydraulic performance.

5 Nomenclature

5.1 Abbreviations and symbols

d Tube diameter;
p_T Transverse pitch, m;
p_L Longitudinal pitch, m;
p_D Diagonal pitch, m;
U Velocity component, m/s;
P Pressure, Pa;
T Temperature, K;
x Cartesian coordinate, m;
k Turbulence kinetic energy, m^2/s^2;
l_{min} Size of the minimum permissible eddies, m;
l_{max} Maximum permissible mixing length, m;
l_m Limited mixing length, m;
Re Reynolds number;
Pr_T Turbulent Prandtl number;
Q Heat transfer rate, W;
A Surface area of a tube bundle, m^2;
c_p Specific heat capacity, J/(kg·K);
h Heat transfer coefficient, W/(m^2·K);
Nu Nusselt Number;
Δp Pressure drop, Pa;
f Friction factor;
n Tubes number;
N Number of main resistance;
η Thermal hydraulic performance factor.

5.2 Greek symbols

ρ Density, kg/m^3;
μ Dynamic viscosity, Pa·s;
μ_T Turbulent eddy viscosity, Pa·s;
η Thermal conductivity, W/(m·K)
ε Dissipation rate, m^2/s^3.

5.3 Subscripts

i, j indexes of vectors;
in “inside”;
out “outside”;
w “wall”.

References

1. Li, X., Wu, X., He, S. (2014). Numerical investigation of the turbulent cross flow and heat transfer in a wall bounded tube bundle. *Int. J. Therm. Sci.*, Vol. 75, pp. 127–139. doi:10.1016/j.ijthermalsci.2013.08.001.
2. Chakrabarty, S. G., Wankhede, U. S. (2012). Flow and heat transfer behaviour across circular cylinder and tube banks with and without splitter plate, Vol. 2.
3. Khan, W. A., Culham, J. R., Yovanovich, M. M. (2006). Convection heat transfer from tube banks in crossflow: Analytical approach. *Int. J. Heat Mass Transf.*, Vol. 49, pp. 4831–4838. doi:10.1016/j.ijheatmasstransfer.2006.05.042.
4. Jeong, J. H., Nam, K. W., Min, J. K., Kim, K. S., Ha, M. Y. (2011). The effects of the evaluation method on the average heat transfer coefficient for a mini-channel tube bundle. *Int. J. Heat Mass Transf.*, Vol. 54, pp. 5481–5490. doi:10.1016/j.ijheatmasstransfer.2011.07.043.
5. Mandhani, V., Chhabra, R., Eswaran, V. (2002). Forced convection heat transfer in tube banks in cross flow. *Chem. Eng. Sci.*, Vol. 57, pp. 379–391. doi:10.1016/S0009-2509(01)00390-6.
6. Li, X., and Wu, X. (2013). Thermal mixing of the cross flow over tube bundles. *Int. J. Heat Mass Transf.*, Vol. 67, pp. 352–361. doi:10.1016/j.ijheatmasstransfer.2013.08.031.
7. Mehrabian, M. (2007). Heat transfer and pressure drop characteristics of cross flow of air over a circular tube in isolation and/or in a tube bank. *Arab. J. Sci. Eng.,* Vol. 32, pp. 365–376.
8. Buyruk, E. (1999). Heat transfer and flow structures around circular cylinders in cross-flow. *Tr. J. Eng. Environ. Sci.*, Vol. 23, pp. 299–315.
9. Bergman, T. L., Lavine, A. S., Incropera, F. P., Dewitt, D. P. (2011). *Fundamentals of Heat and Mass Transfer*. John Wiley and Sons, New Jersey.
10. Mangrulkar, C. K., Dhoble, A. S., Deshmukh, A. R., Mandavgane, S. A. (2017). Numerical investigation of heat transfer and friction factor characteristics from in-line cam shaped tube bank in crossflow. *Appl. Therm. Eng.*, Vol. 110, pp. 521–538. doi:10.1016/j.applthermaleng.2016.08.174.
11. Tahseen, T. A., Rahman, M. M., Ishak, M. (2014). An experimental study of air flow and heat transfer over. *Int. J. Automot. Mech. Eng.*, Vol. 9, pp. 1487–1500.
12. Mohanty, R. L., Swain, A., Das, M. K. (2018). Thermal performance of mixed tube bundle composed of circular and elliptical tubes. *Therm. Sci. Eng. Prog*. doi:10.1016/j.tsep.2018.02.009.
13. Barcellos, S. V., Bartz, C. R., Endres, C. L., Moller, L. A. M. (2003). Velocity and pressure fluctuations on inclined tube banks submitted to turbulent flow. *J. Brazilian Soc. Mech. Sci. Eng.*, Vol. 25.
14. Toolthaisong, S., Kasayapanand, N. (2013). Effect of attack angles on air side thermal and pressure drop of the cross flow heat exchangers with staggered tube arrangement. *Energy Procedia*, Vol. 34, pp. 417–429. doi:10.1016/j.egypro.2013.06.770.
15. Lee, D., Ahn, J., Shin, S. (2013). Uneven longitudinal pitch effect on tube bank heat transfer in cross fl ow. *Appl. Therm. Eng.*, Vol. 51, pp. 937–947. doi:10.1016/j.applthermaleng.2012.10.031.
16. Hofmann, R., Frasz, F., Ponweiser, K. (2007). Heat transfer and pressure drop performance comparison of finned-tube bundles in forced convection. *WSEAS Trans. Heat Mass Transf.*, Vol. 2.
17. Hofmann, R., Frasz, F., Ponweiser, K. (2008). Experimental analysis of enhanced heat transfer and pressure-drop of serrated finned-tube bundles with different fin geometries. *5th WSEAS Int. Conf. Heat Mass Transf.*, pp. 54–62.
18. Hofmann, R., Frasz, F., Ponweiser, K. (2008). Performance evaluation of solid and serrated finned-tube bundles with different fin geometries in forced convection. *5th Eur. Therm. Conf.*, Netherlands.
19. Gaddis, E. S. (2010). Pressure drop of tube bundles in cross flow. *VDI Heat Atlas, Springer-Verlag, Berlin Heidelberg*, pp. 1099–1114.
20. Horvat, A., Leskovar, M., Mavko, B. (2006). Comparison of heat transfer conditions in tube bundle cross-flow for different tube shapes. *Int. J. Heat Mass Transf.*, Vol. 49, pp. 1027–1038. doi:10.1016/j.ijheatmasstransfer.2005.09.030.
21. Nouri-Borujerdi, A., Lavasani, A. M. (2007). Experimental study of forced convection heat transfer from a cam shaped tube in cross flows. *Int. J. Heat Mass Transf.*, Vol. 50, pp. 2605–2611. doi:10.1016/j.ijheatmasstransfer.2006.11.028.
22. Lavasani, A. M., Bayat, H., Maarefdoost, T. (2014). Experimental study of convective heat transfer from in-line cam shaped tube bank in crossflow. *Appl. Therm. Eng.*, Vol. 65, pp. 85–93. doi:10.1016/j.applthermaleng.2013.12.078.
23. Du, X. P., Zeng, M., Dong, Z. Y., Wang, Q. W. (2014). Experimental study of the effect of air inlet angle on the air-side performance for cross-flow finned oval-tube heat exchangers. *Exp. Therm. Fluid Sci.*, Vol. 52, pp. 146–155. doi:10.1016/j.expthermflusci.2013.09.005.
24. Bassi, F., Crivellini, A., Rebay, S., Savini, M. (2005). Discontinuous Galerkin solution of the Reynolds-averaged Navier–Stokes and k-ω turbulence model equations. *Comput. Fluids*, Vol. 34, pp. 507–540. doi:10.1016/j.compfluid.2003.08.004.
25. Kuzmin, D., Mierka, O., Turek, S. (2007). On the implementation of the k-ε turbulence model in incompressible flow solvers based on a finite element discretization. *Int. J. Comput. Sci. Math.*, Vol. 1, pp. 193–206.
26. Park, C. H., Park, S. O. (2005). On the limiters of two-equation turbulence models. *Int. J. Comut. Fluid Dyn.*, Vol. 19, pp. 79–86. doi:10.1080/10618560412331286292.

27. Sveningsson, A., Davidson, L. (2003). Assessment of realizability constraints and boundary conditions in v2-f turbulence models. *Turbul. Heat Mass Transf.*, Vol. 4, pp. 585–592.
28. Young, M. E., Ooi, A. (2004). Turbulence models and boundary conditions for bluff body flow. *Proc. 15th Australas. Fluid Mech. Conf.*, Sydney.
29. Ferziger, J. H., Peric, M. (2002). *Computational Methods for Fluids Dynamics*. Springer-Verlag, Berlin.
30. Tannehill, J. C., Anderson, D. A., Pletcher, R. H. (1997). *Computational Fluid Mechanics and Heat Transfer*. Taylor and Francis, Washington.
31. Wilcox, D. C. (2006). *Turbulence Modeling for CFD*. DCW Industries, California.
32. Gaddis, E. S. (2010). Pressure drop in the outer shell of heat exchangers. *VDI Heat Atlas, Springer-Verlag, Berlin Heidelberg*, pp. 1115–1128.
33. Holman, J. P. (2010). *Heat Transfer*. McGraw-Hill, New York.
34. Zukauskas, A., Ulinskas, R. (1985). Efficiency parameters for heat transfer in tube banks. *Heat Transf. Eng.*, Vol. 6, pp. 19–25.
35. Aiba, S., Tsuchida, H., Ota, T. (1982). Heat transfer around tubes in staggered tube banks. *Bull. JSME*, Vol. 25, pp. 927–933.

УДК 536.24

Числове дослідження впливу кроку труб на теплові та гідравлічні характеристики трубних пучків у поперечному потоці

Пентірін М. О.[1], Товоджу О. А.[2], Аджибове С. А.[1], Зебулун О. Е.[1]

[1] Університет м. Ібадан, шлях Обудува, м. Ібадан, Нігерія;
[2] Університет Аделеке, P.M.B. 250, шлях Еде-Осогбо, м. Еде, штат Осун, Нігерія

Анотація. У різних теплообмінних апаратах трубні пучки застосовуються для передачі теплової енергії між рідинам. Проте, міжтрубний простів будь-якого трубного пучка є визначальним фактором його теплових і гідравлічних характеристик. У цій роботі чисельно проаналізовано вплив зміни поперечного і поздовжнього кроків у нижній частині трубного пучка на характеристики потоку і теплопередачі. Досліджено сім варіантів розташування труб зі змінним кроком для чисел Рейнольдса у діапазоні від 7 381 до 22 214. Аналіз проводився із застосуванням моделі турбулентності k-ε із заданими граничними умовами із комп'ютерною реалізацією методом скінченних об'ємів у COMSOL Multiphysics. Отримані результати добре узгоджуються з існуючими залежностями. Трубні пучки зі зменшеною відстанню дають кращу теплопередачу. Збільшення ж відстані призводить до зменшення гідравлінчного коефіцієнта тертя.

Ключові слова: поперечний потік, змінний крок, трубний пучок, теплопередача, теплотехнічні характеристики.

JOURNAL OF ENGINEERING SCIENCES
ЖУРНАЛ ІНЖЕНЕРНИХ НАУК
ЖУРНАЛ ИНЖЕНЕРНЫХ НАУК

Web site: http://jes.sumdu.edu.ua

DOI: 10.21272/jes.2019.6(2).e2 Volume 6, Issue 2 (2019)

Braking Pattern Impact on Brake Fade in an Automobile Brake System

Towoju O. A.

Adeleke University, P.M.B. 250, Ede-Osogbo Rd., Ede, Osun State, Nigeria

Article info:
Paper received: January 1, 2019
The final version of the paper received: April 4, 2019
Paper accepted online: April 10, 2019

***Corresponding Author's Address:**
olumidetowo@yahoo.com

Abstract. The importance of brake systems in automobiles cannot be overemphasized. Brakes are used in speed control of vehicles and do so by the conversion of kinetic energy into thermal energy. Better stopping performance has favored the disc brake system over the drum brake system and has found wide application in high-performance vehicles. Brake fade, caused by thermal overload has placed a limit on the permissible temperature at which braking systems can function, and it is the task of designers to ensure that this is avoided. However, even with a good design, panic braking at high speeds could lead to high-temperature values. This study is thus undertaken to numerically investigate the effect of selected braking patterns on temperature growth which could lead to brake fade in a disc brake system for a 2 200 kg car moving at a velocity of 40 m/s whose velocity is expected to be reduced to 4 m/s after five seconds with two matches of the brake for a seconds' interval. The peak temperature attained in the system during braking was observed to be different for the different braking patterns, and the best-suited pattern was the 1s-1s-3s with peak temperature values below 600 K.

Keywords: automobile, brake fade, disc brake, temperature distribution.

1 Introduction

Brakes are mechanical devices that restrain motion and does so by the absorption of energy from a moving system which is achieved by friction, pumping on electromagnetic means.

The importance of brakes in automobiles cannot be over-emphasized; it is used for its stoppage and speed control. Automobiles generally use the friction type of braking system which consists of a group of mechanical, hydraulic and electronic activated components.

2 Literature Review

Brakes are basically devices used in the conversion of kinetic energy to thermal energy [1, 2]. Automobiles generally use the friction type of braking system which consists of a group of mechanical, hydraulic and electronic activated components. The automobile friction type braking system is either the disc or the drum system [3], and the choice of one is dependent on the purpose it is required to fulfill. The all-disc braking system is made use of in high-performance vehicles, and rarely will one see the drum braking system used at the front wheels of modern vehicles except on the rear wheels.

Automotive disc brakes are usually made of grey iron [2, 4, 5], and uses calipers to squeeze a pair of pads against a moving/rotating disc thereby causing its retardation as a result of friction. The disc brake is favored over the drum brake system because of its better stopping performance attributable to its better heat dissipation rate, and its better recovery from immersion into liquid [6]. For better heat tolerance, disc brakes can also be manufactured from ceramic composites. However, the impact of cost has limited its use to exotic cars.

Brake fade is caused by overheating of the brake system and results in a temporary reduction or complete loss of brake power, and it is to be avoided [8]. The heat storage and dissipation capacity of the brake system are of upmost importance in the prevention of brake fade which is caused by thermal overload especially during a single stop or repeated stops from a high speed and/or high load condition [4, 6, 8–12].

The impact of the vehicle speed and duration of braking have been undertaken, and it has been reported that it is imperative that the heat generated must be adequately dissipated to ensure the proper functioning of the system [13–17]. The relatively low temperature at which materials could fade has been a major reason for consideration in the choice of materials for disc braking systems, because of the very high temperature which is obtainable during braking. Fading is one of the reasons why aluminum, despite being a good thermal conductor and lightweight is not used in its pure form for disc braking system because of its low operating temperature

[2, 13, 18, 19]. To ensure fast cooling through forced convection, brake discs are usually also ventilated [16, 20], however, ventilation of the brake disc can result into the induction of an uneven temperature distribution field in the disc [21], and by extension Judder effect [21, 22].

Generally, brake pads could be effective up to a temperature of about 600 K [11, 14, 22], while for racing vehicles, the effective operating temperature of the brake pads without fading can be as high as 900 K [14]. Repeated thermal stresses caused by high temperature usually results into the development of hot spots [24, 25] which subsequently can result into heat cracks on the brake disc surface [16, 19, 26, 27].

Asides the vehicle weight, velocity, and time required to bring the vehicle to a halt or reduced velocity, the braking pattern also contributes to the inception of brake fade. This study is thus focused on the impact of braking pattern on brake system fade using six different scenarios.

3 Research Methodology

The thermal distribution of a disc braking system was determined numerically by modeling a brake assembly fitted to a vehicle of total mass 2 200 kg (mass of vehicle plus payload) moving at a velocity of 40 m/s (144 km/hr). The vehicle is to be brought to a speed of 4 m/s in 5 s after the first march of the brake pedals, which is expected to be twice with a time lapse of 1 s in-between the marches.

The model as developed by COMSOL Multiphysics for a disc brake system geometry and material properties was made. The heat transfer module was employed in the numerical solution.

It was assumed that there is no skidding, and all the kinetic energy at the surface of the disc brake is transferred to thermal energy in the brake system, and also the pressure distribution generated by the brake pad on the disc brake surface is uniform. The designed disc brake system is shown in Figure 1.

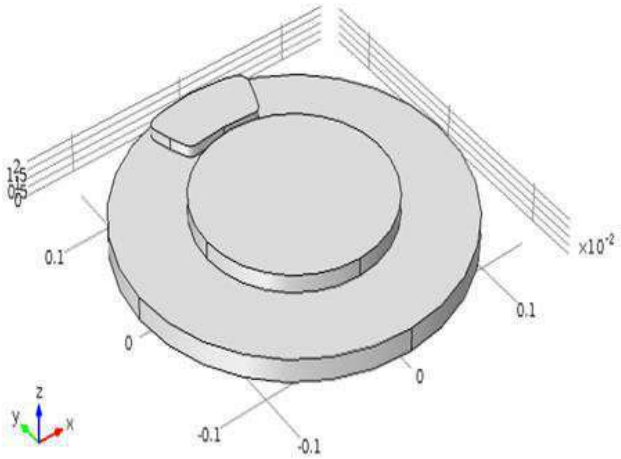

Figure 1 – The designed disc brake dimension

The deceleration power of the brakes while neglecting drag and any other losses outside the brakes is the negative value of the time derivative of the vehicle's kinetic energy.

$$P_d = -\frac{d}{dt}\left(\frac{m_v V^2}{2}\right) \tag{1}$$

$$P_d = -m_v V \frac{dV}{dt} \tag{2}$$

where P_d is the deceleration power; m_v is the vehicle mass; V is the vehicle velocity.

The total frictional heat source of the brakes is equivalent to the brake deceleration power, that is

$$P_{friction} = P_d \tag{3}$$

And since a standard car fitted with an all-disc brake system has eight brake pads, the frictional heat source at each of the brake pads is given by

$$P_{friction,pad} = \frac{P_{friction}}{8} = -\frac{1}{8} m_v V \frac{dV}{dt} \tag{4}$$

The frictional heat source per unit area is related to the contact pressure between the pad and disc according to the equation:

$$p = \frac{P_{friction,pad}}{\mu V} \tag{5}$$

The thermal energy generated at the boundary between the brake pad and the disc is dissipated by convection and radiation, and for this study, the rotation of the disc is modeled as convection in the disc, and the local disc velocity vector is given as

$$V_{disc} = \frac{V}{R}(-y, x) \tag{6}$$

The thermal properties of the disc brake system used for this study are shown in Table 1, and the geometry dimension is as stated in Table 2.

The disc brake was meshed using the free triangular 1, and the parameters are stated in Table 3.

The temperature distribution in the disc brake system were then determined numerically for braking patterns of first march interval, release period, and second march interval as follows, s: 0.5–1.0–3.5, 1.0–1.0–3.0, 1.5–1.0–2.5, 2.0–1.0–2.0, 2.5–1.0–1.5, and 3.0–1.0–1.0.

The ambient temperature was taken to be 300 K, total braking time of four seconds, and the deceleration was assumed to be of an average value of 9 m/s^2.

Table 1 – Thermal properties of brake system

Material	Density (kg/m^3)	Heat capacity at constant pressure, J/(kg·K)	Thermal conductivity, W/(m·K)	Surface emissivity
Disc	7 870	449	82	0.28
Pad	2 000	935	8.7	0.80
Air	1.170	1 100	0.026	–

Table 2 – Brake system dimensions, m

Part	Radius	Thickness
Disc	0.140	0.013
Wheel bearing	0.080	0.010

Table 3 – Disc brake mesh parameters

Element size (max)	0.00980
Element size (min)	0.00042
Maximum element growth rate	1.35
Factor of curvature	0.30
Narrow region resolution	0.85

4 Results and Discussion

The surface temperature was seen to vary with time and position on the disc and brake pad, leading to a temperature distribution and this is evident from the surface distribution plot for the selected braking patterns after a time period of two seconds of the brake application depicted in Figure 2.

The peak temperature value was observed to be at the tip of the brake pad during the period of the brake application.

These temperature values at the tip of the brake pad are plotted against time for each of the investigated braking patterns and depicted as shown in Figure 3.

The different braking patterns result in different temperature values. The peak temperature values for the different patterns were observed to be the same for the first 0.3 s of the brake application, and this was so because an average retardation value was assumed throughout the braking period, and the minimum first match period was 0.5 s.

The peak temperature values for each of the different braking patterns were also observed to occur before the brake is unmatched, and is a function of the time of a match. With the notion of brake fade set in at a temperature above 600 K [9, 14], the best fit braking pattern to avoid brake fade was observed to be as follows, s: 1.0–1.0–3.0, and this is closely followed by the braking pattern 0.5–1.0–3.5.

The temperature of the brake pad two seconds after the braking and attainment of the required velocity; 4 m/s, is also a function of the braking pattern as depicted in Figure 3, while it is highest for 1.0–1.0–3.0 s, it is least for 3.0–1.0–1.0 s. This is attributable to the fact that after the attainment of the peak temperature during the braking pattern 3.0–1.0–1.0 s, the remainder of the braking match period was used in the cooling of the brake pad as against for the other patterns with two separate peak values.

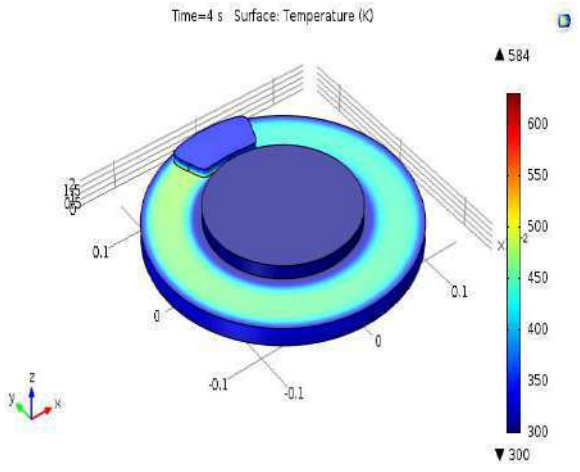

a

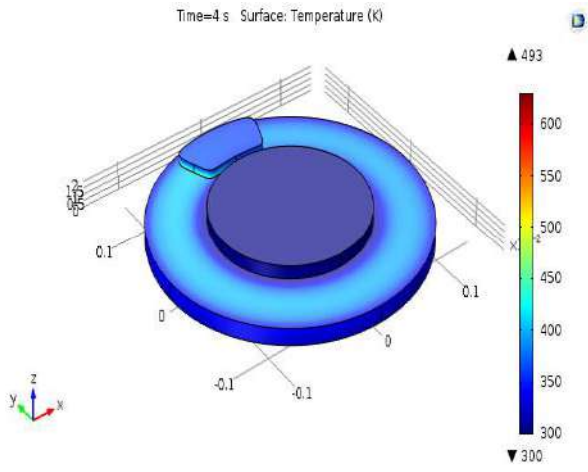

b

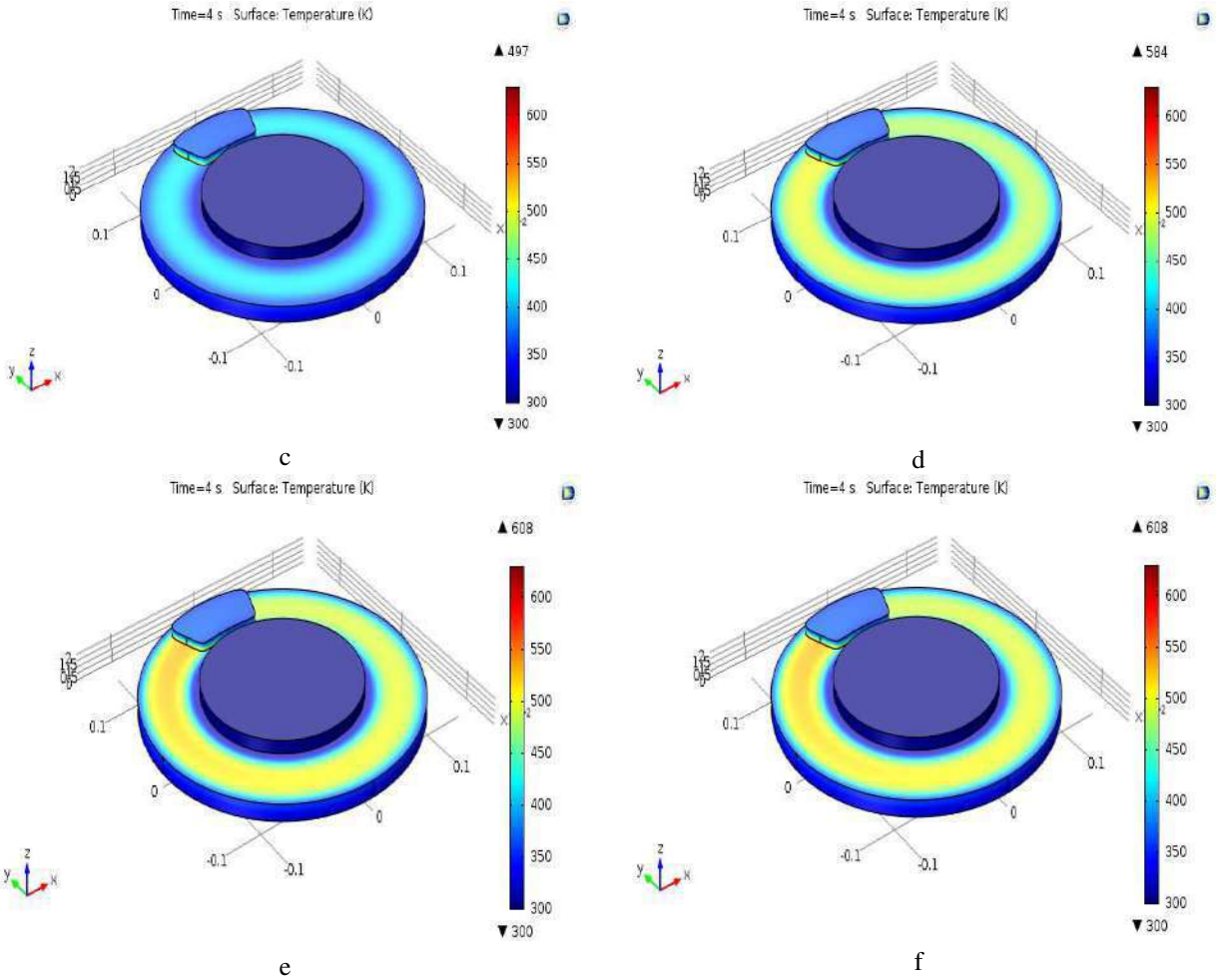

Figure 2 – Brake system surface temperature distribution for the following patterns, s:
a – 0.5–1.0–3.5; b – 1.0–1.0–3.0; c – 1.5–1.0–2.5; d – 2.0–1.0–2.0; e – 2.5–1.0–1.5; f – 3.0–1.0–1.0

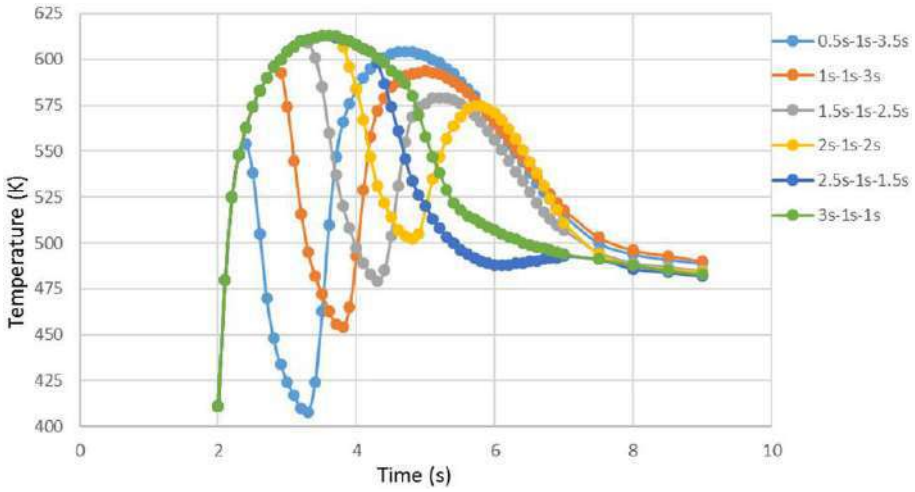

Figure 3 – Brake pad tip temperature

5 Conclusions

The thermal energy generated during braking and the subsequent temperature rise and distribution on the disc brake system have been shown to be dependent on the braking pattern. If need be, for repeated quick braking, the interval should be such that the first match does not lead to excessive heat generation.

The braking pattern "1.0–1.0–3.0 s" was found to be the most suitable to avoid brake fade of the investigated braking patterns, with peak temperature values below 600 K.

References

1. Shi, S. (2016). *Automobile Brake System*. Savonia University of Applied Sciences.
2. Alnaqi, A. A., Kosarieh, S., Barton, D. C., Brooks, P. C., Shrestha, S. (2018). Material characterisation of lightweight disc brake rotors. *Proceedings of the Institution of Mechanical Engineers, Part L: Journal of Materials Design and Applications*, Vol. 232(7), pp. 555–565.
3. *Introduction to Braking System*. SAE Tezpur University, http://www.tezu.ernet.in/sae/Download/Brakingsystem.pdf.
4. Maleque, M. A., Dyuti, S., Rahman, M. M. (2010). Material selection method in design of automotive brake disc. *Proceedings of the World Congress on Engineering*, Vol. 3, London, UK.
5. Maluf, O., Angeloni, M., Milan, M., Spinelli, D., Waldek, W., Bose, F. (2004). Development of materials for automotive disc brakes. *Pesquisa Technol Minerva*, Vol. 2, pp. 149–158.
6. Ganaway, G. (2011). Air disc brake production. *NDIA Tactical Wheeled Vehicles Conference*. Monterey, California, USA.
7. Radhakrishnan, C., Yokeswaran, K., Kumar, N. M., kumar.S. B., Gopinath.M., Inbasekar, B. (2015). Design and optimization of ventilated disc brake for heat dissipation. *International Journal of Innovative Science, Engineering and Technology*, Vol. 2(3), pp. 692–694.
8. Harshal, S. S. (2017). Structural analysis of disc brake rotor for different materials. *International Research Journal of Engineering and Technology*, Vol. 4(7), pp. 2129–2135.
9. Jerew, B. *Understanding Brake Fade and How to Prevent It*. Retrieved from https://www.thoughtco.com/how-to-prevent-brake-fade-4152020.
10. Talati, F., Jalalifar, E. S. (2009). Analysis of heat conduction in a disk brake system. *Heat Mass Transfer*, Vol. 45, pp. 1047–1059.
11. Gowtham, S., Manas, M. B. (2015). Elimination of brake fade in vehicles by altering the brake disc size (a concept). *International Journal of Innovative Research in Science, Engineering and Technology*, Vol. 4(11), pp. 11349–11352.
12. Adamowicz, A., Piotr, G. (2011). Influence of convective cooling on a disc brake temperature distribution during repetitive braking. *Applied Thermal Engineering*, Vol. 31(14), pp. 2177–2185.
13. Grieve, D. G., Barton, D. C., Crolla, D. A., Buckingham, J. T. (1997). Design of a lightweight automotive brake disc using finite element and Taguchi techniques. *Proceedings of the Institution of Mechanical Engineers. Part D: Journal of Automobile Engineering*, Vol. 212(4), pp. 245–254.
14. Streit C. *Solving Brake Fade in Performance Brake Systems*. Retrieved from https://alconkits.com/drmassets/Brake-Fade-Solved.pdf.
15. Zaini, D. (2014). Braking system modeling and brake temperature response to repeated cycle. *Mechatronics, Electrical Power, and Vehicular Technology*, Vol. 5, pp. 123–128.
16. Kudal, G. B., Chopade, M. R. (2016). Heat Transfer characteristics of ventilated disc brake rotor with diamond pillars – a review. *International Journal of Current Engineering and Technology*, Vol. 4, pp. 219–222.
17. Khivsara, S., Bapat, R., Lele, N., Choudhari, A., Chopade, M. (2015). Thermal analysis and optimisation of a ventilated disk brake rotor using cfd techniques. *International Journal of Emerging Technology and Advanced Engineering*, Vol. 5(7), pp. 59–64.
18. Dahm, K. L., Black, A. J., Shrestha, S., Dearnley, P. A. (2009). Plasma Electrolytic Oxidation treatment of aluminium alloys for lightweight disc brake rotors. *IMechE Conference on Braking*, pp. 53–60.
19. Baskara, S. P., Muthuvel, A., Prakash, N., Stanly, W. L., (2015). Numerical analysis of a rotor disc for optimization of the disc materials. *Journal of Mechanical Engineering and Automation*, Vol. 5(3B), pp. 5–14.
20. Choi, B. K., Park, J. H., Kim, M. R. (2008). Simulation of the braking condition of vehicle for evaluating thermal performance of disc brake. *Proceedings of KSAE Autumn Conference*, pp. 1265–1274.
21. Belhocine, A., Cho, C.-D., Nouby, M., Yi, Y. B., Abu Bakar, A. R. (2014). Thermal analysis of both ventilated and full disc brake rotors with frictional heat generation. *Applied and Computational Mechanics*, Vol. 8, pp. 5–24.
22. Lee, S., Yeo, T. (2000). Temperature and coning analysis of brake rotor using an axisymmetric finite element technique. *Proc. 4th Korea-Russia Int. Symp. on Science and Technology*, Vol. 3, pp. 17–22.
23. Gao, C. H., Lin, X. Z. (2002). Transient temperature field analysis of a brake in a non-axisymmetric three dimensional model. *Journal of Materials Processing Technology*, Vol. 129, pp. 513–517.
24. Altuzarra, O., Amezua, E., Aviles, R., Hernandez, A., (2002). Judder vibration in disc brakes excited by thermoelastic instability. *Engineering Computations*, Vol. 19(4), pp. 411–430.
25. Jang, Y. H., Ahn, S. H, (2007). Frictionally-excited thermoelastic instability in functionally graded material. *Wear*, Vol. 262, pp. 1102–1112.
26. Yamabe J., Takagi, M., Matsui, T., Kimura, T., Sasaki, M. (2002). Development of disc rotor for trucks with high thermal fatigue strength. *Japan SAE Paper*, 4017.
27. Patel, P., Mohite, M. A. (2017). Design optimization of passenger car front brake disc for improvement in thermal behavior, weight & Cost. *International Journal of Engineering Development and Research*, Vol. 5(2), pp. 1079–1086.

УДК 629.017

Вплив схеми гальмування на ефективність гальмівної системи автомобіля

Товоджу О. А.

Університет Аделеке, P.M.B. 250, шлях Еде-Осогбо, м. Еде, штат Осун, Нігерія

Анотація. Важливість гальмівних систем в автомобілях не може бути переоцінена. Гальма використовуються для регулювання швидкості транспортних засобів і працюють за рахунок перетворення кінетичної енергії у теплову. Краща зупиняюча дія системи дискових гальм порівняно з барабанними гальмами призвела до їх широкого застосування у високоякісних транспортних засобах. Зниження гальмівної здатності, викликане тепловим перенавантаженням системи, накладає обмеження на допустиму температуру, за якої може ефективно функціонувати гальмівна система. Тому актуальною є проблема уникнення цього негативного ефекту. Однак, навіть при достатньо гарній конструкції, часте гальмування на високих швидкостях може призвести до появи високих температур. Таким чином, ця стаття спрямована на виконання числового дослідження впливу обраних схем гальмування на зростання температури у системі, що може призвести до зниження її ефективності. Дослідження проводяться для автомобіля масою 2 200 кг, що зупиняється за 5 с, починаючи з граничної швидкості 140 км/год і завершуючи 15 км/год. Найбільша температура, досягнута системою при гальмуванні, відрізняється для різних схем гальмування. При цьому як найкращу схему обрано модель «1 с – 1 с – 3 с» з граничним значенням температури 327 °С.

Ключові слова: автомобіль, гальмівна здатність, дискові гальма, розподіл температури.

JOURNAL OF ENGINEERING SCIENCES
ЖУРНАЛ ІНЖЕНЕРНИХ НАУК
ЖУРНАЛ ИНЖЕНЕРНЫХ НАУК
Web site: http://jes.sumdu.edu.ua
DOI: 10.21272/jes.2019.6(2).e3 Volume 6, Issue 2 (2019)

Data Measuring System for Torque Measurement on Running Shafts Based on a Non-Contact Torsional Dynamometer

Vanyeyev S. M.[1*], Miroshnichenko D. V.[1], Rodymchenko T. S.[1], Protsenko M.[2], Smolenko D. V.[1]

[1] Sumy State University, 2 Rymskogo-Korsakova St., 40007 Sumy, Ukraine;
[2] Academy of Management and Administration in Opole, 18 M. Niedzialkowskiego St., 46020 Opole, Poland

Article info:
Paper received: April 16, 2019
The final version of the paper received: August 17, 2019
Paper accepted online: August 22, 2019

***Corresponding Author's Address:**
s.vaneev@kttf.sumdu.edu.ua

Abstract. The need for power measurement transmitted by the running shaft has led to the need for using devices for measuring torque on the shaft. Of particular importance is the power measurement on high-speed machines, wherein some cases conventional measurement systems are either unsuitable or have low accuracy. Currently, data measuring systems are widely used in the researches of turbomachines. They allow to receive, process, transmit, store and display measurement data. Their application is relevant in relation to the priority of experimental study and subsequent modeling of characteristics and performance factors of expansion machines. The purpose of this research is a design and generation of the data measuring system for measuring torque on the running shaft of vortex expansion machines using a non-contact torsional dynamometer (strain-gauge clutch). The research has considered the results of the development of data measuring system, performed a theoretical analysis and presented the results of the practical application of the non-contact strain-gauge dynamometer designed for torque measurement on the shaft of low-power expansion machines when operating under bench test conditions. Has dealt with the problems of development, calibration.

Keywords: data measuring system, torque, coupling, resistive-strain sensor, vortex expansion machine.

1 Introduction

The necessity of power measuring transmitted by the running shaft has led to the need for usage of devices to measure the torque on the shaft. An increase of the accuracy of measuring the effective power on the shaft allows to more accurately determine the efficiency of plants, improves the quality of the experiment and thereby allows to detect an effect of unobtrusive factors on the efficiency of power plants. Of particular importance is the measurement of power in high-speed installations, where in some cases conventional measurement systems are either unsuitable or have low accuracy.

Devices designed to measure the torque can be divided into four classes according to the principle of operation: cradle dynamometers, torsional indicators, transmission dynamometers and transducers for measuring by extrinsic parameters [1–22]. Torsion dynamometers are usually inertialess instruments and perform only the measuring function, enabling to record both the time averages and ever-varying values of the engine torque during its operation in any modes [1–18].

Currently, electronic torque measuring devices that exist on the market have a number of significant drawbacks:

– the need to complicate the design of test benches or the inability of their use for existing structures of installations;

– detector designs contain stator elements (Figures 1, 2);

– large dimensions of the measurement system (Figures 1, 2);

– the inconvenience of visual control and representation of information;

– high cost.

Therefore, the development of data measuring system (DMS) for torque measurement is a pressing challenge. The data measuring system is a collection of functionally integrated measuring, computing and other supporting technologies for obtaining measuring data, its transformation, processing to perform in the required form.

Figure 1 – Torque detector TRC-10K

In the paper, a review is given of the results of developing the data measuring system for measuring torque on the running shaft of a vortex expansion machine using a non-contact torsional dynamometer by a wireless wi-fi connection and information processing on a computer.

2 Literature Review

Torsional dynamometers are divided into strain-gauge [3, 5–7, 10–12] and torque [4, 8, 9, 13–18]. Work process of the torsional torque dynamometer, in contrast to the torsional strain-gauge dynamometer, is based on direct or indirect measurement of a twisting angle of the torsional shaft. This angle, according to Hooke's law, is proportional to the transmitted torque.

Torsional torque dynamometers were invented much earlier than strain-gauges. They are significantly inferior to the latter in size and accuracy but are in a simple design. Torsional torque dynamometers are divided into two groups: contact and non-contact [1]. The latter has lower chatter susceptibility and greater stability of indications, as well as less demanding of maintenance. By the principle of measuring the magnitude of the twisting angle, non-contact torsional dynamometers are divided into temporary, phasic, Vernier, differential and photoelectric. In the operation [2] at the bench (Figures 2 a, b), the torque on the shaft of the vortex expansion machine 1 was measured using a non-contact torsional torque dynamometer 2, operating on a temporary basis. The load on the shaft was made by the air brake 3 (drag compressor).

Torque dynamometer (Figure 2 c) is a torsion shaft 1 of round cross-section, which is fastened at one end in the transmission shaft 2 and the output shaft 3. Disks 4 are fastened on the shafts 2 and 3 where marks are made. Shafts 2 and 3 are set up on bearings in the body structure 6, in which inductive sensors 7 are set up directly above the disks. The time interval between signals from inductive sensors is measured by a frequency meter FM3-33. This time interval is proportional to the twisting angle of the torsion shaft ψ and to the shaft torque accordingly.

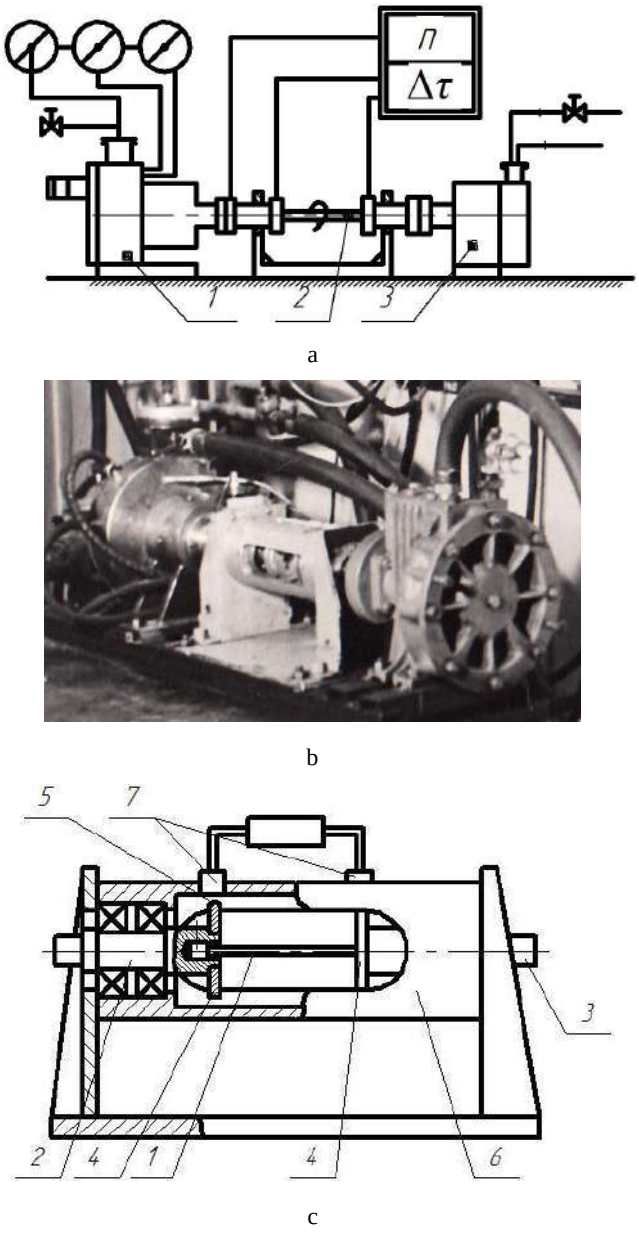

a

b

c

Figure 2 – Test facility for researches of vortex turbomachines with a mean of measuring the torque on the shaft (non-contact torsional torque dynamometer): a – test facility scheme; b – photo of the test facility; c – torque measurement device

Due to the abovementioned, the purpose of the research is a generation of the data measuring system for measuring torque on the running shaft of a vortex expansion machine using a non-contact torsional dynamometer. To achieve this purpose, the following objectives have been formulated:

– generation and calibration of a strain-gauge clutch for torque measurement;

– building software for the transformation of measuring data with the purpose of providing in the required form.

3 Research Methodology

The torque on the shaft was calculated as a function of the twisting angle of the torsion shaft, N·m:

$$M = K_M \cdot (\psi - \psi'); \quad (1)$$

where K_M – dimensionless calibration notice of dynamometer; ψ – the central angle between marks on torsion meter discs under load (deg):

$$\psi = \omega \cdot \tau \cdot 10^{-3} = 6 \cdot n \cdot \tau \cdot 10^{-3}, \quad (2)$$

where $\omega = 6 \cdot n$, deg/s – rotational speed; n – revolution rate (rpm); τ – the time interval between sensor signals when operating under load (ms); ψ' – the central angle between marks on torsion meter discs at idle (no torque load) (deg):

$$\psi' = \omega \cdot \tau' \cdot 10^{-3} = 6 \cdot n \cdot \tau' \cdot 10^{-3}, \quad (3)$$

where τ' – the time interval between sensor signals during idle operation (ms).

By torque-transmitting, the torsion shaft undergoes elastic strain and the angle ψ changes its value. The considered construction design allows one to measure conditionally instantaneous (in one revolution of the crankshaft) torque values.

But this construction design has drawbacks such as:

- sensor designs contain stator components, which leads to complication of the bench design Figure 2;
- large dimensions and complex design of the measurement system Figure 2;
- power loss in bearing frictions should be considered.

Up to date, strain-gauge instruments, the principle on which they operate is based on the dependence between the conductor stretching and its electrical resistance, are developing intensively. Due to the ever-decreasing size and progressive stability of the electronics, it is possible to design sensors with enhanced accuracy and better dynamic performance. Modern strain-gauge instruments are compact, have the highest accuracy relating to other types of dynamometers designed for torque measurement, and can also be placed directly on a running shaft, without requiring the installation of additional means between the engine and the load.

Measurement using resistive-strain sensor is based on the change in its resistance under external actions. In mechanics, the resistance of the resistive-strain sensors is changed due to its deformation, which results under the operating force.

It is known that during torsion, individual shaft elements undergo pure shear deformation and the main strain runs on the platform inclined at an angle of 45° to the shaft axis. Therefore, the resistive-strain sensors are located at the intersection of the main area with the shaft surface, i. e., along a helical curve forming an angle of 45° with the shaft axis.

Using modern advances in the field of strain-gauge instruments and means of transmission facilities it is proposed for measuring the torque on the shaft of the expansion turbomachine, to create data measuring system, which includes a strain-gauge clutch, replacing two clutches and a torque measurement device on the bench shown in Figure 2 (see Figure 3).

Figure 3 – Turbogenerator based on a vortex expansion machine with a strain-gauge coupling

4 Results

To determine and record the torque value, a device (strain-gauge coupling) has been developed, which consists of a torque pin and placed in it resistive-strain gages, boost, wi_fi transmitter and battery. To register fast-changing processes, processing of measured data, upkeeping safe storage of the received information, providing measurement results in a tabular and graphical form, software in C# programming language for the Windows operating system was created (Fig. 4) The use of own software allows to configure the visualization and data storage in a convenient form for the researcher and allows to easily integrate this coupling in the data measurement system of the bench.

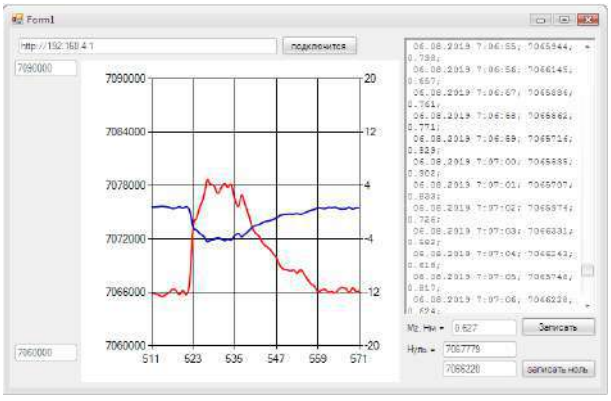

Figure 4 – Software interface

Based on the above-mentioned technical means, a data measurement system for torque measurement has been created, block diagram/structural chart of which is shown in Figure 5.

Strain-gauge clutch for torque measurement is shown in Figure 6.

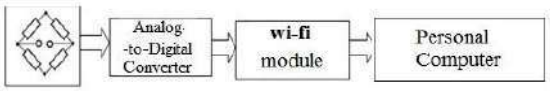

Figure 5 – Block diagram of the data measuring system for torque measurement.

Figure 6 – Strain-gauge clutch for torque measurement

It is known that during torque measuring an output signal (voltage) from strain gauges, connected by complete bridge connection is an analog with a low value (within a few mV). For this reason, to register this signal with electronic devices a boost is required (Fig.5) which increases the measured voltage in the possible registered range of the receiving device. To amplify the signal and transform the analog signal to digital, an HX711 ADC (analog-to-digital converter) strain booster is used. ESP8266 ESP-01 wi-fi module is used as a wireless signal transmission from the bridge of the resistive-strain sensor. Digital signal from the HX711 ADC is transmitted to the transmitter thereafter it is transmitted to the environment to the receiving apparatus (phone or PC). This scheme compared to the frequently used [3–6, 10] provides a number of advantages: usability, affordability at a good transmission quality, ease of use, no need for receiving apparatus production since modern PCs allow to receive wi-fi signal.

The received signal is processing, recording and visualizing by the generated software. The power supply of the circuitry is provided by a 18650 Li-Ion lithium battery.

Mass-dimensional characteristics of the coupling are practically the same as those of standard couplings for torque transmission. Installation of electronic components on the axis of rotation inside the coupling allows avoiding the occurrence of significant centrifugal loads on the scheme elements when operating at high speeds of the turbomachine rotor.

The torsion shaft of the coupling has a bearing length of 100 mm, an internal diameter of 32 mm or 40 mm (Figure 6). The wall thickness is selected considering the range of torque variation and ranges from 0.5 mm to 5.0 mm. Measuring a range of the dynamometer: M = –100–100 N·m, n = 100–10000 rpm; allowable load limit 200 N·m.

Calibration of the created strain-gauge coupling was performed. Calibration allows not only to establish a connection between the indicator of the recording system and the value of the measurand but also to check the system operation in the range of variation of the input magnitude.

Calibration researches were done at room temperature (from 0 to 25 °C) as follows: known beforehand values of the measurand, for example, torque on the shaft is fed to the input of the measuring system, and at the output record the system indicators on these impacts. The torque on the shaft is created by the application of a load of known weight on a measuring beam with a length of 1 m, fixedly connected to the shaft (Figure 7). Measurement error ±0.25 N·m.

As a result, the dependence between the torque and instrument readings (calibration curve) was obtained, as well as the equation of this dependence. Torque changing which recorded the device during the calibration process is shown in Figures 8 and 9 is a calibration curve.

Figure 7 – Calibration of the instrument for torque measurement

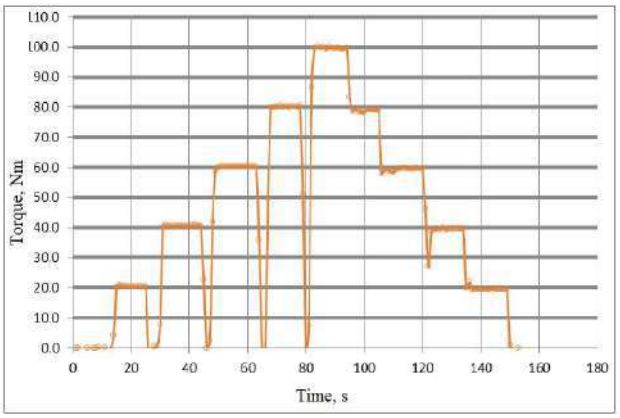

Figure 8 – Torque changing during the calibration process

The dependence of instrument readings on torque is determined by the following equation:

$$M = a \cdot p + b \quad (4)$$

where p – instrument readings; a, b – factors that are determined during calibration for each coupling design Figure 6.

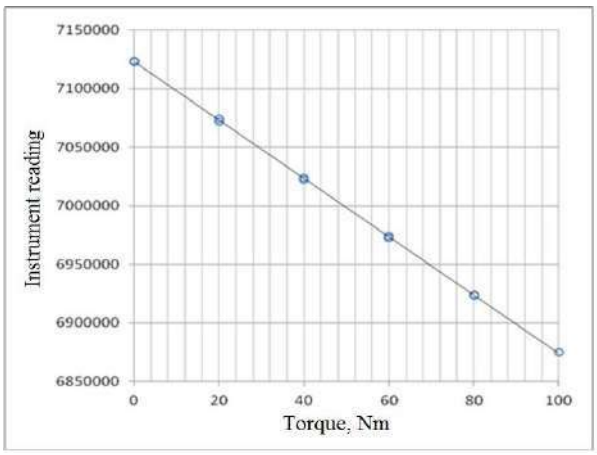

Figure 9 – Calibrated curve

The device was tested in dynamics at the testing facility of low-power turbomachines of the department of Technical Thermal physics of Sumy State University as a part of turbine-generators based on jet-propelled expansion machine (Figure 10) and vortex expansion machine (Figure 3). During the dynamic check, the instrument measured the torque at a variable frequency of rotor spinning from 500 to 10000 rpm.

Fig. 10 – Instrument's dynamic checks for torque measurement

The table shows the main technical characteristics of the developed strain-gauge coupling and TRC-10K clutch (Figure 1).

Table 1 – The main technical characteristics of the strain-gauge coupling

Technical characteristics	Strain-gauge coupling 100	TRC-10K
Torque range, N·m	–100–100	–100–100
Measurement error (including nonlinearities), N·m	±0.25	–
Transmission of an output signal	wi-fi	cable
Permissible maximum rotation frequency of the shaft, rpm	10 000	10 000
Temperature conditions (calibrated), °C	0–30	0–30
Dimensions (L×D), mm	100×90	240×115
Weight, kg	1.0	8.0

On Figures 11 and 12, torque changing, which registered the device during the checks of the vortex expansion machine of Figure 3 at a speed of 2500–3000 rpm is shown.

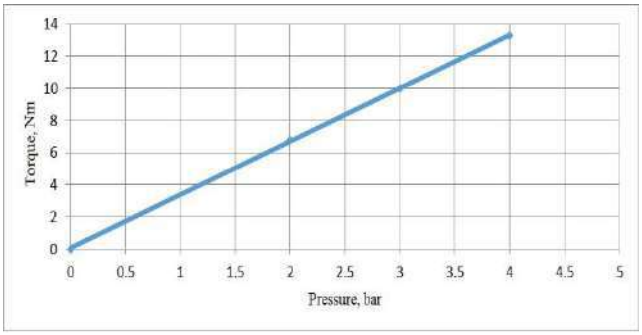

Figure 11 – The dependence of the torque on the shaft of the vortex expansion machine (Figure 3) on the overpressure at the input

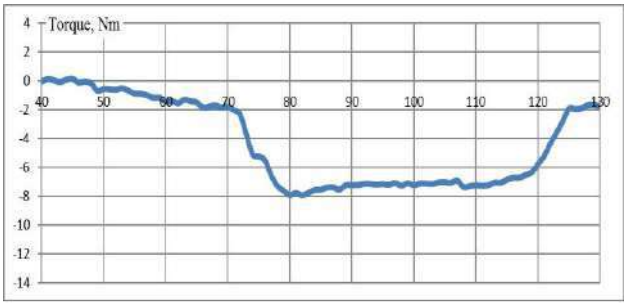

a

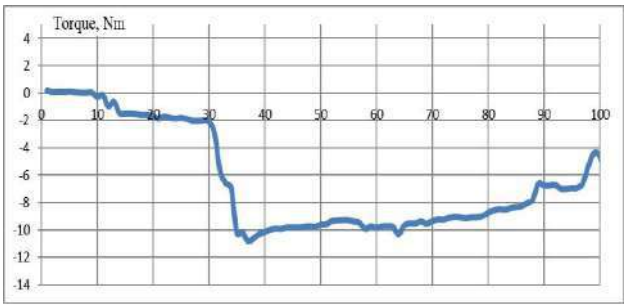

b

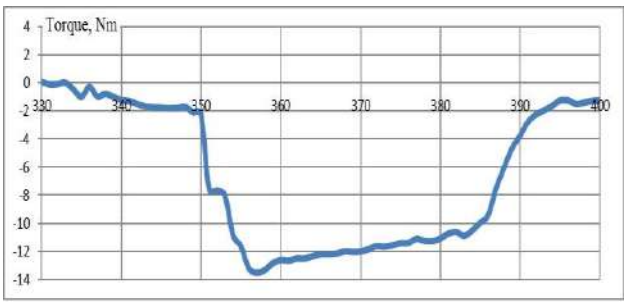

c

Figure 12 – Torque changing during operation of the vortex expansion machine on the bench (Figure 3) with input pressure 2 bar (a), 3 bar (b), and 4 bar (c)

5 Conclusions

A strain gauge coupling was developed to measure the torque on the shaft of the expansion machine, that made it possible to determine the machine shaft power and its efficiency. Mass-dimensional characteristics of the coupling are practically the same as those of standard couplings for torque transmission. The developed clutch can operate at high rotational frequencies of the rotor of the turbomachine. The coupling meets the requirements for measurement error, measurement range and, if possible, for working with other sensors during testing.

Own software that configures the visualization and data storage in a convenient form for the researcher and allows to easily integrate this coupling in the data measurement system of the bench was generated.

Based on the strain-gauge coupling and software, data measuring system has been created, which, in comparison with known ones, has a compact and easy-to-work design with a minimum number of elements. Developed data measuring system allows measuring the torque on the running shafts in a non-contact way without requiring complication of bench design with the required accuracy.

Findings of experimental researches confirm the reliability of the developed data measuring system under static and dynamic load.

References

1. Froliv, L. B. (1967). *Torque Measurement*. Energy, Moscow.
2. Vaneev, S. M. (1986). *Development and Research of a Vortex Pneumatic Drive with an External Peripheral Channel and Nozzle Apparatus*. Ph.D. thesis, Moscow.
3. Sopin, V. A., Nadvotskaya, V. V., Yushkova, V. B. (2016). Development of Information-Measurement System for Measurement of Torque. *Almanac of Altai State Technical University named after I. I. Polzunov*, No. 2, pp. 235–237.
4. Gorozhankin, S. A., Babanin, A. Ya., Savenkov, N. V., Ponyakin, V. V. (2018). Piston Ice Torque Measurement Wheel Machine While its Operation at Unstable Mode by Torsion Torque Dynamometer. *Bulletin of Donbas National Academy of Civil Engineering and Architecture*, pp. 138–147.
5. Ngia, L. V., Le, N. F., Hoan, N. C. (2018). Experienced sample of contactless torque sensor moments on rotating shaft. *Mechanics of Machines, Mechanisms and Materials*, Vol. 3(44), pp. 59–66.
6. Gaponov, V. L., Gurinov, A. S., Dudnik, V. V. (2012). Change in torque on rotating shafts. *Bulletin of Don State Technical University*, Vol. 2, No. 1(62), pp. 25–32.
7. Muftah, M. H., Haris, S. M., Petroczki, K., Khidir, E. A. (2013). An improved strain gauge-based dynamic torque measurement method. *International Journal of Circuits, Systems and Signal Processing*, Vol. 7(1), pp. 66–73.
8. Jiang, K., Zhou, Y., Han, L., Liu, Y., Hu, S. (2019). design of a high-resolution instantaneous torque sensor based on the double-eccentric modulation principle. *IEEE Sensors Journal*, Vol. 19(16), art. no. 8691751, pp. 6595–6601, doi: 10.1109/JSEN.2019.2911392.
9. Turner, J. D. (1988). Development of a rotating-shaft torque sensor for automotive applications. *IEE Proceedings D: Control Theory and Applications*, Vol. 135(5), pp. 334–338, doi: 10.1049/ip-d.1988.0050.
10. Nurprasetio, I. P., Aziz, M., Budiman, B. A., Afwan, A. A. (2018). Development of Static and dynamic online measurement system for ground vehicles. *Proceeding of the 5th International Conference on Electric Vehicular Technology, ICEVT 2018*, art. no. 8628346, pp. 31–35, doi: 10.1109/ICEVT.2018.8628346.
11. Weidinger, P., Foyer, G., Kock, S., Gnauert, J., Kumme, R. (2019). Calibration of torque measurement under constant rotation in a wind turbine test bench. *Journal of Sensors and Sensor Systems*, Vol. 8(1), pp. 149–159, doi: 10.5194/jsss-8-149-2019.
12. Popelka, J., Scholz, C. (2018). Measuring the torque of a combustion engine. MATEC Web of Conferences, Vol. 220, art. no. 03006, doi: 10.1051/matecconf/201822003006.
13. Dmitriev, S., Daryenkov, A. German, L. Gordeev, B., Okhulkov, S., Serebryakov, A. (2018). Torque sensors calibration of electromechanical complexes shafts. *Vibroengineering Procedia*, Vol. 21, pp. 190–195, doi: 10.21595/vp.2018.20355.
14. Zappala, D., Bezziccheri, M., Crabtree, C. J., Paone, N. (2018). Non-intrusive torque measurement for rotating shafts using optical sensing of zebra-tapes. *Measurement Science and Technology*, Vol. 29(6), art. no. 065207, doi: 10.1088/1361-6501/aab74a.
15. Feliks, S., Sergiy, Y., Kostyantyn, P., Sergiy, N. (2018). New approach to torque measurement unit development and its calibration. *journal of KONBIN*, Vol. 46(1), pp. 75–86. doi: 10.2478/jok-2018-0024.
16. Borges, J. C. S., De Deus, D. B. B., Filho, A. C. L., Belo, F. A. (2017). New contactless torque sensor based on the Hall effect. *IEEE Sensors Journal*, Vol. 17(16), art. no. 7967801, pp. 5060–5067.
17. Xiaoxia, J., Huibin, C., Zikai, C., Songxin, L. (2017). The research on torque measurement system based on surface acoustic wave sensor. *Proceedings of the 2017 IEEE International Conference on Information, Communication and Engineering: Information and Innovation for Modern Technology, ICICE 2017*, art. no. 8479286, pp. 400–403.
18. Li, T., Shi, C., Tan, Y., Zhou, Z. (2017). Fiber Bragg grating sensing-based online torque detection on coupled bending and torsional vibration of rotating shaft. *IEEE Sensors Journal*, Vol. 17(7), art. no. 7856991, pp. 1199–2007.
19. Sequeira, M., Alahakoon, S. (2019). Energy efficient variable speed drives empowered with torque estimation. *Energy Procedia*, Vol. 160, pp. 194–201, doi: 10.1016/j.egypro.2019.02.136.

20. Liska, J., Jakl, J., Kunkel, S. (2018). Measurement and evaluation of shaft torsional vibrations using shaft instantaneous angular velocity. *Proceedings of the ASME Turbo Expo*, doi: 10.1115/GT2018-76406.
21. Silva, D., Mendes, J. C., Pereira, A. B., Gegot, F., Alves, L. N. (2017). Measuring torque and temperature in a rotating shaft using commercial saw sensors. *Sensors*, Vol. 17(7), art. no. 1547, doi: 10.3390/s17071547.
22. Mukherjee, A., Lukaschuk, S., Burnishev, Y., Falkovich, G., Steinberg, V. (2018). Precise measurements of torque in von Karman swirling flow driven by a bladed disk. *Journal of Turbulence*, Vol. 19(8), pp. 647–663.

УДК 621

Інформаційно-вимірювальна система для вимірювання обертального моменту на валах, що обертаються, на основі безконтактного торсіонного динамометра

Ванєєв С. М.[1], Мірошниченко Д. В.[1], Родимченко Т. С.[1],
Проценко М.[2], Смоленко Д. В.[1]

[1] Сумський державний університет, вул. Римського-Корсакова, 2, 40007, м. Суми, Україна;
[2] Академія управління та адміністрування м. Ополє, вул. М. Нєдзяловського, 18, 46020, м. Ополє, Польща

Анотація. Необхідність вимірювання потужності, переданої валом, що обертається, призвела до важливості застосовування пристроїв для вимірювання обертального моменту на валу. При цьому, особливого значення набуває вимірювання потужності на високошвидкісних установках, де у більшості випадків традиційні системи вимірювання або непридатні, або мають недостатню точність. У даний час при дослідженнях турбомашин широко розповсюджені інформаційно-вимірювальні системи. Вони дозволяють отримувати, обробляти, передавати, запам'ятовувати і відображати вимірювальну інформацію. Їх застосування актуальне у зв'язку із пріоритетністю експериментального вивчення і подальшого моделювання характеристик та показників ефективності розширювальних машин. Метою даної роботи є розроблення і створення інформаційно-вимірювальної системи для вимірювання обертального моменту на валу розширювальних машин, що обертається з великою швидкістю, за допомогою безконтактного торсіонного динамометра (тензометричної муфти). У роботі наведені результати розроблення інформаційно-вимірювальної системи, виконаний теоретичний аналіз і результати практичного застосування безконтактного тензометричного динамометра, призначеного для вимірювання обертального моменту на валу розширювальних машин малої потужності за умов стендових випробувань. Додатково розглянуто питання проектування, тарування і застосування спроектованого динамометра.

Ключові слова: інформаційно-вимірювальна система, обертальний момент, динамометр, тензорезистор, вихрова розширювальна машина.

JOURNAL OF ENGINEERING SCIENCES
ЖУРНАЛ ІНЖЕНЕРНИХ НАУК
ЖУРНАЛ ИНЖЕНЕРНЫХ НАУК
Web site: http://jes.sumdu.edu.ua
DOI: 10.21272/jes.2019.6(2).e4 Volume 6, Issue 2 (2019)

Computer Engineering and Design of Cast Parts for Internal Combustion Engine Crankcase

Akimov O. V.[1], Marchenko A. P.[1], Alyokhin V. I.[1], Soloshenko V.[2], Shinsky O. Y.[3], Klymenko S. I.[3], Kostyk K. O.[1*]

[1] National Technical University "Kharkiv Polytechnic Institute", 2 Kyrpychova St., 61002 Kharkiv, Ukraine;
[2] "General Electric" Ltd, 110/114 Krakowska Al., 02-256 Warsaw, Poland;
[3] Physico-Technological Institute of Metals and Alloys of the National Academy of Sciences of Ukraine, 34/1 Vernadskogo Blvd., 03142 Kyiv, Ukraine

Article info:
Paper received: September 14, 2019
The final version of the paper received: November 30, 2019
Paper accepted online: December 5, 2019

[*]**Corresponding Author's Address:**
eklitus@gmail.com

Abstract. This paper discusses the formulation of the problem of designing the cast parts block-crankcases engine in order to ensure its quality for the case study of cast iron parts of the cylinder block inline four-cylinder gasoline engine with the capacity of 1.4 dm3. Material Ch190B is gray cast iron with optional chemical composition, and sulfur – no more than 0.15 %, phosphorus – no more than 0.1 %, structure – perlite plate. The results obtained in this work confirm the conclusions about the possibility of reducing the metal content of the casting and changing the technical conditions of its manufacture. According to the results of the research, the developed recommendations are aimed at stabilizing the characteristics of the metal, reducing metal consumption, and changing the technical conditions for the defectiveness of this type of castings. Recommendations for changing the configuration of the partition in order to reduce the metal content of the casting and recommendations for changing the Technical Conditions for casting defects were stated for the casting block crankcase 4ChN12/14. For defects of discontinuity type, the maximum size was defined, and controlled places of their detecting were defined.

Keywords: CAD, CAE, block-crankcase, 3D model, casting defect.

1 Introduction

In the ranking of the international organization of automakers "OICA" Ukraine rose one step and from the fourth group got to the third, among the countries that produce more than 400 thousand cars a year. These findings at a press conference said President of the Association of carmakers of Ukraine "Ukravtoprom" Michael Resnick.

Based on the above, Ukrainian automakers are faced with large science-intensive tasks to improve the performance of modern internal combustion engines produced in Ukraine. Improving the performance of modern internal combustion engines is impossible without a deep modernization of their design, whether the engine as a finished product, its components or individual parts. As shows domestic and world experience, perfect can be only a design based on the design which incorporated the technological aspects of the manufacture of parts and engine components, this approach ensures optimal performance of the engine [1].

Design and experimental methods for determining the structural strength, reliability, Assembly, installation loads and service life must necessarily be consistent with those laws that determine the technological processes occurring in the manufacture of parts – phase transition, shrinkage, residual casting stresses, etc. First of all, this applies to the production of cast engine parts (80–90 % of cast parts by weight in the design of the engine). The level of harmonization of design and technological approaches necessarily implies a compromise between design development and the design and implementation of the technological process of their production, is the determining factor in obtaining quality parts, ensuring the achievement of the specified performance, reliability, and resource engine [2–4]. The technological aspects must be taken into account in the design and application of CAD for engines. The practice of domestic engine-building has not yet reached this vital compromise for many enterprises.

2 Literature Review

The current state of the issue of design of engine parts and CAD of technological preparation of production at one of the defining stages of production of engine parts – the manufacture of cast engine parts – does not allow talking about an effective compromise, often in real production, we can talk about deep contradictions [1, 3–5]. The reason for this is the lack of knowledge of many processes occurring during the formation of the casting and ultimately determine the real, not theoretically designed design of the part, as well as the accuracy of the geometric parameters, which is one of the main indicators of the quality of cast parts of the internal combustion engine. The influence of the deviation fields of the cast parts quality indicators on the parametric and functional reliability of the engine parts is not determined. This, in turn, leads to a decrease in the reliability of the engine parts, reduce their performance and service life [6, 7].

The absence of methods for determining the influence of casting design, size fluctuations, casting defects and dispersion of mechanical properties on the state of the elements of the future parts of the ice does not allow to predict the level of technical perfection of cast parts of the ice at the stage of their design [8, 9]. Therefore, it is not possible to increase the operational level and life of cast parts of the ice, to lay their high performance at the design stage without parallel optimization of the process parameters.

3 Research Methodology

This publication presents a series of studies carried out at the departments of Internal Combustion Engines and Foundry NTU "KhPI" and is dedicated to the problem of ensuring the quality of the cast parts of the internal combustion engine of a difficult geometrical configuration according to the criterion of functional and parametric reliability (of body parts) [10–12]. In accordance with this criterion in the design and technological design it is necessary to set and perform the following tasks:

- identification of marriage cast motor parts;
- identification of "bottlenecks" in the part design from the technological point of view;
- simulation of the stress state of cast parts;
- modeling of crystallization processes;
- identification of residual stress formation factors at the stage of cast parts manufacturing.

This paper discusses the formulation of these problems in order to ensure the quality of the first object of study-cast iron parts of the cylinder block inline four-cylinder gasoline engine capacity of 1.4 dm^3 for the car DAEWOO SENS. Customer "AvtoZAZ-Motor" Melitopol (Ukraine), material Ch190B – gray cast iron with optional chemical composition, sulfur – no more than 0.15 %, phosphorus - no more than 0.1 %, structure – perlite plate. Manufacturer LLC "Ukrainian Foundry Company", serial-700 cast parts per month.

4 Results

The material of such cast parts, in addition to the mechanical strength, must have the necessary density of the structure. On the basis of the conditions and requirements of the material in the article was considered such aspects as:

- analysis of the solidification process of cast parts;
- analysis of places of the possible appearance of shrinkage defects.

As the 3D model created by us shows, a feature of the cylinder block design is a combination of thin-walled (body thickness 2–4 mm) and thick-walled (body thickness 10–20 mm) arrays (Figure 1), which adversely affects the cast part quality control on the direction of metal crystallization.

To solve the problems associated with the crystallization of the metal conducted research related to the processes of solidification of the cast parts of the cylinder block. For this task, the system of automated modeling of LVM Flow casting processes was chosen, which, with respect to our problem, has certain advantages over its analogs, which include the simplicity of the problem statement, the adequacy of the simulation results and, with the correct formulation of the problem, the relative speed of calculation of the filling and crystallization processes.

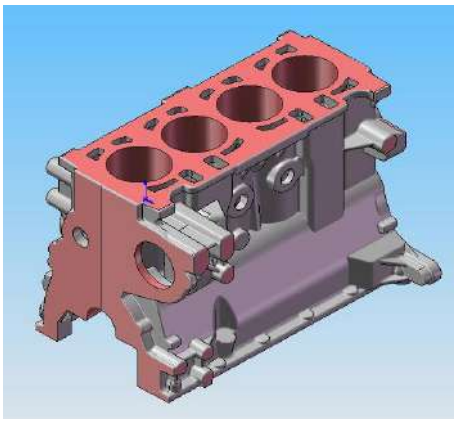

Figure 1 – 3D model of the cylinder block

LVMFlow is a software application package for computer simulation of casting. Computer modeling allows us to trace all the processes occurring in the metal when filling out the form, solidification, the occurrence of shrinkage defects before the industrial manufacture of the products themselves. The model equations are solved by the FDM (finite difference) method on a regular rectangular difference grid.

It is known that the direction of crystallization plays an important role in obtaining high-quality cast parts. The appearance of shrinkage defects in the body casting, which leads to such consequences as the decline of strength characteristics of metal, the appearance, in the process of operation, cracks in the locations of such defects, etc. Uneven curing of the thin-walled and thick-walled arrays in the cylinder block shown in Figure 2.

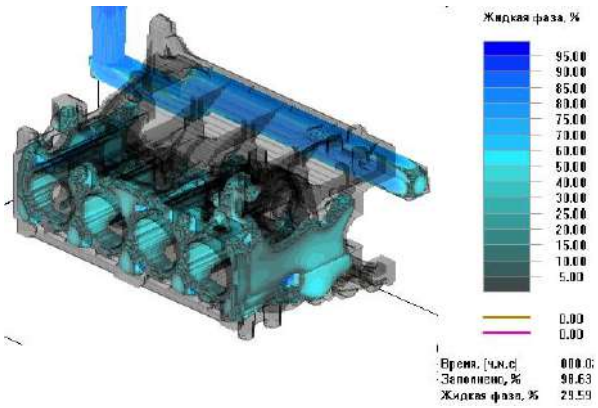

Figure 2 – The nature of solidification of the metal cast part at a liquid phase content of 25 %

According to the results of the simulation performed by the program, the areas of alleged defect formation were identified (in the LVM Flow program, the model of shrinkage defect formation is based on the percolation theory and is determined as a percentage, as shown on the scale), which are presented in (Figure 3).

A qualitative analysis of the solidification of the cast part and the places of possible defects identified by the program allows determining the problematic places in zones A, B, and C (Figure 3).

The following data were used to model the cylinder block-crankcase: cell size 1.996 mm; total number of cells 17.620.200; casting ultrasonic 607.572; separation coating-layer thickness of 0.3 mm and thermal conductivity of 302 W/(m·K); casting material is special cast iron; specified casting temperature 1400 °C; mold material is furan mixture; initial temperature 20 °C.

Based on such initial data, a simulation was carried out, which revealed the places of the possible origin of defects of shrinkage nature.

To eliminate such defects, it was decided to upgrade the existing Gating system (Figure 4 a). As the simulation results (Figure 4 c), the Gating system was not completely filled, leading to reduced efficiency of feeders (used not all of the calculated areas) when filling forms with metal.

Presented in Figure 4 c and Figure 5 e metal flow in the form leads to a decrease in the rate of rising of the metal, resulting in the formation of crusts, usually containing oxides and inclusions. In the future, the crust is pressed against the mold surface with a liquid metal (Figure 4 c), there is a breakthrough with the formation of gas bubbles and non-metallic inclusions. Also, when analyzing the modeling of the pouring process, it can be concluded that in the initial stage, a jet of metal hits the rod, blurs it, leading to blockages and changes in geometric dimensions.

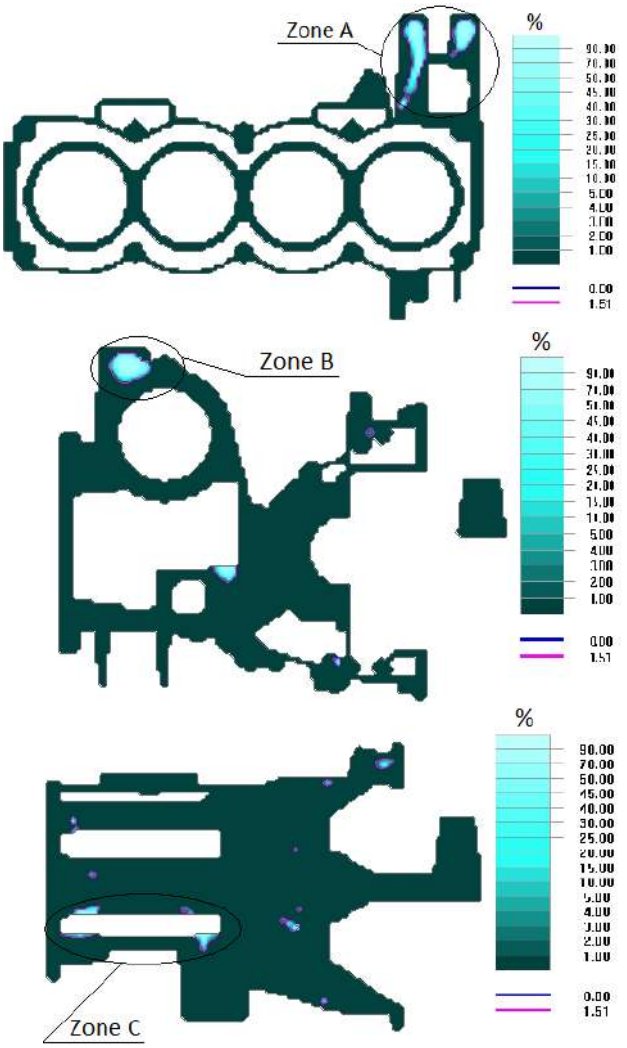

Figure 3 – The area of the possible appearance of defects of shrinkable character

In the streamlined Gating system (Figure 4 b) the feeder was divided. As a result, a more uniform temperature distribution was obtained during the cooling of the metal in the form, thereby reducing the risk of shrinkage shells and shrinkage looseness in the casting. Also, the modernized Gating system began to provide a more uniform filling throughout the cavity of the form, which reduced the probability of splashing, the formation of splashes. A jet of metal does not fall into the end of the rod, thus does not destroy it.

For checking the simulation in the LVM Flow and further research after a minor simplification and smoothing relatively small areas were created by the spatial finite element (FE) model of the casting of the cylinder block in ANSYS Workbench 11SP1, including 911152 nodes and 577648 finite elements of tetrahedral shape (Figure 5).

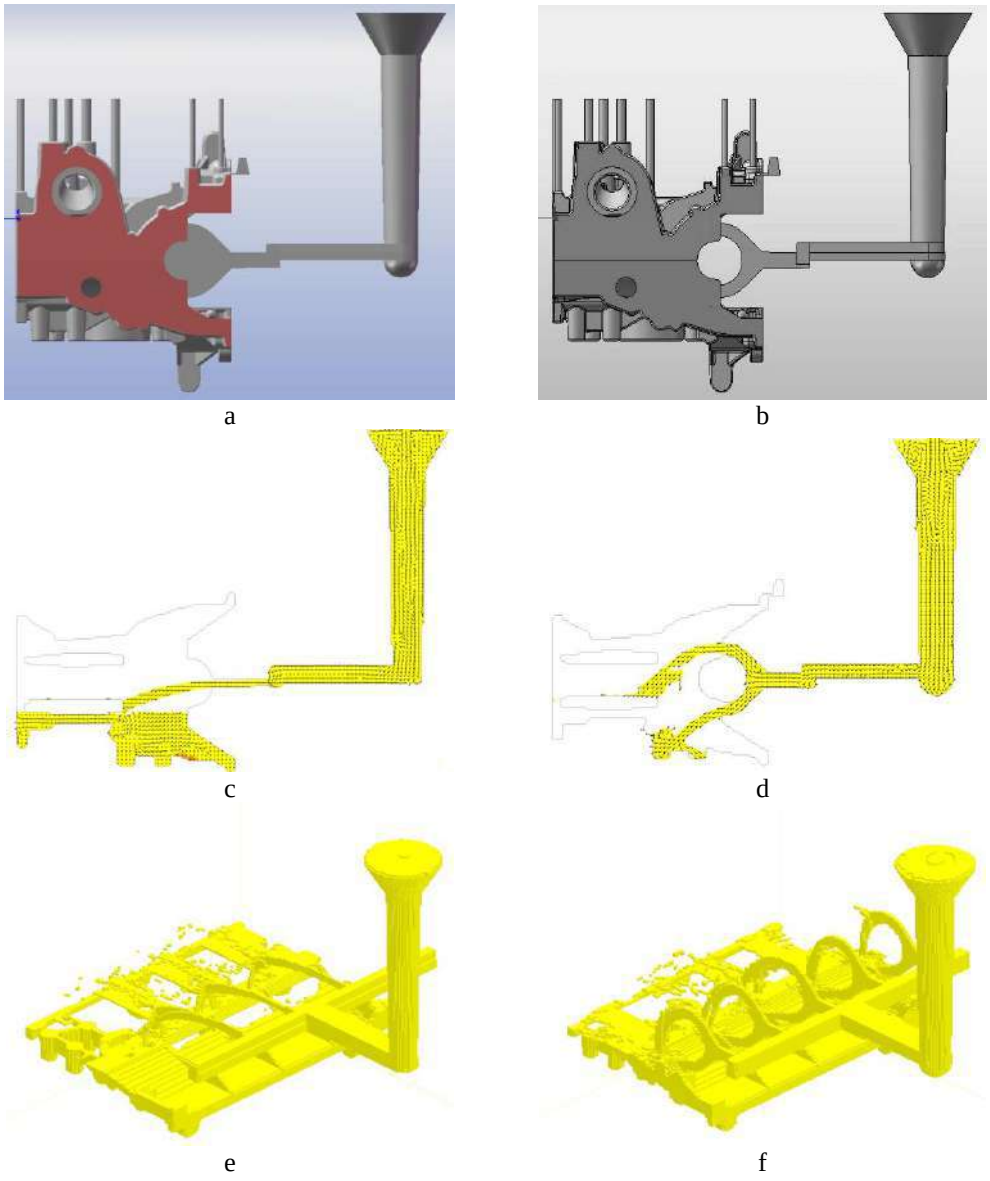

Figure 4 – Examples of gating systems and fill them with metal

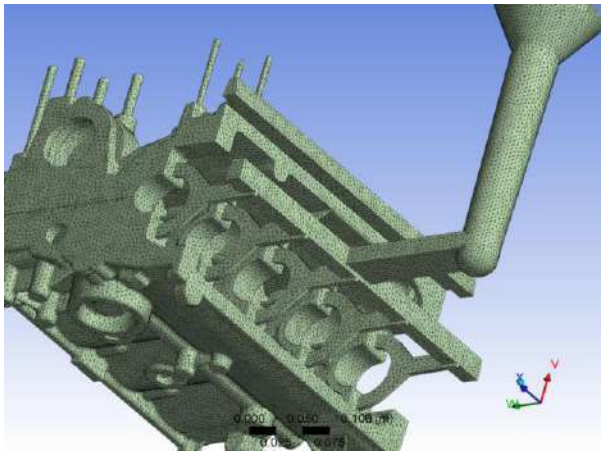

Figure 5 – Finite-element model of the block-crankcase of the internal combustion engine

Thus, the modeling of the pouring process in the LVM Flow program showed that the use of an upgraded Gating system reduced the probability of shrinkage defects, blockages from non-metallic and oxide inclusions, as well as the destruction of the rod by the jet of the poured metal. The use of a streamlined Gating system in the manufacture of the casting block-crankcase of the cylinders of the internal combustion engine will achieve a high quality and performance properties of the finished part.

The analysis of the cooling dynamics, phase transition and the coupling of the zones that solidify the latter allows to identify the places of possible formation of internal shrinkage defects, to form the boundary and initial conditions for the problem of calculating the residual deformations due to temperature equalization throughout the casting part of the cylinder block, and, ultimately, to introduce numerical optimization of the solidification process.

5 Discussion

As the second object of research was selected as a cast-iron casting block-sump inline four-cylinder diesel 4ChN12/14.

The problem of ensuring the quality of cast iron casting block crankcase inline four-cylinder 4ChN12/14 was considered in the following aspects:

- static load analysis of the block-crankcase casting and modeling of the casting load capacity;
- analysis of natural oscillations;
- modeling of phase transition and cooling of block-crankcase casting;
- physical and chemical properties of the melt casting
- dimensional and geometric analysis of castings and stabilization of geometrical parameters;
- some aspects of the use of computer technology to improve the efficiency of foundry production, including the creation of expert systems based on statistical processing of accumulated databases and knowledge of technological defects in castings.

Thus, to estimate the distribution of residual stresses in the block-crankcase casting, a finite element model was used based on $1.3 \cdot 10^6$ tetrahedral finite elements with restrictions on the nodes of the end surfaces, where 2 degrees of freedom from 3 were fixed (Figure 6).

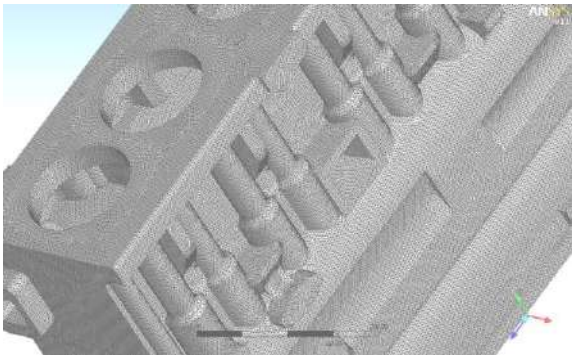

Figure 6 – Finite-element model of the block-crankcase

Figure 7 presents the temperature distribution of the basic casting of the block-crankcase, which occurs after the phase transition of all nodes of the model in the solid-state, C0 and the microstructure of cast iron in the danger zone.

The figure shows that in the central zone of the block crankcase, the most dangerous place for the stress-strain state, graphite is coarse, mechanical properties are low.

In the modernized design, after complete solidification, the microstructure is characterized by a smaller size of graphite inclusions, which is explained by a higher crystallization rate in the thinner wall of the casting. As a result, lower residual stresses and higher mechanical properties (Figure 8.)

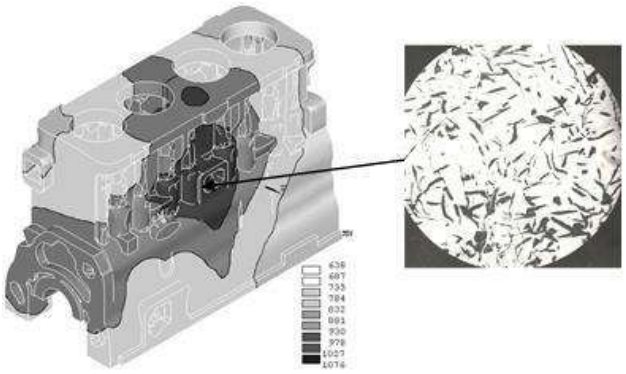

Figure 7 – Temperature distribution on the base casting of the block-crankcase arising after the phase transition of all nodes of the model in the solid-state and the microstructure in the center of the cast part

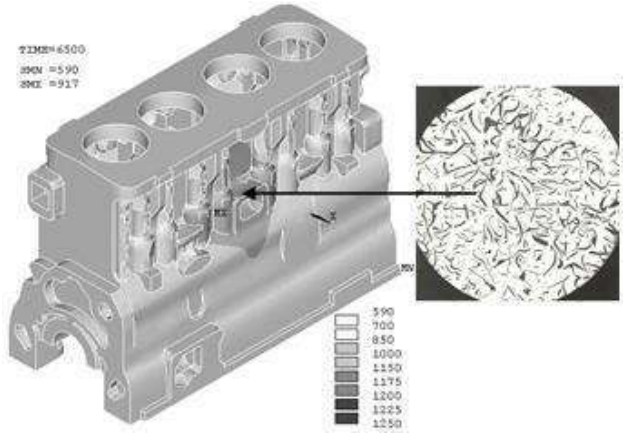

Figure 8 – Temperature distribution in the modernized casting of the block-crankcase arising after the phase transition of all nodes of the model in the solid-state and the microstructure in the central part of the casting

A comparative assessment of the block-crankcase of the basic and manufactured according to the modernized design shows that in the latter case there is no residual stress zone. In the basic design of the zone, the zone of maximum intensity of residual stresses (according to the results of static tests) coincides with the zone of fatigue crack occurrence. On the basis of the analysis of the obtained finite element model of the model to assert that the uneven distribution of stresses and their magnitude in the base casting of the crankcase are a potential source of reducing the functional reliability of the housing during the operation of the engine (Figure 9).

A comparison of the results of dynamic tests on the finite element model confirmed a similar picture (Figure 10). The results are given for the third eigenform of oscillations.

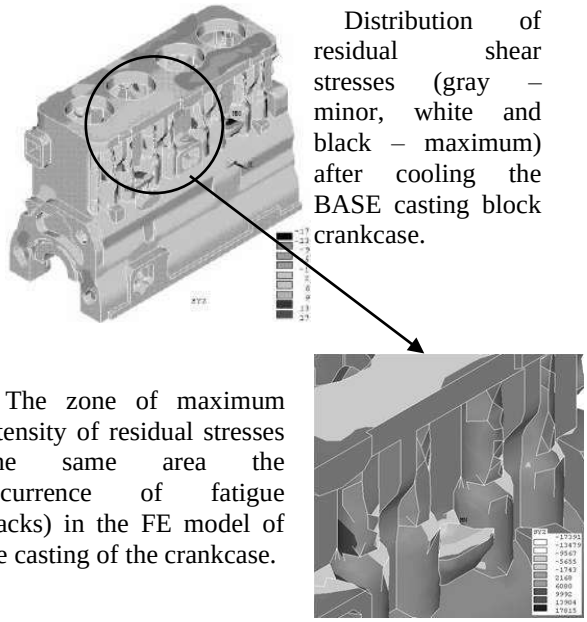

Distribution of residual shear stresses (gray – minor, white and black – maximum) after cooling the BASE casting block crankcase.

The zone of maximum intensity of residual stresses (the same area the occurrence of fatigue cracks) in the FE model of the casting of the crankcase.

6 Conclusions

The results obtained in this work confirmed the conclusions about the possibility of reducing the metal content of the casting, changing the technical conditions of its manufacture. According to the results of the research, recommendations were developed aimed at stabilizing the characteristics of the metal, reducing the metal consumption, and changing the technical conditions for the defectiveness of this type of castings. Recommendations for changing the configuration of the partition in order to reduce the metal content of the casting and recommendations for changing the Technical Conditions for casting defects manifested on the walls and walls of the casting block crankcase 4ChN12/14. For defects of discontinuity type, the maximum size is defined, controlled places of manifestation are redefined.

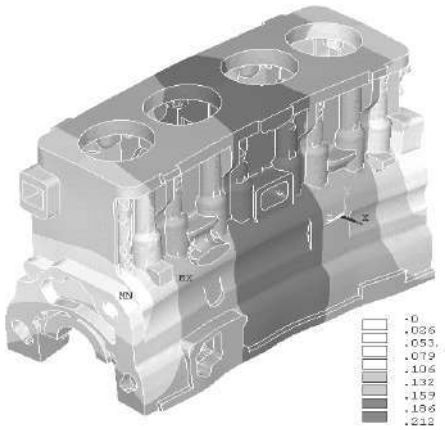

Figure 9 – Distribution of residual shear stresses after cooling of the base casting of the block crankcase

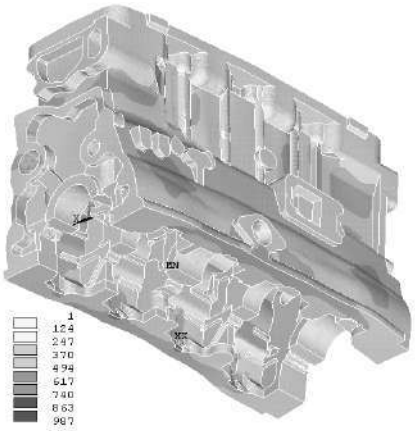

Figure 10 – The results of dynamic testing on FEM for the base of the casting block-crankcase: a – the third own mode shape of the BASE of the block-crankcase 589 Hz; b – the form of intensity of dynamic stresses on the third SF of oscillations of the BASE block crankcase, 589 Hz

7 Acknowledgments

We thank Professor of the Department of aircraft engine design at the National Aerospace University named by N. Ye. Zhukovsky "KhAI", D.Sc., Professor Oleksandr V. Bilohub and Vice-rector of the National Technical University "Kharkiv Polytechnic Institute", D.Sc., Professor Andriy P. Marchenko for theoretical and technical help.

References

1. Becker, E. P. (2004). Trends in tribological materials and engine technology. *Tribology International*, Vol. 37(7), pp. 569–575, doi: 10.1016/j.triboint.2003.12.006.
2. Ye, H. (2003). An overview of the development of Al-Si-alloy based material for engine applications. *Journal of Materials Engineering and Performance*, Vol. 12(3), pp. 288–297, doi: 10.1361/105994903770343132.
3. Carvalho, O., Buciumeanu, M., Madeira, S., Soares, D., Silva, F. S., Miranda, G. (2015). Optimization of AlSi–CNTs functionally graded material composites for engine piston rings. *Materials and Design*, Vol. 80, pp. 163–173, doi: 10.1016/j.matdes.2015.05.018.
4. Shevchenko, Y. N., Savchenko, V. G. (2016). Three-dimensional problems of thermoviscoplasticity: Focus on Ukrainian research. *International Applied Mechanics*, Vol. 52(3), pp. 217–271, doi: 10.1007/s10778-016-0749-3.

5. Harries, S., Abt, C., Brenner, M. (2019). Upfront CAD-Parametric modeling techniques for shape optimization. *Advances in Evolutionary and Deterministic Methods for Design, Optimization and Control in Engineering and Sciences, Springer, Cham*, pp. 191–211, doi: 10.1007/978-3-319-89988-6_12.
6. Seifi, M., Salem, A., Beuth, J., Harrysson, O., Lewandowski, J. J. (2016). Overview of materials qualification needs for metal additive manufacturing. *JOM, Springer*, Vol. 68(3), pp. 747–764, doi: 10.1007/s11837-015-1810-0.
7. Zhang, J. H., Chen, M. (2015). Assessing the impact of China's vehicle emission standards on diesel engine remanufacturing. *Journal of Cleaner Production*, Vol. 107, pp. 177–184, doi: 10.1016/j.jclepro.2015.03.103.
8. Sharma, R. S., Singhal, I., Gupta, S. (2018). Innovative Training Framework for Additive Manufacturing Ecosystem to Accelerate Adoption of Three-Dimensional Printing Technologies. *3D Printing and Additive Manufacturing*, Vol. 5(2), pp. 170–179, doi: 10.1089/3dp.2017.0003.
9. Dhahad, H. A., Alawee, W. H., Marchenko, A., Klets, D., Akimov, O. (2018). Evaluation of Power Indicators of the Automobile Engine. *International Journal of Engineering & Technology*, Vol. 7(4.3), pp. 130–134.
10. Akimov, O., Gusau, I. G., Marchenko, A. P. (2015). An overview of the computer-integrated systems and manufacturing technologies of pistons of internal combustion engines. *Eastern-European Journal of Enterprise Technologies*, Vol. 6, Issue 1(78), pp. 35–42, doi: 10.15587/1729-4061.2015.56318
11. Akimov, O. V. (2004). Modern systems of computer-aided design, engineering analysis and technological preparation of production. *Eastern-European Journal of Enterprise Technologies*, Vol. 6(12), pp. 21–36.
12. Alekhin, V. I., Akimov, O. V., Marchenko, A. P. (2008). Computer-integrated modeling of casting processes in the cylinder block Daewoo Sens. *Bulletin of NTU "KhPI", "Machine Science and CAD"*, Issue. 2, pp. 3–7.

УДК 004.93

Комп'ютерний інжиніринг та проектування литих деталей блок-картерів двигунів внутрішнього згорання

Акімов О. В.[1], Марченко А. П.[1], Альохін В. І.[1], Солошенко В.[2], Шинський О. Й.[3], Клименко С. І.[3], Костик К. О.[1*]

[1] Національний технічний університет «Харківський політехнічний інститут», вул. Кирпичова, 2, 61002, Харків, Україна
[2] ТОВ «Дженерал Електрік», Краківська ал., 110/114, 02-256, м. Варшава, Польща;
[2] Фізико-технологічний інститут металів та сплавів НАН України, бул. Акад. Вернадського, 34/1, 03142, Київ, Україна

Анотація. Відповідно до критерію функціональної і параметричної надійності при конструкторсько-технологічному проектуванні корпусних деталей були поставлені та вирішені наступні задачі: ідентифікація браку литих деталей двигунів внутрішнього згорання; виявлення «вузьких» місць у конструкції деталі з технологічної точки зору; моделювання напружено-деформованого стану литих деталей; моделювання процесів кристалізації; виявлення факторів формування залишкових напружень на етапі виготовлення литих деталей. У цій статті розглядається вирішення вищезазначених питань з метою забезпечення якості першого об'єкта дослідження – чавунної литої деталі блоку циліндрів рядного чотирициліндрового бензинового двигуна об'ємом 1,4 дм^3 для автомобілів DAEWOO SENS. Для вирішення поставленої проблеми, пов'язаної з кристалізацією металу, були проведені дослідження процесів затвердіння литих деталей блоку циліндра. Була обрана система автоматизованого моделювання ливарних процесів LVMFlow. Рівняння моделі розв'язувались методом скінченних різниць (FDM) на регулярній прямокутній різницевій сітці. Отримані у даній роботі результати підтверджуються висновками про можливість зниження металоємності виливки і зміни технічних умов її виготовлення. За результатами проведених досліджень були розроблені рекомендації, спрямовані на стабілізацію характеристик сплаву, зниження металоємності ливарної форми та зміни технічних умов щодо дефектності даного виду виливок. Були надані рекомендації щодо зміни конфігурації перегородки з метою зниження металоємності виливки та рекомендації щодо зміни технічних умов на дефекти виливки, що проявляються на стінках і перетинах ливарного блок-картера 4ЧН12/14. Було встановлено, що для ливарних дефектів типу несуцільності визначається максимальний розмір і перевизначаються контрольовані місця.

Ключові слова: CAD, CAE, блок-картер, тривимірна модель, дефект лиття.

JOURNAL OF ENGINEERING SCIENCES
ЖУРНАЛ ІНЖЕНЕРНИХ НАУК
ЖУРНАЛ ИНЖЕНЕРНЫХ НАУК
Web site: http://jes.sumdu.edu.ua
DOI: 10.21272/jes.2019.6(2).e5 Volume 6, Issue 2 (2019)

Numerical Experiment for the Calculation of Normal Contact Stress in the Deformation Center when Rolling a Metal Strip

Yavtushenko A. V.[1*], Protsenko V. M.[1], Bondarenko Y. V.[1], Kirichenko A. G.[1], Ping F. Y.[2]

[1] Zaporizhzhia National University, 226 Soborny Ave., 69006 Zaporizhzhia, Ukraine;
[2] Fujian Xiangxin Co. Ltd, Fuzhou, Fujian, China

Article info:
Paper received: September 4, 2019
The final version of the paper received: December 1, 2019
Paper accepted online: December 6, 2019

***Corresponding Author's Address:**
znu.kafomt@gmail.com

Abstract. The possibility of application of the program complex called Mathcad Prime 5 for calculation of normal contact stresses in the center of deformation during cold rolling of the strips is considered. The algorithm, the block-scheme and the computer program of calculation of the normal contact stresses during rolling of the strips on the reverse mill 1680 PJSC "Zaporizhstal" are developed. The epures were constructed and a comparative analysis of the formulas used to calculate the normal contact stresses in the deformation center was carried out. Received calculation data in Mathcad Prime 5 coincides with the literary data, which has practical value for both educational process and research and design work. Based on the analysis of the contact stress epures, it can be concluded that the most accurate calculation of the total metal pressure on the rolls during cold rolling is possible only when the formulas used ещ consider the change in the forced yield strength in the deformation center by the law of a straight line or the parabolic law.

Keywords: cold rolling strips, normal contact stress, deformation center, computer program, forced yield strength.

1 Introduction

The theory and practice of cold rolling have a long history of development. With the efforts of many researchers, theoretical and empirical dependencies between the basic parameters have been found that influence the process of cold rolling and are the basis for the design of the created cold rolling mills and mills that are being designed. These dependencies were not designed for the use of computer technology, so they are mostly presented in an explicit way and, in some cases, as nomograms.

The availability of ready-made formulas has its positive aspects, but with the use of computer technology, more opportunities for research and calculation and theoretical work appear. Sometimes the complexity of mathematical expressions does not allow us to solve the equations obtained. This can be avoided by having a computer-based numerical calculation program in place, that is, a numerical experiment method.

2 Literature Review

The aim of the study is the development of an algorithm and computer programs that calculate the normal contact stress in the deformation center during cold rolling of the strips on the reversed mill 1680 PJSC "Zaporizhstal" with the help of the software complex Mathcad Prime 5. Another aim is the comparative analysis of the formulas, which are used to calculate the normal stress in the deformation center.

The application of a modern computer program determines the relevance and practical significance of this article for both the educational process and research and design work.

A considerable number of works [1–10] were devoted to the issue of calculating the normal contact stresses in the deformation center during the rolling of the strips.

The calculation of normal contact stresses during rolling of the thin strips can be performed using the formulas of A. I. Tselikov [4–7]:

for the zone of slippage on the entry side

$$p_x = \frac{K_0}{\delta} \cdot \left[\left(\xi_0 \cdot \delta - 1 \right) \cdot \left(\frac{h_0}{h_x} \right)^{\delta} + 1 \right]; \quad (1)$$

for the zone of slippage on the delivery side

$$p_x = \frac{K_1}{\delta} \cdot \left[\left(\xi_1 \cdot \delta + 1 \right) \cdot \left(\frac{h_x}{h_1} \right)^{\delta} - 1 \right], \quad (2)$$

where p_x – normal contact stress, MPa; h_0 and h_1 – initial and final thickness of the strip, mm; h_x – thickness of the strip in the arbitrary intersection of the deformation center, mm; ξ_0 and ξ_1 – coefficients of the back and front tension.

In these equations the constant coefficients are determined by the formulas:

$$\delta = \frac{2 \cdot f \cdot l_\partial}{\Delta h}; \quad \xi_0 = 1 - \frac{\sigma_0}{K_0}; \quad \xi_1 = 1 - \frac{\sigma_1}{K_1},$$

where σ_0 and σ_1 – front and back tension, MPa; K_0 and K_1 – forced yield strengths before and after rolling in MPa ($K_0 = 1.15 \cdot \sigma_{0.2}^{(0)}$; $K_1 = 1.15 \cdot \sigma_{0.2}^{(1)}$); $\sigma_{0.2}^{(0)}$ and $\sigma_{0.2}^{(1)}$ – conditional yield strengths before and after rolling, MPa; Δh – absolute compression, mm; l_d – length of deformation center, mm; f – coefficient of friction.

The determination of the total metal pressure on the rolls by formulas (1), (2) is the most accurate, which has been confirmed by numerous experiments [4–7]. However, the use of these formulas, taking into account the law of the yield strength change in the deformation center depending on the compression, leads to cumbersome final formulas, which are inconvenient for practical calculations.

Considering $K = p_x$, formulas (1), (2) are simplified to the form [7]:

– for the zone of slippage on the entry side:

$$p_x = \xi_0 \cdot K_0 \cdot \left(\frac{h_0}{h_x}\right)^{\delta - 1}; \tag{3}$$

– for the zone of slippage on the delivery side:

$$p_x = \xi_1 \cdot K_1 \cdot \left(\frac{h_x}{h_1}\right)^{\delta + 1}; \tag{4}$$

The obtained formulas are extremely simple, but they do not sufficiently take into account the change in yield strength during the deformation process.

For more accurate accounting for the change in the forced yield strength in the deformation canter from K_0 to K_1, the following equations are obtained, assuming that the change in the yield strength occurs by the law of a straight line [7]:

– for the zone of slippage on the entry side:

$$p_x = \left[\left(K_0 - \sigma_0\right) + \frac{\left(K_1 - K_0\right) \cdot h_0}{\Delta h \cdot \delta}\right] \cdot \left(\frac{h_x}{h_0}\right)^{1-\delta} - \frac{\left(K_1 - K_0\right) \cdot h_x}{\Delta h \cdot \delta}; \tag{5}$$

– for the zone of slippage on the delivery side:

$$p_x = \left[\left(K_1 - \sigma_1\right) - \frac{\left(K_1 - K_0\right) \cdot h_1}{\Delta h \cdot \delta}\right] \cdot \left(\frac{h_x}{h_1}\right)^{1+\delta} + \frac{\left(K_1 - K_0\right) \cdot h_x}{\Delta h \cdot \delta}; \tag{6}$$

In fact, the change in yield strength in the process of deformation occurs by parabolic law. Taking this into account, the following equations are obtained [7]:

– for the zone of slippage on the entry side:

$$p_x = \left[\xi_0 \cdot K_0 + 2\frac{\left(K_1 - K_0\right)}{\Delta h^2} \cdot h_0 \cdot \left(\frac{h_0}{\delta + 1} - \frac{h_1}{\delta}\right)\right] \cdot \left(\frac{h_x}{h_0}\right)^{1-\delta} - 2\frac{\left(K_1 - K_0\right)}{\Delta h^2} \cdot h_x \cdot \left(\frac{h_x}{\delta + 1} - \frac{h_1}{\delta}\right) \tag{7}$$

– for the zone of slippage on the delivery side:

$$p_x = \left[\xi_1 \cdot K_1 - 2\frac{h_1^2}{\delta \cdot (\delta - 1)} \cdot \frac{\left(K_1 - K_0\right)}{\Delta h^2}\right] \cdot \left(\frac{h_x}{h_1}\right)^{1+\delta} + 2\frac{\left(K_1 - K_0\right)}{\Delta h^2} \cdot h_x \cdot \left(\frac{h_x}{\delta - 1} - \frac{h_1}{\delta}\right) \tag{8}$$

In order to compare the results of the calculation of normal contact stresses for all four considered formulas (1)–(2), (3)–(4), (5)–(6), and (7)–(8) in accordance with the real modes of compression on the reverse mill of 1680 PJSC "Zaporizhstal", an algorithm and a program for the calculation in Mathcad Prime 5 software complex [11] were developed.

3 Research Methodology

In order to determine the values of the pressure in an arbitrary intersection of the deformation center, a calculation algorithm has been developed, which is shown in the block diagram of Figure1. The scheme relates to the calculation of formulas (1), (2); other formulas are calculated using a similar scheme.

The deformation center is divided into a series of intersections (from 0 to k). In each intersection, the current height of the strip h is determined, which is compared with the height of the strip in the neutral intersection h_H. The height h_H is determined by the condition of the equality of pressures in this intersection from the zones of slippage of the entry and delivery sides. For example, when calculating the formulas (1)–(2), to find h_H the equation is solved:

$$\frac{K_0}{\delta}\left[\left(\xi_0 \cdot \delta - 1\right) \cdot \left(\frac{h_0}{h_н}\right)^{\delta} + 1\right] - \frac{K_1}{\delta}\left[\left(\xi_1 \cdot \delta + 1\right) \cdot \left(\frac{h_н}{h_1}\right)^{\delta} - 1\right] = 0. \tag{9}$$

Similarly, h_H is found by calculating formulas (3)–(8).

By changing the different parameters (compression, friction coefficient, a diameter of the rolls, back and front tension coefficient) and dividing the deformation center into any number of intersections, it is possible to numerically determine the influence of each of the above factors on the distribution of normal contact stresses.

The calculation was performed in the Mathcad Prime 5 software complex, according to the block diagram shown in Figure 1. The deformation center was divided into 20 sections (indexes "k" and "i") and in each section, normal

contact stresses were calculated: P_0 – for the zone of slippage on the entry side and P_1 – for the zone of slippage on the delivery side.

Table 1 presents the parameters of the Steel 1008 rolling modes on the reverse mill 1680 PJSC "Zaporizhstal" (as an example, only 4 passes out of 11 are given).

The program and the course of calculating the normal contact stresses in the deformation center in 20 sections according to formulas (1), (2) for the 1st rolling pass on the reverse mill 1680 in the Mathcad Prime 5 software complex are shown in Figure 2.

Table 1 – Table captions should be placed above the tables

Name of the parameters	Pass number			
	I	II	IV	XI
The thickness of the strip, mm				
initial h_0	3.05	2.45	1.95	0.9
final h_1	2.45	2.05	1.76	0.8
Absolute compression Δh, mm	0.60	0.40	0.19	0.1
The diameter of the working rolls D, mm	490	490	490	490
Coefficient of external friction f	0.1	0.1	0.1	0.1
Relative deformation ε, %	19.7	16.3	9.7	11.1
Yield strength, MPa				
before rolling σ_0	410	790	1040	1330
after rolling σ_1	790	990	1140	1340
Forced yield strength, MPa				
before rolling k_0	471.5	908.5	1196	1529.5
after rolling k_1	908.5	1138.5	1311	1541
Tension coefficient:				
back ξ_0	1	0.98	0.988	0.985
front ξ_1	0.98	0.97	0.976	0.979
Coefficient δ	4.041	4.950	7.181	9.899
Horizontal projection l_d of the length of the capture arc, mm	12.12	9.90	6.82	4.95

4 Results

According to the obtained calculation data, the epures of normal contact stresses along the length of the deformation center have been built and shown in Figure 3. The obtained diagrams coincide with those reported in the literature [6, 7].

The area of the epure is the total pressure of the metal on the rolls per width unit of the rolling strip. The area of the epures was determined as follows. All the curves of Figure 3 were plotted on a single graph in Mathcad. Then, these graphs were redrawn and the area of the epures was determined in the software complex AutoCAD Mechanical 2019.

Comparison of the areas of the normal contact stress epures, obtained by simplified formulas (3), (4) and more accurate equations of A. I. Tselikov (1), (2), shows that these areas are almost exactly the same: their maximum difference is no more than 5 %. Therefore, the simplified formulas are equivalent to the accuracy of determining the value of the normal contact stress.

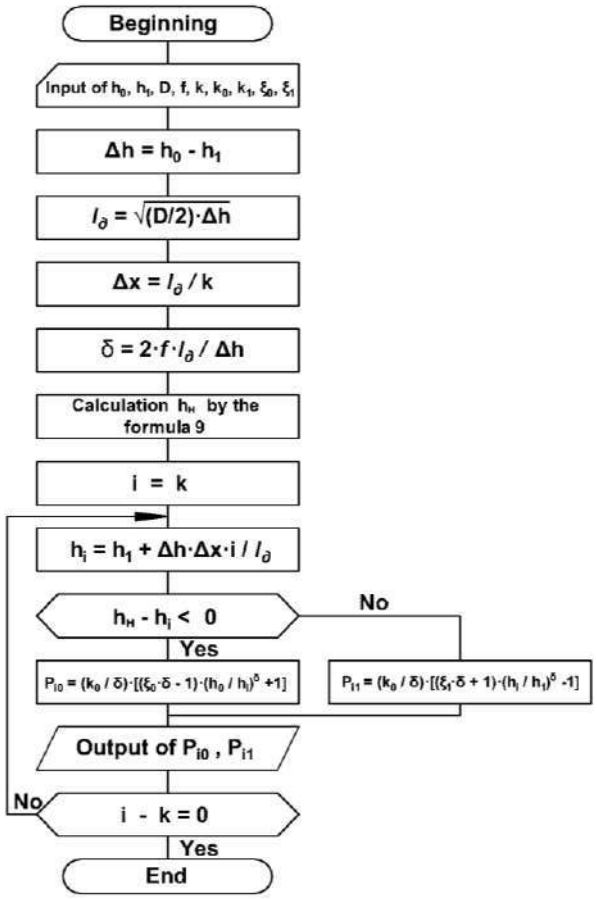

Figure 1 – A block-scheme of calculation of contact stresses during longitudinal rolling of the strips

At the same time, the simplification conducted during the derivation of the differential equation of equilibrium leads to relatively simple formulas, taking into account the change in the forced yield strength, both by the law of a straight line and parabolic law.

5 Discussion

From the above epures, it is noticeable (Table 2) that the maximum difference of their areas by the straight-line law of change of the forced yield strength in the deformation center reaches 29 %, and 43 % by the parabolic law, especially in the first passes, when the metal is intensively hardened.

Based on the analysis of the contact stress epures, it can be concluded that the most accurate calculation of the total metal pressure on the rolls during cold rolling is possible only when the formulas used to consider the change in the forced yield strength in the deformation center by the law of a straight line or the parabolic law.

In this case, the straight-line law of change of the forced yield strength can be used with small compressions. In other cases, such formulas, which take into account the change in the forced yield strength by parabolic law, should be used.

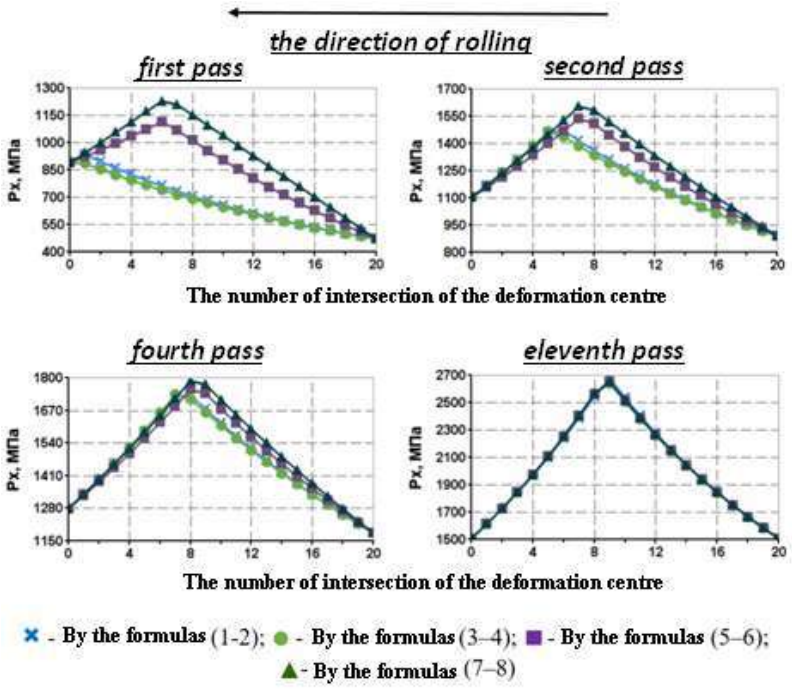

Figure 3 – Epures of normal contact stresses in the passes of a reverse rolling mill 1680

Table 2 – The areas of the normal contact stress epures according to Figure 3

Pass	Epure area, mm^2, obtained by the formulas:				The relative difference of the areas of the epures in %, obtained by the formulas			
	(1), (2)	(3), (4)	(5), (6)	(7), (8)	(1), (2)	(3), (4)	(5), (6)	(7), (8)
I	2346.6	2258.6	3020.8	3361.7	0.00	–3.75	28.73	43.26
II	6629.3	6587.5	6998.3	7334.0	0.00	–0.63	5.57	10.63
IV	8871.8	8829.4	8956.2	9143.6	0.00	–0.48	0.95	3.06
XI	13548.9	13487.1	13566.5	13573.0	0.00	–0.46	0.13	0.18

6 Conclusions

The algorithm, the block-diagram and the computer program of calculation of normal contact stresses in the deformation center during cold rolling of the strips at the reverse mill 1680 PJSC "Zaporizhstal" have been developed with the help of Mathcad Prime 5 software complex. The results of the calculations coincide with the literature data. The epures were constructed and a comparative analysis of the formulas used to calculate the normal contact stresses in the deformation center was performed. It is shown that the most reliable results can be obtained by using formulas that take into account the change in the forced yield strength in the deformation center, according to the parabolic law.

References

1. Panjkovic, V. (2014). *Friction and the Hot Rolling of Steel* (2nd ed.). Boca Raton, FL: CRC Press.
2. Lee, W., Kwak, J., Park, C. (1996). A new approach to predict rolling forces in the tandem cold rolling mill. *In Proc. 2nd International Conference on Metal Rolling Processes*. London, pp. 473–477.
3. Ginzburg, V., Ballas, R. (2000). *Fundamentals of Flat Rolling.* Marcel Dekker, New York.
4. Hensel, A., Spittel, T. (1982). *Kraft-und Arbeitsbedarf bildsamer Formgebungs-verfahren.* VEB Deutscher Verlag fur Grundstoffindustrie, Leipzig.
5. Nikolaev, V. (2018). *Napryazheniya, deformatsii i sluzhba valkov v kleti kvarto.* Monografiya. ZGIA, Zaporozhe.
6. Nikitin, G. (2009). *Teoriya nepreryivnoy prodolnoy prokatki.* Uchebnoe posobie. MGTU im. Baumana, Moscow.
7. Himich, G. (1972). *Mehanicheskoe oborudovanie tsehov holodnoy prokatki.* Mashinostroenie, Moscow.
8. Zabelin, I., Protsenko, V. (2003). Status of non-ferrous metal industry in Ukraine and problems in its development. *Metallurgicheskaya i Gornorudnaya Promyshlennost*, Issue 4, pp. 75–78.

9. Sereda, B., Kruglyak, I., Zherebtsov, A. and Belokon, Y. (2011). The influence of deformation process at titan aluminides retrieving by SHS-compaction technologies. *Metallurgical and Mining Industry*, Vol. 3, pp. 59–62.
10. Vasilchenko, T., Yavtushenko, G., Bondarenko, Y., Belokon, Y. (2015). Calculation of planetary drive of mechanical press. *Metallurgical and Mining Industry*, Vol. 7 (12), pp. 178–182.
11. Shestakov, N. (2008). Raschetyi protsessov obrabotki metallov davleniem v Mathcad (reshenie zadach energeticheskim metodom). Uchebnoe posobie. MGIU, Moscow.

УДК 621.771:514.18

Числовий експеримент з розрахунку нормальних контактних напружень в осередку деформації при прокатуванні штаб

Явтушенко О. В.[1], Проценко В. М.[1], Бондаренко Ю. В.[1], Кириченко О. Г.[1], Пінг Ф. Й.[2]

[1] Запорізький національний університет, пр. Соборний, 226, 69006, м. Запоріжжя, Україна;
[2] ТОВ «Фуцзянь Сянгсін», Фужоу, Фуцзянь, Китай

Анотація. У статті розглянуто можливості застосування програмного комплексу “MathCAD Prime 5” для розрахунку нормальних контактних напружень в осередку деформації при холодному прокатуванні штаб. Розроблено алгоритм, блок-схему і комп’ютерну програму розрахунку нормальних контактних напружень під час прокатування штаб на реверсивному стані 1680 ПАТ «Металургійний комбінат «Запоріжсталь». Побудовано епюри і виконано порівняльний аналіз формул, що використовують для розрахунків нормальних контактних напружень в осередку деформації. Розрахункові дані, отримані за допомогою програмного комплексу “Mathcad Prime 5”, співпадають з літературними даними, що визначає практичну значимість отриманих результатів для науково-дослідної та проектно-конструкторської робіт. Грунтуючись на аналізі епюр контактних напружень, можна зробити висновок, що найточніший розрахунок загального тиску металу на валки під час холодного прокатування реалізується у випадку, коли формули, які визначають математичну модель, ураховують змінювання вимушеної межі текучості в осередку деформації за прямолінійним або параболічним законами. При цьому прямолінійний закон змінювання вимушеної межі текучості може бути використаний лише для випадку порівняно невеликих обтиснень. У інших випадках необхідно використовувати формули, що враховують змінювання вимушеної межі текучості за параболічним законом.

Ключові слова: холодне прокаткування штаб, нормальне контактне напруження, осередок деформації, комп’ютерна програма, вимушена межа текучості.

JOURNAL OF ENGINEERING SCIENCES
ЖУРНАЛ ІНЖЕНЕРНИХ НАУК
ЖУРНАЛ ИНЖЕНЕРНЫХ НАУК
Web site: http://jes.sumdu.edu.ua
DOI: 10.21272/jes.2019.6(2).e6 Volume 6, Issue 2 (2019)

Simulation and Optimization Studies on the Ring Rolling Process Using Steel and Aluminum Alloys

Teja P. S.*, Kumar M. D., Krishna R., Sreenivasan M.

PACE Institute of Technology and Sciences, 523 272 Ongole, Andhra Pradesh, India

Article info:
Paper received: September 12, 2019
The final version of the paper received: December 6, 2019
Paper accepted online: December 11, 2019

***Corresponding Author's Address:**
pstr1516@gmail.com

Abstract. The current research was carried out using ANSYS to optimize the process parameters for the ring rolling process. In order to optimize the ring rolling process, parameters such as speed, axial roller feed, and driving rollers have been assessed. As a process optimization approach, the optimum values of the parameters and their relationships need to be evaluated. The stress and strain levels were evaluated at various speeds and forces and the critical failure values were determined. The structural steel and aluminum alloys were chosen for this research because they are used as a roller and job part components in the solid wheels for locomotive applications, respectively. The study was conducted by varying the guide roller's angular velocity from 40 to 45 rad/sec and varying the work piece's angular velocity from 200 to 250 rad/sec. Additionally, the work part and roller's fatigue strengths were determined based on the number of cycles before failure. To evaluate the stresses of plastic strain and von failures, the full stress analysis was also performed.

Keywords: roller, ANSYS, workpiece, plastic strain, von Misses stress, metal alloy.

1 Introduction

Rolling is a continuous metal shaping between a series of spinning or rotating rolls, whose shape or height is gradually decreased to produce the desired segment by applying strong plastic deformation pressures. It is the method of thickness reduction which reduces the length without significantly increasing the width. The ring rolling method can be carried out at high temperature (hot) or at ambient temperature (cold) with the product initially. Ring rolling is an innovative technique in the development of smooth rings of elastic cross-sectional form, enhanced grain structure, and reduced scrap. The ring is formed by a local continuum rolling method as shown in the figure from an initial void, incrementally from a small diameter and thick section to a wide diameter and thin section. In the area of metal plastic manufacturing, research and development of ring rolling techniques with rings complicated in form or wide in length or with high precision have become an important topic. Because of the process's nature and strong nonlinearity, it is difficult to describe the process correctly by analytical methods alone. Although quantitative explanations are appropriate for the system they are being based on, findings are challenging to extrapolate accurately. The finite element approach for researching and developing innovative ring rolling techniques is, therefore, inspired [1]. Developing a realistic 3D finite-element ring rolling model has become an urgent issue, and the problem of how to properly monitor guide rolls is one of the key issues in achieving a good 3D finite-element ring rolling simulation, particularly for rings that are complicated in shape or wide in size or with high precision [2].

2 Literature Review

Some journal papers were selectively studied which have direct relevance with the current research work and their results are discussed here.

Yu-Min Zhao explained ring rolling as an advanced technique of plastic forming used in the production of precise seamless rings. The rolling ratio is a decisive parameter for the rolling process as it determines the blank dimension, reflects the degree of ring deformation and influences the results of the forming. Nonetheless, the importance of rolling is always overlooked. In this paper, the impact of the rolling ratio on the rolling of the groove-section profile circle is explored. The relationships between rolling ratio and blank length, rolling ratio and degree of ring deformation are theoretically analyzed and a rolling ratio conceptual quality array is proposed [3]. Then the influences of the rolling ratio on the forming results are revealed with the simulation of finite ele-

ments. A fair quality scope of the rolling ratio is calculated based on comparison and observational validation.

To simulate the non-linear problem that characterizes the ring rolling process, finite element codes are available [4]. The analysis is done using ANSYS. The parameters including speed, axial roller feed, and driving rollers were analyzed from the study [5]. The optimal relationship between the process parameters is identified from the analysis. The stress and strain values are generated at different speeds. Critical and failure values are also obtained. The research was carried out for structural steel and aluminum as the workpiece, taking the characteristics of the metal into the account [6].

3 Research Methodology

3.1 Process of ring rolling

The design scheme of the ring rolling process is presented in Figure 1.

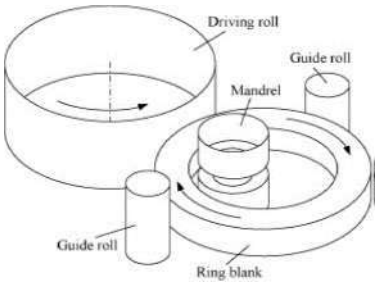

Figure 1 – The ring rolling process

Two rollers that rotate in the opposite direction are fed in the ring rolling material. The gap between the rollers is lower than the material thickness caused by deformation. It is caused to elongate due to reduced material thickness. Material-roller resistance induced the material to move [2]. The volume of deformation in a single pass is limited by roller friction. If the thickness varies, rollers can be slipped. Certain procedures such as shearing, flattening and punching are to be completed before the ring rolling process in order to generate the final product. Shearing is the method of removing a necessary blank from the stock. Flattening is a method of adding sufficient force to reduce the height of the original element [5]. Eventually, the punch and dies design creates a gap in the part [7]. The processing of ring rolling is given in Figure 2

3.2 Typical Ring Rolling Products

Rolled rings find application in bearings, slewing bearings, turbine disks and gear blanks [8]. Ring rolling machines are also used in producing solid wheels and wheel disks for high-speed trains, locomotives, railway carriages, trams, and subway trains. More examples of the varied uses of ring rolling items includes bevel gear and axle drive wheels for the automotive industry, transmission manufacturing, turbine manufacturing (turbine disks for plane propulsion engines), flanges in the computer and plant construction industry, rings for tower flanges (in off-shore wind turbines) and roller bearings (cold spinning) [9].

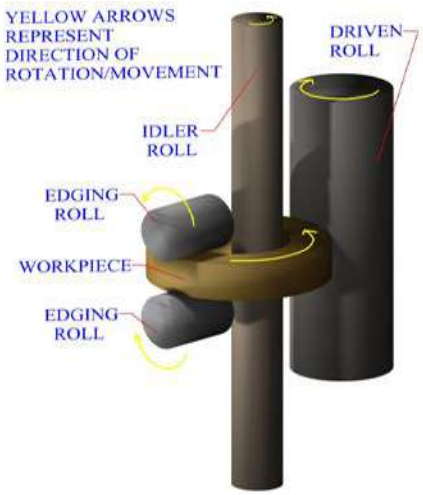

Figure 2 – The process of ring rolling

3.3 Analytical description of ring rolling

Kalpak Jian and Schmidt's flat rolling analysis is extended to the process of ring rolling [9]. Process parameters are defined as given in Figure 3.

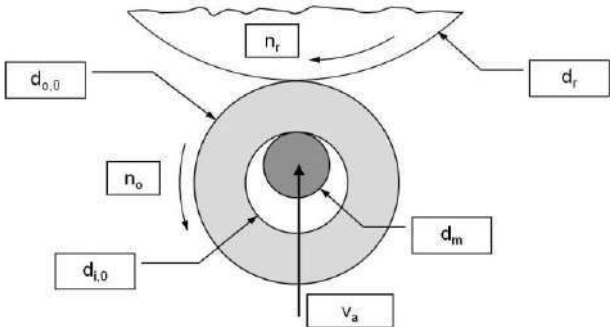

Figure 3 – Description of the ring rolling process

The parameters used in the analysis are d_i – inner diameter; d_o – outer diameter; d_r – roll diameter; d_m – mandrel diameter; n_r – roller rotational speed; n_o – ring rotational speed; v_a – advance velocity of the mandrel.

The first relationship to be developed is the dependency by volume preservation between cross-sectional thickness and diameter. The plain strain is presumed in this situation, therefore there is no strain in the width direction.

The main geometric dependencies are based on the following requirement of the constant volume:

$$\pi(d_o^2 - d_i^2)w/4 = \pi(d^2_{o,0} - d^2_{i,0})w/4;$$
$$d_i = [d_o^2 - (d^2_{o,0} - d^2_{i,0})]^{1/2}. \quad (1)$$

Therefore, the internal diameter relies on the external diameter and the actual empty volume as determined from the initial measurements of the circle. The next step in the analysis is to provide equivalence to the process of flat rolling by equating the contact lengths between the material and the roll or mandrel. This analysis targets defining the equivalent diameter of a flat rolling process roll to represent the more complex curvilinear ring roll.

A result for the forming roll which undergoes convex-convex contact is given by

$$d_{r,eq} = d_r/[1 + 2d_r/(d_{o,0} + d_o)]. \quad (2)$$

Therefore, the corresponding flat rolling size is less than the true diameter of the greater convex-convex touch roll. Similarly, the diameter of a mandrel is given by

$$d_{m,eq} = d_m/[1 - 2d_m/(d_{i,0} + d_i)]. \quad (3)$$

The conversion of the convex-concave touch of the mandrel to the inner ring surface leads the corresponding flat roll size to increase than convex-flat contact for plain rolling. Now that the rolling phase of the circle has been converted into flat rolling, the draft issue needs to be addressed [10]. The draft is defined as the reduction of rolling height. The initial and final heights were independent of the rolling system itself for flat rolling. In-ring rolling, though, the heights of entry and exit are combined as the height of exit in one rotation becomes the height of entry for the next rotation. This coupling effect can be given in terms of the advance mandrel speed and the system's rotational speed [11]. When we consider the advanced instantaneous velocity $v_a = d_h/d_t$, and if the velocity of the mandrel is unchanged, the height shift in a single revolution can be interpreted as a finite difference $v_a = (h_1 - h_2)/t_r$, the period for a single rotation is determined from the ring and roll size and rotational velocity: $t_r = 60/n_{o,1} = 60\pi d/v_1 \approx 60\pi d/n_r = 60d_0/(d_r n_r)$.

Therefore, the height change can be described as

$$h_1 - h_2 = 60d_0 v_a/(d_r n_r). \quad (4)$$

The h_1 and h_2 reflect the heights inside and outside the rolling area and the stress applied to the ring segment is proportional to the original sectional size, as there is no rotational annealing process. When we consider the peak draft state as the point of equilibrium of frictional and natural forces in the direction of rolling, a total approval angle for flat rolling can be given [12]. This condition is shown in Figure 4, where F_n describes the normal force against the piece of work and F_f the tangential frictional force to the move.

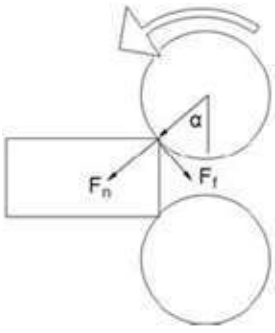

Figure 4 – Force balancing at critical rolling height

The following force component constraint must be considered in order to pull the material into the process:

$$F_f \cos\alpha > F_n \sin\alpha;$$
$$F_f = \mu F_n > F_n \operatorname{tg}\alpha; \quad (5)$$
$$\mu > \operatorname{tg}\alpha.$$

If we assume that the rolling radius exceeds the change in height (large rolling assumption),

$$\operatorname{tg}\alpha \approx \sin\alpha \approx (\Delta h/R)^{1/2}; \Delta h_{max} = \mu^2 R. \quad (6)$$

This analysis is summarized in [4]. Setting these maximum drafts in the following relationship

$$\Delta h_{max} = \mu^2 d_r/2 = 60d_0 v_a^{max}/(d_r n_r);$$
$$v_a^{max} = \mu^2 d_r^2 n_r/(120d_0). \quad (7)$$

Therefore, to maintain the rotation of the ring during rolling, an upper limit is established on the prescribed mandrel advance velocity [2].

3.4 Numerical simulation

Figure 6 describes the modeling of ring rolling that includes workpiece, mandrel, and roller guide. Modeling is done using solids works and the mesh analysis is done in ANSYS. Wire modeling and meshing of ring rolling are given in Figure 5. The mesh domain is created for quality analysis.

Finite Element Analysis (FEA) is performed using the FEA software package called ANSYS. The computer package introduces and solves the formulas that control the action of elements. The material used for the process is Aluminum 6061 alloy [12]. The material properties are provided in Table 1.

The pressure of the roller against the workpiece could be either increased or decreased, based on the desired shape of the workpiece [8].

The roller moves around the workpiece that is fixed at the stationary state. The rotational speed of the roller is 40 rad/sec to get the desired dimensional output of the workpiece.

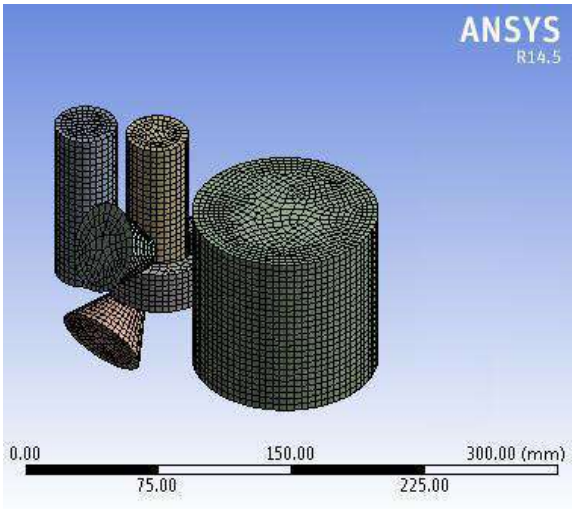

Figure 5 – The meshing of the ring rolling process

Table 1 – Properties of Aluminum 6061 alloy

Density, kg/m^3	2700
Brinell's hardness	95
Rockwell hardness	40
Tangent modulus, MPa	1330
Ultimate tensile strength, MPa	310
Tensile yield strength, MPa	276
Young's modulus, MPa	68.9
Ultimate bearing strength, MPa	607
Bearing yield strength, MPa	386
Poisson's ratio	0.33
Fatigue strength, MPa	96.5
Shear modulus, MPa	26
Shear strength, MPa	207
Specific heat capacity, J/(kg·K)	896
Thermal conductivity, W/(m·K)	167
Elongation at break, %	12

4 Results

Rotational velocity is directly proportional to the time, which means that when the velocity is increasing the time taken for the process increases linearly. In this case, the rotational acceleration is equal to 50 rad/s2.

From Figure 6 a, it can be observed that the maximum and minimum static structural deformations for the process are 5.96 nm. Figure 6 b describes the maximum static structural equivalent stresses equal to 0.027 MPa.

Figure 7 a, b describes that deformations and stress increase with an increase in time. It can be observed from Figure 8 that the maximum static structural normal stress for the process is equal to 19.8 kPa.

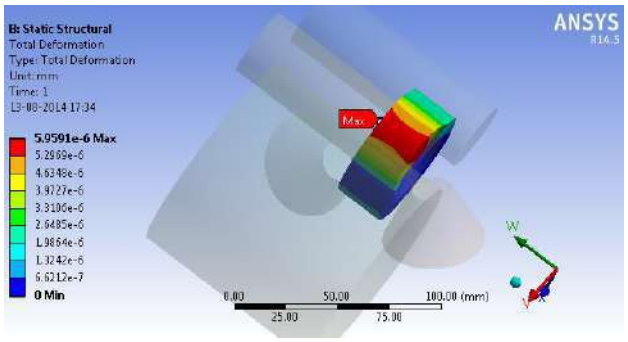

a

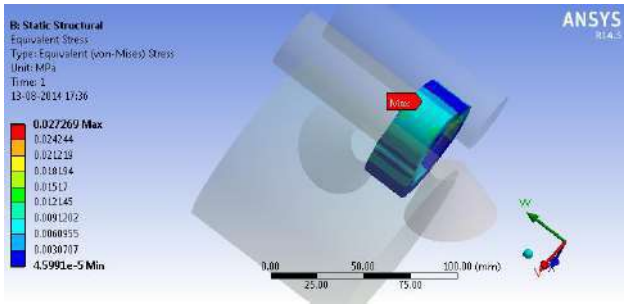

b

Figure 6 – Total deformations (a) and von Mises equivalent stresses (b)

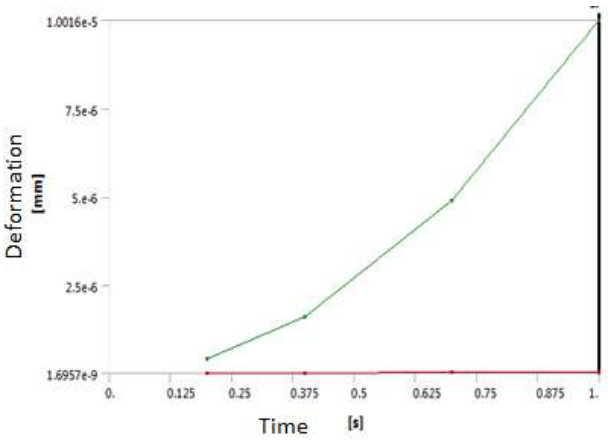

a

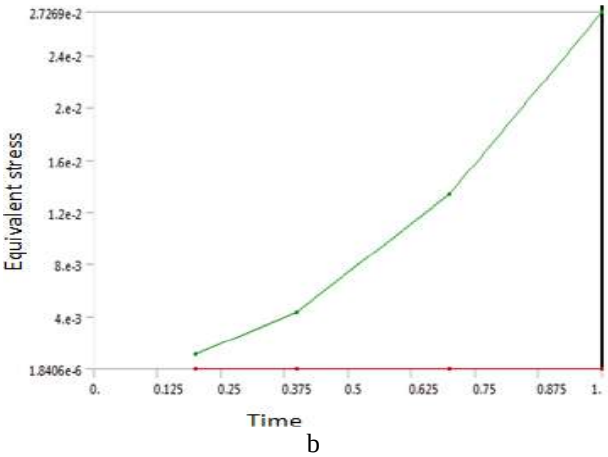

b

Figure 7 – The maximum values of deformations (a) and equivalent stresses (b) in time

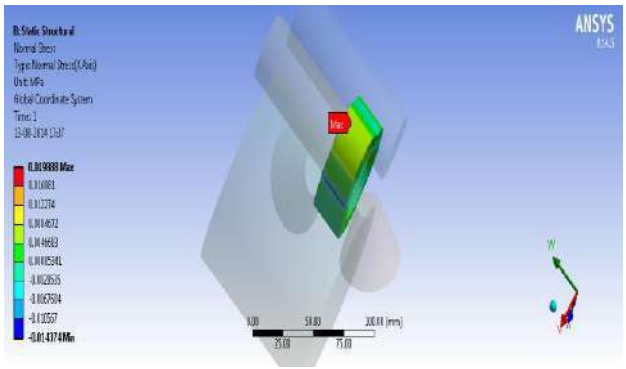

Figure 8 – Normal stresses

5 Conclusions

The finite element analysis is done by considering aluminum 6061 alloys as workpiece material and structural steel as roller material in the ring rolling process. The values of normal stress, von Misses stresses, and strain energy are obtained. Fatigue power, mandrel life is accomplished by considering the number of cycles it could withstand. From the analysis, it is observed that von Misses stress of the work material is below the actual values. Workpiece strength is determined by changing the velocity of idle role and workpiece.

References

1. Banerjee, P., Huir, N. B. (2019). Finite element modeling of ring rolling process. *Materials Today: Proceedings*, Vol. 11, pp. 843–848.
2. Yang, H., Guo, L., Zhan, M., Sun, Z. (2006). Research on the influence of material properties on cold ring rolling processes by 3D-FE numerical simulation. *Journal of Materials Processing Technology*, Vol. 177, pp. 634–638.
3. Allegri, G., Giorleo, L., Ceretti, E., Giardini, C. (2017). Driver roll speed influence in ring rolling process. *Procedia Engineering*, Vol. 207, pp. 1230–1235.
4. Guilleaume, C. and Brosius, A., 2019. Simulation methods for skew rolling. Procedia Manufacturing, 27, pp.1-6.
5. Dandagwhal, R. D., Kalyankar, V. D. (2019). Design optimization of rolling element bearings using advanced optimization technique. *Arabian Journal for Science and Engineering*, pp. 1–16.
6. Tripathi, A., Medhavi, A. (2014). Finite element simulation of hot rolling for an aluminum 2024 plate. *International Journal of Scientific and Research Publications*, Vol. 4(12), pp. 361–365.
7. Allegri, G., Giorleo, L., Ceretti, E. (2019). Roll gap per rotation optimization in a radial ring rolling process. *AIP Conference Proceedings*, Vol. 2113(1), article number 040008.
8. Hua, L., Deng, J., Qian, D. (2017). Recent development of ring rolling theory and technique. *International Journal of Materials and Product Technology*, Vol. 54(1-3), pp. 65–87.
9. Quagliato, L., Berti, G. A. (2016). Mathematical definition of the 3D strain field of the ring in the radial-axial ring rolling process. *International Journal of Mechanical Sciences*, Vol. 115, pp. 746–759.
10. Sun, B., Xu, J., Xing, C. (2019). Numerical and experimental investigations on the effect of mandrel feeding speed for high-speed rail bearing inner ring. *The International Journal of Advanced Manufacturing Technology*, Vol. 100(5-8), pp. 1993–2006.
11. Meng, W., Zhao, G. Q. (2014). Effects of key simulation parameters on conical ring rolling process. *Procedia Engineering*, Vol. 81, pp. 286–291.
12. Wu, Q., Wu, J., Zhang, Y. D., Gao, H. J., Hui, D. (2019). Analysis and homogenization of residual stress in aerospace ring rolling process of 2219 aluminum alloy using thermal stress relief method. *International Journal of Mechanical Sciences*, Vol. 157, pp. 111–118.
13. Wasa, N., Fukui, T. (2019). *Ring Rolling Mill and Method for Manufacturing Ring Rolled Material*. U.S. Patent Application 10/286,443.
14. Yagami, T., Teramae, T., Fujita, E., Nagao, S., Mukouse, R., Iwasa, N., Fukui, T., Aoki, C. (2018). *Material for Ring Rolling*. U.S. Patent 10,094,238.

УДК 624.014

Моделювання та оптимізаційний розрахунок процесу прокатування кілець з конструкційної сталі сталі та алюмінієвого сплаву

Тея П. С., Кумар М. Д., Крішна Р., Срінівасан М.

Інститут технологій та наук ім. Пейс, 523 272, м. Онголе, Індія

Анотація. Поточні дослідження проводилися за допомогою програмного комплексу ANSYS для оптимізації параметрів процесу прокатування кілець. Для оптимізації процесу прокатування були оцінені такі параметри, як швидкість, осьова подача ролика і параметри приводних роликів. Як підхід до оптимізації процесу було оцінено оптимальні значення параметрів та взаємозв'язки між ними. Параметри напружено-деформованого стану оцінювались для різних швидкостей і сил, а також визначались відповідні значення критичних параметрів. Для проведення дослідження було обрано конструкційні сталі та алюмінієві сплави, оскільки саме вони використовуються для виготовлення функціональних елементів і деталей коліс. Дослідження проводилось шляхом зміни кутової швидкості направляючого ролика у діапазоні від 40 до 45 рад/с і зміни кутової швидкості деталі у діапазоні від 200 до 250 рад/с. Крім цього, втомна міцність робочих частин пристрою визначалася на основі аналізу кількості циклів навантаження до відмови. Також було проаналізовано напруження і пластичні деформації.

Ключові слова: валик, ANSYS, заготовка, пластичні деформації, еквівалентне напруження за Губером-Мізесом-Генки, металевий сплав.

JOURNAL OF ENGINEERING SCIENCES
ЖУРНАЛ ІНЖЕНЕРНИХ НАУК
ЖУРНАЛ ИНЖЕНЕРНЫХ НАУК
Web site: http://jes.sumdu.edu.ua
DOI: 10.21272/jes.2019.6(2).e7 Volume 6, Issue 2 (2019)

Airplane Waste Disposal System Tank Designing Using Numerical Simulation and Experimental Bench Results

Medvediev S. V.[1*], Lantin D. H.[2]

[1] ANTONOV State Enterprise, 1 Academic Tupolev St., 03062 Kyiv, Ukraine;
[2] United Interiors International, LLC, 2535 Seabrook Island Rd., Johns Island, SC 29455, USA

Article info:
Paper received: March 22, 2019
The final version of the paper received: December 7, 2019
Paper accepted online: December 12, 2019

[*]Corresponding Author's Address:
s.medvedev.v@gmail.com

Abstract. Modern passenger aircraft cannot be considered without the requirements to ensure the safety and comfort of passengers on board. One of the systems that provide the necessary comfort on the plane is the waste disposal system, which is designed to meet the physiological needs of the human body. Today, a promising waste disposal system type is a vacuum principle of operation. The vacuum-type waste disposal system is a combination of complex multifunctional subsystems: waste collection, waste storage, vacuumization, drain and flush, system control. Such systems development, consisting of devices, based on heterogeneous physical principles of operation, is a complex scientific and technical problem associated with the conduct of diverse applied research in the field of design, development and targeted use of the system. One main system element is a waste storage tank. An important step in the tank design is to determine its weight and size characteristics in the early stages of development. These characteristics are significantly influenced by the tank filling process, which also determines the placement of equipment in it. The aim of the work presented in the article is to study the tank filling process with the help of numerical simulation methods.

Keywords: vacuum, waste tank, design, experimental bench.

1 Introduction

Modern design (creation) of any system onboard an aircraft is a complex, multifactor, branch task to finding the optimal ratio of parameters [1], in which the main criteria are the safety and passengers' comfort on board.

One of the systems providing the necessary comfortable conditions on board the aircraft is a waste disposal system, which is designed to meet the physiological needs of the human body.

Today, a promising type of waste disposal system is a vacuum principle of operation, in which one of the main elements of the system is a waste storage tank. An important step in the design of the system and the waste storage tank is the determination of its characteristics in the early design stages.

2 Literature Review

The development of vacuum systems on civil aviation aircraft began its history from the mid-70s of the twentieth century. So, in 1975, inventor James Kemper patented a vacuum waste disposal system, the principle which is used today on modern passenger aircraft.

The vacuum toilet was first installed on Boeing aircraft in 1982.

From now on the vacuum waste removal system becomes popular and promising on airplanes. Improvements and development of new equipment for vacuum systems lead to the creation of more advanced systems, such as the "Revolutionary" vacuum toilet by Zodiac Water and Waste Aero Systems. Further development of vacuum waste removal systems is used not only on aircraft but also in the entire transport industry.

In the CIS, the Research Institute of Standardization and Unification (RISU) was engaged in vacuum waste disposal systems. Research and development of a vacuum-type waste disposal system were carried out for the Tu-334 aircraft.

A simplified aircraft vacuum waste disposal system diagram is shown in Figure 1. The main elements of the system are waste receptacle (toilet bowl unit) 1, waste disposal pipeline 2, waste storage tank 3 (with waste braking device installed at the inlet and dehumidification device at the tank outlet), vacuumization subsystem (vacuum generator 5, vacuum pipelines 4).

The principle system operation is as follows: when a difference in air pressure occurs between the cavity of the

waste storage tank and the passenger cabin, the waste from receiver 1 through waste disposal pipe 2 is moved to tank 3, where it should be stored until the end of the flight. On the ground, the air pressure drop is created by a vacuum pump (vacuum generator). The flight uses a natural air pressure drop between the atmosphere and the passenger cabin.

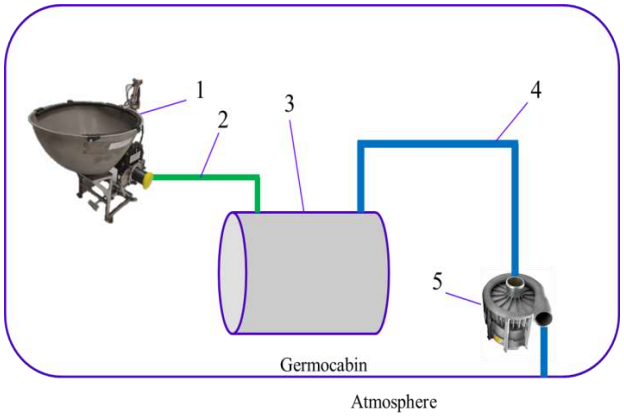

Figure 1– Design scheme of an aircraft vacuum system

The waste storage tank is one of the key system elements [2, 3]. When designing the tank and determining its required volume, you must perform:

– determine the maximum amount of waste to be stored in the tank;

– determine the device configuration of waste braking when it enters the tank;

– determine the configuration of the dehumidification device;

– explore the process of filling the tank with waste (gas-dynamic calculation);

– perform a strength calculation of the tank and the whole system.

One of the important requirements that arise when developing a waste disposal system is the tightness requirement. The system tightness is caused not only by the tightness of the pipeline joints network but also by the requirement to preserve the waste in the tank without further movement through the vacuumization subsystem. If the developed system design does not comply with this requirement, the following negative consequences may occur:

– formation of significant ice formations on the aircraft outer surface at the exit point of the vacuumization pipelines, which, after detachment, may damage the aircraft structure;

– vacuum generator breakdown;

– entering the waste on the airfield during a stop leads to the imposition of significant fines by the airport authority.

Despite recent research in this area, some aspects of system development have not been fully resolved. The development of methods for calculating the main characteristics of the waste tank basically remains the prerogative of aircraft manufacturers and firms developing specialized equipment for aircraft and was not published in the open press.

The information presented in the literature regarding methods for calculating vacuum systems [4–14] does not allow one to determine the necessary characteristics of the system and the waste tank. In this regard, the development of methods for designing and calculating the waste disposal system, as well as its individual elements, particularly, the waste storage tank is an important task.

At the stage of research work, when conducting full-scale tests is extremely difficult and requires significant costs, the actual task is to determine the volume of the tank, which is necessary for storing a given amount of waste, as well as its configuration taking into account the zonal equipment distribution in the aircraft compartments. The required tank volume largely depends on the filling process, the study of which is presented below.

3 Research Methodology

3.1 Waste storage tank filling processes investigation using numerical modeling

In the study of the tank filling process using numerical simulation methods [15–19], ANSYS CFX software was used.

The object of the study is a waste storage tank designed for the An-148-100 passenger aircraft. The appearance of the tank is shown in Figure 2.

Initial data:

– maximum tank diameter d_{max} = 521 mm;

– tank length L = 828 mm;

– pressure in the tank after turning off the vacuum generator P_{tank} = 0.51531 kgf / cm^2;

– cabin pressure $P_{cab} = 1.03 \cdot 10^5$ Pa.

The three-dimensional model of the tank is made using the software NX 8.5.

Figure 2 – Antonov-148-100 aircraft waste storage tank model

The computational grid was constructed using the ICEM software package. The volume of the tank is broken by an unstructured tetrahedron grid using the Robust (octree) method, Figure 3. The maximum mesh element in the tank volume was 20 mm, for entry and exit

7 mm, with a tank volume of 140 l and input/output diameter 50 mm, respectively. The number of design elements was 5.5 million.

A two-phase air-water medium separated by a free surface is considered. The air is presented as an ideal gas SST turbulence model.

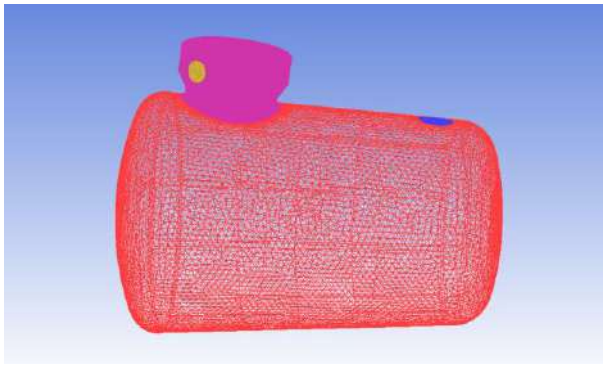

Figure 3 – Calculated waste tank mesh

The flow was modeled in a non-stationary setting (Transient). The simulation time of the tank filling process is about 1.0 s and includes the following stages of the system unit's operation: the vacuum generator starts, the waste receiver flap opening, the ingress of a portion of water into the tank, the flap closing.

At the initial moment of time in the tank, there is a certain water level, the height of the column of which is equal to y_h (Figure 4).

The initial values of the velocity vector are 0 m/s. The initial pressure value is set by the P_{ref} functions, which are determined by the function:

$$P_ref = \{P_(w\ ) with\ y < y_h\ \ P_in\ with\ y \geq y_h$$

where P_{in} = $1.03 \cdot 10^5$ Pa – air pressure; P_w – water pressure determined using the following function:

$$P_w = P_{in} + (y_h - y) * 1000 \left[\frac{kg}{m^3}\right] * g$$

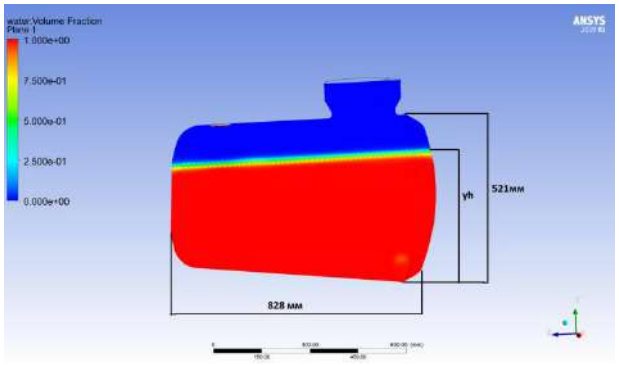

Figure 4 – Tank water level at the initial time

The initial temperature of both phases is t = 22 ° C. The volume coefficient content of each phase in the computational domain is determined through the function WVF:

$$WVF\ air = \{0\ with\ y < y_h\ \ 1\ with\ y \geq y_h$$
$$WVF\ water = 1 - WVF\ air$$

The first studies showed that the stability of the calculation is ensured with a time step of 1.0 ms or less.

Visualization of vacuum creating process in a tank at a height of waste level y_h = 400 mm shown in Figures 5–8.

Investigation of the creating vacuum process revealed that separation of particles of water (waste) is due to the high air velocity in the gap between the free surface and the tank housing.

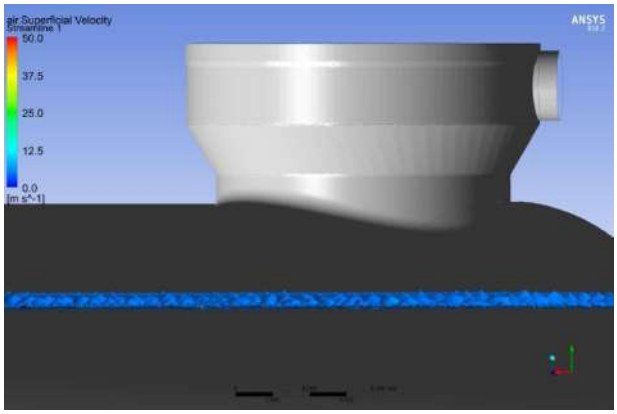

Figure 5 – Initial time

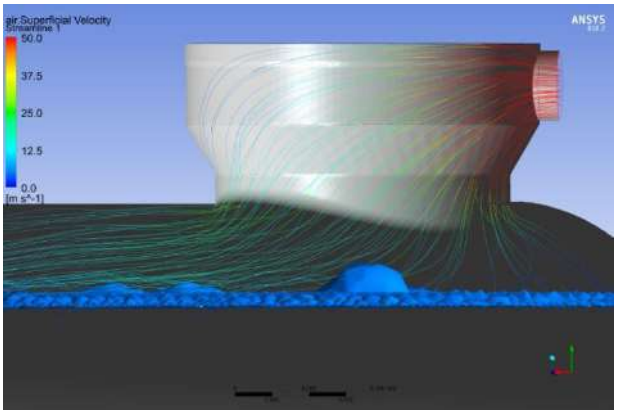

Figure 6 – After vacuum generator switching

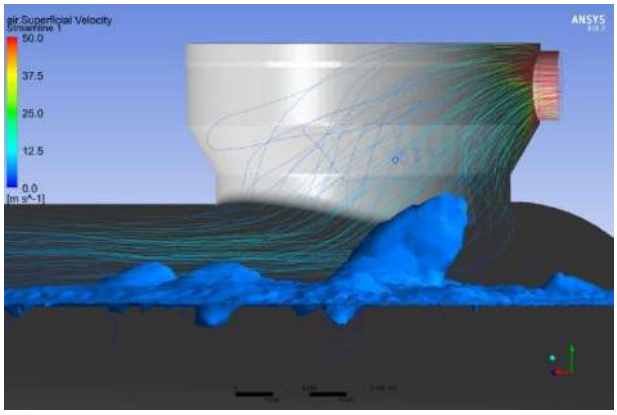

Figure 7 – The beginning of separation formation

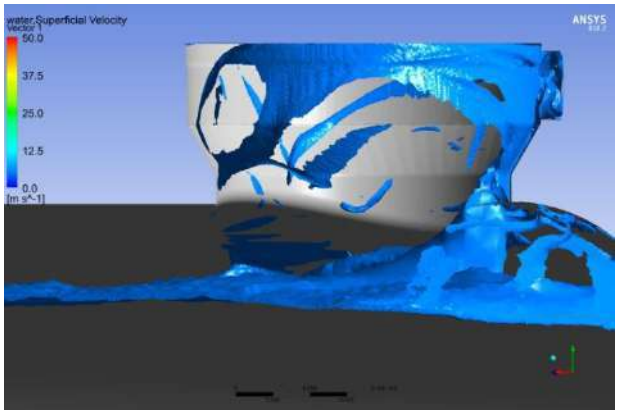

Figure 8 – The moment after vacuum generator turning off

When reducing the cross-sectional area of this gap, associated with an increase in the level of waste in the tank, the separation process occurs with greater intensity.

The results of the numerical tank filling process simulation made it possible to determine the dependence of the volumetric water content coefficient in the outlet pipeline on various values of the initial water level in the tank. The results of the calculations are presented in Table 1.

Table 1 –The result of a numerical study of the filling process

y_h, mm	Water volume fraction
500	0.009
450	0.018
400	0.002
371	0.004
350	$1.052 \cdot 10^{-5}$
300	$3.880 \cdot 10^{-7}$

Figure 9 shows the volumetric content of water that enters the pipelines of the vacuumization subsystem depending on the thickness of the air gap above the water.

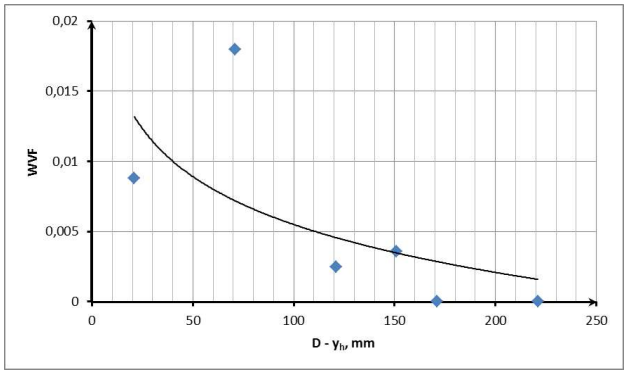

Figure 9 – Percentage of water fraction from the change in the height of the water column

3.2 The hydraulic processes research experimental bench of filling the waste storage tank

For carrying out field tests, a functional stand was developed, for which a special waste tank was designed.

A stand schematic diagram is shown in Figure 10. The stand consists of the following units:

1 – waste receptacle;
2 – splitter valve;
3 – damper;
4 – valve control unit;
5 – flush button;
6 – system management controller;
7 – waste storage tank;
8 – tank level sensor ¾";
9 – sensor level 100 % tank;
10 – separator;
11 – waste dispenser;
12 – waste discharge valve;
13 – vacuum generator;
14 – starting relay of vacuum generator;
15 – waste disposal pipeline;
16 – vacuum pipe (the material is plexiglass);
17 – personal computer;
18 – power supply.

An experimental tank 7 is made based on a regular tank and has differences in terms of the presence of built-in observation windows, to ensure control and monitoring of the experiment process. The vacuum system pipe 16, which connects the tank with the vacuum generator, is made of transparent Plexiglas for visual observation.

For the tests, an experiment plan was developed, allowing a comprehensive assessment of the tank's capabilities and its characteristics in terms of filling, assessment of sensor placement and tank spray nozzles, waste diverter efficiency, complete removal (draining) of waste from the tank. The tests were carried out in two stages: at the first stage, the testing of filling processes was carried out with the help of a working medium - water. In the second stage, the tests were carried out with the help of a working environment – a waste simulator.

Figure 10 shows the assembled stand on which the experimental part of the work was carried out.

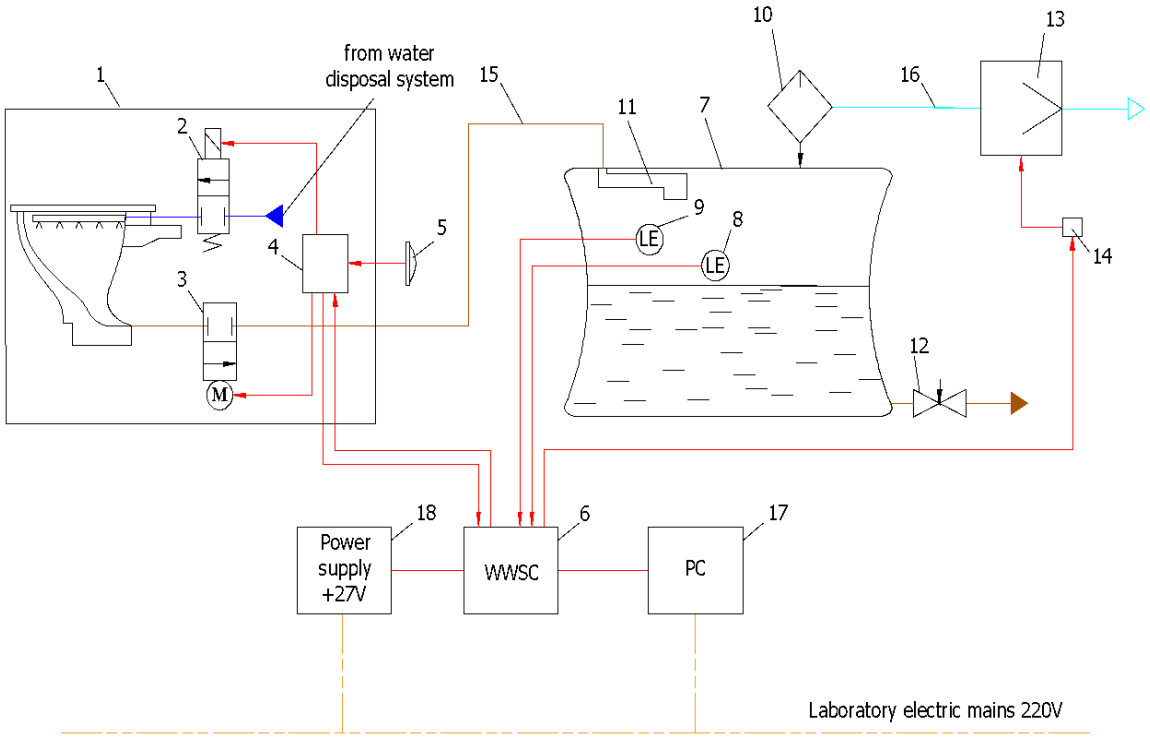

Figure 10 – Experimental bench schematic diagram

4 Results and Discussion

According to the results of numerical simulation (Figure 9), the maximum level of waste at which the separation of the fraction from the surface begins to occur is y_h = 371 mm (which corresponds to an air gap height of 150 mm).

These numerical results are used to calculate the required tank volume.

The test results carried out on the stand showed that up to the height of the air gap of about 150 mm and more visual signs of water ingress, waste and their traces on the walls of the vacuum system pipeline are not observed.

5 Conclusions

The compiled computational model of the filling processes the waste storage tank using the software Ansys CFX adequately describes the hydraulic processes in the tank, which is confirmed by evidenced full-scale tests.

Studies of the filling process have shown that the waste gets into the vacuum main due to an increase in air velocity now of creating a vacuum while reducing the gap between the waste surface and the tank body.

The dependences of the amount of water leaving the tank on the change in the height of the air gap are determined, and the maximum level of waste at which separation begins to occur fraction from the surface.

The obtained numerical method results showed the possibility and necessity of using the software Ansys CFX in the design work on the tank creation for the waste disposal system.

The waste disposal system tank test bench has been developed for conducting a physical experiment.

When comparing the results of a physical experiment and a numerical study, it was established that they provide the stated requirements for the tank.

With this tank configuration and its positioning (horizontal installation of the tank) in the aircraft to prevent the fraction of water from the tank from entering the atmosphere, 43% of the space above the tank waste surface should remain free in case.

6 Acknowledgments

The main part of the presented research, numerical modeling was obtained on the basis of the state-owned enterprise ANTONOV (Kyiv, Ukraine) as part of the national program to create a passenger aircraft of the new generation An-148 (“The State Integrated Program for the Development of the Aviation Industry of Ukraine”).

The experimental part of the tank check was carried out on the test base of the company Monogram Systems (Karson, Los Angeles, USA).

References

1. Staack, I., Chaitanya, R. M. V, Berry, P., Melin, T., Amadori, K., Jouannet, C., Lundstrom, D., Krus, P. (2012). Parametric aircraft conceptual design space. *28th International Congress of the Aeronautical Sciences (ICAS-2012)*, pp. 1–10.
2. Bondyra, A. Klasztorny, M., Muc, A. (2015). Design of composite tank covers. *Composite Structures*, Vol. 134, pp. 72–81.
3. Frohlingsdorf, U. (2018). Designing effective waste storage systems. Reinforced Plastics, Vol. 62(6), pp. 304–306.
4. Nesterov, S. B., Vasilyev, U. K., Androsov, A. V. (2004). *Vacuum Systems Calculating Methods.* MEI, Moscow.
5. Dorothy, M. Hoffman, J. H. T., Singh, B. (1997). *Handbook of Vacuum Science and Technology.* Elsevier Science and Technology Books.
6. Tjagunov, G. A. (1948). *Basics of Calculating Vacuum Systems.* State Publishing House, Moscow.
7. Desman, S. (1964). *The Scientific Fundamentals of Vacuum Technology.* Peace, Moscow.
8. Pipko, A. I, Pliskovskiy, V. Y., Penchko E. A. (1970). *Design and Calculation of Vacuum Systems.* Energy, Moscow.
9. Danilin, B. S., Minaychev, V. E. (1971). *Fundamentals of Designing Vacuum Systems.* Energy, Moscow.
10. Hablanjn, G. L., Saksaganskiy, A. V., Burmistrov, A. V. (2013). *Vacuum Technology. Equipment, Design, Technology, Operation. Part 1 - Engineering and Physical Fundamentals.* KNITU Publishing House, Kazan.
11. Nesterov, S. B., Burmistrov, A. V., Androsov, A. V., Bronshtein, M. D., Vasilyev, U. K., Erofeev, A. I., Salikeev, S. I. (2012). *Vacuum Systems Complex Calculating Methods.* Technosfera, Moscow.
12. Rozanov, L. N. (2007). *Vacuum Technology.* High School, Moscow.
13. Frolov, E. S., Minaychev, V. E, Aleksandrova, A. T. (1992). *Vacuum Technology.* Mashynostroyeniye, Moscow.
14. Pipko, A. I, Pliskovskiy, V. Y., Korolev, B. I., Kuznecov, V. I. (1981). *Fundamentals of Calculating Vacuum Systems.* Energoizdat, Moscow.
15. Aftab, S. M. A., Rafie, M. A. S., Razak, N. A., Ahmad, K. A. (2016). Turbulence model selection for low Reynolds number flows. *PLoS One*, Vol. 11(4), article number e0153755, doi: 10.1371/journal.pone.0153755.
16. Stephens, D. W., Mohanarangam, K. (2010). Turbulence model analysis of flow inside a hydrocyclone. *Progress in Computational Fluid Dynamics*, Vol. 10(5/6), pp. 366–373.
17. Shams, M., Raeini, A. Q., Blunt, M. J., Bijeljic, B. (2018). A numerical model of two-phase flow at the micro-scale using the volume-of-fluid method. *Journal of Computational Physics*, Vol. 357, pp. 159–182.
18. Hirt, C. W., Nichols, B. D. (1981). Volume of Fluid (VOF) method for the dynamics of free boundaries. *Journal of Computational Physics*, Vol. 39(1), pp. 201–225.
19. Menter, F. R. (1994). Two-equation Eddy-viscosity turbulence models for engineering applications. *AIAA Journal*, Vol. 32(8), pp. 1598–1605.

УДК 62-82:681.587.34

Проектування баку для системи видалення відходів літака з використанням методів числового моделювання і результатів стендових випробувань

Медведєв С. В.[1], Лантін Д.[2]

[1] Державне підприємство «АНТОНОВ», вул. Академіка Туполєва, 1, 03062, м. Київ, Україна;
[2] ТОВ «Юнайтед Інтеріорс Інтернешнл», вул. Сібрук Айленд, 2535, Джонс Айленд, 29455, Південна Кароліна, США

Анотація. Сучасний пасажирський літак неможливо розглядати без вимог щодо забезпечення безпеки і комфорту перебування пасажирів на борту. Однією із систем, що забезпечує необхідні комфортні умови в літаку, є система видалення відходів. На сьогоднішній день перспективним типом систем видалення відходів є система вакуумного принципу дії. Система видалення відходів цього типу є сукупністю складних багатофункціональних підсистем збору відходів, зберігання відходів, вакуумування, зливання і промивання та управління системою. Розроблення таких систем, що складаються з пристроїв, що працюють на різних фізичних принципах функціонування, є комплексною наукоємною проблемою, пов'язаною з проведенням різнопланових прикладних досліджень у області проектування, розроблення і цільового застосування систем даного типу. Одним із основних елементів системи є бак зберігання відходів. Важливим етапом при проектуванні бака є визначення його масогабаритних характеристик на ранніх етапах розроблення. На ці характеристики чинись вагомий вплив процес наповнення бака, який є визначальним і для розміщення функціонального обладнання у ньому. У зв'язку з вищезазначеним, метою цієї статті є дослідження процесу наповнення бака за допомогою методів чисельного моделювання.

Ключові слова: вакуум, бак відходів, проектування, випробувальний стенд.

JOURNAL OF ENGINEERING SCIENCES
ЖУРНАЛ ІНЖЕНЕРНИХ НАУК
ЖУРНАЛ ИНЖЕНЕРНЫХ НАУК
Web site: http://jes.sumdu.edu.ua
DOI: 10.21272/jes.2019.6(2).f1 Volume 6, Issue 2 (2019)

Analysis of Machined Depth and Hole Diameter on Soda-lime Glass Using Electrochemical Discharge Machining Process

Pawar P.*, Kumar A., Ballav R.

National Institute of Technology Jamshedpur, 831014 Jamshedpur, Jharkhand, India

Article info:
Paper received: February 19, 2019
The final version of the paper received: April 6, 2019
Paper accepted online: April 11, 2019

***Corresponding Author's Address:**
pravin.1900@gmail.com

Abstract. The machining of a glass material is highly complicated due to its physical as well as chemical properties. The electrochemical discharge machining is an integrated hybrid machining process which has utilized to machining of conducting materials as well as high strength non-conducting materials having brittleness and high hardness. In this research article, the electrochemical discharge machining experimental setup was built and fabricated for machining of non-conducting materials. The electrochemical discharge machining process was applied for drilling on soda-lime glass material. The experiments were done with reference to Taguchi L_{27} orthogonal array approach and scrutinized by utilizing the MINITAB 17 software. The machined depth and hole diameter results were inspected after electrochemical discharge drilling on soda-lime glass material with considering the machining conditions such as voltage, electrolyte concentration, and rotation. The observation results showed that voltage is the major parameter for machined depth and hole diameter followed by electrolyte concentration and rotation of tool electrode.

Keywords: electrochemical discharge machining, machined depth, hole diameter, Taguchi method, soda-lime glass.

1 Introduction

The machining technology is utilized to make the high-quality product by changing shape, tolerance, dimensions and surface quality of the product. The advanced non-traditional technique is employed for machining of hard and brittle materials [1]. The electrochemical discharge machining (ECDM) technique is combinations of two manufacturing process viz. electrochemical machining process (ECM) and electro-discharge machining (EDM) process [2]. The ECDM process is beneficial to machined non-conducting materials by combined machining effect i.e. electric discharge and electrochemical reaction process [3]. The ECDM machining technology invented firstly by Kurafuji et al. in the year 1968 [4]. In this process at higher machining voltage and higher electrolyte concentration machining conditions can produce micro holes with maximum precision [5]. The maximum machining depth was achieved by using abrasive cutting tools in the ECDM drilling process at the highest electrolyte concentration and supply voltage [6]. In ECDM process the mean stationary current-voltage characteristics have mainly five notable regions such as instability region, thermodynamic and over the potential region, Ohmic region, arc region and limiting current region [7]. In the area of ECDM process, the many researchers utilized NaOH as electrolyte medium, Tungsten carbide as cathode tool electrode material and Graphite as anode tool material [8]. The glass is the most important material for engineering and medical field from the very long period because of vast development in the glass industry. It has very important properties such as high electrical resistivity, various reflective indices, homogeneity, high hardness, non-porosity, durability, isotropy, temperature stability, high chemical and corrosion resistance, attractive appearance, optical transparency and biocompatibility [9].

In this research work the ECDM was designed and fabricated which was used to machined soda-lime glass material. The machined depth and hole diameter were investigated with consideration of machining conditions such as voltage, rotation of tool electrode, and electrolyte concentration.

2 Research Methodology

2.1 Basic working principle and experimental setup of ECDM

Figure 1 represents the basic working principle of the ECDM process. In this process, a cathode, anode and workpiece are immersed inside an aqueous electrolyte medium.

The size of the cathode tool is smaller than the anode tool electrode. When D.C. voltage supply approx. 20 to 30 V applied between cathode and anode tool electrode then electrolysis takes place. Then, oxygen bubbles and Hydrogen gas bubbles are developed at the anode and cathode. When the voltage is raised, the current rises and a large number of bubbles formed a bubble layer around the cathode and anode. The bubbles coalesce into a gas film at the round surface of the cathode when voltage utmost than the critical voltage. At that time the light emission is seeing and electrical discharges take place. The fabricated ECDM machining setup is shown in Figure 2.

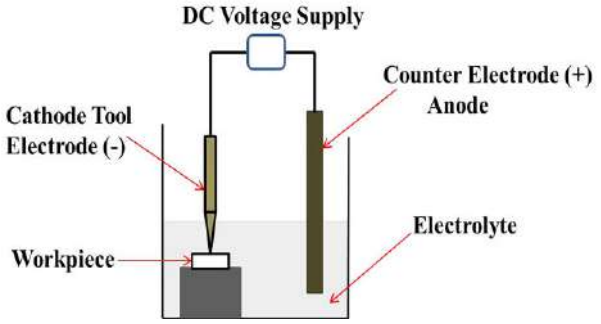

Figure 1 – Basic working principle of ECDM

Figure 2 – Experimental setup of ECDM

2.2 Experimental conditions

In this setup X, Y and Z axis movement was controlled by manually using compound sliding (X and Y) and single axis sliding (Z) mechanism. The workpiece was holding on fixture and fixture was placed on ECDM electrolyte cell. The ECDM cell fixed on the X-Y axis compound slide which was mounting on the machine table. The cathode electrode was attached to the Z-axis sliding table. The gravity feeding mechanism was used to move workpiece in the upward direction during the ECDM machining process. The cathode tool electrode was fixed to stepper motor spindle and its speed is controlled with Arduino Uno board through the computer. The D.C. voltage was given between the cathode tool and the anode tool electrode [10]. The conically shaped cathode electrode (gunmetal) having tooltip diameter 1 mm and increased up to 3 mm diameter was utilized. The stainless steel 416 was taken as the anode electrode having 15 mm diameter. For the experimentation, KOH electrolyte chemical was used and machining time is set to be 15 minutes for each experiment. The micro-hole was drilled on 150×140×3 mm^3 Soda-lime glass material plate by using the ECDM process. The Taguchi L_{27} orthogonal array method was applied during ECDM drilling. An assortment of the design of experiments with reference to the total degree of freedom required for an experiment. In this experimental work selecting, three factors with three levels and their two-way interactions taking into consideration thus. The total degree of freedom is 18. Therefore, for experimental work L_{27}, an orthogonal array was utilized, which has 26 degrees of freedom. In this machining process voltage, rotation and electrolyte concentrations were taken as input machining factors with machined depth and hole diameter were taken as output responses. Table 1 indicates that input process parameters and their individual levels [11].

Table 1 – Process parameters and their levels

Factor	Parameters	Unit	Levels		
			1	2	3
V	Voltage	V	45	55	65
R	Rotation speed	rpm	15	30	50
C	Electrolyte Concentration	%	05	10	15

The Table 2 shows that experimental results which include input process parameters and output responses. The signal indicates the influence of each factor on the response, while noise is the measure of the effect of deviation as of average responses. S/N ratio is being contingent on the nominal-the-better, lower-the-better, larger-the-better criteria. The S/N ratio is selected based on the previous research work information and expertise. In current experimental work, hole diameter was considered as nominal is best because average hole diameter results were taken into consideration and the targeted nominal hole diameter is set for 2 mm. In the case of machined depth larger-the-better criteria has been chosen. The S/N ratio is evaluated by utilizing the following formula shown in equations [12]:

1) for larger is better:

$$S/N = -10\log_{10}\left(\frac{1}{n}\sum_{i=1}^{n}\frac{1}{y_i^2}\right) \quad (1)$$

2) for nominal is the best:

$$S/N = -10\log_{10}\left(\sigma^2\right) \quad (2)$$

where σ – standard deviation of the responses for all noise factors for the given factor level combination. The analysis of experimental results which is shown in Table 2 was estimated with the MINITAB 17 software.

Microscopic images of experimental results are presented in Figure 3.

Table 2 – Taguchi L_{27} Orthogonal array and experimental results

No.	Voltage, V	Rotation speed, rpm	Electrolyte concentration, %	Hole diameter, mm	Machined depth, mm
1	45	15	05	0.70	0.05
2	45	15	10	1.06	0.08
3	45	15	15	1.20	0.10
4	45	30	05	1.02	0.07
5	45	30	10	1.13	0.08
6	45	30	15	1.18	0.10
7	45	50	05	1.15	0.08
8	45	50	10	1.21	0.11
9	45	50	15	1.28	0.10
10	55	15	05	1.52	0.09
11	55	15	10	1.58	0.13
12	55	15	15	1.70	0.18
13	55	30	05	1.50	0.11
14	55	30	10	1.62	0.14
15	55	30	15	1.75	0.19
16	55	50	05	1.55	0.12
17	55	50	10	1.60	0.16
18	55	50	15	1.74	0.20
19	65	15	05	1.64	0.15
20	65	15	10	1.81	0.17
21	65	15	15	1.92	0.24
22	65	30	05	1.61	0.14
23	65	30	10	1.77	0.26
24	65	30	15	1.95	0.25
25	65	50	05	1.58	0.17
26	65	50	10	1.88	0.28
27	65	50	15	2.02	0.32

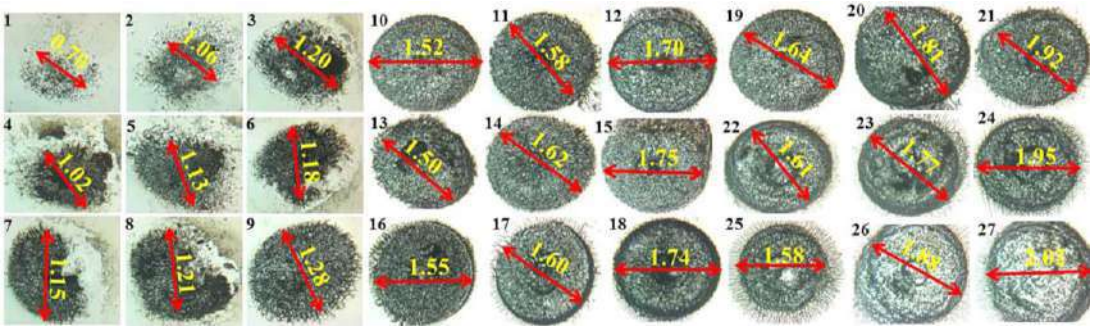

Figure 3 – Microscopic images of experimental results

3 Results and Discussion

3.1 Effect on the machined depth

The rotary speed of tool electrode may possibly influence the efficiency, cutting ability and quality of machining performance [13, 14].

The voltage has utmost significant parameters during the ECDM drilling process because it creates more sparks energy when the voltage is increased. Consequently, it increases the machined depth when increasing voltage. Also, high electrolyte concentration raises chemical etching of glass which rises machining depth [7]. In this study, the machining depth is raised when the applied voltage rises from 45 to 65 V. This is due to the applied voltage is primarily because of field emission law [13, 18].

Figure 4 shows the mean S/N ratios plot for machined depth which indicates the effect of each parameter on

machined depth. Figures 5–7 show surface plots for machined depth which indicates the influence of three different parameters viz. voltage, rotation and electrolyte concentration on the machined depth output response. The following figures exhibit the linear increase in voltage resulting in the increase in machined depth hence it is the major parameter.

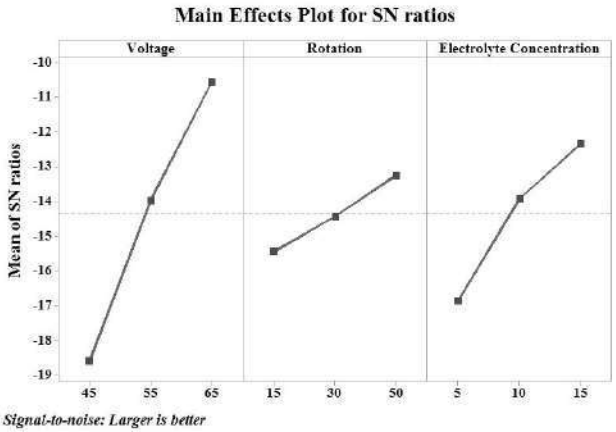

Figure 4 – Mean S/N ratios plot for machined depth

The mathematical model for machined depth was getting through the MINITAB 17 software which is presented as follows:

$$Machined..Depth = 0.179 + (1.60V^2 + 0.04R^2 + \\ + 0.36C^2 - 6.42V - 0.30R - 8.68C)\cdot 10^{-3} + \\ + (41.70VC + 2.10RC - 7.10VR)\cdot 10^{-5}. \quad (3)$$

The ANOVA table (Table 3) shows the P-value of voltage, the concentration of electrolyte and rotation is smaller than 0.05 therefore, is it most significant parameters. The value of R-squared is 90.2 %. The Pred. R-squared of 82.1 % is in reasonably similar to the Adj. R-squared of 87.2 %. The response table 4 reveals the average of each output response characteristic for each level of each factor. The ranks and delta values showed that voltage has the maximum effect on machined depth and is followed by electrolyte concentration and rotation.

Table 3 – ANOVA table for machined depth

Source	DF	Adj SS	Adj MS	F value	P value
Voltage	2	0.0816	0.0408	64.35	0.000
Electrolyte conc.	2	0.0277	0.0135	21.85	0.000
Rotation	2	0.0069	0.0034	5.41	0.013
Error	20	0.0127	0.0006	–	–
Total	26	0.1288	–	–	–
S		R-sq.	R-sq. (adj.)	R-sq. (pred.)	
0.025		90.2 %	87.2 %	82.1 %	

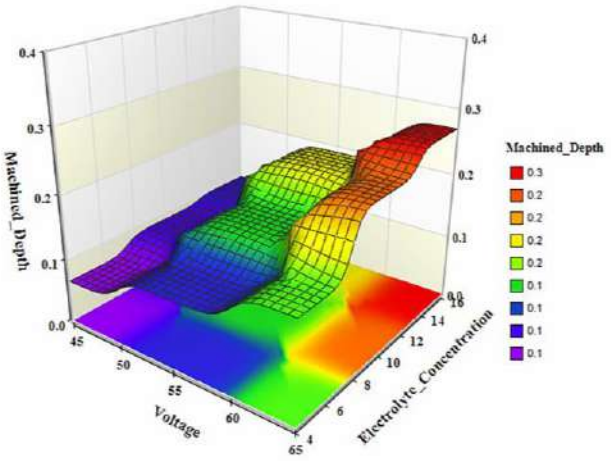

Figure 5 – Surface plot for machined depth vs. voltage, electrolyte concentration

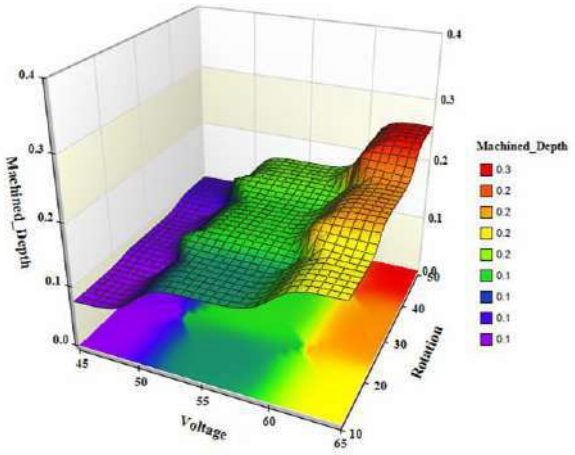

Figure 6 – Surface plot for machined depth vs. voltage, rotation

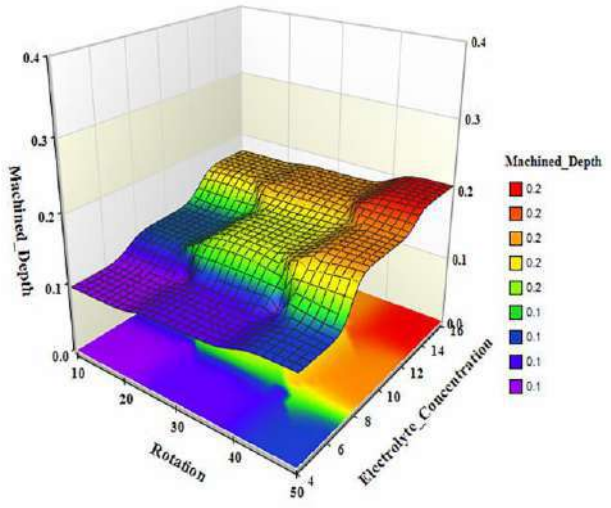

Figure 7 – Surface plot for machined depth vs. rotation, electrolyte concentration

Table 4 – Response table for S/N ratios of machined depth

Level	Voltage, V	Electrolyte concentration, %	Rotation, rpm
1	–21.6	–19.8	–18.4
2	–17.0	–16.9	–17.4
3	–13.5	–15.3	–16.2
Delta	8.1	4.5	2.2
Rank	1	2	3

3.2 Effect on hole diameter

When voltage and electrolyte concentration raises then hole diameter also rises. Thus, voltage and electrolyte concentration are the utmost important parameters for hole diameter during ECDM drilling process [15, 16]. Figure 8 shows the mean plot for hole diameter during ECDM soda-lime glass drilling process which indicates the effect of each parameter on hole diameter.

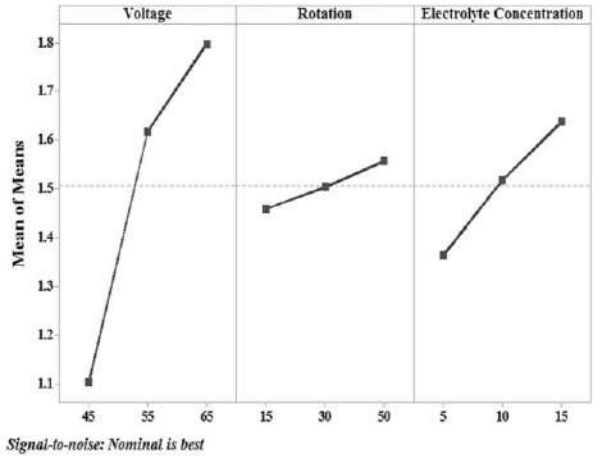

Figure 8 – Mean plot for hole diameter

Figures 9–11 show surface plots for hole diameter which indicates the influence of three different parameters viz. voltage, rotation and electrolyte concentration on the hole diameter output response. The figure exhibits the linear increase in voltage subsequent into linearly increases in hole diameter, as a result, it is the major parameter.

ANOVA indicated that the total sum of squares of the deviation is the same as the sum of the square of standard deviation initiated by each input factor which is shown in table 5 for hole diameter. The statistical consequence to the output response is calculated by using the F-values and P-values of ANOVA. If the P-value is lesser than 0.05 then the parameter is significant. The highest value F shows the most significant parameter. The R-squared is statistical measures of the intimacy of the data are to fit the regression line. In this experimental study, attained the value of R-squared is 95.78%. The Pred. R-squared of 92.30% is in reasonably similar with the Adj. R-squared of 94.51%.

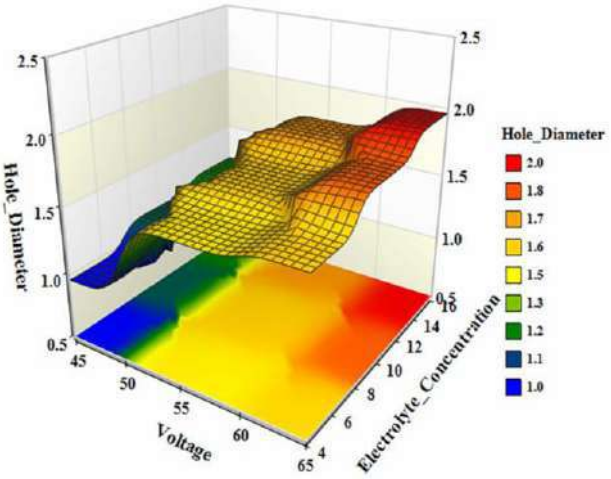

Figure 9 – Surface plot for hole diameter vs. voltage, electrolyte concentration

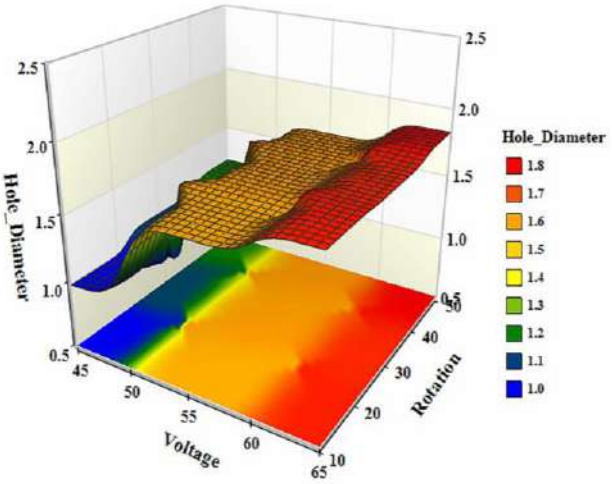

Figure 10 – Surface plot for hole diameter vs. voltage, rotation

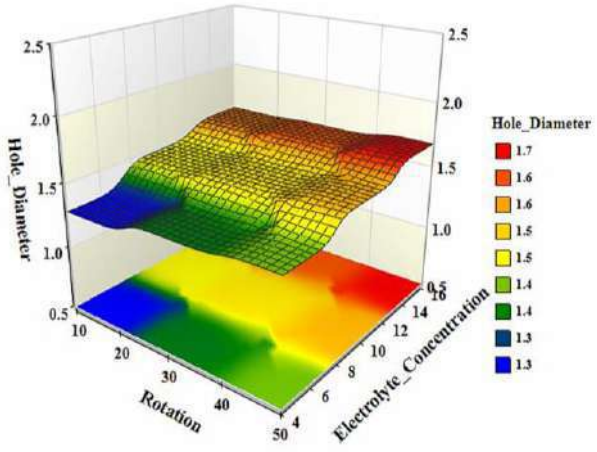

Figure 11 – Surface plot for hole diameter vs. rotation, electrolyte concentration

The F value is highest for the parameter of voltage therefore, it is the most significant parameter. The P value of voltage and electrolyte concentration is lower than 0.05 as a result, it is most dominant parameters [17]. The response Table 6 demonstrates the average of each output response characteristic for each level of each factor. The ranks and delta values showed that voltage has the highest influence on hole diameter and is followed by electrolyte concentration and rotation.

Table 5 – ANOVA table for hole diameter

Source	DF	Adj SS	Adj MS	F value	P value
Voltage	2	2.3379	1.1690	194.80	0.000
Electrolyte conc.	2	0.3407	0.1704	28.38	0.000
Rotation	2	0.0431	0.0216	3.59	0.046
Error	20	0.1201	0.0060	–	–
Total	26	2.8418	–	–	–
S		R-sq.	R-sq. (adj.)	R-sq. (pred.)	
0.077		95.8 %	94.5 %	92.3 %	

Table 6 – Response table for hole diameter

Level	Voltage, V	Electrolyte concentration, %	Rotation, rpm
1	1.1	1.4	1.4
2	1.6	1.5	1.5
3	1.8	1.6	1.6
Delta	0.7	0.3	0.1
Rank	1	2	3

The mathematical model for hole diameter was getting through the MINITAB 17 software which is presented as follows:

$$Hole.Diameter = -6.047 + 0.2225V + 0.01965R + \\ + 0.0221C - 0.001672V^2 + 0.00008R^2 - 0.0069C^2 - \\ - 0.00264VR + 0.000450VC - 0.000179RC. \quad (4)$$

3.3 Confirmation tests

Confirmation test has been carried out to validate the enhancement of performance characteristics while ECDM of soda-lime glass material. The optimum parameters are selected for the confirmation test from response surface methodology optimization graph which is shown in Figure 12. It can be seen that the overall performance of the ECDM process for soda-lime glass material has been improved which is shown in Table 7.

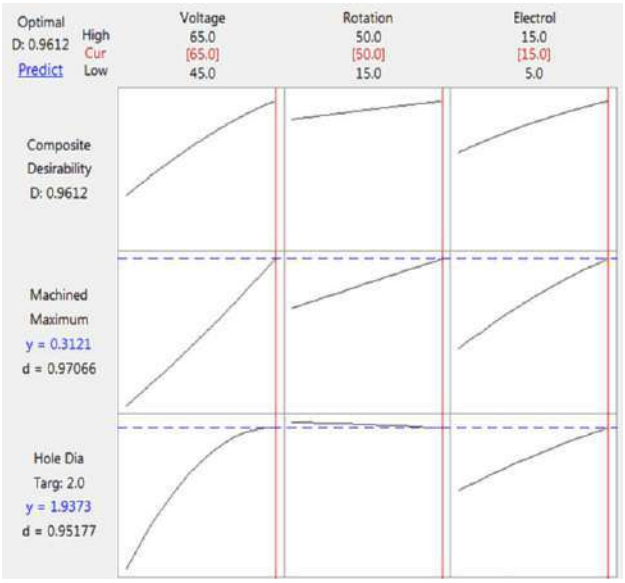

Figure 12 – Response surface methodology optimization plot for machined depth and hole diameter

Table 7 – Confirmation test results

Optimal parameters			Output results	Predicted results	Exper. res.	Error, %
Volt.	Conc.	Rot.				
65	15	50	Machined depth, mm	0.31	0.29	7.6
			Hole diameter, mm	1.94	2.05	5.8

4 Conclusions

The ECDM setup was built, design and manufactured for machining of non-conducting materials. In this work, two output responses are investigated viz. machined depth and hole diameter by considering the three input factors such as voltage, electrolyte concentration, and rotation. The experimental work was carried out using the ECDM process on soda-lime glass material using gunmetal as a cathode electrode. From the current experimental observations, it can be concluded that the voltage was the most significant factor for the machined depth and hole diameter followed by electrolyte concentration and rotation. The optimum input factors combination for maximum machined depth and the nominal value for hole diameter are voltage 65 V, electrolyte concentration 15 %, and rotation 50 rpm.

References

1. Slatineanu, L., Dodun, O., Coteata, M., Goncalves-Coelho, A.M., Besliu, I., Pop, N. (2009). Machining methods based on the impact effects. *International Journal of Modern Manufacturing Technologies*, Vol. 1(1), pp. 83–88.
2. Goud, M., Sharma, A. K., Jawalkar, C. (2016). A review on material removal mechanism in electrochemical discharge machining (ECDM) and possibilities to enhance the material removal rate. *Precision Engineering*, Vol. 45, pp. 1–17.
3. Singh, T., Dvivedi, A. (2016). *Developments in electrochemical discharge machining: A review on electrochemical discharge machining, process variants and their hybrid methods. International Journal of Machine Tools and Manufacture*, Vol. 105, pp. 1–13.

4. Kurafuji, H., Suda, K. (1968). Electrical discharge drilling of glass, *Annals of the CIRP*, Vol. 16, pp. 415–419.
5. Yang, C. T., Ho, S. S., Yan, B. H. (2001). Micro hole machining of borosilicate glass through electrochemical discharge machining (ECDM). *Key Engineering Materials*, Vol. 196, pp. 149–166.
6. Jain, V. K., Choudhury, S. K., Ramesh, K. M. (2002). On the machining of alumina and glass, *International Journal of Machine Tools and Manufacture*, Vol. 42(11), pp. 1269–1276.
7. Wuthrich, R., Fascio, V. (2005). Machining of non-conducting materials using electrochemical discharge phenomenon – an overview. *International Journal of Machine Tools and Manufacture*, Vol. 45(9), pp. 1095–1108.
8. Pawar, P., Ballav, R., Kumar, A. (2015). Revolutionary developments in ECDM process: an overview. *Materials Today: Proceedings*, Vol. 2(4–5), pp. 3188–3195.
9. Bansal, N. P., Doremus, R. H., (2013). Handbook of Glass Properties (1st ed.). *Elsevier Publishing*.
10. Pawar, P., Ballav, R., Kumar, A. (2018). *Development and manufacturing of Arduino based electrochemical discharge machine*, *Journal of Machine Engineering*, Vol. 18(1), pp. 45–60.
11. Pinar, A. M., Uluer, O., Kırmaci, V. (2009). Optimization of counter flow Ranque–Hilsch vortex tube performance using Taguchi method. *International Journal of Refrigeration*, Vol. 32(6), pp. 1487–1494.
12. Roy, A., Nath, N., Nedelcu, D. (2017). Experimental investigation on variation of output responses of as cast TiNiCu shape memory alloys using wire EDM. *International Journal of Modern Manufacturing Technologies*, Vol. 9(1), pp. 90–101.
13. Jiang, B., Lan, S., Ni, J. (2014). Experimental investigation of drilling incorporated electrochemical discharge machining. *Proceedings of the ASME 2014 International Manufacturing Science and Engineering Conference*, Vol. 2, pp. 1–8.
14. Chak, S. K., Rao P. V. (2008). The drilling of Al_2O_3 using a pulsed DC supply with a rotary abrasive electrode by the electrochemical discharge process. *The International Journal of Advanced Manufacturing Technology*, Vol. 39(7–8), pp. 633–641.
15. Mallick. B., Sarkar. B. R., Doloi. B., Bhattacharyya. B. (2014). Multi criteria optimization of Electrochemical Discharge Micromachining process during micro-channel generation on glass. *Applied Mechanics and Materials*, Vol. 592–594, pp. 525–529.
16. Madhavi, B. J., Hiremath, S. S. (2016). Investigation on machining of holes and channels on borosilicate and sodalime glass using µ-ECDM Setup. *Procedia Technology*, Vol. 25, pp. 1257–1264.
17. Greenland, S., Senn, S. J., Rothman, K. J., Carlin, J. B., Poole, C., Goodman, S. N., Altman, D. G. (2016). Statistical tests, P values, confidence intervals, and power: a guide to misinterpretations. *European Journal of Epidemiology*, 3Vol. 1(4), pp.337–350.
18. Wei C., Ni J., Hu, D. (2010). Electrochemical discharge machining using micro-drilling tools. *Transactions of NAMRI/SME*, Vol. 38, pp. 105–111.

УДК 621.793

Аналіз глибини і діаметра отворів при електрохімічному обробленні силікатного скла

Павар П., Кумар А., Баллав Р.

Національний технологічний інститут м. Джамшедпур, 831014,м. Джамшедпук, штат Джаркханд, Індія

Анотація. Механічна обробка скляного матеріалу є надзвичайно важкою через його фізичні та хімічні властивості. Оброблення електрохімічним розрядом є інтегрованим гібридним процесом оброблення провідних матеріалів, високоміцних непровідних матеріалів з високою твердістю і крихкістю. У цьому дослідженні спроектована і виготовлена експериментальна установка для механічного оброблення непровідних матеріалів електрохімічним розрядом. Електрохімічний процес застосовується для свердління отворів у силікатному матеріалі. Експерименти були проведені із застосуванням ортогонального масиву L_{27} методу Тагучі та релізовано у комп'ютерній програмі MINITAB 17. Результати оброблених електрохімічним способом глибини і діаметра отворів у силікатному склі перевірялись з урахуванням таких умов оброблення як напруга, концентрація електроліту і частота обертання. Результати досліджень показали, що основним параметром отримання необхідної глибини і діаметра оброблюваного отвору є у першу напруга. Концентрація електроліту і частота обертання інструмента є також важливими, але другорядними параметрами.

Ключові слова: електрохімічне оброблення, оброблювана глибина, діаметр отвору, метод Тагучі, силікатне скло.

JOURNAL OF ENGINEERING SCIENCES
ЖУРНАЛ ІНЖЕНЕРНИХ НАУК
ЖУРНАЛ ИНЖЕНЕРНЫХ НАУК

Web site: http://jes.sumdu.edu.ua

DOI: 10.21272/jes.2019.6(2).f2 Volume 6, Issue 2 (2019)

General Features of the Metallic Corrosion in Raw Crude Oils

Aluvihara S.[1*], Premachandra J. K.[2]

[1] Department of Chemical and Process Engineering, University of Peradeniya, 20400 Peradeniya, Sri Lanka;
[2] Department of Chemical and Process Engineering, University of Moratuwa, 10400 Katubedda, Sri Lanka

Article info:
Paper received: April 2, 2019
The final version of the paper received: June 12, 2019
Paper accepted online: June 17, 2019

[*]**Corresponding Author's Address:**
sureshaluvihare@gmail.com

Abstract. Raw crude oils are mainly composed of various hydrocarbons while having trace amounts of corrosive compounds such as sulphur compounds, naphthenic acids, and salts. In the existing research, there were expected to investigate the impact of such corrosive properties on the corrosion of seven different types of ferrous metals. As the methodology, the major corrosive properties of selected two different types of crude oils and the chemical compositions of seven selected metal types were measured and analyzed by the standard methodologies and recommend instruments. The corrosion rates of such metals were determined by the relative weight loss method after certain immersion time periods simultaneously with the microscopic analysis of corroded metal surfaces. In addition, the decayed metallic elemental concentrations from metals into crude oils were analyzed by the atomic absorption spectroscopy (AAS) and the impact of the corrosion on the initial hardness of metals were measured by the Vickers hardness tester. As the results and outcomes of the entire research that there observed relatively lower corrosion rates from stainless steels with at least 12 % of chromium and some amount of nickel, higher corrosive impact from salts on the metallic corrosion, formations of FeS, Fe_2O_3, corrosion cracks and pitting on the metal surfaces, decay of copper and ferrous from some of metals sometimes in significantly and small reductions of the initial hardness of most of metals due to the corrosion.

Keywords: raw crude oils, corrosive compounds, metals, weight loss, decay, corrosion.

1 Introduction

Raw crude oils are dominant earth resources that found from the interior part of the earth that mostly composed with various hydrocarbons since having less amounts of some other compounds foremost of the corrosive compounds [1–6]. According to the explanations of the phenomenon of corrosion it is usually defined as the formations of the relevant metal sulfides, oxides or hydroxides on the metal surface as the result of either chemical or electrochemical reaction on the metallic surfaces due to the interactions of such metals either with some strong oxidizing chemical compound or any system which is composed with both water and oxygen. The corrosion process may be quietly different with the conditions of such corrosive compounds or the supportive conditions such as the temperature [4–15].

According to the recently performed experiments and literature reviews of the chemical engineering concepts that there were speculated some significant impact from various sulfur compounds such as sulfoxides, thiophenes, hydrogen sulfides and also elemental sulfur in the most of investigations under different conditions and the impact of salts and organic acids also play a dominant background in the metallic corrosion [6–15].

In the existing research mainly, there were expected to analyze the impact of elemental sulfur, Mercaptans, organic acids and salts of different types of selected crude oils on the corrosion of seven different types of selected ferrous metals which are widely used in the industry of crude oils refining. The investigations were based on both qualitatively and quantitatively analysis of the corrosion.

2 Research Methodology

According to the availability and the requirements of the existing research two different types of crude oils were selected for the experiments which are slightly different in their chemical compositions including corrosive composites. Those are namely as Murban and Das Blend also with the sulfur content Das Blend may have higher amount of sulfur which is an important factor for the corrosion. The elemental sulfur contents, Mercaptans contents, organic acid contents and salt contents of both crude oils were measured by the standard methods and instruments as explained in Table 1.

Table 1 – Analysis of the corrosive properties of crude oils

Property	Method	Readings
Sulfur content	Directly used the crude oil samples to the XRF analyzer	Direct reading
Acidity	Each sample was dissolved in a mixture of toluene and isopropyl and titrated with potassium hydroxide	End point
Mercaptans content	Each sample was dissolved in sodium acetate and titrated with silver nitrate	End point
Salt content	Each sample was dissolved in organic solvent and exposed to the cell of analyzer	Direct reading

By considering the applicability of the metals in the industry of crude oil refining and the variability of the chemical compositions of such metals seven different types of metals were selected as the corrosion determination samples. The selected metals and some of their applications are given in the below:

– carbon steel (high) – transportation tubes, storage tanks;

–carbon steel (medium) – storage tanks, transportation tubes;

– carbon steel (mild steel) – storage tanks;

– 410-MN: 1.8 420-MN: 2.8 (stainless steel) – heat exchangers, pre-heaters;

– 410-MN: 1.7 420-MN: 1.7 (stainless steel) – crude distillation columns, pre-heaters;

– 321-MN: 1.4 304-MN: 1.9 (stainless steel) – crude distillation columns;

– Monel 400 – pre-heaters, heat exchangers, desalting units.

The chemical compositions of such metals were tested by the X-ray fluorescence detector. A batch of similar sized metal coupons was prepared from such metal types and the surfaces of such metal coupons were cleaned by the isooctane and sand papers. The initial weight and the dimensions of such metal coupons were measured by in order of analytical balance and micrometer. The prepared metal coupons have been shown in Figure 1.

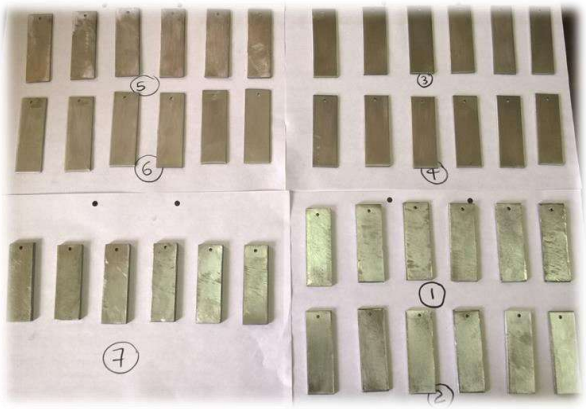

Figure 1 – Prepared metal coupons for the experiment

The prepared metal coupons were immersed in beakers which are filled with crude oils as three homogeneous metal coupons in each crude oil container.

After 15 days immersion time period one metal coupon from each crude oil container was taken out and the corroded metal surfaces were observed through 400X lens of an optical microscope. The corroded metal surfaces of such metal coupons were cleaned by the isooctane and sand papers, and the final weight of each metal coupon was measured by the analytical balance based on the determinations of the corrosion rate of each metal coupon by the weight loss method as discussed in the below [9, 10]:

$$CR = W \cdot k / (D \cdot A \cdot t), \quad (1)$$

where CR – corrosion rate of metal piece; W – weight loss due to the corrosion, g; $k = 22.3$ – constant; D – metal density, g/cm^3; A – area of metal piece, inch^2; t – time, days.

By following the same methodology, the corrosion rates of another two similar sets of metal coupons were determined in order of after 30 and 45 days from the immersion including each analysis stage that mentioned for the first set of metal coupons.

In addition to the basic analysis the decayed metallic concentrations from each metal while the immersion in crude oil samples were tested by the atomic absorption spectroscopy (AAS). The actual reason for this investigation was the observed invisible weight loss of some metals during the determinations of the corrosion rates of metals. In the sample preparation 1 ml of each crude oil sample was diluted with 9 ml of 2-propanol and filtered.

As the last experiment of the current research the variations of the initial hardness of metal coupons after the corrosion were measured by the Vickers hardness tester. The working theories of such instruments have been applied using the following equation:

$$HV = 1.854 \cdot (P/L)^2, \quad (2)$$

where HV – hardness; P – applied Load on the surface of metal; L – diagonal length of a square.

As the essential measurements the initial hardness and hardness after the corrosion of metal coupons were measured by such instrument. By considering the accuracy the hardness of at least three positions on the metal coupons were measured for on measurement.

3 Results and Discussion

The basic results for the analysis of the chemical compositions of the selected ferrous metals have been given in Table 2.

According to the above results it can be obtained some higher ferrous contents in carbon steels, moderate ferrous contents in stainless steels and trace ferrous concentrations in Monel metal. Beside of that there were observed some trace compositions of d-block elements such as nickel, copper and chromium especially in stainless steels because of the aims and objectives of the enhancements

of the strength and corrosive reduction method. Because the combination of the chromium and nickel is a good buffer for the corrosion on the metal surfaces itself when having at least 12 % of chromium and sufficient amount of nickel [1, 3–6].

Table 2 – Chemical compositions of metals, %

Metal	Fe	Ni	Cr	Cu
carbon steel (high)	98.60	0.17	0.14	0.37
carbon steel (medium)	99.36	–	–	–
carbon steel (mild steel)	99.46	–	< 0.07	–
410-MN: 1.8 420-MN: 2.8 (stainless steel)	88.25	0.18	10.92	0.10
410-MN: 1.7 420-MN: 1.7 (stainless steel)	87.44	–	11.99	–
321-MN:1.4 304-MN:1.9 (stainless steel)	72.47	8.65	17.14	–
Monel 400	1.40	64.36	< 0.04	33.29

According to the analysis of the corrosive compounds of both crude oils the obtained results have been shortlisted in Table 3.

Table 3 – Corrosive properties of crude oils

Property	Murban	Das Blend
sulfur content, Wt. %	0.758	1.135
salt content, ptb	4.4	3.6
acidity, mg KOH/g	0.01	0.02
Mercaptans content, ppm	25	56

After referring above numerical values that it is possible to conclude the Das Blend crude oil may have higher corrosive tendency because the above results show higher elemental sulfur content, Mercaptans content, organic acid content and lower salt content in Das Blend crude oils when comparing with Murban crude oil. But, the corrosive impact of some crude oil cannot be estimated only considering the magnitudes of the concentrations of the corrosive compounds in crude oils and it must be considered the supporting conditions for the happening of relevant chemical reactions as well. It has been discussed in ahead with the obtained results in the existing research.

Organic acids are the dominant corrosive compounds presence in most of crude oils since the occurrences because of the abundance of different organic acids in the early living organisms. Such organic acid is also known as naphthenic acids which are having the chemical formula of “RCOOH” and the total amount of organic or naphthenic acids of some crude oil is known as the acidity or total acid number (TAN) of such crude oil. The general chemical reactions of the oxidizing process of organic acids are given in the below [2, 4, 9, 12, 13, 15]:

$$Fe + 2RCOOH \rightarrow Fe(RCOO)2 + H2; \quad (3)$$

$$FeS + 2RCOOH \rightarrow Fe(COOR)_2 + H_2S; \quad (4)$$

$$Fe(COOR)2 + H2S \rightarrow FeS + 2RCOOH. \quad (5)$$

Salts are the foremost corrosive compounds find from crude oils since the occurrences mainly as the forms of NaCl, $MgCl_2$ and $CaCl_2$.The total amount of such salts presence in some crude oil is known as the salt content of such crude oil. When increasing the temperature of crude oils such salts tend to be broken into HCl molecules which are inert in the same conditions. When decreasing the temperature of the system such HCl molecules tend to be reacted with water of even moisture and formed highly corrosive hydrochloric acids. The general chemical reactions between the salts and metals have been given in the following equations [2, 4, 7, 11].

$$CaCl_2 + H_2O \rightarrow CaO + 2HCl; \quad (6)$$

$$HCl + Fe \rightarrow FeCl_2 + 2H_2; \quad (7)$$

$$H2 + S \rightarrow H_2S; \quad (8)$$

$$FeCl_2 + H_2S \rightarrow FeS + 2HCl. \quad (9)$$

Sulfur compounds are some sort of corrosive compounds because of the availability of wide range of various active sulfur compounds with the highly volatile functional groups. Among sulfur compounds most of them are corrosive compounds such as elemental sulfur, Mercaptans, sulfoxides and thiophenes. Mercaptans are highly corrosive compounds which are having a molecular formula of “RSH” because of the high reactivity of relevant functional group. The corrosion reactions may be differing with the behaviors of such corrosive compounds [4, 14]. The corrosion process due to the elemental sulfur is known as the “localized corrosion” which is usually happened at the temperature 80 °C properly.

Additionally, the corrosion process due to the Mercaptans is known as the “sulfidation” which is likely to be happened at about 230 °C properly. The initiation chemical reactions of such corrosion processes have been given in the flowing reactions [2, 4, 11, 13, 14]:

$$S8\ (s) + 8H_2O\ (l) \rightarrow 6H_2S\ (aq) + 2H_2SO_4\ (aq); \quad (10)$$

$$8Fe + S8 \rightarrow 8FeS. \quad (11)$$

Altogether the impact of such corrosive properties on the metallic corrosion it is mandatory to mention about the required supporting conditions when analyzing the impact of such corrosive compounds. According to the determinations of the corrosion rates of metals by the weight loss method the obtained results have been interpreted with respect to the immersion time periods in Tables 4, 5.

Table 4 – Corrosion rates of metals in Murban, $cm^3/(inch \cdot day)$

Metal	Number of days			Average
	15	30	45	
carbon steel (high)	0.812	0.466	0.069	0.449
carbon steel (medium)	0.818	0.180	0.073	0.357
carbon steel (mild steel)	0.110	0.048	0.039	0.066
410-MN: 1.8 420-MN: 2.8 (stainless steel)	0.042	0.016	0.012	0.023
410-MN: 1.7 420-MN: 1.7 (stainless steel)	0.116	0.012	0.008	0.045
321-MN: 1.4 304-MN:1.9 (stainless steel)	0.017	0.007	0.006	0.010
Monel 400	0.356	0.035	0.027	0.139

Table 5 – Corrosion rates of metals in Das Blend, $cm^3/(inch \cdot day)$

Metal	Number of days			Average
	15	30	45	
carbon steel (high)	0.350	0.225	0.025	0.200
carbon steel (medium)	0.481	0.141	0.059	0.227
carbon steel (mild steel)	0.163	0.141	0.101	0.135
410-MN: 1.8 420-MN: 2.8 (stainless steel)	0.044	0.034	0.006	0.028
410-MN: 1.7 420-MN: 1.7 (stainless steel)	0.054	0.035	0.016	0.035
321-MN: 1.4 304-MN:1.9 (stainless steel)	0.023	0.007	0.003	0.011
Monel 400	0.062	0.038	0.016	0.038

The concluded interpretation of the above results has been shown in Figure 2.

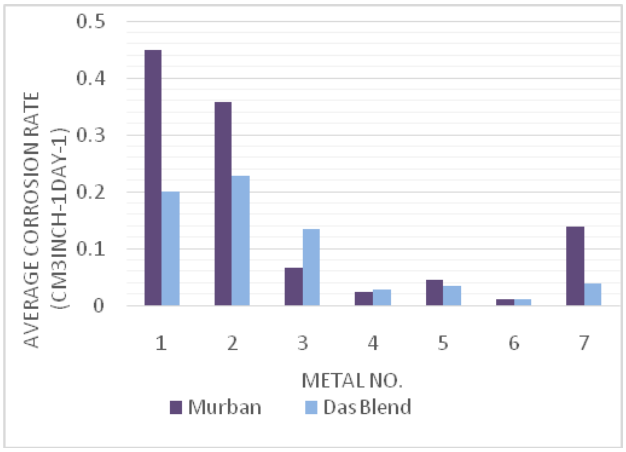

Figure 2 – Average corrosion rates of metals

According to the above graph that it can be concluded the higher corrosion rates from carbon steels, moderate corrosion rates from Monel metal and the relatively lower corrosion rates of stainless steels with respect to both Murban and Das Blend crude oils. When comparing with the corrosion rates of stainless steels the least corrosion rates were observed from 321-N: 1.4304-MN: 1.9 (stainless steel) with respect to both Murban and Das Blend crude oils which is having a chemical composition of 18 % of chromium and 8.65 % of nickel also a good enough combination for the formation of the self-corrosive protection film on the metal surfaces itself because the chromium and nickel are presence with the sufficient amounts [1, 3–6].

When comparing the corrosion rates of metals in both crude oils four types of metals showed their higher corrosion rates in Murban crude oil since the other three types of metals were showing their higher corrosion rates in Das Blend crude oil. According to such observations it is possible to suggest the higher corrosive impact of salts on the metallic corrosion when comparing with the other corrosive compounds. Although it is better to recommend some advanced corrosion rate analysis instrument such as electrical instrument simultaneously with the weight loss method and also investigations of the impact of some more corrosive compounds in various temperature and other supplementary conditions for future works [6–15].

According to the above results the variations of the corrosion rates of metals with respect to the immersion time periods in both crude oils have been interpreted in Figures 3, 4.

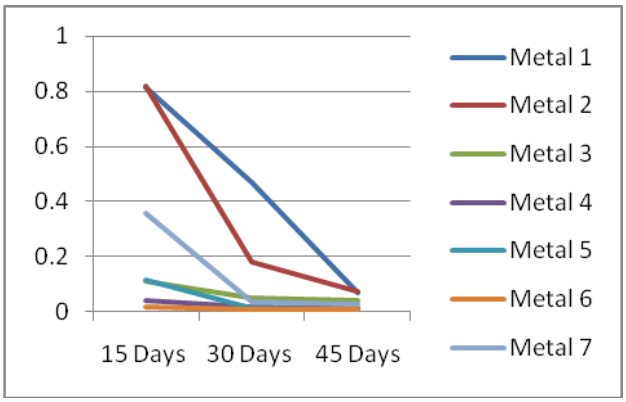

Figure 3 – Variations of the corrosion rates of metals in Murban

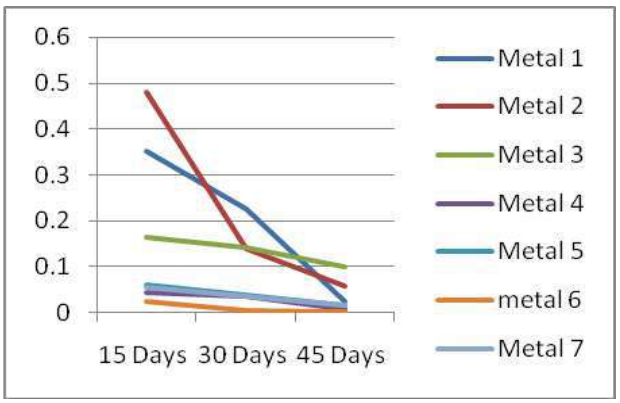

Figure 4 – Variations of the corrosion rates of metals in Das Blend

The above corrosion curves showed some similar distributions of the corrosion rates of metals with the exposure time by following the inversely proportional relationship between the two parameters of the corrosion rate and the exposure time as explained under the weight loss method [9, 10].

According to the explanations of the material and chemical engineering the reductions of the corrosion rate with the exposure time period is happened as the results of the generating corrosion barrio from the formerly formed corrosion compounds on the metal surfaces that the continuously formation of the corrosion in the same rate ahead.

Regarding the analysis of the corroded metal surfaces through the 400X lens of an optical microscope there were observed few of various results that similar with the explanations in the corrosion processes and some sort of different compounds as well. The most highlighted and recognizable corrosion compounds have been interpreted in Figure 5.

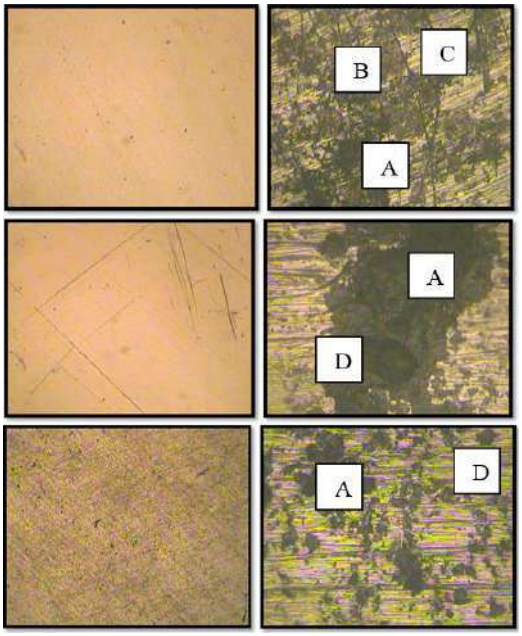

Figure 5 – Corroded metal surfaces:
A – ferrous sulfide (FeS); B – ferrous oxide (Fe_2O_3);
C – corrosion cracks; D – pitting corrosion

Among the various observations some of distinguished features have been emphasized with their physical appearances in Table 6 [1, 3, 6].

Table 6 – Visible appearemces of the corrosion compounds

Compound	Appearances	Observations
FeS	black, brownish black, property of powder, pitting, cracks	observed most of features in each metal piece
Fe_2O_3	rusty color	Observed rarely
CuS	dark indigo / dark blue, property of powder	unable to specify

According to the observations and the identifications of the microscopic analysis results basically it is possible to conclude the formations of the ferrous sulfides (FeS) in most of occasions same as the explanations of under the theoretical conditions, rarely formations of ferrous oxides (Fe_2O_3) due to the presence of both water and oxygen in little amounts, corrosion cracks and some pitting on the metal surfaces due to the decay of metals into crude oils. As the uncertain observations some corrosion compounds were identified that similar with the ferrous sulfides with the visible features and most probably it might be copper sulfide (CuS) although it is impossible to conclude as CuS only having the visible features [1, 3–6, 13]. Therefore, it is better to recommend some compositional analysis of the corrosion compounds by an advanced analytical method such as X-ray diffraction (XRD) for better analysis.

According to the analysis of the decay of metallic elements from metals into crude oils by the atomic absorption spectroscopy (AAS) the obtained results have been interpreted in Table 7.

Table 7 – Decayed metallic concentrations into crude oils / ppm

Metal	Crude oil	Fe	Cu
Carbon Steel	Murban	0.47	–
	Das Blend	1.10	–
Carbon Steel	Murban	0.54	–
	Das Blend	0.02	–
Carbon Steel	Murban	–0.08	–
	Das Blend	–0.48	–
410-MN: 1.8 420- MN: 2.8	Murban	–0.65	–
	Das Blend	–0.78	–
410-MN: 1.7 420-MN: 1.7	Murban	–0.71	–
	Das Blend	–0.79	–
321-MN:1.4 304-MN:1.9	Murban	–0.44	–
	Das Blend	–0.17	–
Monel 400	Murban	–	10.47
	Das Blend	–	9.49

Brief conclusions of above results have been shown in Figures 6, 7.

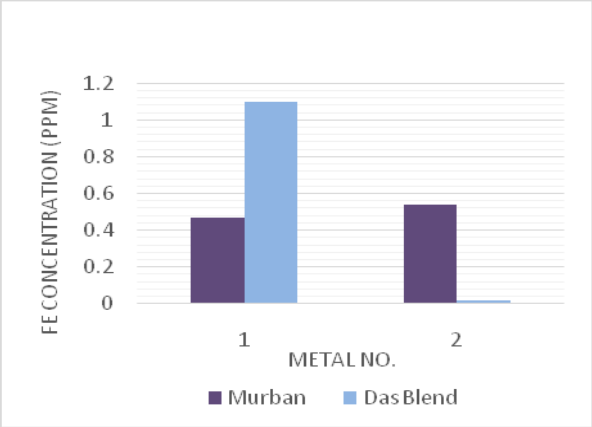

Figure 6 – Decayed ferrous concentrations into crude oils

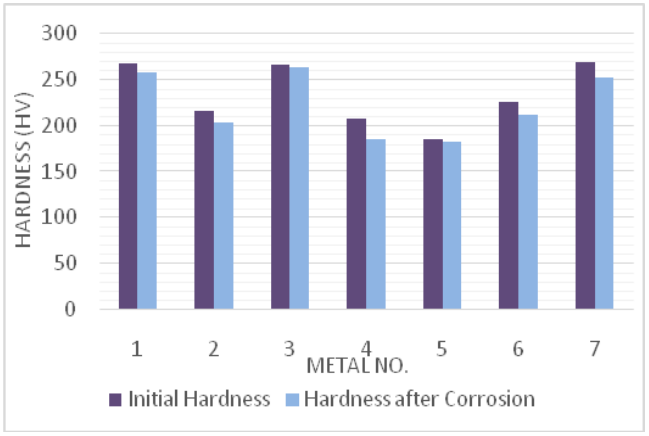

Figure 8 – Variations of the initial hardness of metals due to the corrosion in Murban

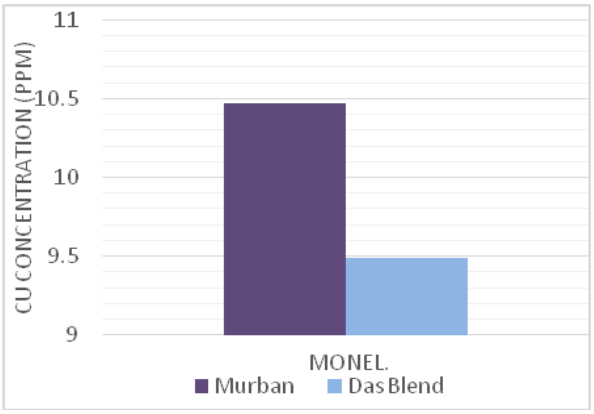

Figure 7 – Decayed copper concentrations into crude oils

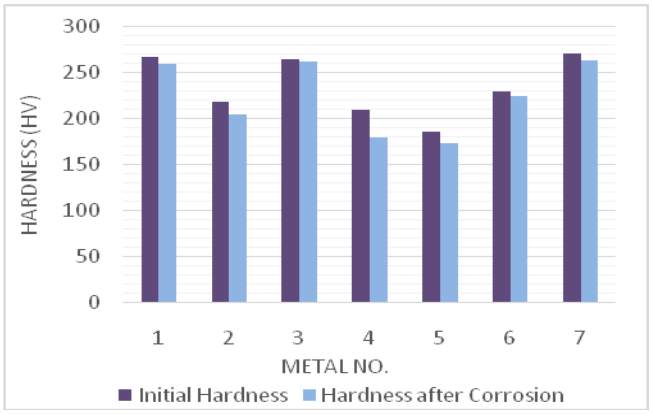

Figure 9 – Variations of the initial hardness of metals due to the corrosion in Das Blend

Basically with the above graphs that there can be seen significant decays of copper from Monel metal which showed some intermediate corrosion rate, higher decays of ferrous from carbon steels which showed the highest corrosion rates and it was not observed any decay of neither copper nor ferrous from any stainless steel into crude oils while the immersion which showed least corrosion rates. According to the reasonable explanations that it is possible to explain with the electron repulsive theory that after formations of the corrosion compounds such corrosion compounds tend to be removed from the metal surfaces either partially or completely from the metal surfaces due to the repulsive and attractive forces between the successive electrons and protons of the relevant compounds [1, 3, 5, 6]. Therefore, the decayed metallic compounds from metals into crude oil may be happened simultaneously with the process of corrosion.

According to the analysis of the variations of the initial hardness of the metals due to the corrosion by the Vicker's hardness tester the obtained results have been interpreted in Figures 8, 9.

The above results showed slight reductions of the initial hardness of most of metals after the formations of the corrosion. This incident is possible to explain with the electron repulsive concept and heterogeneity [1, 3, 5, 6]:

1) due to the repulsive and attractive forces between successive electrons and protons it is possible to be formed some uncertain conditions on the metal surfaces;

2) due to the heterogeneity of the corroded metal surfaces due to the contamination with the corrosion compounds.

4 Conclusions

According to the results of the entire results of the research there were investigated the lower corrosion rates from stainless steels which are having at least 12 % of chromium with sufficient amount of nickel because of the nickel chromium corrosive protection film, relatively higher corrosive impact from salts when comparing with the corrosive impact of other corrosive compounds, formations of FeS, Fe_2O_3, corrosion cracks and cavities on the metal surfaces as the corrosion compounds, significant decay of copper and ferrous from some of metals into crude oils and small reductions of the initial hardness of most of metals due to the corrosion.

5 Acknowledgments

The important guides of the supervisor and technical supports from the laboratory staff are admired prestigiously.

References

1. Khana, O. P. (2009). *Materials Science and Metallurgy*. New Delhi: Dhanpet Rai and Sons Publication.
2. Fahim, M. A., Alsahhaf, T. A., Elkilani, A. (2010). *Fundamentals of Petroleum Refining*. Elsevier, 516, doi: 10.1016/c2009-0-16348-1.
3. Calister, W. D. (2003). *An Introduction of Materials Science and Engineering*. New York: John Wiley and Sons, 820.
4. Davis, M. E., Davis, R. J. (2003). *Fundamentals of Chemical Reaction Engineering*. New York: McGraw-Hill.
5. Singh, R. (2006). *Introduction to Basic Manufacturing Process and Engineering Workshop*. New Delhi: New Age International Publication, 475.
6. Bolton, W. (1993). *Engineering Materials Technology*. Elsevier,468, doi: 10.1016/c2013-0-04622-1.
7. Ajimotokan, H. A., Badmos, A. Y., Emmanuel, E. O. (2009). Corrosion in petroleum pipelines. *New York Science Journal*, Vol. 2 (5), pp. 36–40.
8. Speight, J. G. (1999). *The Chemistry and Technology of Petroleum*. Boca Raton, 934. doi: 10.1201/9780824742119.
9. Afaf, G. A. (2007). *Corrosion Treatment of High TAN Crude*. Khartoum.
10. Okpokwasili, G. C., Oparaodu, K. O. (2014). Comparison of percentage weight loss and corrosion rate trends in different metal coupons from two soil environments. *International Journal of Environmental Bioremediation and Biodegradation*, Vol. 2 (5), pp. 243–249.
11. Usman, A. D., Okoro, L. N. (2015). Mild steel corrosion in different oil types. *International Journal of Scientific Research and Innovative Technology*, Vol. 2 (2), pp. 9–13.
12. Ahmed, I. M., Elnour, M. M., Ibrahim, M. T. (2014). Study the effects of naphthenic acid in crude oil equipment corrosion. *Journal of Applied and Industrial Sciences*, Vol. 2 (6), pp. 255–260.
13. Rickard, D., Luther, G. W. (2007). Chemistry of iron sulfides. *Chemical Reviews*, Vol. 107 (2), pp. 514–562. doi: 10.1021/cr0503658.
14. Fang, H., Nesic, S., Young, D. (2008). Corrosion of mild steel in the presence of elemental sulfur. *International Corrosion Conference and Expo*.
15. Bota, G. M., Nesic, S., Qu, D., Wolf, H. A. (2010). Naphthenic acid corrosion of mild steel in the presence of sulfide scales formed in crude oil fractions at high temperature. *International Corrosion Conference and Expo*.

УДК 665.6:553.982

Загальні особливості металевої корозії у сирій неочищеній нафті

Алувіхара С.[1], Премахандра Дж. К.[2]

[1] Кафедра хімічного і технологічного машинобудування, Університет м. Параденія, 20400, м. Параденія, Шрі-Ланка;
[2] Кафедра хімічного і технологічного машинобудування, Університет Моратува, 10400, м. Катубедда, Шрі-Ланка

Анотація. Сира нафта увосновному складається з різних вуглеводнів, маючи у своєму складі деяку кількість корозійних сполук сірки, нафтенових кислот і солей. У даному дослідженні досліджувався вплив корозійних властивостей на корозію семи різних типів чорних металів. У основі методології досліджень обране визначення основних корозійних властивостей двох різних видів сирої нафти і хімічного складу семи обраних типів металів. Результати вимірювань проаналізовані за стандартною методологією із застосуванням запропонованих інструментів. Швидкість корозії металів визначався методом відносної втрати ваги після заданих періодів занурення та одночасно з мікроскопічним аналізом корозії металевих поверхонь. Крім того, розподіл концентрації металевих включень у сирій нафті був проаналізований методом атомно-абсорбційної спектроскопії, а вплив корозії на початкову твердість металів вимірювався за методом Віккерса. У результат і всього дослідження спостерігалися відносно низькі швидкості корозії нержавіючих сталей з вмістом принаймні 12 % хрому і деякої кількості нікеля. Також спостерігався більш високий корозійний вплив солей на корозію з утворенням хімічних сполук FeS, Fe_2O_3, а також корозійні тріщини і виразки на металевих поверхнях.

Ключові слова: сира нафта, складові корозії, метали, втрати ваги, розкладання, корозія.

JOURNAL OF ENGINEERING SCIENCES
ЖУРНАЛ ІНЖЕНЕРНИХ НАУК
ЖУРНАЛ ИНЖЕНЕРНЫХ НАУК

Web site: http://jes.sumdu.edu.ua

DOI: 10.21272/jes.2019.6(2).f3 Volume 6, Issue 2 (2019)

Numerical Simulation of Viscous Dissipation and Chemical Reaction in MHD of Nanofluid

Govardhan K.[1], Narender G.[2*], Sarma G. S.[2]

[1] GITAM University, Hyderabad, India;
[2] CVR College of Engineering, Hyderabad, India

Article info:
Paper received: May 4, 2019
The final version of the paper received: August 26, 2019
Paper accepted online: August 31, 2019

[*]Corresponding Author's Address:
gnriimc@gmail.com

Abstract. A study of viscous dissipation and chemical reaction effects of nanofluid flow passing over a stretched surface with the MHD stagnation point and the convective boundary condition has been analyzed numerically. The constitutive equations of the flow model are solved numerically and the impact of physical parameters concerning the flow model on dimensionless velocity, temperature and concentration are presented through graphs and tables. Also, a comparison of the obtained numerical results with the published results of W. Ibrahim has been made and found that both are in excellent agreement. As a result of the research, it was obtained that the magnetic parameter has the same increasing influence on the temperature and the concentration field but opposite on the velocity field, the temperature field, and the concentration field reduce with an increase in the Prandtl number, increase in viscous dissipation increases temperature and concentration profile, and concentration as well as the thickness of concentration decrease by increasing values of chemical reaction parameter.

Keywords: magnetohydrodynamic, stretching sheet, nanofluid, viscous dissipation, chemical reaction.

1 Introduction

During the past few years, investigating the stagnation point flow of nanofluids has become more popular among the researchers. Nanofluids are formed by the suspension of the nanoparticles in conventional base fluids. Examples of such fluids are water, oil or other liquids. The nanoparticles conventionally made up of carbon nanotubes, carbides, oxides or metals, are used in the nanofluids. Keen interest has been taken by many researchers in the nanofluids as compared to the other fluids because of their significant role in the industry, medical field and a number of other useful areas of science and technology. Some prominent applications of these fluids are found in magnetic cell separation, paper production, glass blowing, cooling the electronic devices by the cooling pad during the excessive use, etc. Choi [1] introduced the idea of nanofluids for improving the heat transfer potential of conventional fluids. He experimentally concluded with evidence that injection of these particles helps in improving the fluid's thermal conductivity. This conclusion opened the best approach to utilize such fluids in mechanical engineering, chemical engineering, pharmaceuticals, and numerous different fields. Buongiorno [2], Kuznetsov and Nield [3] followed him and extended the investigation. They worked on the effects of Brownian motion in convective transport of nanofluids and the investigation of natural convective transport of nanofluids passing over a vertical surface in a situation when nanoparticles are dynamically controlled at the boundary. Khan and Pop [4] used this concept to evaluate the laminar boundary layer flow, nanoparticles fraction and heat transfer for nanofluids passing over a stretching surface.

2 Literature Review

In the industrial sector and modern technology, non-Newtonian fluids play a vital role. Non-Newtonian fluids have some interesting applications as they are used in the manufacturing of sports shoes, flexible military suits, and viscous coupling. Rising inception of the non-Newtonian fluids like emulsions, molten plastic pulp, petrol, and many other chemicals has triggered an appreciable interest in the study of the behavior of such fluids during motion. The mathematical solutions of the models involving the non-Newtonian fluids are quite interesting and physically applicable. Makinde [5] investigated the buoyancy effect on magnetohydrodynamic stagnation point flow and heat transfer of nanofluids passing over a convectively heated stretching/shrinking sheet. The MHD fluid passing over a stretched sheet, through the porous media with the thermal radiation and the thermal conductivity was examined by Cortell [6].

Naramgari and Sulochana [7] outlined the mass and heat transfer of the thermophoretic fluid flow past an exponentially stretched surface inserted in porous media in the presence of internal heat generation/absorption, infusion, and viscous dissemination. Afify [8] examined the MHD free convective heat and fluid flow passing over the stretched surface with chemical reaction. A numerical analysis of insecure MHD boundary layer flow of a nanofluid past a stretched surface in a porous media was carried out by Anwar et al. [9]. Nadeem and Haq [10] studied the magnetohydrodynamic boundary layer flow with the effect of thermal radiation over a stretching surface with the convective boundary conditions.

Our prime objective is, we first reproduce an analysis study of [11] and then extend the MHD stagnation point flow of nanofluid past a stretching sheet with convective boundary condition. According to our information, viscous dissipation and chemical reaction effects on MHD mixed convection stagnation point flow of nanofluid over a stretching surface is not yet examined. An appropriate similarity transformation has been utilized to acquire the system of nonlinear and coupled ODEs from the system of PDEs. Results are acquired numerically by using the comprehensive shooting scheme. The numerical results are analyzed by graphs for different parameters which appear in the solution affecting the MHD mixed convection stagnation point.

3 Research Methodology

3.1 Mathematical Modeling

Consider the stagnation point flow of two-dimensional viscous steady flow of nanofluid passing over a stretched surface with the convective boundary condition (BC). The stretching sheet was heated with the temperature T_f and the heat transfer coefficient h_f at its lower surface. Here, concentration and uniform ambient temperature are respectively C_∞ and T_∞.

Assume that at the surface, there is not any nanoparticle flux and the impacts of the thermophoresis are taken as a BC. In flow model, $u_w(x) = ax$ is the velocity of the stretching surface, where "a" is any constant. In the direction of the flow, normal to the surface, it is directed towards the magnetic field of strength B_0 which is supposed to be applied in the direction of $+ve$ y-axis. Here magnetic field is negligible because of assumption of very small when compared with the applied magnetic field. The preferred system of coordinates is such as x-axis is directed to the flow and y-axis is perpendicular to it. Proposed coordinate system and flow model are presented in Figure 1.

Flow model of W. Ibrahim [11] shows that in the presence of magnetic field over the surface, the governing equations of conservation of momentum, energy, mass and nanoparticle fraction, under the boundary layer approximation, are as follows:

$$\frac{\partial u}{\partial x} + \frac{\partial v}{\partial y} = 0 \tag{1}$$

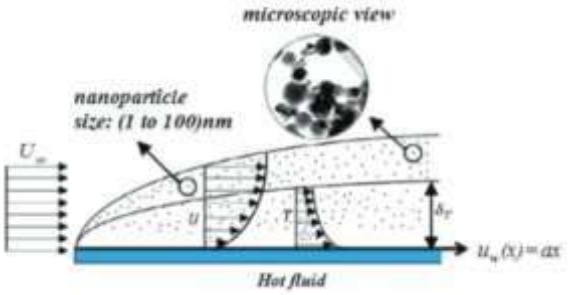

Figure 1 – Geometry for the flow under consideration

$$u\frac{\partial u}{\partial x} + v\frac{\partial v}{\partial y} = \nu\nabla^2 u + U_\infty \frac{\partial U_\infty}{\partial x} + \frac{\sigma B_0^2}{\rho_f}(U_\infty - u) \tag{2}$$

$$u\frac{\partial T}{\partial x} + v\frac{\partial T}{\partial y} = \alpha\nabla^2 T - \frac{1}{\rho c_p}\frac{\partial q_r}{\partial y} + \frac{\nu}{\rho c_f}\left(\frac{\partial u}{\partial y}\right)^2 + \tau\left(D_B \nabla\varphi.\nabla T + \frac{D_T}{T_\infty}\nabla T.\nabla T\right) \tag{3}$$

$$u\frac{\partial \varphi}{\partial x} + v\frac{\partial \varphi}{\partial y} = \alpha\nabla^2 T + D_B\nabla^2\varphi + \frac{D_T}{T_\infty}\nabla^2 T - k_0(C - C_\infty) \tag{4}$$

The associated boundary conditions are:

$$\left.\begin{array}{c} u = u_w = ax, v = 0, \\ -k\frac{\partial T}{\partial y} = h_f(T_f - T), \\ D_B\frac{\partial \varphi}{\partial y} + \frac{D_T}{T_\infty}\frac{\partial T}{\partial y} = 0 \text{ at } y = 0; \\ u \to U_\infty = bx,\ v = 0, \\ T \to T_\infty,\ \varphi \to \varphi_\infty \text{ as } y = \infty \end{array}\right\} \tag{5}$$

where x is the coordinate axis along the continuous surface in the direction of motion and y is the coordinate axis along the continuous surface in the direction perpendicular to the motion. The components of velocity along x- and y-axis are respectively u and v. Here kinematic velocity is represented by ν and T represents the temperature inside the boundary layer. The parameter τ is defined by $\tau = (\rho c)_p/(\rho c)_f$, where $(\rho c)_p$ is effective heat capacity of nanoparticles and $(\rho c)_f$ is heat capacity of the base fluid, ρ is the density and T_∞ is the ambient temperature far away from the surface.

The radiative heat flux q_r is given as

$$q_r = \frac{-4\sigma^*}{3k^*}\frac{\partial T^4}{\partial y} \tag{6}$$

where σ^* and k^* stand for the Stefan-Boltzmann constant and coefficient of mean absorption, and T^4 is the linear sum of temperature and it can expand with the help of Taylor series along with T_∞

$$T^4 = T_\infty^4 + 4T_\infty^3(T - T_\infty) + 6T_\infty^2(T - T_\infty)^2 + \cdots \tag{7}$$

ignoring higher order terms, we get

$$T^4 = 4T_\infty^3 T - 3T_\infty^4 \tag{8}$$

substituting (8) into (6), we get

$$q_r = \frac{-16T_\infty^3\sigma^*}{3k^*}\frac{\partial T}{\partial y} \tag{9}$$

To convert the PDEs (1)–(4) along with the BCs (5) into the dimensionless form, we use the similarity transformation [11]:

$$\eta = y\sqrt{\frac{a}{\nu}},\quad \psi = \sqrt{avx}f(\eta),$$
$$\theta(\eta) = \frac{T-T_\infty}{T_f-T_\infty}, \beta(\eta) = \frac{\varphi-\varphi_\infty}{\varphi_w-\varphi_m}. \tag{10}$$

In above, $\psi(x, y)$ denotes stream function obeying

$$u = \frac{\partial\psi}{\partial y},\quad v = -\frac{\partial\psi}{\partial x} \tag{11}$$

The equation of continuity (1) is satisfied identically, the effect of stream function on the remaining three equations, the momentum equation (2), the temperature equation (3) and concentration equation (4) are

$$f''' + ff'' - (f')^2 + M(A-f') + A^2 = 0 \tag{12}$$

$$\frac{\left(1+\frac{4}{3}Nr\right)\theta''}{Pr} + f\theta' + Nb\theta'\beta' + Nt(\theta')^2 + Ec\,(f'')^2 = 0 \tag{13}$$

$$\beta'' + Lef\beta' + \frac{Nt}{Nb}\theta'' - Le\,k_c\beta = 0 \tag{14}$$

The BCs get the form:

$$f(0) = 0,\ f'(0) = 1,\ \theta'(0) = -Bi[1-\theta(0)],$$
$$Nb\beta'(0) + Nt\theta'(0) = 0, \text{ at } \eta = 0, \tag{15}$$

$$f'(\infty) \to A,\quad \theta(\infty) \to 0, \beta(\infty) \to 0 \text{ as } \eta \to \infty \tag{16}$$

In equations (12)–(14), the governing parameters are defined as $Nr = \frac{-4T_\infty^3\sigma^*}{3k^*k}$ is the radiation parameter, $Pr = \frac{\nu}{\alpha}$, is Prandtl number, $Le = \alpha/D_B$ is Lewis number, $M = \sigma B_0^2/\rho_f a$ is a magnetic parameter, $A = b/a$ is velocity ratio parameter, $Nb = \rho_p D_B(C_w - C_\infty)/\rho_f\alpha$ is Brownian motion parameter, $Nt = \rho_p D_T(T_w - T_\infty)/\rho_f\alpha T_\infty$ thermophoresis parameter, $Bi = \frac{h_f}{k}\sqrt{\frac{\nu}{a}}$ Biot number, $Ec = u_w^2/\rho_f(T_w - T_\infty)$ is the Eckert number and $k_c = K_0U(C_w - C_\infty)/v$ is the chemical reaction parameter.

In this problem, the desired physical quantities are the local Nusselt number Nu_x, and reduced Sherwood number Sh_x and the skin-friction coefficient C_f. These quantities are defined as

$$C_f = \frac{\tau_w}{\rho u_w^2},\quad Nu_x = \frac{x\,q_w}{k((T_w-T_\infty)},$$
$$Sh_x = \frac{xh_m}{D_B((\varphi_w-\varphi_\infty)} \tag{17}$$

Here, τ_w is the shear stress along the stretching surface, q_w is the heat flux from the stretching surface and h_w is the wall mass flux, are given as

$$\tau_w = \mu\left(\frac{\partial u}{\partial y}\right)_{y=0},\ q_w = -k\left(\frac{\partial T}{\partial y}\right)_{y=0},\ h_m = -D_B\left(\frac{\partial\varphi}{\partial y}\right)_{y=0} \tag{18}$$

With the help of the above equations, we get

$$C_f\sqrt{R_x} = -f''(0),\ \frac{Nu_x}{\sqrt{R_x}} = -\theta'(0),\ \frac{Sh_x}{\sqrt{R_x}} = -\beta'(0) \tag{19}$$

where $R_x = ax^2$ is the local Reynolds number.

3.2 Numerical calculations

The analytic solution of the system of equations with corresponding boundary conditions (12)–(14) cannot be found because they are nonlinear and coupled. So, we use numerical technique, i. e., shooting–Newton technique with fourth-order Adam's–Moultan method. In order to solve the system of ordinary differential equations (12)–(14) with boundary conditions (15), (16) using shooting method, we have to convert these equations into a system of first-order differential equations, let

$$\left.\begin{aligned} f = y_1, f' = y_1' = y_2, f'' = y_2' = y_3,\\ \theta = y_4, \theta' = y_4' = y_5, \theta'' = y_5',\\ \beta = y_6, \beta' = y_6' = y_7, \beta'' = y_7'. \end{aligned}\right\} \tag{20}$$

Then the coupled nonlinear momentum, temperature and concentration equations are converted into system of seven first-order simultaneous equations and the corresponding boundary conditions transform the following form:

$$\begin{gathered} y_1' = y_2,\ y_1(0) = 0,\ y_2' = y_3,\ y_2(0) = 1,\\ y_3' = y_2^2 - M(A-y_2) - y_1y_3 - A^2,\ y_3(0) = r\\ y_4' = y_5,\ y_4(0) = s,\\ y_5' = -Pr(y_1y_5 + Nby_5y_7 + Nty_5^2 + Ecy_3^2)/(1+R),\\ y_5(0) = Bi(s-1),\ y_6' = y_7,\ y_6(0) = t,\\ y_7' = -Ley_1y_7 - \frac{Nt}{Nb}y_5',\ y_5' + Lek_cy_6,\ y_7(0) = -\frac{Nt}{Nb}y_5(0). \end{gathered} \tag{21}$$

The above equations (21) are solved using Adam's–Moultan method of order 4 with an initial guess $r^{(0)}, s^{(0)}, t^{(0)}$. These guesses are updated by Newton's method. The iterative process is repeated until the following criteria is $max(|y_2(\eta_\infty)|, |y_4(\eta_\infty)|, |y_6(\eta_\infty)|) < \epsilon$, where $\epsilon > 0$ is tolerance.

For all computation in this paper, we have fixed $\epsilon = 10^{-5}$. The step sizes of $\Delta\eta = 0.01$ and $\eta_{max} = 10$ were found to be satisfactory in obtaining sufficient accuracy.

4 Results

The objective of this section is to analyze the numerical results displayed in the shape of graphs and tables. The computations are carried out for various values of the magnetic parameter *M*, velocity ratio parameter *A*, radiation parameter *Nr*, Eckert number *Ec*, Lewis number *Le*, Brownian motion parameter *Nb*, thermophoresis parameter *Nt* and Prandtl number *Pr*, and the impact of these parameters on the velocity, temperature, and concentration profiles are also discussed in detail.

Table 1 shows the comparison of calculated values with [11, 12] and strong agreement with the values is found which showed high confidence of present simulation. In Table 1, by taking M = 0 and update the velocity ratio parameter A, numerical results of the skin-friction coefficient $-f''(0)$ are reproduced.

Table 1 – Comparison of the skin-friction coefficient $-f''(0)$ for different values of velocity ratio parameter *A* and *M* = 0

A	Ibrahim [11], Ishak [12]	Present result
0.1	−0.9694	–0.9693874
0.2	−0.9181	–0.9181041
0.3	−0.8494	–0.8494202
0.4	−0.7653	–0.7653250
0.5	−0.6673	–0.6672632
0.8	−0.2994	–0.2993885
1.0	0.0000	0.0000000
2.0	2.0175	2.0175020
3.0	4.7293	4.7292940
5.0	11.7520	11.7519900
7.0	20.4979	20.4980600
10.0	36.2574	36.2575000

To further investigate the numerical technique used, by ignoring the impacts of thermophoresis parameter *Nt* and Brownian motion parameter *Nb* and then compare the local Nusselt number $-\theta'(0)$ by updating the Prandtl number as shown in Table 2. Excellent agreement of current results with those previously published results encourages us to use the present code.

Table 2 – Comparison of the local Nusselt number $-\theta'(0)$ when $Nt = 0$ and $Nb \to 0$ for different values of *Pr*

Pr	*A*	Present result	Ibrahim [11]	Mahapatra [13]	Hayat [14]
1.0	0.1	0.6008148	0.6028	0.603	0.602156
1.0	0.2	0.6246567	0.6246	0.625	0.624467
1.0	0.3	0.6926060	0.6924	0.692	0.692460
1.5	0.4	0.7760525	0.7768	0.777	0.776802
1.5	0.5	0.7969141	0.7971	0.797	0.797122
1.5	0.8	0.8648634	0.8648	0.863	0.864771
2.0	1.0	0.9256601	0.9257	–	–
2.0	2.0	0.9447336	0.9447	–	–
2.0	3.0	1.0114910	1.0116	–	–

Furthermore, we reproduce the results of [11] for the local Nusselt number $-\theta'(0)$. Table 3 presents the local Nusselt number $-\theta'(0)$ by taking random values of different physical parameters used such as Brownian motion, thermophoresis parameter, Biot number, and the velocity ratio. It is observed in the table that the local Nusselt number $-\theta'(0)$ is decreasing function of the thermophoresis parameter Nt and an increasing function of the Biot number *Bi*.

Table 3 – Comparison of the local Nusselt number $-\theta'(0)$ for the different values of *Nt* and *Bi* if *Nb* = 5, *A* = 0.3, *Pr* = *M* = 1, *Le* = 5

Nt	$-\theta'(0)$									
	Bi = 0.1		*Bi* = 2		*Bi* = 5		*Bi* = 10		*Bi* = 100	
	Ibrahim [11]	Present result	Ibrahim [11]	Present result	Ibrahim [11]	Present result	Ibrahim [11]	Present result	Ibrahim [11]	Present result
0.0	0.0861	0.0861460	0.4744	0.4743371	0.5531	0.5530363	0.5855	0.5854118	0.6180	0.6179690
0.2	0.0861	0.0860621	0.4605	0.4604263	0.5313	0.5312279	0.5598	0.5596828	0.5880	0.5878806
0.5	0.0859	0.0859333	0.4395	0.4394668	0.4993	0.4992715	0.5225	0.5224806	0.5415	0.5450010
1.0	0.0857	0.0857102	0.4047	0.4046166	0.4486	0.4485220	0.4647	0.4646182	0.4798	0.4797399
1.5	0.0855	0.0854758	0.3705	0.3704567	0.4017	0.4015988.	0.4125	0.4124254	0.4224	0.4223108
2.0	0.0852	0.0852291	0.3377	0.3376793	0.3591	0.3590596	0.3662	0.3661501	0.3725	0.3724754
5.0	0.0834	0.0834207	0.1925	0.1924764	0.1940	0.1939228	0.1944	0.1943392	0.1948	0.1946867

Figure 2 divulges the impact of the magnetic parameter on the velocity $f'(0)$. Here, due to magnetic field, an opposing force which is called Lorentz force appears which resist the flow of fluid and consequently the flow of velocity declines.

Figure 3 designates the impact of *Pr* on the temperature profile $\theta(\eta)$. It is clear from the figure that the temperature of the flow field is the decreasing function of *Pr*. It is because of the way when *Pr* of fluid is high then thermal diffusion is low if it is compared with the viscous diffusion. Consequently, the coefficient of heat transfer declines as well as shrinks the thickness of the boundary layer.

Figure 4 delineates the influence of *Nt* on the temperature profile. When the effects of the thermophoretic increase, the relocation of the nanoparticles relocate from hot part of the surface to the cold ambient fluid and consequently, at the boundary, temperature is increased. This sequel in the thickening of thermal boundary layer.

Figure 5 describes the effect of the convective heating which is also known as the Biot number on the temperature profile $\theta(\eta)$. Numerically, it can be calculated by dividing the convection on the surface to the conduction into the surface of an object. When Bi increases, it causes an increase in the temperature on surface which sequels in the thickening of the thermal boundary layer.

The effect of velocity ratio parameter A on the temperature profile $\theta(\eta)$ has been highlighted in Figure 6. As we increase the value of velocity ratio parameter A, the temperature at the surface declines, and furthermore, it also declines the thickness of the thermal boundary layer.

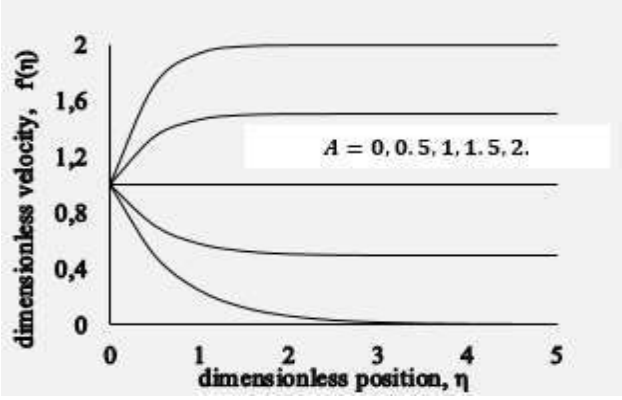

Figure 2 – Velocity profile $f'(0)$ for different values of velocity ratio A, when Pr = 1.0, Nr = 3, Ec = 1.0, k_c = 1.0, Nt = 0.5, Nb = 0.5, Le = Bi = 5.0, M = 1.0

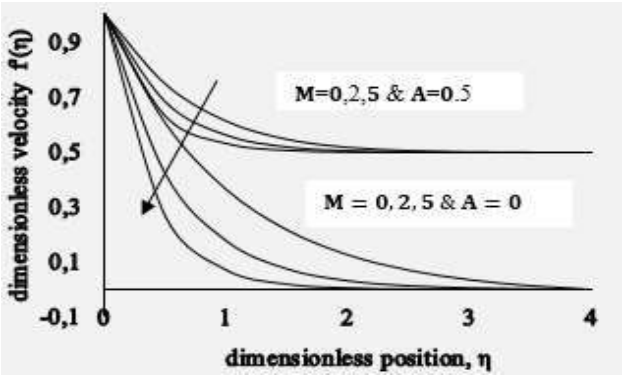

Figure 3 – Velocity profile $f'(0)$ for different values of M when Pr = 1.0, Nr = 3, Ec = 1.0, k_c =1.0, Nt = 0.5, Nb = 0.5, Le = Bi = 5.0

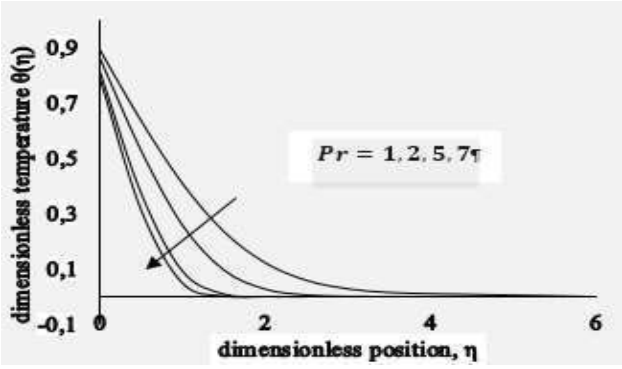

Figure 4 – Variation of $\theta(\eta)$ for various values of Pr when M = 1.0, A = Nt = Nb = 0.5, Bi = Le = 5.0, Ec = Nr = 0, and k_c = 1.0

The influence of radiation parameter on the profile of temperature distribution is displayed in Figure 7. Temperature increases with the increase of thermal radiation parameter Nr. The effect of radiation intensifies the heat transfer thus radiation should be at its minimum in order to facilitate the cooling process.

Figures 8 show the impact of the viscous dissipation on the temperature profile. When the value of the viscous dissipation is increased, the fluid region is allowed to store the energy. As a result of dissipation due to frictional heating, heat is generated.

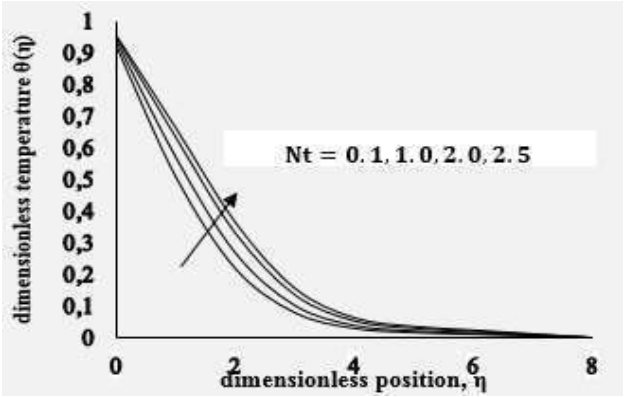

Figure 5 – Variation of $\theta(\eta)$ for various values of Nt when Pr = M = 1.0, A = Nb = 0.5, Le = 5.0, Ec = Nr = 0.5, and k_c = 1.0

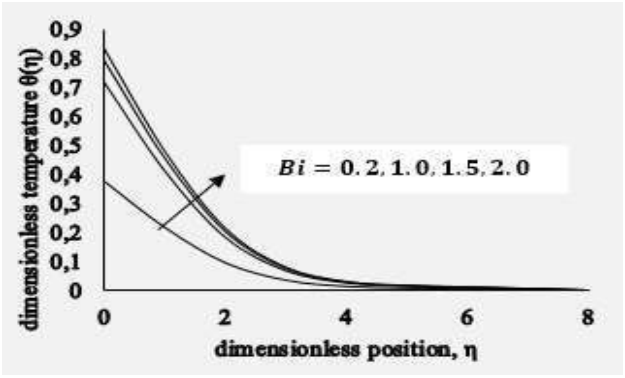

Figure 6 – Variation of $\theta(\eta)$ for various values of Bi when Pr = M = 1.0, A = Nt = Nb = 0.5, Le = 5.0, Ec = Nr = 0.5, and k_c = 1.0

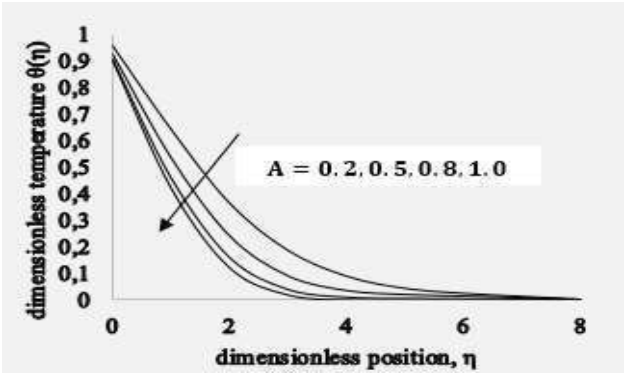

Figure 7 – Variation of $\theta(\eta)$ for various values of A when Pr = M = 1.0, Nt = Nb = 0.5, Le = 5.0, Ec = Nr = 0.5, and k_c = 1.0

The effect of the variation in the *Pr* on the concentration profile is observed in Figure 9. It is noticed from the figure, as the value of Prandtl number rises, the nanoparticles scattered out toward the outward, consequently, the nanoparticles concentration at the surface decreases.

The impact of the Brownian motion parameter *Nb* on the concentration $\beta(\eta)$ is illustrated in Figure 10. When we increase the effect of *Nb*, the concentration profile $\beta(\eta)$ also increases initially but it starts decreasing far away from the wall.

It seems clear from the Figure 11 that if we increase the thermophoretic force, it causes decline in the concentration profile $\beta(\eta)$ at the surface, which is reverse in nature to the case of the *Nt*.

The concentration vs Lewis number has been illustrated in Figure 12. Increasing *Le* corresponding to the concentration. As a result, initially the concentration on surface increases but after a while, a bit away from the surface it starts decreasing.

Figures 13 and 14 demonstrate the concentration vs velocity ratio. It has similar effects on the concentration profile as the effect of the Lewis number is noted on concentration. As the concentration distribution decreases by increasing the velocity ratio parameter *A*.

Figure 15 display the influence of Eckert number *Ec* on the concentration profile. It is observed that the concentration of the fluid decreases near the plate. However, it rises away from the surface as the value of Eckert number is enhanced.

Figure 16 explains the influence of the chemical reaction parameter on the profile of concentration. It is noted that increasing values of chemical reaction parameter concentration as well as the thickness of concentration decrease. It is because of the fact that the chemical reaction in this system results in chemical dissipation and therefore results in a decrease in the profile of concentration. The most significant influence is that chemical reaction tends to increase the overshoot in the concentration profiles and their associated boundary layer.

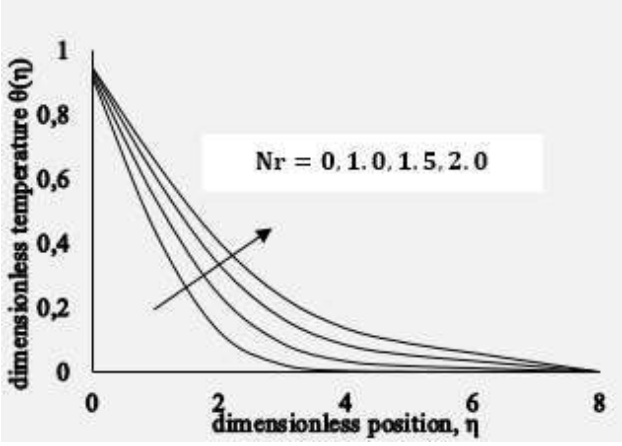

Figure 8 – Variation of $\theta(\eta)$ for various values of *Nr* when *Pr* = *M* = 1.0, *A* = *Nt* = *Nb* = 0.5, *Bi* = *Le* = 5.0, *Ec* = 0.5, and k_c = 1.0

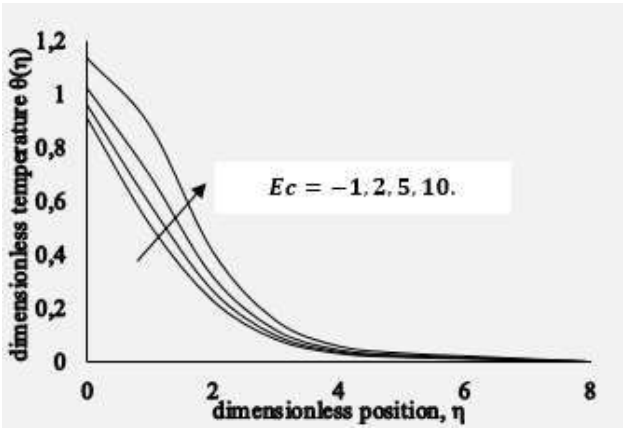

Figure 9 – Variation of $\theta(\eta)$ for various values of *Ec* when *Pr* = *M* = 1.0, *A* = *Nt* = *Nb* = 0.5, *Bi* = *Le* = 5.0, *Nr* = 0.5, and k_c = 1.0

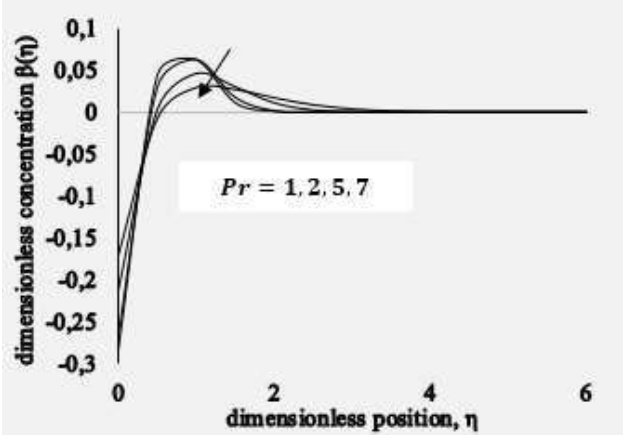

Figure 10 – Variation of $\beta(\eta)$ for various values of *Pr* when *M* = 1.0, *A* = *Nt* = *Nb* = 0.5, *Bi* = *Le* = 5.0, *Ec* = *Nr* = 0.5, and k_c = 1.0

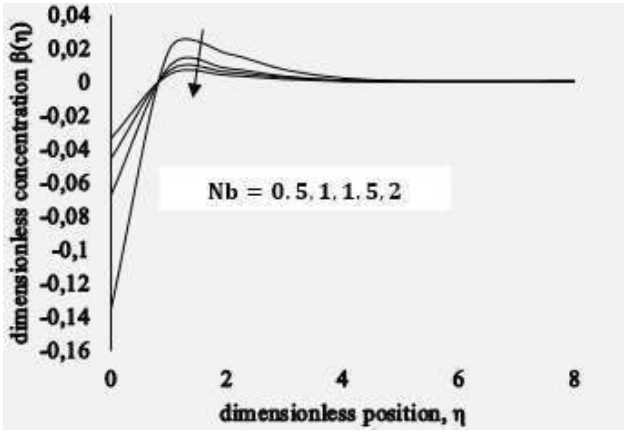

Figure 11 – Variation of $\beta(\eta)$ for various values of *Nb* when *Pr* = *M* = 1.0, *A* = *Nt* = 0.5, *Bi* = *Le* = 5.0, *Ec* = *Nr* = 0.5, and k_c = 1.0

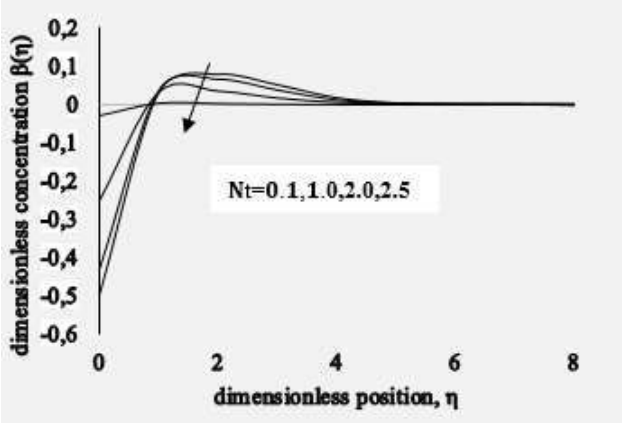

Figure 12 – Variation of $\beta(\eta)$ for various values of Nt when $Pr = M = 1.0$, $A = Nb = 0.5$, $Bi = Le = 5.0$, $Ec = Nr = 0.5$, and $k_c = 1.0$

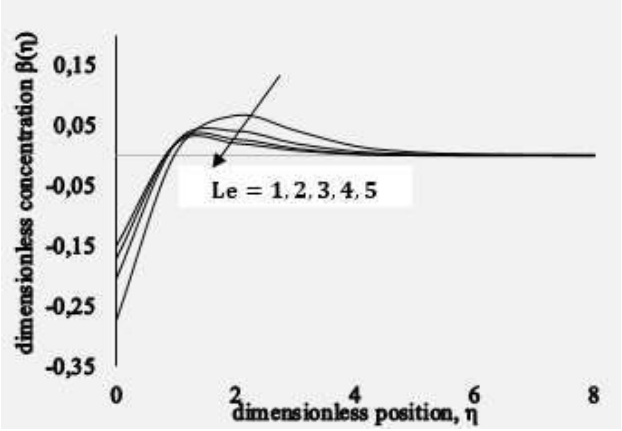

Figure 13 – Variation of $\beta(\eta)$ for various values of Le when $Pr = M = 1.0$, $A = Nt = Nb = 0.5$, $Bi = 5.0$, $Ec = Nr = 0.5$, and $k_c = 1.0$

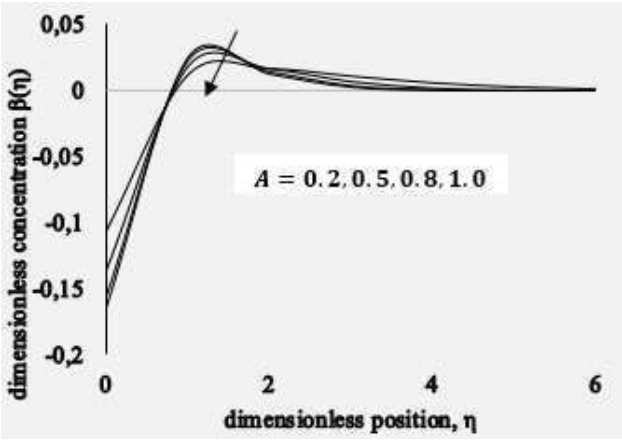

Figure 14 – Variation of $\beta(\eta)$ for various values of A when $Pr = M = 1.0$, $Nt = Nb = 0.5$, $Bi = Le = 5.0$, $Ec = Nr = 0.5$, and $k_c = 1.0$

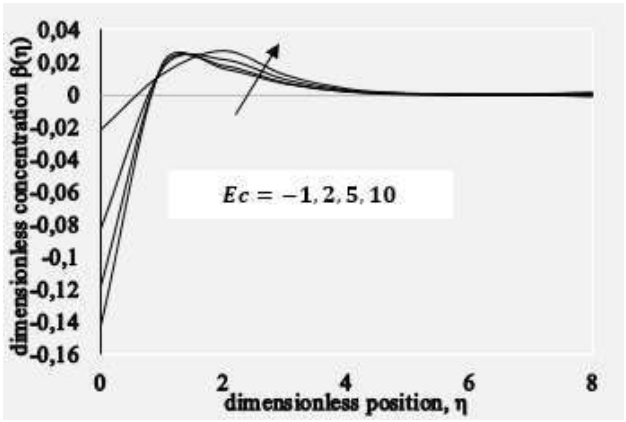

Figure 15 – Variation of $\beta(\eta)$ for various values of Ec when $Pr = M = 1.0$, $A = Nt = Nb = 0.5$, $Bi = Le = 5.0$, $Nr = 0.5$, and $k_c = 1.0$

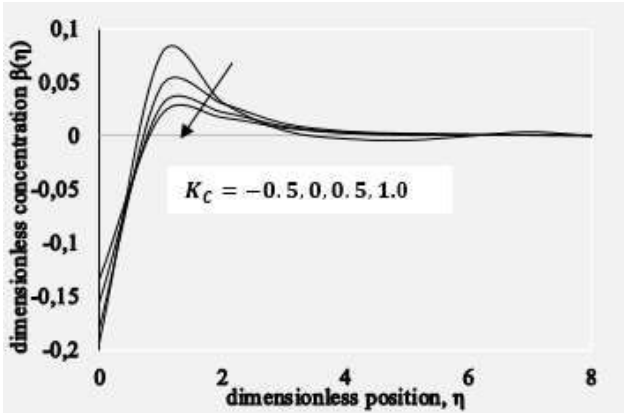

Figure 16 – Variation of $\beta(\eta)$ for various values of k_c when $Pr = M = 1.0$, $A = Nt = Nb = 0.5$, $Bi = Le = 5.0$, $Nr = 0.5$, and $Ec = 1.0$

5 Conclusions

After a thorough investigation, we have reached the concluding observation. Particularly, the velocity profile increases by increasing the parameter A, but the temperature and concentration profiles decrease by increasing this parameter. The magnetic parameter M has the same increasing influence on the temperature and the concentration field but opposite on the velocity field. The temperature field $\theta(\eta)$ and the concentration field $\beta(\eta)$ reduce with an increase in the Prandtl number. Temperature field $\theta(\eta)$ increases with an increase in thermal radiation Nr.

For larger values of Lewis number Le, thermophoresis parameter Nt, and Brownian motion parameter Nb has an increasing effect on the concentration field $\beta(\eta)$.

Moreover, an increase in viscous dissipation increases temperature and concentration profile. Finally, by increasing values of chemical reaction parameter, the concentration and the thickness of concentration are decreased.

6 Acknowledgments

The authors would like to thanks to Prof. Koneru S. R., Retired Professor, Department of Mathematics, Indian Institute of Technology Bombay for his support throughout this research work.

7 Nomenclature

B	magnetic field strength $(Wb\,m^{-2})$
a	Constant (s^{-1})
D_B	Brownian diffusion coefficient
D_T	thermophoretic diffusion coefficient
κ	thermal conductivity $(Wm^{-1}K^{-1})$
σ^*	Stefan-Boltzmann constant$(kgm^{-2}K^{-4})$
k^*	mean absorption
Ec	Eckert number
Le	Lewis number
M	magnetic parameter
Nb	Brownian motion parameter
Nt	thermophoresis parameter
Nu	Nusselt number
Nur	reduced Nusselt number
Pr	Prandtl number
p	pressure
c_f	heat capacity of the fluid $(Jm^{-3}K^{-1})$
c_p	effective heat capacity of the nanoparticle material $(Jm^{-3}K^{-1})$
q_r	radiative heat flux $(kg\,m^{-2})$
q_m	wall mass flux
q_w	wall heat flux
Re_x	local Reynolds number
Shr	reduced Sherwood number
Sh_x	local Sherwood number
T	fluid temperature (K)
T_w	the temperature at the stretching sheet (K)
T_∞	ambient temperature (K)
u, v	velocity components along x and y axis $(m.s^{-1})$
u_w	the velocity of the stretching sheet $(m.s^{-1})$
x, y	Cartesian coordinates (x axis is aligned along the stretching surface and y axis is normal to it) (L)
α	thermal diffusivity (m^2s^{-1})
β	dimensionless nanoparticle volume fraction
η	similarity variable
ψ	stream function(m^2s^{-1})
θ	dimensionless temperature
ρ_f	fluid density (kgm^{-3})
ρ_p	nanoparticle mass density (kgm^{-3})
σ	the electrical conductivity of the fluid
τ	parameter defined by the ratio between the effective heat capacity of the nanoparticle material and heat capacity of the fluid.$\tau = (\rho c)_p/(\rho c)_f$

References

1. Choi, S. (1995). Enhancing thermal conductivity of fluids with nanoparticles. *ASME-Publications-Fed*, Vol. 231, pp. 99–106.
2. Buongiorno, J. (2006). Convective transport in nanofluids. *Journal of Heat Transfer*, Vol. 128(3), pp. 240–250.
3. Kuznetsov, K. V., Nield, D. A. (2010). Natural convective boundary-layer flow of a nanofluid past a vertical plate. *International Journal of Thermal Sciences*, Vol. 49(2), pp. 243–247.
4. Khan, W. A., Pop, I. (2011). Flow and heat transfer over a continuously moving at plate in a porous medium. *Journal of Heat Transfer*, Vol. 133(5), art. no. 054501.
5. Makinde, O. D., Khan, W. A., Khan, Z. H. (2013). Buoyancy effects on MHD stagnation point flow and heat transfer of a nanofluid past a convectively heated stretching/shrinking sheet. *International Journal of Heat and Mass Transfer*, Vol. 62, pp. 526–533.
6. Cortell, R. (2012). Heat transfer in a fluid through a porous medium over a permeable stretching surface with thermal radiation and variable thermal conductivity. *The Canadian Journal of Chemical Engineering*, Vol. 90(5), pp. 1347–1355.
7. Naramgari, S., Sulochana, C. (2016). Dual solutions of radiative MHD nanofluid flow over an exponentially stretching sheet with heat generation/absorption. *Applied Nanoscience*, Vol. 6(1), pp. 131–139.
8. Afify, A. A. (2004). MHD free convective flow and mass transfer over a stretching sheet with chemical reaction. *Heat and Mass Transfer*, Vol. 40(6–7), pp. 495–500.
9. Beg, O. A., Khan, M. D. S., Karim, I., Alam, M. D. M., Ferdows, M. (2014). Explicit numerical study of unsteady hydromagnetic mixed convective nanofluid flow from an exponentially stretching sheet in porous media. *Applied Nanoscience*, Vol. 4(8), pp. 943–957.
10. Nadeem, S., Haq, R. U. (2014). Effect of thermal radiation for magnetohydrodynamic boundary layer flow of a nanofluid past a stretching sheet with convective boundary conditions. *Journal of Computational and Theoretical Nanoscience*, Vol. 11(1), pp. 32–40.
11. Ibrahim, W., Haq, R. U. (2016). Magnetohydrodynamic (MHD) stagnation point flow of nanofluid past a stretching sheet with convective boundary condition. *Journal of the Brazilian Society of Mechanical Sciences and Engineering*, Vol. 38(4), pp. 1155–1164.

12. Ishak, A., Nazar, R., Pop, I. (2006). Mixed convection boundary layers in the stagnation point flow toward a stretching vertical sheet. *Meccanica*, Vol. 41(5), pp. 509–518.
13. Mahapatra, T. R., Gupta, A. S. (2002). Heat transfer in stagnation-point flow towards a stretching sheet. *Heat and Mass Transfer*, Vol. 38(6), pp. 517–521.
14. Hayat, T., Mustafa, M., Shehzad, S. A., Obaidat, S. (2012). Melting heat transfer in the stagnation-point flow of an upper convected Maxwell (UCM) fluid past a stretching sheet. *International Journal for Numerical Methods in Fluids*, Vol. 68, art. no. 233243.

УДК 537.84

Числове дослідження в'язкої дисипації та хімічної реакції у магнітогідродинаміці нанорідини

Говардхан К.[1], Нарендер Г.[2], Сарма Г. С.[2]

[1] Університет технологій та управління ім. Ганді, м. Гайдарабад, Індія;
[2] Інженерний коледж CVR, м. Гайдарабад, Індія

Анотація. У роботі розглядається числове дослідження впливу в'язкої дисипації та хімічної реакції потоку нанорідини, що проходить через натягнуту поверхню з магнітогідродинамічною зоною застою для заданих граничних умов. Основні рівняння моделі потоку розв'язуються чисельно. Вплив фізичних параметрів математичної моделі потоку на безрозмірну швидкість, температуру і концентрацію подано із застосуванням відповідних графіків і таблиць. Також було проведено порівняння отриманих числових результатів з опублікованими результатами. У результаті встановлено, що результати узгоджуються із високою точністю. Також було отримано, що магнітний параметр має однаковий вплив на температуру і поле концентрації. Проте навпаки, вплив на поля швидкості, температури і концентрації зменшується зі збільшенням числа Прандтля. Також збільшення в'язкої дисипації збільшує температуру і концентрацію, а також товщина шару зменшується за рахунок збільшення значень параметра хімічної реакції.

Ключові слова: магнітогідродинаміка, розтягувальний лист, нанорідина, в'язка дисипація, хімічна реакція.

JOURNAL OF ENGINEERING SCIENCES
ЖУРНАЛ ІНЖЕНЕРНИХ НАУК
ЖУРНАЛ ИНЖЕНЕРНЫХ НАУК
Web site: http://jes.sumdu.edu.ua
DOI: 10.21272/jes.2019.6(2).f4 Volume 6, Issue 2 (2019)

The Estimation of Feed Solution Composition Influence on Concentration Polarization Layer Resistance during Reverse Osmosis

Huliienko S. V.[1*], Protsiuk O. O.[1], Gatilov K. O.[2], Kaminskyi V. S.[1, 3]

[1] National Technical University of Ukraine "Igor Sikorsky Kyiv Polytechnic Institute", 37 Peremohy Ave., 03056 Kyiv, Ukraine;
[2] Archer Daniels Midland Company ADM Europoort B.V., 125 Elbeweg, 3198 LC, Rotterdam, Netherlands;
[3] Technical University of Kosice, 9 Letna St., 042 00 Kosice, Slovak Republic

Article info:
Paper received: May 14, 2019
The final version of the paper received: August 29, 2019
Paper accepted online: September 3, 2019

[*]Corresponding Author's Address:
sergii.guliienko@gmail.com

Abstract. The experimental determination of concentration polarization layer resistance during reverse osmosis of mineral salts solutions was carried out with the aim to estimate the influence of solution composition on the value of mentioned resistance. In experimental conditions, the membrane resistance remains constant (the mean value was $0.534 \cdot 10^{14}$ m^{-1}) which means that the membrane compaction was not observed. Moreover, under experimental conditions, the hypothesis about linear dependence between the concentration polarization layer and applied pressure was confirmed for all solutions under investigations. It was defined that value of concentration polarization layer resistance different salt solutions was varied less than 10 % although under experimental conditions the diffusion coefficient values of magnesium sulfate were more than three times higher than corresponded values for other salts. The increasing of solutions concertation determines the increasing of concentration polarization layer resistance. At the same time, in previous study it was defined that changes in hydrodynamic regime in membrane module under similar conditions could determine the change in concentration polarization layer resistance in 3–5 times, while in both studies the trends of impact of hydrodynamic conditions still similar to the value of considered resistance decrease with Reynolds number increasing. Such results showed that in considered range of concentrations the hydrodynamic conditions have a lower influence on concentration polarization layer resistance than solution composition. The obtained results are in agreement with the film theory of concentration polarization.

Keywords: membrane, reverse osmosis, concentration polarization, diffusion coefficient, Reynolds number, Schmidt number.

1 Introduction

The pressure-driven membrane processes, i. e. reverse osmosis, are widely used in the chemical industry and additionally in allied branches such as biotechnological, pharmaceutical and food proceedings, water treatment systems and environmental protection [1]. The concentration polarization phenomenon and fouling formation on the membrane surface is the main problem in the exploration of membrane apparatuses and set-ups [2]. The numbers of researches are dedicated to this topic but there is no sufficient attention to the determination of mass transfer resistance due to concentration polarization layer.

Current research is the extension of our previous work [3] which was dedicated to the development of the technique for the experimental determination of concentration polarization layer resistance and additionally to defining of influence of working parameters on the value of mentioned resistance. However, in work [3] the experiments were carried out with using sodium chloride with various concentrations as feed solution. This does not allow to define the influence of feed solution composition on the value of concentration polarization layer resistance. For estimation of this impact, the experimental research was carried out for three different salt solutions.

2 Literature Review

For concentration polarization phenomenon description, it was proposed several models, the main of them are: film model, Spiegler–Kedem model, osmotic pressure model, gel layer model and others [1, 2]. At that, in some models, including osmotic pressure and gel layer models, the transmembrane flux is described by an equation in such form [2]:

$$J = \frac{\Delta p - \Delta \pi}{\mu \cdot \left(R_m + R_{cp} + R_f + R_p\right)}, \quad (1)$$

where Δp – applied pressure (driving force); $\Delta\pi$ – osmotic pressures difference; R_m – membrane resistance; R_{cp} – concentration polarization layer resistance; R_f – fouling layer resistance; R_p – pore blocking resistance.

According to [2], in an ideal case, there should be only membrane resistance which can be determined experimentally by measuring transmembrane flux for pure solvent. In that case, this value can be calculated from such equation as [2]:

$$R_m = \frac{\Delta p}{\mu \cdot J}. \quad (2)$$

In work [3], it was mentioned set of works dedicated determination to techniques of determination of fouling layer resistance, i. e. defining of the relation between specific cake layer resistance and applied pressure during dead-end ultrafiltration of carbohydrates solutions in work [5].

The pore-blocking resistance is typical only for the microfiltration process [1] so that in some works for pressure-driven membrane description this value is not considered as in work [5] during the analysis of the nanofiltration process.

At the same time works dedicated to the determination of the concentration polarization layer resistance are almost absent in literature sources. In the review [2] it was mentioned about using indirect methods in preceding works. On the other hand, the majority of concertation polarization researches have theoretical character and dedicated to problems of numeric simulation of this phenomenon and influence to the intensity of scaling formation [6]; development of models for inorganic salts transport through the membrane [7]; simulation of the concentration field during flow in channels with spacers [8], determination of limiting fluxes [9] and impact to fouling formation [10, 11].

In work [3] it was mentioned out that the most comprehensive study of the concentration polarization layer resistance was carried out by Macedo and al. [12]. Particularly, in mentioned research it was assumed that the value of R_{cp} is directly proportional to applied pressure, that is:

$$R_{cp} = \varphi \cdot \Delta p. \quad (3)$$

Additionally, in work [12], it was shown that taking into account the equation (3) the equation (1) can be rewritten in a form:

$$\frac{1}{J} = \mu\left(R_m + R_f\right)\frac{1}{\Delta p} + \mu\varphi. \quad (4)$$

The proposed equation is a practical tool for the determination of fouling layer resistance, which allows estimating the necessity of regeneration using transmembrane flux data. If there was a reliable relationship for the concentration polarization layer resistance or the value of coefficient φ the equation (4) would be suitable for use in automatic control of the membrane separation process.

In our previous work [3] it was defined, that assumption about the linear dependence between concentration polarization layer resistance and the applied pressure is reasonable, and it was determined the influence of operating parameters (applied pressure and hydrodynamic conditions in membrane module) on the concentration polarization layer resistance. However, those results do not allow to define the relationship for determination of concentration polarization layer resistance due to the absence of information about the influence of solution composition on the value of mentioned resistance, since the experiments were carried out with using of one solution namely NaCl.

3 Research Methodology

3.1 Materials

As it has been done in work [3], the researches were carried out with commercially available membrane modules but anther trademark namely HID TFC 1812-75 GPD (Made in China). As membrane modules, Dow Filmtec TW30-1812-50, which used in work [3] the membrane module under investigation is destined for tap water post-treatment. The membrane modules HID TFC 1812-75 GPD have higher productivity up to 50 % and lower selectivity up to 10 % by comparison with the membrane modules Dow Filmtec TW30-1812-50.

For measuring the membrane resistance, the deionized water (reverse osmosis permeate with total dissolved solids in the range of 5–15 mg/dm^3) was used. For measuring of concentration polarization layer resistance, the solutions of sodium chloride (NaCl), magnesium sulfate ($MgSO_4$) and sodium nitrate ($NaNO_3$) were used. The experiments were carried out with using solutions with concentrations of 100 and 200 mg/dm^3.

3.2 Description of the experimental set-up

The research was carried out on the same experimental set-up as in work [3] (Figure 1), which includes feed solution tank 1, pump 2, membrane apparatus 3 and contain-ers and tanks 5-8. For control of flow rate, valve 5 is provided. The applied pressure was monitored using the manometer 9.

The set-up provides the measurements of permeate and retentate flor rates be volumetric technique, using tanks 5 and 6 with the accuracy of ±2 and ±10 ml, respectively (the direct measuring include measuring of volume and time) and also allows to measure total dissolved sol-ids using portative TDS-meter with accuracy ±1 mg/dm3. The applied pressure was measured by manometer 9, the temperature was controlled by the block of Chromel-Copel thermocouples with accuracy up to ±0.2 °C (is not shown on the design scheme).

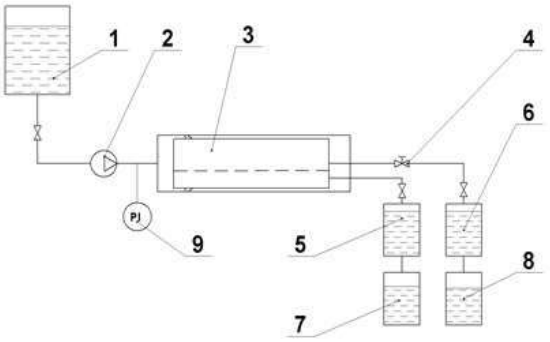

Figure 1 – The design scheme of the experimental set-up

3.3 Experimental procedure and main measurements

In the current research, the same experimental technique as in work [3] was used. It involves the pumping the feed solution under predetermined applied pressure by pump 9 into membrane apparatus 3 and measurements of permeate and retentate flor rates be volumetric technique. Firstly, measurements were carried out for mew membrane module HID TFC 1812-75 GPD with using of deionized water as a test solution, then measurements were carried out for salt solution separation. After each membrane module working cycle with each salt solutions the mem-brane cleaning was carried out using deionized water. It was done with the aim to remove the salt solution remains.

The measurements were carried out for each test solution in a range of applied pressure of 0.2–0.6 MPa and under ambient temperature. In this case, the ambient temperature was varied in a range of 13–17 °C.

The processing of results and determination of concentration polarization layer resistance were carried out according to the technique represented in [3]. The physical properties of the solution were determined according to reference literature [13, 14].

For determination of salt diffusivities in solution, the experimental result represented in work [15] were used. Since experiments were carried out under temperatures which differs from 25 °C for that experimental data represented in [15], for the revaluation it was used following equation [16]:

$$D(T) = D(T_0)\cdot\left(\frac{T}{T_0}\right)\cdot\left[\frac{\mu(T)}{\mu(T_0)}\right]. \qquad (5)$$

where $D(T_0)$ – diffusion coefficient under the base temperature; T – solution temperature under operation condition; T_0 – base temperature (in this case the temperature for which the experimental results are represented, namely 25 °C), $\mu(T)$ – dynamic viscosity coefficient under operation temperature; $\mu(T_0)$ – dynamic viscosity coefficient under base temperature. The values of dynamic viscosity coefficients were defined using reference literature [13, 14].

4 Results and Discussion

The total membrane resistance of mass transfer through the membrane, which was measured according to the mentioned technique, is represented in Figures 2, 3. The obtained results, in general, confirmed the conclusion obtained in work [3]. In a case, during the measurement of productivity for pure solvent (deionized water) the value of total resistance was varied less than 1 % and the average value was $0.534\cdot10^{14}$ m^{-1}. Therefore, the influence of membrane compaction was negligible and obtained value can be assumed equal to membrane resistance Rm. It should be noticed membrane resistance value for modules HID TFC 1812-75 GPD is lower than one for modules Dow Filmtec TW30-1812-50 (R_m = 0,755·10^{14} m^{-1}), which are used in work [3].

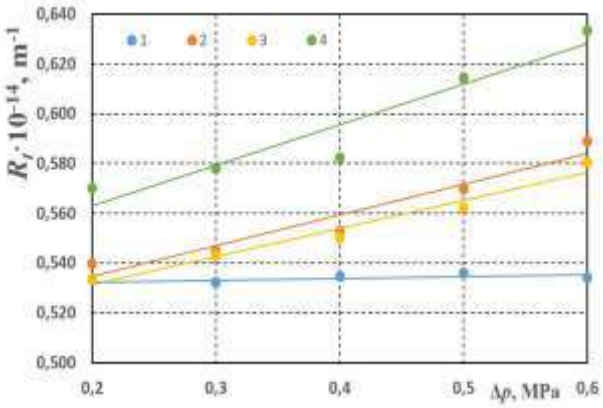

Figure 2 – The dependence of total resistance to membrane transfer thorough the membrane from applied pressure: 1 – deionized water; 2 – $MgSO_4$ solution (100 mg/dm^3); 3 – $NaNO_3$ solution (100 mg/dm^3); 4 – NaCl solution (100 mg/dm^3)

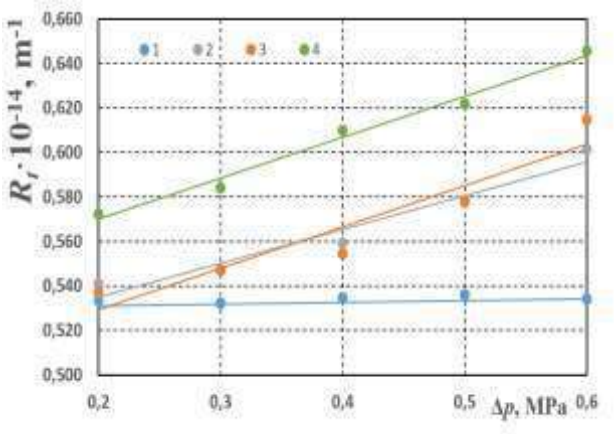

Figure 3 – The dependence of total resistance to membrane transfer thorough the membrane from applied pressure: 1 – deionized water; 2 – $MgSO_4$ solution (200 mg/dm^3); 3 – $NaNO_3$ solution (200 mg/dm^3); 4 – NaCl solution (200 mg/dm^3)

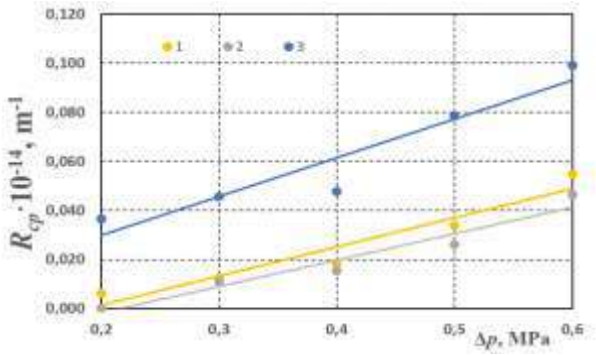

Figure 4 – The dependence of concentration layer resistance from applied pressure: 1 – $MgSO_4$ solution (100 mg/dm^3); 2 – $NaNO_3$ solution (100 mg/dm^3); 3 – NaCl solution (100 mg/dm^3)

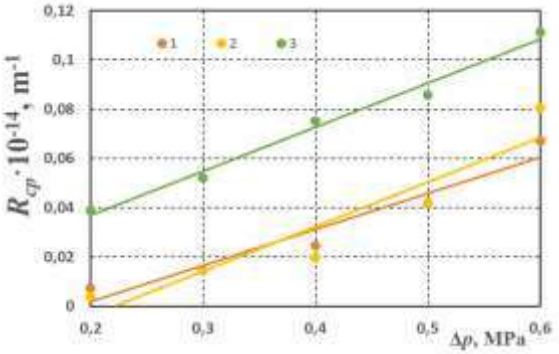

Figure 5 – The dependence of concentration layer resistance from applied pressure: 1 – $MgSO_4$ solution (200 mg/dm^3); 2 – $NaNO_3$ solution (200 mg/dm^3); 3 – NaCl solution (200 mg/dm^3)

In this case, the hypothesis about linear dependence between applied pressure and concentration polarization layer resistance is confirmed not only for NaCl and for others salts which were used in experiments.

It should be noticed that the value of concentration polarization layer resistance for MgSO4 and NaNO3 was on the approximately same level (the difference was less than 2 %) for the same concentration (curves 1 and 2 in Figures 4, 5), whereas for NaCl these values were higher for 5–8 % (curves 3 for the same figures). Such results were unexpected considering the properties of solutions. According to [15] and with correction using equation (5) the values of diffusion coefficient for $MgSO_4$ under experimental conditions were in a range of $D = (7.715–7.744)\cdot 10^{-9}$ m^2/s, for $NaNO_3$ these values were $D = (1.788–1.789)\ 10^{-9}$ m^2/s and correspondingly for NaCl these ones were $D = (1.800–1.803)\cdot 10^{-3}$ m^2/s. Considering that values of diffusion coefficient were close for NaNO3 and NaCl solutions, the bigger difference should expect for the case of $MgSO_4$ solution. The probable reason for this difference is temperature condition. As mentioned above the experiments were carried out under ambient temperatures with variated in a range 13–17 °C. Moreover, during experiments with $NaNO_3$ and $MgSO_4$ solutions, the temperature was approximately the same namely 16.5–17.0 °C whereas in a case of NaCl the experiments were carried out under lower temperatures (13–14 °C).

The impact of solution concentration in all cases corresponded to results obtained in work [3] namely increasing of concentration polarization layer with increasing of concentration (Figures 6, 7).

It should be noticed, that influence of solution composition on concentration polarization layer resistance value under experimental conditions in particularly considered salts and their concentrations was lower than the influence of hydrodynamic conditions which was investigated in work [3]. Moreover, the obtained in that work behavior is confirmed. In particular, the value of concentration layer polarization resistance is decreased with increasing the Reynolds number (Figure 8) as it was predicted by the film theory of concentration polarization [1, 2].

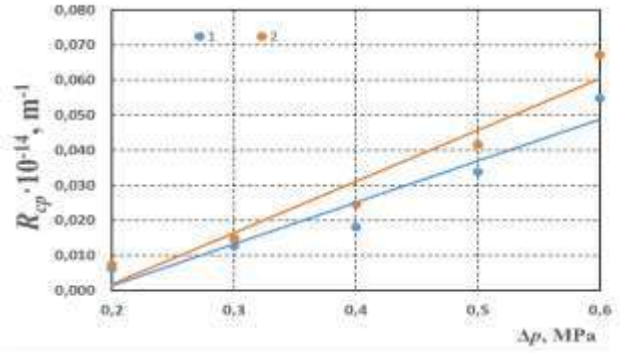

Figure 6 – The dependence of concentration polarization layer resistance from applied pressure during $MgSO_4$ solutions separation: 1 –100 mg/dm^3; 2 – 200 mg/dm^3

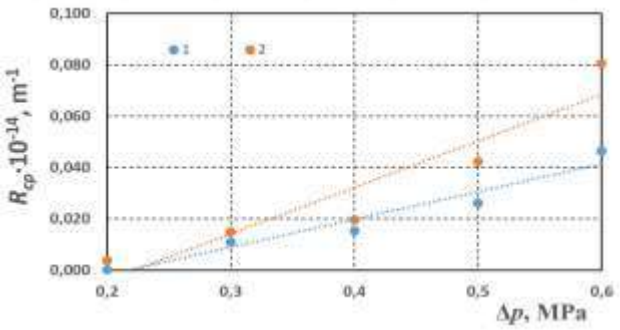

Figure 7 – The dependence of concentration polarization layer resistance from applied pressure during $NaNO_3$ solutions separation: 1 –100 mg/dm^3; 2 – 200 mg/dm^3

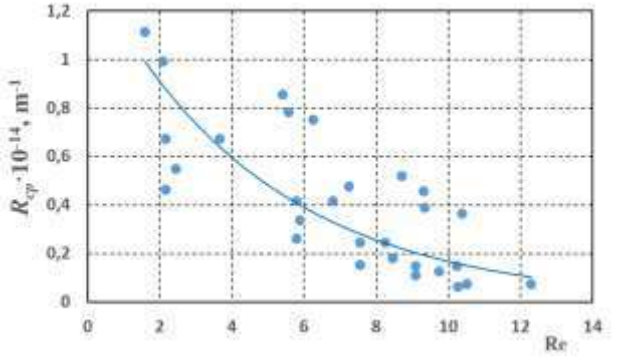

Figure 8 – The dependence of concentration polarization layer resistance from the Reynolds number

The obtained data did not allow to define influence the Schmidt number on values of concentration polarization layer resistance since the value of this parameter for $NaNO_3$ and NaCl were close (Sc = 630–640) whereas for $MgSO_4$ it was substantively different (Sc = 140–150).

This was determined by mentioned above values of diffusivity coefficients of salts under investigation under experimental conditions. This fact also can be the reason of low correlation (correlation coefficient was lower than 0.6) between the concentration polarization layer resistance and the Reynolds number with observed in Figure 8.

For determination of such relationship the further experiments with corresponding selections of solutions, its concentrations, and operating temperatures are needed.

5 Conclusions

The evaluation of influence of solution composition on concentration polarization layer resistance during the reverse osmosis and it shown that during reverse osmosis separation of diluted salt solutions (concentration up to 200 mg/dm^3) the value on considered does not change by more than 10 %, whereas variations in hydrodynamic conditions can change R_{cp} value 3–5 times in a range of applied pressure of 0.2–0.6 MPa or in range of Reynolds number 2–13, as it was shown in previous work [3].

Therefore, the influence of hydrodynamic condition is more significant than the impact of solution composition.

The obtained results did not allow to define a dependence of concentration polarization layer resistance from the Schmidt number.

The obtained results confirm the hypothesis about linear dependence of concentration polarization layer resistance from applied pressure not only for NaCl but also for other mineral salts. The results also are in agreement with the film theory of concentration polarization.

References

1. Mulder, M. (1996). *Basic Principles of Membrane Technology*. Dordrecht, Kluwer Academic Publishers.
2. Shirazi, S., Lin, C.-J., Chen, D. (2010). Inorganic fouling of pressure-driven membrane processes – A critical review. *Desalination*, Vol. 250(1), pp. 236–248, doi: 10.1016/j.desal.2009.02.056.
3. Huliienko, S., Leshchenko, O. (2019). Influence of operating pressure on concentration polarization layer resistance in reverse osmosis. *Ukrainian Food Journal*, Vol. 8(1), pp. 119–132, doi: 10.24263/2304-974X-2019-8-1-13.
4. Sioutopoulos, D., Karabelas, A. (2015). The effect of permeation flux on the specific resistance of polysaccharide fouling layers developing during dead-end ultrafiltration. *Journal of Membrane Science*, Vol. 473, pp. 292–301, doi: 10.1016/j.memsci.2014.09.030.
5. Luo, J., Ding, L., Su, Y., Wei, Sh., Wan, Y. (2010). Concentration polarization in concentrated saline solution during desalination of iron dextran by nanofiltration. *Journal of Membrane Science*, Vol. 363, pp. 170–179, doi: 10.1016/j.memsci.2010.07.033.
6. Li, W., Su, X., Palazzolo, A., Ahmed, S. (2019). Numerical modelling of concentration polarization and inorganic fouling growth in the pressure-driven membrane filtration process. *Journal of Membrane Science*, Vol. 569, pp. 71–82, doi: 10.1016/j.memsci.2018.10.007.
7. Jang, E.-S., Mickols, W., Sujanani, R., Sujanani, R., Dilenschneider, T., Kamcev, J., Paul, D., Freeman, B. (2019). Influence of concentration polarization and thermodynamic non-ideality on salt transport in reverse osmosis membranes. *Journal of Membrane Science*, Vol. 572, pp. 668–675, doi: 10.1016/j.memsci.2018.11.006.
8. Amokrane, M., Sadaoui, D., Koutsou, C. P., Karabelas, A. J., Dudeck, M. (2015). A study of flow field and concentration polarization evolution in membrane channels with two-dimensional spacers during water desalination. *Journal of Membrane Science*, Vol. 477, pp. 139–150.
9. McGovern, R. K., Lienhard, J. H. (2016). On the asymptotic flux of ultrapermeable seawater reverse osmosis membranes due to concentration polarization. *Journal of Membrane Science*, Vol. 520, pp. 560–565, doi: 10.1016/j.memsci.2016.07.028.
10. Freire-Gormaly, M., Bilton, A. M. (2019). Impact of intermittent operation on reverse osmosis membrane fouling for brackish groundwater desalination systems. *Journal of Membrane Science*, Vol. 583, pp. 220–230, doi: 10.1016/j.memsci.2019.04.010.
11. Suwarno, S. R., Chen, X., Chong, T. H., McDougald, D., Cohen, Y., Rice, S. A., Fane, A. G. (2014). Biofouling in reverse osmosis processes: The roles of flux, crossflow velocity and concentration polarization in biofilm development. *Journal of Membrane Science*, Vol. 467, pp. 116–125, doi: 10.1016/j.memsci.2014.04.052.
12. Macedo, A., Duarte, E., Pinho, M. (2011). The role of concentration polarization in ultrafiltration of ovine cheese whey. *Journal of Membrane Science*, Vol. 381, pp. 34–40, doi: 10.1016/j.memsci.2011.07.012.
13. Nikolskij, B. (2013). *Chemist's Handbook, Vol. 3 – Chemical Equilibrium and Kinetics. Properties*. Demand Ltd.
14. Yaws, C. (1999), *Chemical Properties Handbook: Physical, Thermodynamic, Environmental, Transport, Safety and Heals Related Properties for Organic and Inorganic Chemicals*. McGraw-Hill, New York.
15. Dytnerskii, Iu. I. (1986). *Baromembrane Processes. Theory and Calculation*. Chemistry, Moscow.
16. Thibodeaux, L., Mackay, D. (2011). *Handbook of Chemical Mass Transport in the Environment*. CRC Press, New York.

УДК 66.081.63

Оцінювання впливу складу розділюваного розчину на опір шару концентраційної поляризації при зворотному осмосі

Гулієнко С. В.[1], Процюк О. О.[1], Гатілов К. О.[2], Камінський В. С.[1, 3]

[1] Національний технічний університет України «Київський політехнчний інститут ім. Ігоря Сікорського», просп. Перемоги, 37, 03056, м. Київ, Україна;
[2] Archer Daniels Midland Company ADM Europoort B.V., 3198 LC, м. Роттердам, Нідерланди;
[3] Технічний університет м. Кошице, вул. Літня, 9, 042 00, м. Кошице, Словаччина

Анотація. У роботі експериментально визначено опір шару концентраційної поляризації при зворотно-осмотичному розділенні розбавлених розчинів мінеральних солей з метою оцінювання впливу складу розчину на величину зазначеного опору. Як модельне середовище обрано розчини хлориду натрію, сульфату магнію та нітрату натрію з концентраціями 100 та 200 мг/дм^3, а також знесолена вода для визначення опору мембрани. Робочий тиск варіювався у межах 0,2–0,6 МПа. Дослідження проводилися за температур оточуючого середовища 13–17 °С. За таких умов опір мембрани залишався постійним, а його середнє значення становило $0{,}534 \cdot 10^{14}$ м$^{-1}$, тобто ущільнення мембрани не спостерігалось. Окрім того, в умовах проведення експериментальних досліджень підтверджується гіпотеза лінійної залежності опору шару концентраційної поляризації від тиску не лише для хлориду натрію, але й для всіх досліджуваних солей. Також встановлено, що значення опору шару концентраційної поляризації для різних солей відрізнялося не більше, ніж на 10 %. Проте, за умов проведення досліджень значення коефіцієнту дифузії для розчину сульфату магнію більше, ніж утричі перевищували відповідні значення для інших солей. Зростання концентрації розчину обумовлює відповідне збільшення опору шару концентраційної поляризації. У той же час, у попередніх дослідженнях було встановлено, що зміна гідродинамічного режиму в мембранному модулі за аналогічних умов може обумовити зміну опору шару концентраційної поляризації у 3–5 разів. Більше того, в обох дослідженнях тенденції впливу гідродинамічних характеристик залишаються однаковими. Зокрема, значення досліджуваного опору зменшується зі збільшенням критерію Рейнольдса. Такі результати свідчать, що в розглядуваному діапазоні концентрацій гідродинамічні умови чинять більший вплив на величину опору шару концентраційної поляризації, ніж склад розчину, що розділюється. Результати досліджень узгоджуються з плівковою теорією концентраційної поляризації. Проте, отримати залежність опору шару концентраційної поляризації від критерію Шмідта не вдалось.

Ключові слова: мембрана, зворотній осмос, концентраційна поляризації, опір, коефіцієнт дифузії, критерій Рейнольдса, критерій Шмідта.

JOURNAL OF ENGINEERING SCIENCES
ЖУРНАЛ ІНЖЕНЕРНИХ НАУК
ЖУРНАЛ ИНЖЕНЕРНЫХ НАУК
Web site: http://jes.sumdu.edu.ua
Volume 6, Issue 2 (2019)

JOURNAL OF ENGINEERING SCIENCES
ЖУРНАЛ ІНЖЕНЕРНИХ НАУК
ЖУРНАЛ ИНЖЕНЕРНЫХ НАУК

Web site: http://jes.sumdu.edu.ua

DOI: 10.21272/jes.2019.6(2).h1 Volume 6, Issue 2 (2019)

Ecologically Safe Directions of the Low Rank Coal Bioconversion

Chernysh Y.[1*], Plyatsuk L.[1], Ablieieva I.[1], Yakhnenko E.[1],
Roubik H.[2], Miakaieva H.[1], Bataltsev E.[1], Lis D.[1]

[1] Sumy State University, 2 Rymskogo-Korsakova St., 40007 Sumy, Ukraine;
[2] Czech University of Life Sciences Prague, 129 Kamycka St., 165 00 Prague, Czech Republic

Article info:
Paper received: March 4, 2019
The final version of the paper received: June 30, 2019
Paper accepted online: July 5, 2019

[*]Corresponding Author's Address:
e.chernish@ssu.edu.ua

Abstract. This paper deals with theoretical research of the biochemical features of low rank coals (LRC) treatment. The biochemical bases of the organic component degradation of LRC and the biochemical principles of bioleaching of sulfur compounds and metals from LRC are presented. The analysis of microorganisms' groups was carried out and the optimal conditions of their cultivation were determined. Electronic databases such as KEGG, BacDive, and EAWAG-BBD were used to identify the necessary ecological and trophic groups of microorganisms and to realize the patterns of trophic interactions in associations of different groups of microorganisms both under anaerobic and aerobic conditions. The methodological approach was applied and principle diagram of biochemical research of LRC processing was formed in order to develop the environmentally friendly direction of biogas and humic products production.

Keywords: low rank coal, biochemical features, biogas, humic substances, ecological-trophic groups of microorganisms.

1 Introduction

The past fifteen years have seen unprecedented change in the consumption of energy resources. Increasing the share of renewable energy in Central and Eastern Europe is one of the factors that improve the quality of economic growth [1]. Unexpected high growth in the renewables market, in terms of investment, new capacity and high growth rates in different countries have changed the landscape for the energy sector. However, coal still provides around 40 % of the world's electricity [2].

The coal industry was and remains to be an important basis for the Ukrainian economy. Coal is the main energy source for this country. Today the importance of the coal issue has risen more than ever because of the objective necessity of Ukraine's inclusion into the world economy. The rise of the coal consumption is accompanied by an increase in the anthropogenic impact on the environment, because coal burning, and processing produce more harmful by-products compared to oil and gas [3].

One of the ways of solving this problem is expanding the scope of use new technological treatment decisions of low rank coals (LRC), which will contribute to stabilize the fuel and energy balance and create a stock of time for the coal industry development.

In [4] it was shown that with an increase in the duration of the process of aerobic treatment brown coal by the bacterial strain Acinetobacter calcoaceticus VKPM B-4833 the relative hydrogen content decreases (by 5.9–18.6 wt. %) and the oxygen content increases (by 6.4–11.5 wt. %) in biomodified coals relative to the original coal. The most noticeable changes in the content of these elements occur when the duration of the biotreatment process is 10 h [4].

Biomodification of brown coal leads to an increase of the humic acids formation by 22.9–30.6 % compared with the original LRC. The maximum humic acids formation (32.4 wt. %) was received for coal that was bioprocessed for 10 h write as [4]. It was determined by Ivanov et al that the brown coal biotreatment is accompanied with a change its thermochemical properties in the temperature range of 30–900 °C.

The LRC such as lignite have a soft, friable consistency, opaque appearance, humidity of 30–45 %, high ash content, low fixed carbon content (low energy content) and are considered by-products of open pit mining. LRC as understood by its low degree of carbonization is a great source of humic substances (HS) and has high contents of elements that stimulate microbial growth and development, and, through different mechanisms, its macrostructure allows the release of HS. Consequently, LRC could be

used as an organic amendment for the management of degraded soils. Among the microorganisms that can solubilize LRC to generate substances with similar characteristics to HS obtained from LRC by chemical extraction are bacteria isolated from coal samples; some genera and species of Escherichia freundii, Pseudomonas rathonis, Pseudomonas fluorescens, Streptomyces setoni, Pseudomonas putida, Bacillus sp., Staphylococcus, Rhodococcus and others have been reported. Three new LRC biotransformers were reported: Bacillus mycoides, Acinetobacter baumannii and Microbacterium sp.; these were isolated from environmental samples with coal residues, with the ability to solubilize LRC, producing up to 300 mg/l of HS in liquid medium (Figure 1) [5].

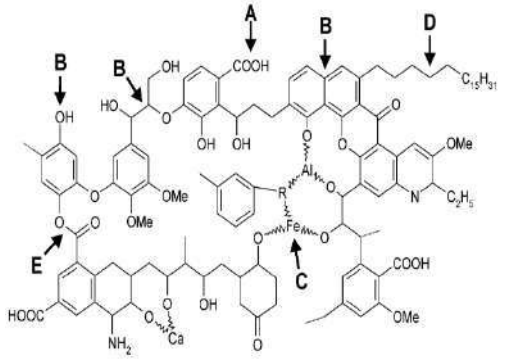

Figure 1 – The so-called ABCDE-mechanism of biological conversion of brown coal (modified after Fakoussa, 1991). The arrow syndicate structures that can be attacked by different microbial agents: A – alkaline substances; B – biocatalysts (oxidative enzymes); C – chelators; D – detergents; E – esterases [5]

The nature and direction of the processes occurring during diagenesis can be viewed by comparing the properties of peat and LRC. The most noticeable differences are in their group composition. Peat still contains the constituent parts of the original plants (carbohydrates, lignin, etc.), but they are almost absent in LRC. Humic acids are present in both peat and LRC. However, humic acids are formed and accumulated during peat formation and its' quantity decreases in the diagenesis process (Table 1) [6].

Table 1 – Group composition of fossil fuels (wt. %)

Substance groups	Fossil fuels				
	Peat	Coal			
		Soft brown coal (LRC)	Solid brown coal (LRC)	Bitumi-nous coal	Anthra-cite
Bi-tumoids	8	12	6	5	2
Poly-saccha-rides	29	3	–	–	–
Humic acids	47	65	22	–	–
Humin (resid-ual coal)	16	20	72	95	98

There are three groups in the brown coal group composition: bitumoids, humic acids and residual coal. During carbonization, humic acids of earthy brown coal are transferred to residual coal of solid brown coal [7].

Table 2 shows the comparative characteristics of brown coal and HS by elemental composition [8].

Table 2 – LRC and HS similarities

Element	Humic Acid, %	Coal
Carbon	53.8–58.7	60–70
Hydrogen	3.2–6.2	6.0–5.8
Oxygen	32.8	34
Nitrogen	0.8–4.3	1.5
Sulfur	0.1–1.5	0.2–10

The paper focused on theoretical research of the biochemical features of LRC treatment. To achieve the aim, the following tasks were set:

– theoretical analysis of biochemical features of coal treatment with the methodological approach forming;

– review of bioactivators of intensification processes of LRC bioconversion.

2 Research Methodology

2.1 Biochemical principles of metals leaching from coal

Biological leaching is one of the most successful biotechnological approaches of heavy metals' removal [9]. Unlike other environmental pollutants, the removal of heavy metals from the environment is difficult. These metals cannot be chemically or biologically degradable. Various methods of physico-chemical treatment are effectively used to extract toxic heavy metals from soil and water, but they have some unavoidable disadvantages, such as low productivity and a huge price, unlike the biological methods. In the research works [10, 11] several principles and mechanisms of the bio-leaching process were determined.

Fig. 2 shows the flowchart of features of the bio-leaching process.

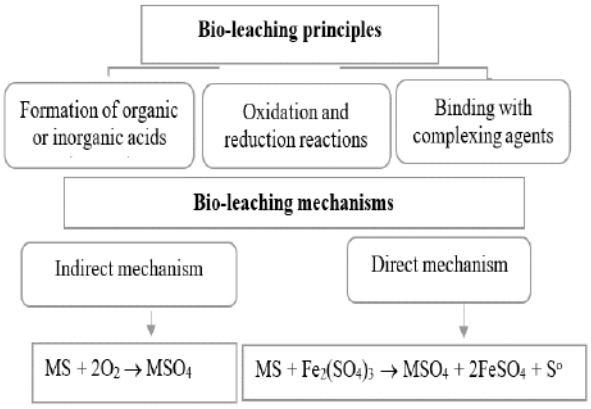

Figure 2 – Principle diagram of biochemical features of leaching

There are two types of mechanisms such as direct and indirect. First needs physical contact between bacteria and metal sulfide particles. Under the indirect mechanism, bacteria oxidize the ferrous ion to the ferric ion state, regenerating the ferric ion, which is necessary for the chemical oxidation of the sulfide mineral [9].

Figure 3 shows the contact, contactless and cooperative mechanisms of the bio-leaching process.

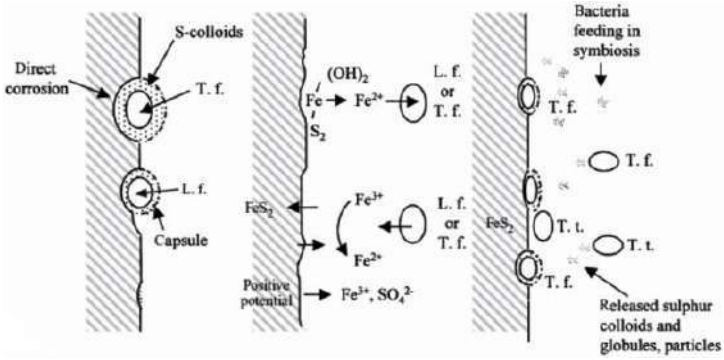

Figure 3 – Patterns of direct and indirect interaction of the bacteria with pyrite: a – contact leaching; b – non-contact leaching; c – cooperative leaching [12]

Sulfuric acid is the main inorganic acid that is found in leaching conditions. Many organic acids are formed by bacterial (and fungal) metabolism that leads to organic acidosis, the complexes and chelates formation [13].

The bacteria then enter the reaction by oxidizing ferrous ions to the ferric state, thereby regenerating the primary oxidant. The direct contact mechanism is independent of the action of ferric ions, requiring only intimate physical contact between the bacteria and the sulphide mineral under aerobic conditions.

The dissolution of metal sulphides is controlled by two different reactions, i.e. the thiosulfate and polysulfide pathways.

The thiosulfate pathway is applicable only to acid insoluble sulfides of metals, such as pyrite.

The mechanism of the pyrite bio-leaching is given below [13]:

$$FeS_2 + 6Fe^{3+} + 3H_2O \rightarrow S_2O_3^{2-} + 7Fe^{2+} + 6H^+ \quad (1)$$

$$S_2O_3^{2-} + 8Fe^{3+} + 5H_2O \rightarrow 2SO_4^{2-} + 8Fe^{2+} + 10H^+ \quad (2)$$

In total, these two equations can be presented in this form:

$$FeS_2 + 14Fe^{3+} + 8H_2O \rightarrow 2SO_4^{2-} + 15Fe^{2+} + 16H^+ \quad (3)$$

The main role of microorganisms in this mechanism is to catalyze the regeneration of ferric ions by aeration. It's shown in the equation:

$$14Fe^{2+} + 3.5O_2 + 14H+ \rightarrow 14Fe^{3+} + 7H_2O \quad (4)$$

Equations (3) and (4) describe the indirect mechanism.

The general reaction based on the primary of oxygen oxidation is given below:

$$FeS_2 + 3.5O_2 + H_2O \rightarrow Fe^{2+} + 2SO_4^{2-} + 2H^+ \quad (5)$$

Equation 5 represents the direct mechanism of pyrite removal from coal.

The polysulfide pathway is applicable to acid-soluble metal sulfides, such as PbS, ZnS, FeAsS and $CuFeS_2$.

The mechanism of the zinc sulfide bio-leaching reaction is shown below:

$$8ZnS + 14Fe^{3+} + 2H^+ \rightarrow 8Zn^{2+} + 14\,Fe^{2+} + H_2S_8 \quad (6)$$

$$H_2S_8 + 2Fe^{3+} \rightarrow S_8 + 2Fe^{2+} + 2H^+ \quad (7)$$

The role of the microorganisms in this mechanism is twofold:

– catalyzation of the regeneration of ferric ions used for the chemical oxidation of intermediate hydrogen sulfide to elemental sulfur through the formation of polysulfides;

– catalyzation of the generation of sulfuric acid in order to maintain the required number of protons in the first stage of the mineral dissolution reaction.

It is obvious that the high oxidation rate from ferrous to ferric iron is important for an efficient biological leaching process of sulfide minerals.

2.2 Bio-desulphurization of coal

The organisms can be classified based on whether they can remove inorganic or organic sulfur from coal: (a) obligate autotrophs oxidize only pyritic sulfur, (b) facultative autotrophs oxidize pyritic sulfur and some organic sulfur compounds, (c) heterotrophs oxidize only some organic sulfur compounds [14].

Bioleaching process using acidophilic sulfur oxidizing bacteria (Acidithiobacillus ferrooxidans, Acidithiobacillus thioosidans) and neutrophilic microorganisms (Aspergillus niger) has been intensively investigated for successful removal of metals from sediment, municipal solid, and sludge [15].

Mesophilic and moderately thermophilic acidophilic chemolithotrophic bacteria (ACB) and archaea, particularly, mesophilic representatives of the genus Acidithiobacillus – Acidithiobacillus ferrooxidans and Acidithiobacillus thiooxidans dominate in the process of inorganic sulfur's removing. Information about the use of other ACB's representatives in the process of coal desulfurization is not enough. There is information about the use for these purposes of a representative of the genus Acidithiobacillus – a strain of Acidithiobacillus ferrivorans, which has distinctive ability to grow on tripton and soy broth along with the properties common to typical representatives of Acidithiobacillus. The strain isolated from the acidic drainage waters of the Balıkesir field (Turkey) and identified by molecular genetic analysis using 16S rRNA as Acidithiobacillus ferrivorans was able to oxidize sulfur and iron [16].

The data showed that 26.7 % of sulfur was removed by Alicyclobacillus in a few days; however, 49.1 % of sulfur was removed by Acidithiobacillus in 30 days. This was interesting since the leachings of zinc, strontium, titanium,

and iron by Alicyclobacillus, obtained in a few days, were almost the same as the leachings by Acidithiobacillus in 30 days. The results obtained also showed that the Alicyclobacillus cells growing at 55 °C removed most of the coal impurities without any change in the carbon content of this fuel. To the best of our knowledge, coal leaching by Alicyclobacillus is reported for the first time [17].

According to study [18] Acidithiobacillus ferrooxidans had significantly promoted the biodesulfurization of coal and bioleaching of coal's pyrite. After 16 days of processing, the total sulfur removal rate of coal was 50.6 %, and among them the removal of pyritic sulfur was up to 69.9 %.

The adapting of the Acidithiobacillus ferrooxidans population at higher concentrations of ferrous sulphate (18g/l Fe^{2+}) determined a raised efficiency of coal desulphurization at values between 63.1–88.5 %. In addition, raising the solid/liquid ratio from 0.05 to 0.1 g/ml determined the increasing of the coal biodesulphurization efficiency, which gets to 57.3–76.4 % for the pit coal and 72.2–82.5 % for lignite. The comparative results regarding the efficiency of coal desulphurization in the presence of A ferrooxidans cultures illustrated that the P7 population oxidized the highest percentages of sulphur from coal (54.8–63.1 %) [19].

In study [20], low-rank lignite coal sample collected from Jining coalfield of Shandong province in China was subjected to desulphurization by using a new bacteria and Acidithiobacillus ferrooxidans isolated from the native coal mine site. The molecular identification of the 16S rRNA gene showed that the new native bacteria was Pseudomonas sp., denoted as NP22, and it is reported for the first time for the capability to remove about 46 % of total sulphur from the lignite coal. Analytical characterization indicated that total sulphur content of lignite coal was reduced to 2.8 % and 3.2 % by using two microorganisms. In addition, the calorific value of lignite coal was not affected adversely after two microorganisms' desulphurization but rather its calorific value increased from 6.2 to 6.4 kcal/g, and 6.3 kcal/g, however, the ash content of the lignite coal was eliminated.

Accordingly, the removal of sulfur compounds and heavy metals from LRC occurs in the same biochemical process of the coal components transformation by sulfur-oxidizing microorganisms under aerobic conditions.

With certain coals, the direct mechanism for oxidation of pyrite may be limited because the microorganisms are too large to enter most of the coal pores as shown in Figure 4.

The process is accompanied by the acid's formation, which supports the low pH values, favorable for the vital and oxidative activities of ACB [16].

Bio-desulphurisation of organic sulphur was carried out in most of the literature by using model compounds, which are frequently recognized as the organo-sulphur compounds in coal. Various organisms such as Rhodococcus erythropolis IGTS8 (ATCC 53968), Shewanella putrefaciens, Brevibacterium, Rhodococcus sp. IGTS8, thermophilic Paenibacillus sp. A11-2 and B. Subtilis WUS2B, Mycobacterium sp., Gordonia sp., Microbacterium, Lysinibacillus sphaericus and so forth, were also explored for bio-desulphurisation of coals. Most of these investigations stressed upon the relevance of bio-desulphurisation of coal with the microbes while testing their potency to degrade the organic S-compounds expected in coals [21].

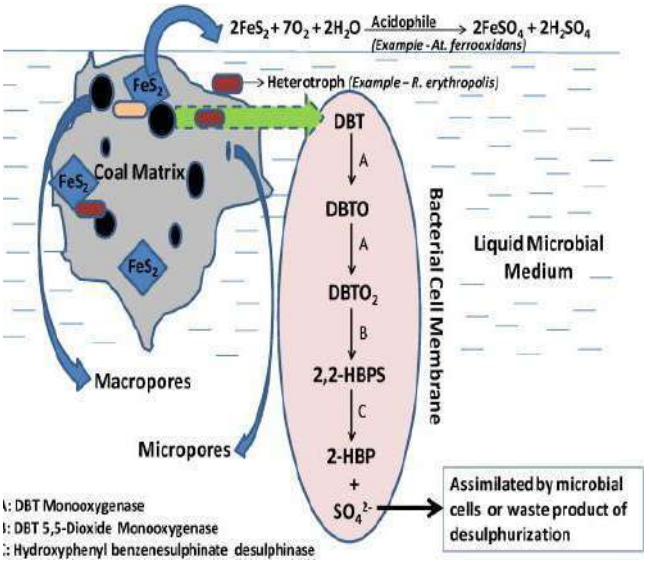

Figure 4 – Bimodal pore structure of coal and pyrite oxidation [7, 8]

Dibenzothiophene (DBT) is a model compound for organic sulfur in fossil fuels, and its desulfurization pathway removes this sulfur. Rhodococcus sp. IGTS8 can use dibenzothiophene as a sole source of sulfur [22].

Pseudomonas sp. C18 can metabolize dibenzothiophene, naphthalene and phenanthrene by a single pathway. The names of the enzymes in the pathway are not given, only the DOX operon, which encodes them in its 9 open reading frames (ABDEFGHIJ). The pathway is very similar to the one of naphthalene and the enzymes have high sequence identity with the naphthalene enzymes, thus the corresponding names have been used for the enzymes. Naphthalene dioxygenase, the enzyme that initiates this pathway, is used in a biotechnological process to synthesize the blue jean dye indigo. This versatile enzyme has many other catalytic abilities, which are documented in a table of the Reactions of Naphthalene 1,2-Dioxygenase [23] (Figure 5).

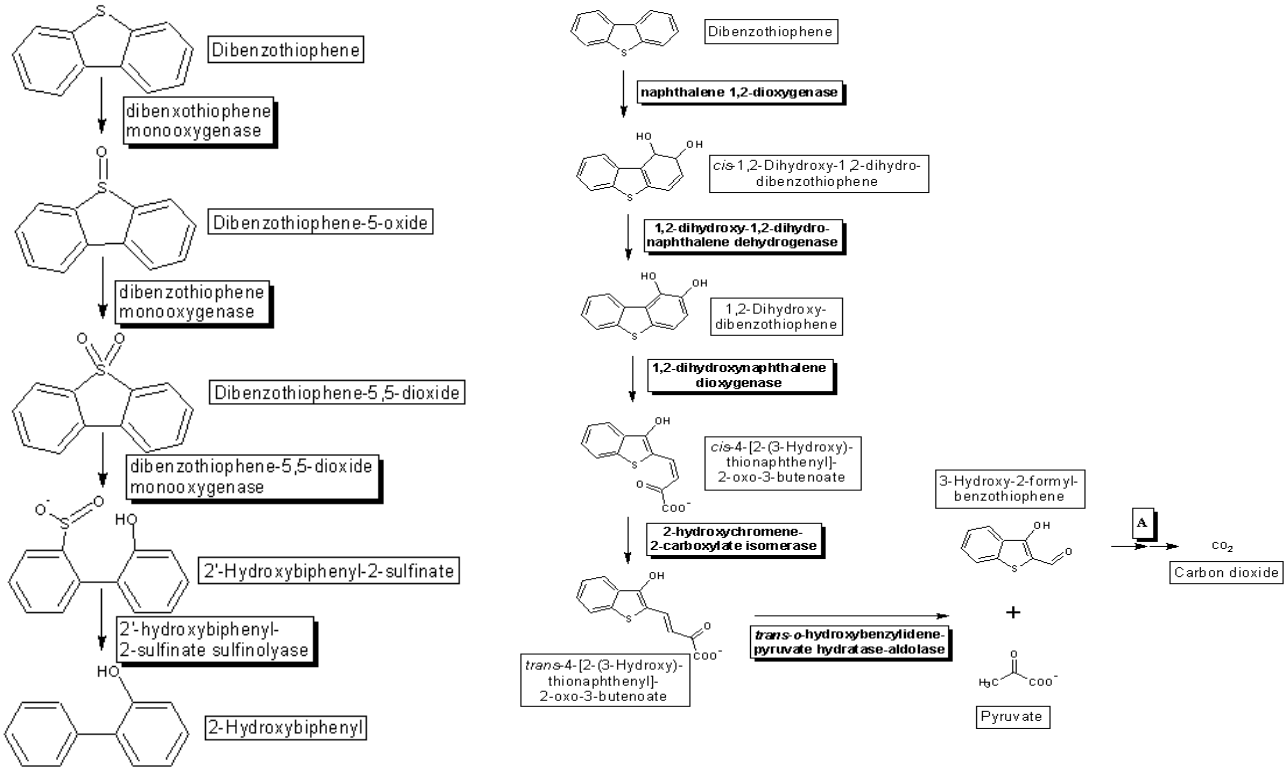

a b

Figure 5 – Graphic representation of biotransformation paths in coal desulphurisation processes:
a – dibenzothiophene desulfurization graphical pathway map; b – dibenzothiophene degradation graphical pathway map

2.3 Development of the methodological approach of the biotechnological integrated processing of LRC with biogas production

Bioconversion is accomplished by adapting microorganisms to coal in the presence of other appropriate nutrient components. This processing can have several step that includes different type of transformation LRC under aerobic and anaerobic conditions (Figure 6).

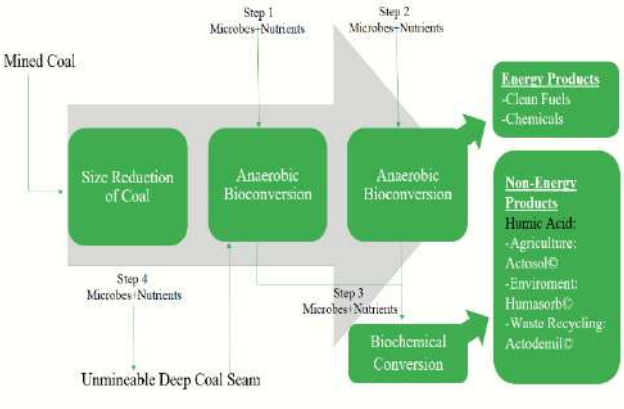

Figure 6 – Integrated MicGAS™ biotechnology process flow scheme [8]

The model for biochemical parameters determining has been developed (Figure 7) to assess the effectiveness of the coal use as a mineral substrate by various groups of microorganisms.

In the work [24], mixed cultures of T. ferrooxidans AM and T. thiooxidans AM were used for desulphurization of coal. These cultures were isolated from sediments of river, which flows through a coal belt containing high sulphur. Isolated cultures were stored and maintained on a nutrient medium with coal containing sulphur.

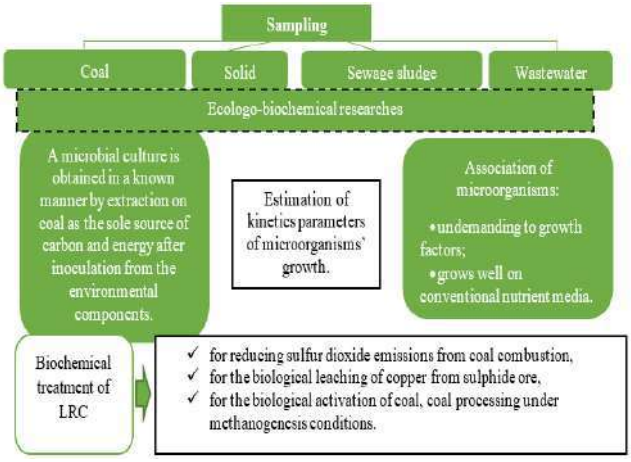

Figure 7 – Principle model of biochemical researches

Seeding methods on dense and in liquid nutrient substrates consider only viable cells of microorganisms. If we need to isolate and consider the widest possible range of microorganisms inhabiting this substrate, we use the Koch method and at the same time select a substrate where microorganisms with different properties can grow. However, it is not possible to identify all groups of microorganisms on the same substrate due to significant physiological and biochemical differences between them. The basis for isolating and determining the number of representatives of microorganisms' individual groups is the obtaining of accumulative cultures by creating elective conditions. This was in similarity with findings in different studies by [25, 26].

Bacteria are isolated from the soil in the following way. Individual soil samples are taken with a clean tool from each horizon, mixed samples are taken across several horizons by a cylindrical drill from no less than five points of the field along one or two diagonals. The larger the field area, the more individual samples are needed. According to [27] numbers of colonies appearing on solid media were determined by examining the plates at a magnification of ×10 with a stereomicroscope. Each count represents the mean for a series of dilution steps with three plates at each dilution and was calculated based on the dry weight of the soil and dilution factors.

Further, a soil suspension is prepared from water and the soil protected from impurities, and it is used to prepare dilutions. Dilutions are made in sterile 0.5 % aqueous solution of NaCl. Decimal dilutions are most often made; that was confirmed in [28].

The suspension of microorganisms obtained after dilution is used to determine the number of microorganisms by sowing on various nutrient substratum and/or to consider the number of microorganisms using direct microscopy, as well as to study the qualitative composition and morphology of microorganisms by microscopic methods.

Vinogradsky–Shulgin–Brida method is used in various modifications to determine the number of microorganisms in a variety of natural substrates – in soil, polluted water, optically opaque environments. Counting cells on fixed stained smears is reduced to the fact that in a certain volume of the investigated suspension, directly under the microscope, the number of microorganism cells is counted. The use of fixed smears makes it possible to save preparations for a long time and to count not in the course of experience, but at a time convenient for the researcher.

Meat-peptone agar (MPA) is often used as a nutrient substrate for cultivating soil microorganisms. It is suitable for cultivating of many heterotrophic microorganisms. Microorganisms of various systematic and physiological groups grow on MPA after seeding from the soil: Gram-negative bacteria of the genus Pseudomonas, Flavobacterium, gram-positive spore-forming bacillus of the genus Bacillus, cocci of the Micrococcus and Sarcin genus, various mycobacteria (Mycobacterium genus) and some higher actinomycetes (Streptomyces genus).

The microbes that are present in the test material and grow on a selective substrate can be isolated into pure culture. This can be confirmed by microscopy. The Gram stain was carried out in accordance with the generally accepted method [29]. Identification of cultures was carried out according to Bergey's Manual of Determinative Bacteriology [30] based on data from morphology, physiology and biochemical properties of microbial cells.

The research is carried out in two directions: the first one – the allocation of accumulated culture from the soil or another environment; the second is the research of the development's dynamics of the required ecological and trophic microorganisms' groups on the proposed substrate (LRC, etc.).

The advantage of deep cultivation is that this method does not require large areas and cumbersome equipment, the capacity of fermenter can be increased by the height enlargement. Easy maintenance, the possibility of automation, convenience of removing the intact solid product from the culture fluid are also the advantages of this method.

In this case the removal of aerobic bacterias occurs on the surface in a laboratory thermostat TGU-01-200, where microorganisms receive oxygen directly from the air.

Chemical methods include:

1) the use of chemicals that absorb molecular oxygen. Pyrogallol alkaline solution, sodium dithionite ($Na_2S_2O_4$), metallic iron, monovalent copper chloride and some other reagents are used as molecular oxygen absorbers in laboratory practice.

2) the use of reducing agents that are added to most substrates for decreasing their redox potential: sodium thioglycolate, cysteine, ascorbic acid.

The methods that limit the access of air to the growing culture for the cultivation of anaerobic bacteria use:

– growing in a high layer of substrate;

– growing in a dense substrate's layer;

– cultivation in viscous substrates where the diffusion of molecular oxygen into a liquid decrease with an increasing its density;

– filling the substrate with a high layer of sterile vaseline oil or paraffin.

Research has been continued on seeking new and mutant microorganisms for different biotransformations and on biodegradation of organic compounds as models for microbial studies such as destructions of lignin, organic sulfur compounds, car-boxyl groups and organic nitrogen bonds [31].

The most common compound used as a model for organic sulphur compounds in coal is dibenzothiophene (DBT) [21]. Two new bacterial isolates capable of dibenzothiophene (DBT) degradation to benzoic acid through the 4S-pathway were isolated from different Egyptian hydrocarbon polluted soil samples. These organisms, designated NShB1 and NShB2, were tentatively identified as Aureobacterium sp. and Enterobacter sp., respectively as determined by 16S rDNA gene sequence analysis. DBT degradation pathway has been identified by GC-MS. The NShB1 and NShB2 strains were capable to degrade up to

approximately 49 % and 36 % of 1 000 ppm DBT, respectively within 7 days of incubation at 30 °C and pH 7 [32].

However, the important direction is the research of the natural microorganisms' associations capable to effectively carry out complex bioconversion of LRC with the formation of an integral biochemical model of the process in artificially created cultivation conditions.

The analysis of the ecological-trophic groups of microorganisms was carried out and Table 3 with the conditions of their cultivation was formed with using electronic databases such as KEGG database, BacDive and EAWAG-BBD. Thus, the main groups of microorganisms and the conditions in which they can be cultivated were analyzed, which will further help to choose the best option for combining them for carrying out a complex bioconversion of brown coal.

Table 3 – Analysis of the cultivation conditions of different ecological-trophic microorganisms' groups involved in the desulfurization and methanogenesis in the LRC processing

Genus	Bacterium species	Culture substrate	pH	Temperature	Aerobic or anaerobic
Acinetobacter	Acinetobacter calcoaceticus	strain is undemanding to growth factors, grows well on conventional nutrient substrates (meat peptone broth (MPB), meat peptone agar (MPA), dry nutrient agar (SPA)). It forms small, round, non-pigmented colonies, shiny, with a smooth edge on agar substrates	7.0–7.2	30 °C	Aerobic
Acidithiobacillus	Acidithiobacillus ferrooxidans	strain is cultivated on substrates with iron (II), manganese (II) ion, elemental sulfur, thiosulfate and sulfide ions as the sole source of energy. It is not able to use sugar and peptone	1.0–4.0	25–30 °C	Aerobic
	Acidithiobacillus thiooxidans		1.5–2.15	20–23 °C	Aerobic
Aureobacterium	–	strain is cultivated with constant mixing (150 rpm) during 12 days in an environment that does not contain phosphates, and which is prepared on 50 mm HEPES buffer	7.2	28 °C	Aerobic
Desulfobacter	–	cultivated in the substrate of Postgate C	7.0–7.6	28 °C	Anaerobic
Methanosaeta	Methanosaeta concilii	De Ley Method	8.0	37 °C	Anaerobic
Methanosarcina	Methanosarcina barkeri	tested with 0.1 M sodium formate or with a headspace of 200 kPa H_2-CO_2 (80:20) substituted for trimethylamine.	6.0–7.0	25 °C	Anaerobic
Rhodococcus	Rhodococcus erythropolis	agar medium (meat-peptone agar, wort agar, glucose-potato agar agar)	6.0–8.5	28–30 °C	Aerobic
Lysinibacillus	Lysinibacillus sphaericus	cultivation on the Munz's agar substrate	6.5–8.0	10–37 °C	Aerobic

The goal of some coal bed producers is to extend coal bed methane productivity and to utilize hydrocarbon wastes such as coal slurry to generate new methane. However, the process and factors controlling the process, and thus ways to stimulate it, are poorly understood. Subbituminous coal from a nonproductive well in south Texas in [33] was stimulated to produce biogas in microcosms when the native population was supplemented with nutrients (biostimulation) or when nutrients and a consortium of bacteria and methanogens enriched from wetland sediment were added (bioaugmentation). The native population enriched by nutrient addition included Pseudomonas spp., Veillonellaceae, and Methanosarcina barkeri. The bioaugmented microcosm generated methane more rapidly

and to a higher concentration than the biostimulated microcosm. Dissolved organics, including long-chain fatty acids, single-ring aromatics, and long-chain alkanes accumulated in the first 39 days of the bioaugmented microcosm and were then degraded, accompanied by generation of methane. The bioaugmented microcosm was dominated by Geobacter sp., and most of the methane generation was associated with growth of Methanosaeta concilii.

The ability of the bioaugmentation culture to produce methane from coal intermediates was confirmed in incubations of culture with representative organic compounds.

Thus, methane production could be stimulated at the nonproductive field site and that low microbial biomass may be limiting in situ methane generation. In addition, the microcosm study suggests that the pathway for generating methane from coal involves complex microbial partnerships.

Figure 8 shows that only completely unspecific enzymes have a chance of attacking the coal structure recently according to [35].

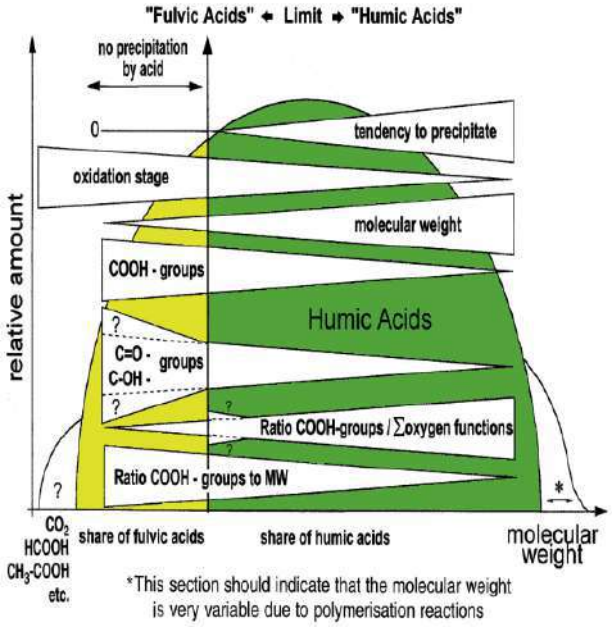

Figure 8 – Flow diagram of different features of coal-derived humic and fulvic acids, modelling their heterogeneity (the relation of humic to fulvic acid is optional) [35]

The population isolated in [34] includes strains of the genera Rhodococus sp., Pseudomonas sp., Mycobactenum sp. and sulfate-reducing microorganisms. Clostridium sp. and Bacillus sp. were morphologically defined.

The concentration of microorganisms in the mixture injected into the LRC is equal to the sum of their concentration in the sludge and in the accumulative culture, diluted 20 times during preparing the mixture of accumulative culture and sludge from digester in a ratio of 5:95.

Should be noted, in Ukraine humic products are mainly used as soil regulator for fruit trees, oil vegetables and short-term nutrition absorbing crops such as rice, wheat, etc. It can also be used as multi-functional high effective compound fertilizer after combination with the elements of nitrogen, phosphorus and potassium.

Further research is expected to lab-scale investigate ability to support biomethane production under brown coal bioconversion. The important direction of the research is microbiological investigation of the natural microorganisms' associations capable to effectively carry out complex bioconversion of LRC with the formation of an integral biochemical model of the process in artificially created cultivation conditions.

3 Conclusions

The biochemical parameters of LRC treatment were analyzed and methodological model of their using was formed to assess the effectiveness of the coal use as a mineral substrate by various groups of microorganisms. Thus, biotechnological approach is the promising way for the integrated processing of LRC to produce biogas and humic substances. At the same time, an important technological aspect is the removal of sulfur compounds and heavy metals from processing products. In this way, it is important to expand the bioenergy potential of brown coal to produce methane after biogas purification from impurities.

Different bacteria genera were considered under LRC biotreatment with biogas production and their cultivation conditions such as Desulfobacter sp., Methanosaeta sp., Methanosarcina sp., Rhodococcus sp., Lysinibacillus sp. etc. Thus, the main groups of bioactivators were analyzed, which will further help to choose the best option for combining them for carrying out a complex bioconversion of brown coal.

References

1. Marinaș, M. C., Dinu, M., Socol, A. G., Socol, C. (2018). Renewable energy consumption and economic growth. Causality relationship in Central and Eastern European countries. *PLoS One*, Vol. 13(10), e0202951, doi: 10.1371/journal.pone.0202951.
2. *World Energy Resources*. World Energy Council, 2016, http://www.worldenergy.org.
3. Burlakova, I. M., Us, Ya. O. (2015). The current state and prospects of development of the coal industry in Ukraine. Economic *Problems of Sustainable Development*, pp. 207–208, https://essuir.sumdu.edu.ua/bitstream/123456789/43674/3/Byrlakova_vygilna.pdf.
4. Ivanov., I. P., Teremova, M. I., Yeremina, A. O., Golovina, V. V., Fetisova, O. Yu., Skvortsova, G. P., Chesnokova, N. V., Kuznetsov, B. N. (2014). Aerobic processing of brown coal by Acinetobacter calcoaceticus strain. *Journal of Siberian Federal University, Chemistry*, Vol. 2(7), pp. 209–220.

5. Hinojosa, C., Guillermo, J., et al. (2017). Effect of a low rank coal inoculated with coal solubilizing bacteria for the rehabilitation of a saline-sodic soil in field conditions. *Revista Facultad Nacional de Agronomia*, Vol. 70(3), pp. 8271–8283.
6. Samoylik, V. G. (2016). *Classification of Solid Fossil Fuels and Their Research Methods*. Kharkiv, Vodnyy Spektr GMP, http://scicenter.online/gornoe-delo-scicenter/uglefikatsiya-143353.html.
7. Samoylik, V. G., Korchevskiy, A. N. (2016). *Theory and Technique of Experiment in the Enrichment of Minerals*. Donetsk, Tekhnopark DonGTU "UNITEKH" Ltd., http://scicenter.online/gornoe-delo-scicenter/izmenenie-gruppovogo-sostava-tgi-protsesse-143385.html.
8. Daman, S. W. (2015). Coal biotechnology: A creative approach for carbon reduction, environmental foot print, while moving coal up the value chain. *32nd International Pittsburgh Coal Conference*, Pittsburgh, Pennsylvania, USA, http://www.arctech.com.
9. Satarupa, R., Madhumita, R. (2015). Bioleaching of heavy metals by sulfur oxidizing bacteria: A review. *International Research Journal of Environment Sciences*, Vol. 4(9), pp. 75–79.
10. Costaa, M. C., Carvalhoa, N., Iglesiasb, N., Palencia, I. (2003). Bacterial leaching studies of a Portuguese flotation tailing. *15th International Biohydrometallurgy Symposium Athens*, pp. 75.
11. Brandl, H. (2008). *Microbial Leaching of Metals*. Zürich, Switzerland, pp. 194–197.
12. Chandra, S. G. (2009). *Possibilities to Use Industrial Oxidic By-products as Neutralising Agent in Bioleaching and the Effect of Chloride on Biooxidation*. Lulea University of Technology.
13. Krebs, W., Brombacher, C., Bossard, P. P., Bachofen, R., Brandl, H. (1997). Microbial recovery of metals from solids. *FEMS Microbiology Reviews*, Vol. 20, pp. 605–610.
14. Sattar, A., Shaheen, J., Suhail, A., Soomro, A. (2016). Biological removal of sulfur from coal through use of microorganism. A review. *4th International Conference on Energy, Environment and Sustainable Development*.
15. Yang, J., Wang, Q.-H., Wang, Q., Wu, T. (2009). Heavy metals extraction from municipal solid waste incineration fly ash using adapted metal tolerant Aspergillus niger. *Bioresource Technology*, Vol. 100(1), pp. 254–260.
16. Blayda, I. A., Vasyl'yeva, T. V. (2017). Bacterial desulphurization of coals (review). *Microbiology and Biotechnology*, Vol. 3, pp. 6–23, doi: 10.18524/2307-4663.2017.3(39).110877.
17. Etemadzadeh, S. S., Emtiazi, G., Etemadifar, Z. (2018). XRF analysis of coal bioleaching by chemolithoheterotrophic Alicyclobacillus HRM5 and chemolithoautotrophic Acidithiobacillus ferrooxidans. *Journal of Mining and Environment*, Vol. 9(3), pp. 559–566, doi: 10.22044/jme.2017.5573.1369.
18. Hong, F.-F., He, H., Liu, J.-Y., Tao, X.-X., Zheng, L., Zhao, Y.-D. (2013). Comparison analysis of coal biodesulfurization and coal's pyrite bioleaching with Acidithiobacillus ferrooxidans. *The Scientifc World Journal, Hindawi*, Vol. 2013, 184964, doi: 10.1155/2013/184964.
19. Cismasiu, C. M. (2010). The acidophilic chemolithotrophic bacteria involved in the desulphurization process of lignite and pit coal from Halanga, Mintia and Petrila mines. *Romanian Biotechnological Letters*, Vol. 15(5), pp. 5602–5610.
20. Liu, T., Hou, J.-H., Peng, Y.-L. (2017). Effect of a newly isolated native bacteria Pseudomonas sp. NP 22 on desulfurization of the low-rank lignite. *International Journal of Mineral Processing*, Vol. 162, pp. 6–11, doi: 10.1016/j.minpro.2017.02.014.
21. Abhilash, P., Pandey, B. D., Natarajan, K. A. (2015). *Microbiology for Minerals, Metals, Materials and the Environment. 1st Chapter: Microbial Biodesulphurisation of Coal*. CRC Press Editors, pp. 153–179.
22. *Dibenzothiophene Desulfurization Map*. EAWAG Biocatalysis/Biodegradation Database. Retrieved from http://eawag-bbd.ethz.ch/dbt/dbt_map.html.
23. *Dibenzothiophene Degradation Pathway*. EAWAG Biocatalysis/Biodegradation Database. Retrieved from http://eawag-bbd.ethz.ch/dbt2/dbt2_map.html.
24. Pandey, R. A., Raman, V. K., Bodkhe, S. Y., Handa, B. K., Bal, A. S. (2005). Microbial desulphurization of coal containing pyritic sulphur in a continuously operated bench scale coal slurry reactor. *Fuel*, Vol. 84(1), pp. 81–87.
25. Steubing, P. M. (1993). Isolation of an unknown bacterium from soil. *Proceedings of the 14th Workshop/Conference of the Association for Biology Laboratory Education (ABLE)*, pp. 81–114.
26. Gougoulias, C, Clark, J. M., Shaw, L. J. (2014). The role of soil microbes in the global carbon cycle: tracking the below-ground microbial processing of plant-derived carbon for manipulating carbon dynamics in agricultural systems, Journal of the Science of Food and Agriculture, Vol. 94(12), pp. 2362–2371.
27. Janssen, P. H., Yates, P. S., Grinton, B. E., Taylor, P. M., Sait, M. (2002) Improved culturability of soil bacteria and isolation in pure culture of novel members of the divisions Acidobacteria, Actinobacteria, Proteobacteria, and Verrucomicrobia. Applied and Environmental Microbiology, Vol. 68(5), pp. 2391–2396.
28. Begum, K., Mannan, S., Rezwan, R., Rahman, M. M., Rahman, M. S., Kamal, A. (2017). Isolation and characterization of bacteria with biochemical and pharmacological importance from soil samples of Dhaka city. *Dhaka University Journal of Pharmaceutical Sciences*, Vol. 16(1), pp. 129–136.
29. Sato, T. A. (1973). Simple rapid polychrome stain for epoxy-embedded tissue. *Stain. Technol, Baltimore, Williams and Wilkins*, Vol. 8, pp. 223–227.
30. Khoult, D., Krig, N., Spit, P. (1997). *Bergey's Manual of Determinative Bacteriology*. Moscow, Mir, Vol. 1.
31. Tanyolac, A., Durusoy, T., Ozbaş, T., Yurum, Y. (2013). Bioconversion of coal. *Clean Utilization of Coal*, pp. 97–107.

32. El-Gendy, N. S. (2006). Biodegradation potentials of dibenzothiophene by new bacteria isolated from hydrocarbon polluted soil in Egypt. *Biosciences Biotechnology Research Asia*, Vol. 31(1), pp. 95–106.
33. Elizabeth, J., Jones, P. M., Voytek, A., William, H. (2010). Stimulation of methane generation from nonproductive coal by addition of nutrients or a microbial consortium. *Environmental Microbiology*, Vol. 76(21), pp. 7013–7022.
34. Patent of RF for utility model No. 2139426. Coal Processing Method. Published on 10.10.1999. Retrieved from http://www.findpatent.ru/patent/213/2139426.html.
35. Fakoussa, R. M., Hofrichter, M. (1999). Biotechnology and microbiology of coal degradation. *Applied Microbiology and Biotechnology*, Vol. 52, pp. 25–40.

УДК 552.57

Екологічно безпечні напрямки біоконверсії низькоякісного вугля

Черниш Є.[1*], Пляцук Л.[1], Аблєєва І.[1], Яхненко О.[1],
Рубік Г.[2], М'якаєва Г.[1], Батальцев Є.[1], Ліс Д.[1]

[1] Сумський державний університет, вул. Римського-Корсакова, 2., 40007, м. Суми, Україна;
[2] Чеський агротехнічний університет, вул. Камицка, 129, 165 00, м. Прага, Чехія

Анотація. У цій статті наведені теоретичні дослідження біохімічних особливостей оброблення низькоякісного вугілля. Представлені біохімічні основи деградації органічних компонентів низькоякісного вугілля і біохімічні принципи біологічного вилучення з нього металів та сполук сірки. Проведено аналіз груп мікроорганізмів і визначені оптимальні умови вирощування останніх. Для ідентифікації необхідних екологічних і трофічних груп мікроорганізмів, а також для реалізації закономірності трофічних взаємодій у асоціаціях різних груп мікроорганізмів як в анаеробних, так і в аеробних умовах використовувались електронні бази даних KEGG, BacDive і EAWAG-BBD. З метою розроблення екологічно безпечного напрямку виробництва біогазу і гумінових продуктів застосовано методологічний підхід та сформована принципова схема біохімічних досліджень переробки низькоякісного вугілля.

Ключові слова: низькоякісне вугілля, біохімічні особливості, біогаз, гумінові кислоти, еколого-трофічні групи мікроорганізмів.

JOURNAL OF ENGINEERING SCIENCES
ЖУРНАЛ ІНЖЕНЕРНИХ НАУК
ЖУРНАЛ ИНЖЕНЕРНЫХ НАУК
Web site: http://jes.sumdu.edu.ua
Volume 6, Issue 2 (2019)

5th EAI International Conference on Management of Manufacturing Systems (MMS 2020) October 2020, Opatija, Croatia

Organizer: European Alliance for Innovation (EAI), Gent, Belgium
Co-organizers:

- Association for Promoting Innovative Technologies (InnovativeFET), Zagreb, Croatia (Udruga Innovative FET)
- Department of Information and Communication Traffic, Faculty of Transport and Traffic Sciences, University of Zagreb, Zagreb, Croatia
- Faculty of Manufacturing Technologies, Technical University of Košice, Košice, Slovakia

General Chair of MMS 2020: prof. Dragan Perakovic, Ph.D.
General Co-Chairs:

- Michal Balog, Ph.D., Assoc. Prof.
- Lucia Knapčíková, Ph.D., Assoc. prof, Ing. Paed. IGIP

Official website: http://manusystems.org

JOURNAL OF ENGINEERING SCIENCES
ЖУРНАЛ ІНЖЕНЕРНИХ НАУК
ЖУРНАЛ ИНЖЕНЕРНЫХ НАУК
Web site: http://jes.sumdu.edu.ua
Volume 6, Issue 2 (2019)

HERVICON + PUMPS

September 8-11, 2020, SumSU, Sumy, Ukraine

XVI International Scientific and Engineering Conference

Hermetic Sealing, Vibration Reliability and Ecological Safety of Pump and Compressor Machinery

Dedicated to the Memory of Professor, Dr.H.C. Volodymyr Martsynkovskyy

Organizers

Sumy State University
Hydraulic Machines and Systems Group
TRIZ Ltd.
Kielce University of Technology
Institute Pprime of University of Poitiers
Wroclaw University of Technology
Sumy National Agrarian University

Topics

- *Problems of reducing life-cycle cost of pump and compressor equipment.*
- *Static seals, axially movable and rotating shaft seals, improvement of reliability and efficiency of sealing units of pumps and compressors.*
- *Problems of fluid dynamics, optimization, dynamics and strength of turbomachines and their units.*
- *Reducing noise and vibration, vibration diagnostics and predicting of remaining life, balancing, identification of parameters, pump and compressor rotordynamics.*
- *Problems of tribology and metrology for seals and bearings, new materials and technologies.*
- *Ecologically safe operation of pump and compressor machinery, resource and energy-saving technologies.*
- *Computational engineering and computational mechanics.*

Deadline to submit the abstract is March 15, 2020

Deadline for registration is August 15, 2020

Contact Address

Sumy State University,
2, Rimsky - Korsakov Str.,
Sumy 40007, Ukraine
Tel./fax: *+38(0542) 33-35-94*

E-mail*: a.zagorulko@omdm.sumdu.edu.ua*

Web: *hervicon.sumdu.edu.ua/en/*

JOURNAL OF ENGINEERING SCIENCES
ЖУРНАЛ ІНЖЕНЕРНИХ НАУК
ЖУРНАЛ ИНЖЕНЕРНЫХ НАУК
Web site: http://jes.sumdu.edu.ua
Volume 6, Issue 2 (2019)

Copyright Agreement

We, the Authors of the Manuscript publishing in the Journal of Engineering Sciences, in the case of acceptance for publication, transfer to Founders and Editorial Board the underlined rights:

– publishing this article in English and distribution of the printed version;

– English translation of the article and distribution the hard copy of the translation;

– distribution of the electronic version of the article through any electronic means (by hosted on the official website of the Journal, in electronic databases, repositories, etc.).

We reserve the rights without the consent with the Editorial Board or Founders:

– to use the article materials partially or in whole for educational purposes;

– to use the article materials partially or in whole to write own dissertations;

– to use the article materials for thesis preparing, conference materials, as well as for presentations;

– to post electronic copies (including the final electronic version downloaded from the official web-site of the Journal):

– on the personal web-sources of all the co-authors (websites, webpages, blogs, etc.);

– on the web-sources of authors working organizations (including electronic institutional repository);

– on the International Scientometric Databases (CrossRef, DOAJ, Index Copernicus Indexing, etc.);

– on non-commercial Open Access sources (e.g. arXiv.org).

In all cases, the presence of citations to the article or hyper-link to the electronic copy of the official website of the journal is obligatory.

By this agreement, we also certify that the submitted manuscript:

– does not violate the copyrights of other persons or organizations;

– has not been published previously in other publishing houses and submitted for publication in other Journals.

© Sumy State University, 2019

JOURNAL OF ENGINEERING SCIENCES
ЖУРНАЛ ІНЖЕНЕРНИХ НАУК
ЖУРНАЛ ИНЖЕНЕРНЫХ НАУК
Web site: http://jes.sumdu.edu.ua
Volume 6, Issue 2 (2019)

Dear Authors of the Journal of Engineering Sciences!

The Editorial Board of the Journal of Engineering Sciences pays special attention to the structure of the articles according to the **List of Scientific Professional Editions of Ukraine** (Category "B", Minutes No. 1208 of 07.11.2018, Appendix No. 8). Only original articles by the authorship of up to 5 authors are accepted for the publication according to the **Template** with the following elements:

– general statement of the problem and its relationship with the important scientific or practical problems;
– analysis of the recent investigations and publications in the same research field;
– statement of the significance of the general problem that was not solved before;
– statement of the purpose of the research article;
– description of the initial data of the research with the justification of the achieved scientific results;
– conclusions and ways for further development of the research.

All the articles are reviewed by the independent double-blind procedure.

All the authors should send via e-mail jes@sumdu.edu.ua the electronic version of the following materials:
– article **in English** according to the **Template**;
– information about authors and their affiliation with the related address.

ATTENTION!
If one of the mentioned components is not sent or there are many stylistic, orthographic and grammatical errors, the article will not be taken into consideration by the Editorial Board and will not be reviewed.

The minimum size of the materials:
1. Scientific – theoretical articles (up to 25,000 symbols; about 14 pages) that deal with the theoretical research and descriptions of physical laws concerning the investigated phenomena; theoretical generalizations and fundamental principles proved by the experimental research data.
2. Scientific-practical articles (up to 10,000 symbols; about 6 pages) that deal with scientific experiments and real experience. They include the statement of the proposed methods for the experimental research or means for the observation of the studied phenomena. An essential part of these articles is the description of the achieved results and their explanation acquired in the process of immediate interaction with the object of investigations, its significance, and practical implementations.
3. Scientific-methodological articles (up to 15,000 symbols; about 8 pages) that deal with the review of processes, methods, instruments for solving scientific and applied problems; the statement of the new methodology, results of which allow creating more precise methodology on the basis of an up-to-date methodology for the implementation of discovered laws.

© Sumy State University, 2019

The Ministry of Education and Science of Ukraine

Міністерство освіти і науки України

Министерство образования и науки Украины

JOURNAL OF ENGINEERING SCIENCES

ЖУРНАЛ ІНЖЕНЕРНИХ НАУК

ЖУРНАЛ ИНЖЕНЕРНЫХ НАУК

Scientific Journal

Науковий журнал

Научный журнал

Відповідальний за випуск
Д. В. Криворучко
Комп'ютерне складання та верстання:
І. В. Павленко
Коректори:
Н. З. Клочко, С. М. Симоненко

Responsible for release:
D. V. Kryvoruchko
Computer design and typesetting
I. V. Pavlenko
Correctors:
N. Z. Klochko, S. M. Symonenko

Підписано до друку 23.12.2019. Формат 60x84/8.
Папір офс. Друк офс.
Ум. друк. арк. 17,68. Обл.-вид. арк. 24,04.
Наклад 100 прим. Замовлення №
Сумський державний університет, вул. Римського-Корсакова, 2, 40007, м. Суми, Україна
Свідоцтво про внесення суб'єкта видавничої справи до Державного реєстру
ДК № 3062 від 17.12.2007.

Надруковано у друкарні Сумського державного університету,
вул. Римського-Корсакова, 2, 40007, м. Суми, Україна

Editorial Board: 2 Rymskogo-Korsakova St., 40007 Sumy, Ukraine
Contact Phones: +38 (0542) 331024; +38 (099) 3845740
E-mail: jes@sumdu.edu.ua
Web-site: http://jes.sumdu.edu.ua

State registration certificate of the print mass-media No. 20499-10299 ПР.

© Sumy State University, 2019